Manipulation und Verschränkung von Quantenzuständen durch vollständige Kontrolle der Atom-Licht Wechselwirkung
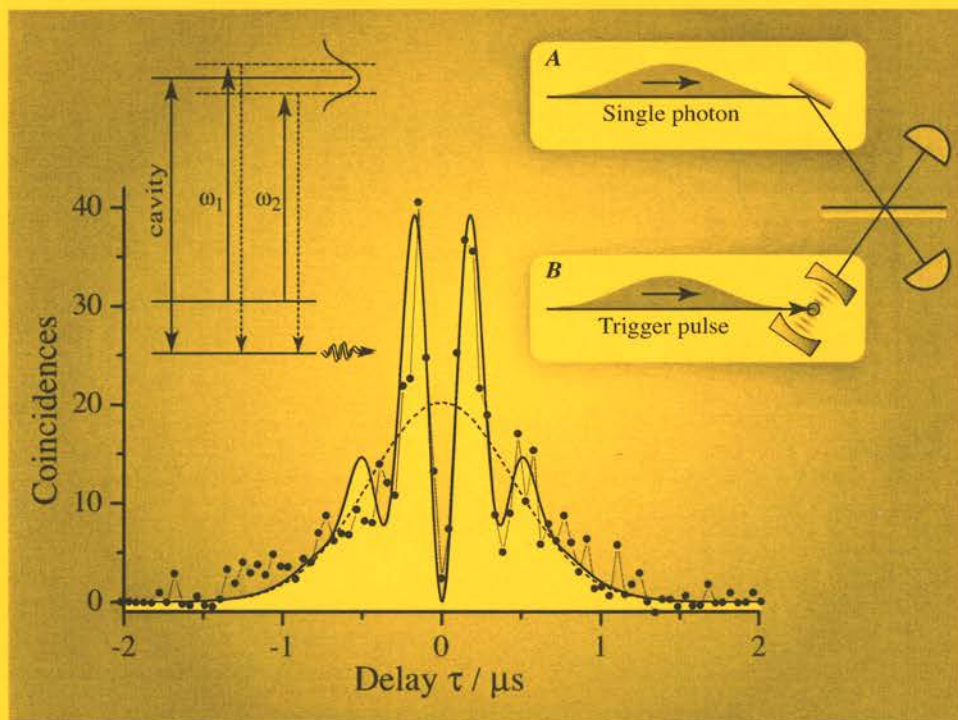

Axel Kuhn

MAX-PLANCK-INSTITUT FÜR QUANTENOPTIK

Manipulation und Verschränkung von Quantenzuständen durch vollständige Kontrolle der Atom-Licht Wechselwirkung

Axel Kuhn

Manipulation und Verschränkung von Quantenzuständen durch vollständige Kontrolle der Atom-Licht Wechselwirkung
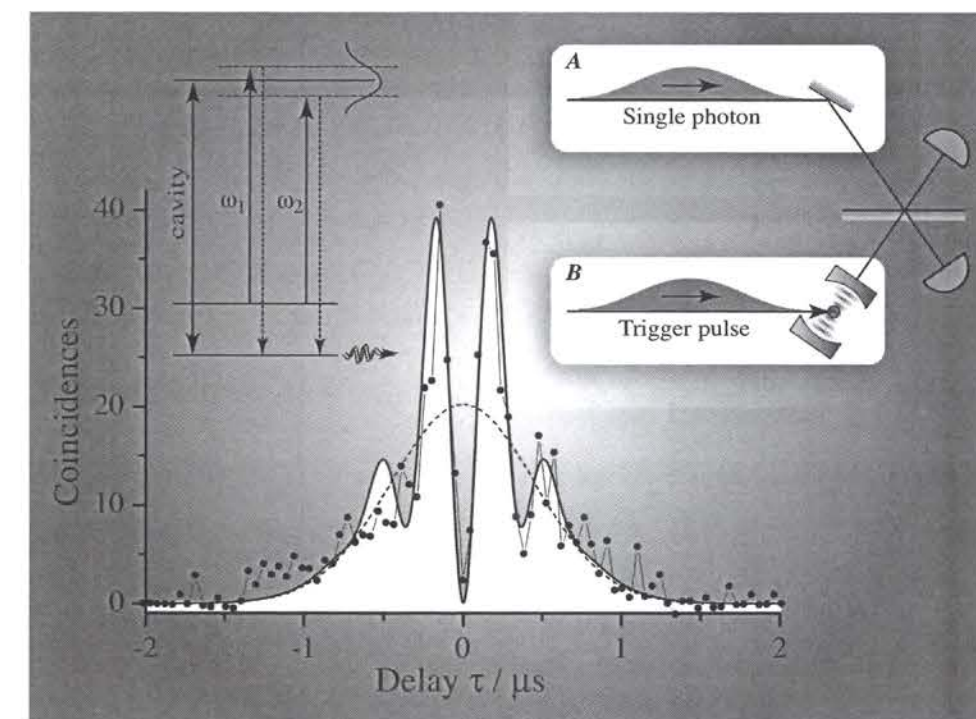
Axel Kuhn, Max-Planck-Institut für Quantenoptik, 85748 Garching, Deutschland
und Physik Department an der Technischen Universität München

In den letzten Jahren wurden mit der gezielten Manipulation und Verschränkung von Quantenzuständen, wie inneren und äußeren Freiheitsgraden von Atomen und Photonen, die Voraussetzungen für die Realisierung von Quantencomputern geschaffen. Aspekte davon sind hier gezeigt: Durch Kontrolle der Atom-Licht Wechselwirkung werden neutrale Atome in den Schwingungsgrundzustand einer Dipolkraftfalle gekühlt und anschließend gezielt in einem angeregten Fockzustand präpariert. Zudem ist es gelungen, durch Kopplung von Atomen an das Lichtfeld eines optischen Resonators eine Schnittstelle zwischen Atom und Licht zu realisieren. Diese ermöglicht nicht nur die Emission einzelner Photonen mit wohldefinierten spektralen Eigenschaften quasi auf Knopfdruck, sondern gestattet im Prinzip auch eine Verschränkung entfernter Atome durch Bell-Messungen an den emittierten Photonen. Beides ist wesentlich für einen skalierbaren Quantenprozessor, in dem einzelne Photonen und Atome als Informationsträger bzw. Datenspeicher dienen.

Manipulation and Entanglement of Quantum States by full Control of the Atom-Light Interaction

Axel Kuhn, Max-Planck-Institut für Quantenoptik, 85748 Garching, Germany
and Physics Department at the Technische Universität München

During the last years, the essential prerequesites for the technical realisation of quantum computers became available with the deterministic manipulation and entanglement of quantum states, like inner and outer degrees of freedom of atoms and photon number states of light. Aspects thereof are presented here. The complete control of the atom-light interaction allows to cool atoms down to the vibrational ground state of a surrounding atom trap, and starting from there, an adiabatic passage is used to populate specific excited Fock states. Moreover, it is possible to control the coupling of single atoms to the light field of an optical cavity. This interface between atom and light allows to deterministically generate single photons on demand with well-defined spectral properties, and it offers the possibility to entangle a single atom with the quantum state of a distant light field. These are essential steps towards a scalable quantum processor, where photons and atoms act as information carriers and quantum memories, respectively.

Inhaltsverzeichnis

Kapitel 1

Zustandsmanipulation im Wandel der Zeit

Die gezielte Manipulation von Quantensystemen hat in den letzten Jahrzehnten die Entwicklung vom Traum zur Realität durchlebt. Mit dem Einzug des Lasers [1] in die moderne Physik gab es erstmals die Möglichkeit, optische Übergänge zwischen diskreten atomaren Energiezuständen gezielt zu treiben [2–4], und somit atomare Ensembles signifikant aus dem thermischen Gleichgewichts zu bringen. Selbst dem zufälligen Charakter, der einer Besetzung angeregter Zustände mit anschließender spontaner Emission zu einer Vielzahl von Niveaus innewohnt, konnte man mit ausgefeilten Verfahren begegnen. Diese bauen auf unitären Prozessen auf, die nur Übergänge zwischen langlebigen Zuständen ermöglichen [5].

Mit der Manipulation innerer Zustände bot sich die Chance, auch die Bewegung von Atomen zu beeinflussen. Einzelne absorbierte oder emittierte Photonen übertragen Impulse der Größe $\hbar k$ auf ein Atom. Durch Beschränkung des Impulsübertrags auf bestimmte Geschwindigkeitsklassen, z.B. durch den Dopplereffekt, lassen sich optische Melassen und magnetooptische Fallen realisieren und freie Atome in den sub-nK Bereich abkühlen [6]. In Ionenfallen oder optischen Dipolkraftfallen können durch gezieltes Treiben von Vibrationsübergängen Ionen bzw. Atome in den Schwingungsgrundzustand gebracht und von dort in andere Vibrationsniveaus überführt werden. Dies gestattet durch Verschränkung innerer und äußerer Zustände einfache Quantengatter zu realisieren [7, 8].

Auf ähnliche Art lässt sich auch der Zustand von Lichtfeldern kontrollieren. Jede Emission oder Absorption erniedrigt bzw. erhöht die Photonenzahl im Strahlungsfeld um Eins. In einem Laserstrahl fällt dies kaum ins Gewicht, doch im quantisierten Lichtfeld eines optischen Resonators hat dies eine drastische Auswirkung. Ein einziges Atom im Resonator genügt, um die Photonenzahl gezielt zu manipulieren und nichtklassische Zustände des Strahlungsfeldes zu erzeugen.

Die Kontrolle von Quantensystemen eröffnet vielfältige Perspektiven: (1) Kalte Atome sind der Schlüssel zu kohärenter Atomoptik, Atominterferometrie und hochpräzisen Atomuhren. (2) Bose-Einstein Kondensate (BEC), die sich in Verbindung mit weiteren Kühlverfahren realisieren lassen, haben eine Vielzahl neuer grundlegender Experimente ermöglicht. (3) Die Quanteninformationsverarbeitung baut auf der Möglichkeit zur Kontrolle und Präparation einzelner Quantensysteme und Methoden zur gezielten Verschränkung verschiedenartiger Quantensysteme auf, wie z.B. inneren Energiezuständen von Ionen mit Vibrationszuständen in Ionenfallen, oder atomaren Energiezuständen mit Photonenzahlzuständen in Resonatoren [9–11].

In den hier vorgestellten Arbeiten wird durch geschickten Einsatz der Atom-Licht Wechselwirkung in Form einer adiabatisch getriebenen stimulierten Raman-Streuung eine nahezu vollständige Kontrolle von Quantensystemen erreicht. Demonstriert wird dies anhand der Raman- und Raman-Seitenbandkühlung von Atomen in optischen Dipolkraftfallen und anhand der deterministischen Atom-Photon Kopplung und Verschränkung in optischen Resonatoren hoher Finesse.

1

Kapitel 2

Atom-Licht Wechselwirkung im Griff

Die Wechselwirkung von Atomen mit kohärenten Lichtfeldern ist in [2, 3, 12, 13] ausführlich dargelegt. An dieser Stelle sind daher nur wesentliche Aspekte geschildert, die für die vollständige Zustandskontrolle relevant sind.

2.1 Zwei- und Drei-Niveau Atome

Zunächst beschränken wir die Betrachtung auf einen einzigen atomaren Übergang mit Übergangsdipolmoment μ_{eg} und Resonanzfrequenz ω_{eg} zwischen zwei atomaren Energieniveaus, $|g\rangle$ und $|e\rangle$, der von kohärentem Licht der Frequenz ω_L und elektrischer Feldamplitude E_0 getrieben wird. Unter Vernachlässigung jedweder Relaxationsprozesse wird dieses gekoppelte System in Rotating-Wave Approximation (RWA) durch den Hamilton-Operator

$$\hat{H} = \hbar\Delta\hat{\sigma}_{gg} - \frac{\hbar}{2}\Omega\left[\hat{\sigma}_{eg} + \hat{\sigma}_{ge}\right] \tag{2.1}$$

beschrieben, wobei $\Delta = \omega_L - \omega_{eg}$ die Verstimmung des Lichts von der atomaren Resonanz angibt und $\Omega = \mu_{eg}E_0/\hbar$ die Rabi-Frequenz des treibenden Felds bezeichnet. Dieses System besitzt die Eigenfrequenzen $\omega^\pm = \frac{1}{2}\left(\Delta \pm \sqrt{\Omega^2 + \Delta^2}\right)$ mit den zugehörigen Eigenvektoren

$$|\phi^+\rangle = \cos\phi|g\rangle - \sin\phi|e\rangle \qquad \text{und} \qquad |\phi^-\rangle = \sin\phi|g\rangle + \cos\phi|e\rangle, \tag{2.2}$$

wobei der Mischungswinkel durch $\tan\phi = (\sqrt{\Omega^2 + \Delta^2} - \Delta)/\Omega$ festgelegt ist. Die Frequenzaufspaltung der Eigenzustände, $\Omega_{\text{eff}} = \sqrt{\Omega^2 + \Delta^2}$, wird auch als effektive Rabi-Frequenz bezeichnet, mit
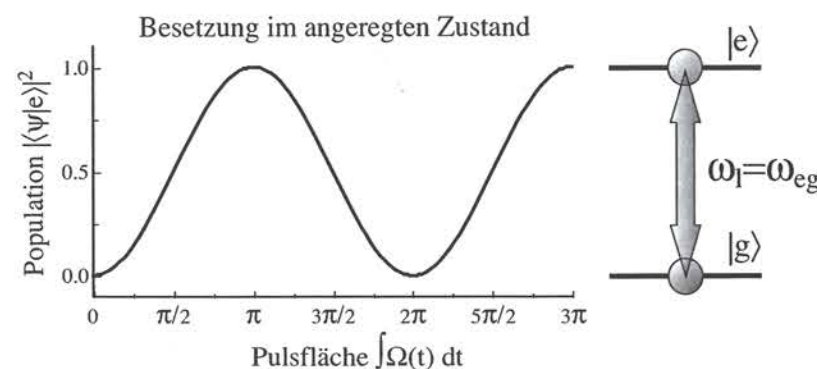
Abbildung 2.1: Besetzungsoszillation im resonant getriebenen Zwei-Niveau System. Vollständige Inversion wird bei einer Laserpulsfläche von π erreicht, entsprechend einer Pulsdauer von $t = \pi/\Omega$ bei konstanter Rabifrequenz.
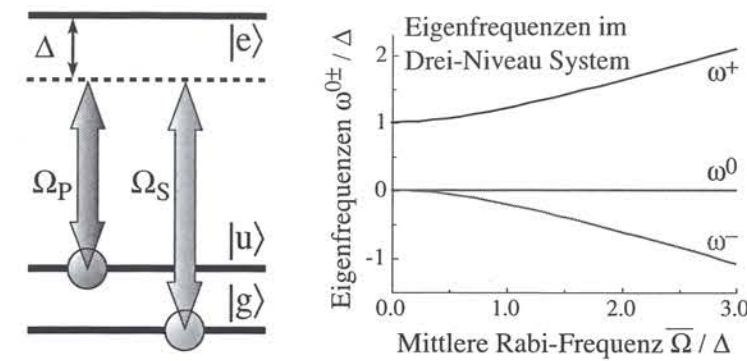
Abbildung 2.2: Drei-Niveau System in Λ-Anordnung. Eigenfrequenzen als Funktion der mittleren Rabifrequenz, $\bar{\Omega} = \sqrt{\Omega_P^2 + \Omega_S^2}$.

der ein Teil der Besetzung zwischen $|g\rangle$ und $|e\rangle$ oszilliert. Sind Zerfallsprozesse (wie z.B. spontane Emissionen) auf der Zeitskala der Anregung vernachlässigbar, lässt sich eine beliebige Superposition der Zustände $|g\rangle$ und $|e\rangle$ durch geeigneten Abbruch der Besetzungsoszillation einstellen. Abbildung 2.1 zeigt, dass eine resonante Anregung der Dauer π/Ω, die auch als π-Puls bezeichnet wird, zu einer vollständigen Inversion des Systems führt.

Wesentlich mehr Flexibilität bietet die in Abb. 2.2 gezeigte $\Lambda-$förmige Anordnung von drei Niveaus. Hier werden zwei Übergänge der Frequenzen ω_{eu} und ω_{eg} von Lichtfeldern der Frequenzen ω_P bzw. ω_S getrieben. Sind die Verstimmungen der Felder von den jeweiligen Resonanzen identisch, $\omega_P - \omega_{eu} = \omega_S - \omega_{eg} \equiv \Delta$, dann wird das System in RWA durch den Hamilton-Operator

$$\hat{H} = \hbar\Delta\hat{\sigma}_{ee} - \frac{\hbar}{2}\Omega_S\left[\hat{\sigma}_{eg} + \hat{\sigma}_{ge}\right] - \frac{\hbar}{2}\Omega_P\left[\hat{\sigma}_{eu} + \hat{\sigma}_{ue}\right] \tag{2.3}$$

beschrieben, wobei Ω_P und Ω_S die entsprechenden Rabi-Frequenzen bezeichnen. Das gekoppelte System besitzt drei Eigenfrequenzen, $\omega^0 = 0$ und $\omega^\pm = \frac{1}{2}(\Delta \pm \sqrt{\Omega_P^2 + \Omega_S^2 + \Delta^2})$, mit den Eigenzuständen

$$\begin{aligned}
|\phi^0\rangle &= \left(\Omega_S|u\rangle - \Omega_P|g\rangle\right)\big/\sqrt{\Omega_P^2 + \Omega_S^2}, \\
|\phi^+\rangle &= \cos\phi\sin\Theta|u\rangle - \sin\phi|e\rangle + \cos\phi\cos\Theta|g\rangle, \\
|\phi^-\rangle &= \sin\phi\sin\Theta|u\rangle + \cos\phi|e\rangle + \sin\phi\cos\Theta|g\rangle,
\end{aligned} \tag{2.4}$$

wobei die Mischungswinkel durch $\tan\phi = \sqrt{\Omega_S^2 + \Omega_P^2}/(\sqrt{\Omega_S^2 + \Omega_P^2 + \Delta^2} - \Delta)$ und $\tan\Theta = \Omega_P/\Omega_S$ gegeben sind. Im Folgenden ist nur der Eigenzustand $|\phi^0\rangle$ von Interesse, da zu diesem (im Gegensatz zu $|\phi^\pm\rangle$) der elektronisch angeregte Zustand $|e\rangle$ nicht beiträgt, so dass eine spontane Emission von Photonen ausgeschlossen ist. Dies bedeutet, dass in $|\phi^0\rangle$ präparierte Atome kein Fluoreszenzlicht aussenden, selbst wenn sie zwei Lichtfeldern ausgesetzt sind, die prinzipiell in der Lage wären das strahlende Niveau $|e\rangle$ zu bevölkern. In Raman-Spektren führt dieser Effekt zu Dunkelresonanzen, die auftreten, sobald die Raman-Resonanzbedingung erfüllt ist. Aus diesem Grund wird $|\phi^0\rangle$ häufig als Dunkelzustand bezeichnet.

2.2 Stimulierte Raman-Übergänge

Prinzipiell ist ein kontrollierter Besetzungstransfer in Atomen oder Molekülen nur zwischen Zuständen möglich, deren Lebensdauer deutlich über der Dauer des Transferprozesses liegt. Dies trifft z.B.

auf Hyperfeinzustände im elektronischen Grundzustand eines Atoms, auf Rotations- und Vibrations-
zustände von Molekülen im Grundzustand, und auch auf Vibrationszustände von Atomen im umge-
benden künstlichen Potential einer Atomfalle zu. Sind, wie zuvor betrachtet, $|u\rangle$ und $|g\rangle$ die langle-
bigen Zustände eines Drei-Niveau Systems, dann entspricht ein optischer Übergang zwischen diesen
Niveaus einer Raman-Streuung von Licht, bei der sich die Frequenzen des einfallenden (absorbier-
ten) Lichts von der des gestreuten (emittierten) Lichts voneinander unterscheiden. Im Λ-förmigen
Drei-Niveau System entspricht dies einem indirekten Übergang zwischen den beiden energetisch
niedriger gelegenen Zuständen, wobei das einfallende Licht den Übergang von $|u\rangle$ nach $|e\rangle$ anregt
und die Emission von $|e\rangle$ nach $|g\rangle$ erfolgt. Typischerweise stehen jedoch meist mehr als drei Zustände
zur Verfügung, so dass die Emission zu einer Vielzahl anderer Niveaus erfolgen kann. Dies ist nicht
erwünscht, und um derartige Verluste zu vermeiden oder zumindest zu reduzieren, wird die Emission
auf dem gewünschten Übergang häufig durch ein weiteres Lichtfeld stimuliert. Dies kann auf meh-
rere Arten geschehen:

(1) Eine Folge von π-Pulsen entspricht der intuitiven Vorgehensweise, bei der ein erster π-Puls den
Übergang von $|u\rangle$ nach $|e\rangle$ treibt und anschließend ein weiterer π-Puls den zweiten Übergang von $|e\rangle$
nach $|g\rangle$. Falls die Pulsfolge kurz im Vergleich zur Lebensdauer des angeregten Niveaus $|e\rangle$ ist, wird
dadurch ein nahezu vollständiger Transfer von $|u\rangle$ nach $|g\rangle$ realisiert.

(2) Durch simultanes Anregen beider Übergänge nahe der Resonanz oszilliert die Besetzung im
Drei-Niveau System und ein Teil geht durch spontane Emission aus $|e\rangle$ verloren. Nur etwa die Hälfte
der angeregten Atome gelangt in $|\phi^0\rangle$ und ist diesem Verlustmechanismus nicht unterworfen. Von
diesen entfällt ein Teil auf Zustand $|g\rangle$, so dass insgesamt etwa 25% der Atome von $|u\rangle$ nach $|g\rangle$
gelangen.

(3) Ein effektives Zwei-Niveau System erhält man bei großer simultaner Verstimmung Δ der bei-
den Lichtfelder von den jeweiligen Übergangsfrequenzen. In diesem Fall lässt sich das elektronisch
angeregte Niveau aus dem Zustandsvektor, $|\Psi\rangle = c_u|u\rangle + c_e|e\rangle + c_g|g\rangle$, mit dem Ansatz $\frac{d}{dt}c_e = 0$
adiabatisch eliminieren. Der Hamilton-Operator (2.3) nimmt daraufhin die Form

$$\hat{H}_{\text{eff}} = \hbar\Delta_{\text{DS}}\hat{\sigma}_{gg} - \frac{\hbar}{2}\Omega_{\text{Raman}}\left[\hat{\sigma}_{ug} + \hat{\sigma}_{gu}\right] \qquad (2.5)$$

an, wobei $\Omega_{\text{Raman}} = \Omega_P\Omega_S/(2\Delta)$ die effektive Rabi-Frequenz des Raman-Übergangs angibt und
$\Delta_{\text{DS}} = (\Omega_P^2 - \Omega_S^2)/(4\Delta)$ die differentielle dynamische Stark-Verschiebung, die bei unterschiedli-
chen Rabi-Frequenzen der beiden Felder von Null verschieden ist. Abgesehen von Verlusten durch
spontane Emission, die hier nicht auftreten, verhält sich dieses System exakt wie ein Zwei-Niveau
Atom. Daher ist ein vollständiger Transfer von $|u\rangle$ nach $|g\rangle$ z.B. durch einen Raman-π-Puls zu be-
werkstelligen.

(4) Anti-intuitiv zeitverzögerte Laserpulse erlauben, den stimulierten Raman-Übergang mit einer
adiabatischen Passage zu treiben. Diese Technik ist als *STIRAP* bekannt und wurde von K. Berg-
mann und Mitarbeitern entwickelt und zum Besetzungstransfer in Atomen und Molekülen einge-
setzt [5, 14–16]. Dazu ist eine starke Wechselwirkung der Atome mit dem stimulierenden Laserpuls
notwendig, bevor der Pumplaserpuls einsetzt. Im Idealfall endet die Wechselwirkung mit dem sti-
mulierenden Feld, sobald der Pumplaserpuls sein Maximum erreicht. Diese Pulsfolge gestattet eine
vollständige und verlustfreie Inversion des Systems. Im Abschnitt 2.3 ist dies näher erläutert.

Alle Methoden einen Raman-Übergang zu stimulieren haben gemein, dass jedes betroffene Atom
ein Photon aus dem Pumpfeld absorbiert und ein anderes in das stimulierende Feld emittiert. Dies
ist zwangsweise mit einem Impulsübertrag von $\hbar k$ pro emittiertem und absorbiertem Photon an das
Atom verbunden, der parallel bzw. antiparallel zu den jeweiligen Strahlrichtungen erfolgt. In Kapitel
3 wird gezeigt, dass sich dies gezielt einsetzen lässt, um die Bewegung von Atomen zu beeinflussen.

Zudem erlaubt die Änderung der Photonenzahl des stimulierenden Feldes die in Kapitel 4 disku-
tierte Quantenschnittstelle zwischen Atomen und Licht zu realisieren, die sich z.B. zur Erzeugung
einzelner Photonen verwenden lässt.

2.3   Adiabatische Passage

Anregung und kohärenter Besetzungstransfer von Atomen oder Molekülen durch adiabatische Pas-
sage ist eine Technik, die seit vielen Jahren zum Einsatz kommt [17]. Diese Vorgehensweise zeichnet
sich dadurch aus, dass die Zeitentwicklung des Zustandsvektors des betrachteten Systems, $|\Psi\rangle$, nicht
durch Rabi-Oszillationen bestimmt ist, sondern durch die Evolution der Eigenzustände, $|\phi_i(t)\rangle$, des
zeitabhängigen Wechselwirkungs-Hamiltonoperators, $\hat{H}(t)$. Bei hinreichend langsamer und somit
adiabatischer Änderung des Hamilton-Operators folgt der Zustandsvektor jeder Änderung der Ei-
genzustandsbasis und ist somit zu jedem Zeitpunkt gegeben durch

$$|\Psi(t)\rangle = \sum_i \alpha_i \exp\left(-i\int_0^t \omega_i(t')dt'\right)|\phi_i(t)\rangle, \qquad (2.6)$$

wobei die Linearkoeffizienten α_i bereits zu Beginn der Wechselwirkung durch Projektion des An-
fangszustands auf die Eigenzustandsbasis festgelegt sind. Die anschliessende Zeitentwicklung der
Eigenzustände wird in Zwei-Niveau Atomen häufig durch einen Frequenz-Chirp des treibenden Fel-
des über die Resonanz bewerkstelligt, während in Drei-Niveau Systemen entweder die Amplitu-
den der treibenden Felder systematisch variiert werden, oder ebenfalls ein Frequenz-Chirp über die
Raman-Resonanz zur Anwendung kommt, um Übergänge im effektiven Zwei-Niveau System zu trei-
ben.

Nach ersten Realisierungen dieser Technik im Radiofrequenzbereich [18] folgten optische An-
regungen mit Frequenz-Chirp in Zwei- und Drei-Niveau Systemen [19–22], die sich auch zur ge-
schwindigkeitsselektiven Anregung und zur Raman-Kühlung neutraler Atome eignen [23, 24]. Ohne
Frequenz-Chirp, aber durch Variation der Amplituden der Laserpulse, die einen Raman-Übergang
treiben, konnten Effekte wie elektromagnetisch induzierte Transparenz (EIT) [25, 26], langsames
Licht [27–30] und stimulierte Raman-Streuung durch adiabatische Passage, *STIRAP* [5, 14–16], be-
obachtet werden.

Abbildung 2.3: Adia-
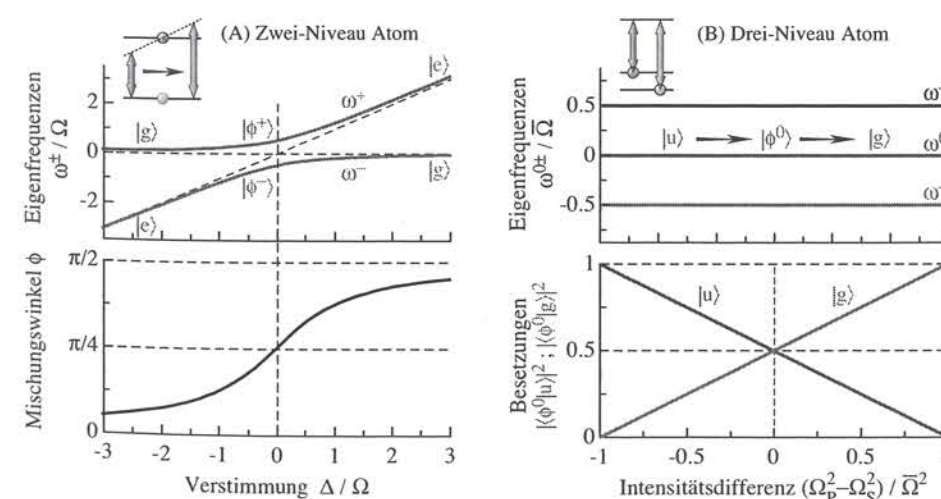batische Passage. **(A)**
Bei Frequenzchirp über
die Resonanz im Zwei-
Niveau Atom wechselt
ϕ von 0 nach $\pi/2$, und
$|\phi^+\rangle$ von $|g\rangle$ nach $|e\rangle$.
(B) Im Drei-Niveau
Atom bestimmen die
Intensitäten den Antei-
le von $|u\rangle$ und $|g\rangle$ an
$|\phi^0\rangle$. Das Verhältnis
der Eigenfrequenzen zu
$\bar{\Omega} = \sqrt{\Omega_P^2 + \Omega_S^2}$ ist fest.

Im Folgenden beschränken wir die Betrachtung auf Drei-Niveau Systeme in Λ-Konfiguration. Diese können, wie zuvor erwähnt, bei hinreichend grosser mittlerer Verstimmung, $\Delta = (\Delta_P + \Delta_S)/2 \gg \Omega_{P,S}$, auch als effektive Zwei-Niveau Systeme aufgefasst werden. In diesem Fall sind Verluste durch spontane Emission aus dem angeregten Zustand $|e\rangle$ vernachlässigbar, so dass sich die Eigenzustände $|\phi^+\rangle$ oder $|\phi^-\rangle$ des Zwei-Niveau Systems bestens zum adiabatischen Besetzungstransfer eignen. Hier gilt es jedoch einige Besonderheiten zu beachten: Beide Eigenzustände sind verlustfrei und weisen unterschiedliche Eigenfrequenzen auf. Werden beide zu Beginn des Anregungsprozesses besetzt, so führt dies zu einer Besetzungsoszillation zwischen $|u\rangle$ und $|g\rangle$ mit der Differenzfrequenz $\omega^+ - \omega^-$. Dies ist einer Rabi-Oszillation äquivalent, die zu vermeiden ist, um eine adiabatische Passage zu treiben. Dazu es notwendig, die Anfangsbesetzung in nur einen der beiden Eigenzustände zu überführen. Dies gelingt indem die Frequenzdifferenz der Felder anfangs so gewählt ist, dass sie von der Raman-Resonanz abweicht. Im weiteren Verlauf wird die relative Verstimmung der beiden Felder, $\delta := \Delta_P - \Delta_S$, langsam über die Raman-Resonanz gefahren (Frequenz-Chirp). Dabei entwickelt sich $|\phi^-\rangle$ (bzw. $|\phi^+\rangle$) von $|u\rangle$ nach $|g\rangle$ bei anfangs negativer (bzw. positiver) Verstimmung. Abbildung 2.3(A) zeigt die damit einhergehenden Variationen der Eigenfrequenzen und des Mischungswinkels, ϕ, der die Beiträge der ungestörten Zustände eines Zwei-Niveau Atoms an den Eigenzuständen angibt. Folgt der Zustandsvektor des Systems dem Eigenzustand adiabatisch, dann führt dies zu einer vollständigen Inversion des Systems. Adiabatisches Folgen im Bild der veränderlichen Eigenfrequenzen bedeutet hier, dass die gezeigte Zustandskreuzung bei hinreichend starker Kopplung vermieden wird. Die freie Wahl der Anfangs- und Endfrequenz des Frequenz-Chirps gestattet es, die Anregung in dopplerverbreiterten Medien auf beliebige Geschwindigkeitsklassen zu beschränken, oder auch eine bestimmte Gruppe von Energieniveaus in einem äußeren Potential anzusprechen. Daher konnten wir diese Methode zur Raman- und Raman-Seitenbandkühlung gefangener Atome in Dipolkraftfallen einsetzen [23, 24].

Bei Betrachtung eines vollständigen Drei-Niveau Systems (d.h. bei kleinem Δ) kommt dem Dunkelzustand, $|\phi^0\rangle$, eine besondere Bedeutung zu, da davon ausgehend kein spontaner Zerfall möglich ist. Ein entsprechend präpariertes System verbleibt im Prinzip immer in diesem Zustand, und die relative Besetzung in den dazu beitragenden atomaren Zuständen, $|u\rangle$ und $|g\rangle$, lässt sich durch Änderung des Verhältnisses der beiden Rabi-Frequenzen, Ω_P und Ω_S, nach Belieben einstellen. Um dies zu veranschaulichen betrachten wir ein anfangs in $|u\rangle$ präpariertes System. Aus Gleichung (2.4) folgt, dass dieser Zustand dem Dunkelzustand $|\phi^0\rangle$ entspricht, falls zu Beginn der Wechselwirkung $\Omega_S \gg \Omega_P$ gilt:

$$|\langle u|\phi^0\rangle|^2 = \frac{\Omega_S^2}{\Omega_P^2 + \Omega_S^2} \xrightarrow{\Omega_S \gg \Omega_P} 1. \qquad (2.7)$$

Nach erfolgreicher Präparation folgt $|\Psi\rangle$ dem Dunkelzustand, falls jede Änderung des Hamilton-Operators hinreichend langsam, d.h. adiabatisch, erfolgt. In diesem Fall ist das Besetzungsverhältnis stets gegeben durch

$$\frac{|\langle u|\Psi(t)\rangle|^2}{|\langle g|\Psi(t)\rangle|^2} = \frac{|\langle u|\phi^0(t)\rangle|^2}{|\langle g|\phi^0(t)\rangle|^2} = \frac{\Omega_S^2(t)}{\Omega_P^2(t)} \qquad (2.8)$$

Dies erlaubt nicht nur einen vollständigen STIRAP-Transfer der Besetzung von $|u\rangle$ nach $|g\rangle$ durch Änderung der Feldamplituden nach $\Omega_P \gg \Omega_S$, sondern prinzipiell auch die Präparation beliebiger Superpositionszustände. Das Prinzip ist in Abb. 2.3(B) veranschaulicht. Die normierte Intensitätsdifferenz überträgt sich 1:1 in eine Besetzungsdifferenz der zum Dunkelzustand $|\phi^0\rangle$ beitragenden ungestörten atomaren Zustände, $|u\rangle$ und $|g\rangle$. Im Gegensatz zum Zwei-Niveau Atom ist hier das Verhältnis der Eigenfrequenzen zu $\bar{\Omega}$ konstant, so dass der Besetzungstransfer nicht anhand ihres Verlaufs erkennbar ist.

Die STIRAP-Technik wurde ursprünglich zum Besetzungstransfer in Atomen und Molekülen eingesetzt [5, 14–16]. Diese Experimente basieren auf einer Zeitverzögerung zwischen dem stimulierenden Feld und dem Pumpfeld, um die gewünschte Entwicklung des Dunkelzustands von $|u\rangle$ nach $|g\rangle$ sicherzustellen. Daran angelehnt haben in [31] vorgeschlagen, den stimulierenden Laserstrahl durch die Wechselwirkung eines Atoms mit der Feldmode eines optischen Resonators zu ersetzen. Diese Mode ist anfangs mit $n - 1$ Photonen besetzt, und sie ist resonant mit dem $|g\rangle \leftrightarrow |e\rangle$ Übergang im Atome. Dies führt zu einer äquivalenten Rabi-Frequenz von $\Omega_S = 2g\sqrt{n}$, wobei g die Atom-Resonator Kopplungskonstante bezeichnet. Auch in diesem Fall erlaubt ein zusätzlich eingestrahlter Pumplaser den Raman-Übergang im Atom adiabatisch zu treiben. Gleichzeitig ändert dies die Zahl der Photonen im Resonator, denn allein aus Gründen der Energieerhaltung muss sich das System aus Atom und Resonator vom Anfangszustand $|u, n - 1\rangle$ nach $|g, n\rangle$ entwickeln, d.h. ein Photon wird der Feldmode des Resonators hinzugefügt. Für einen verlustfreien Resonator ließe sich auf diese Art jeder beliebige Photonenzahlzustand (Fock-Zustand) generieren. Im vorliegenden Fall ist jedoch der zunächst lichtlose Resonator von besonderem Interesse. Der Raman-Übergang erfolgt von $|u, 0\rangle$ nach $|g, 1\rangle$ mit einer äquivalenten stimulierenden Rabi-Frequenz des Resonators von $\Omega_S = 2g$. Ein Photon wird im Resonator erzeugt und aufgrund der endlichen Güte des Resonators schließlich aus diesem emittiert.

Kapitel 3

Optisches Kühlen und Präparation von Fock-Zuständen

Aus der Vielzahl optischer Kühlverfahren, die in den letzten Jahren für neutrale Atome entwickelt wurden [6], greift dieses Kapitel nur Methoden heraus, die auf adiabatisch getriebenen Raman-Übergängen in Drei-Niveau Atomen basieren. Einerseits gestattet dieser Ansatz unter Ausnutzung des Dopplereffekts eine breite Geschwindigkeitsklasse von Atomen anzusprechen, so dass es auf diese Art möglich ist, spinpolarisierte Cäsiumatome in einer optischen Dipolkraftfalle auf 640 nK abzukühlen. Andererseits sind Raman-Übergänge so schmalbandig, dass Schwingungsniveaus in hinreichend steilen Atomfallen aufgelöst werden können. Dies erlaubt die Raman-Seitenbandkühlung gefangener Atome im Potential eines eindimensionalen optischen Gitters, das durch Interferenz zweier Laserstrahlen gebildet wird. Auf diese Art gelang es, 92(5)% eines Ensembles gefangener Cäsiumatome in einer Dimension in den Schwingungsgrundzustand der Falle zu bringen und diese Atome anschließend mit einem Raman-Laserpuls gezielt in den ersten angeregten Vibrationszustand zu überführen.

3.1 Raman-Kühlen mit Frequenz-Chirp

Erste Experimente zur eindimensionalen Raman-Kühlung freier Atome stießen mit Temperaturen von 3 nK in ein Regime weit unterhalb des Ein-Photonen Rückstoßlimits vor [32–35]. Dies macht eine Anwendung dieses Kühlverfahrens auf gefangene Atome in einer harmonischen Falle sehr attraktiv, da in dieser die Phasenraumdichte mit T^{-3} ansteigt, so dass ein entartetes Quantengas in Reichweite scheint. Uns ist es gelungen, Cäsiumatome in einer optischen Dipolkraftfalle durch Raman-Kühlen mit frequenzgechirpten Laserpulsen fast bis zum Rückstoßlimit abzukühlen [23, 36].

Das Schema der Raman-Kühlung ist in Abb. 3.1 gezeigt. Zwei gegenläufige Laserpulse treiben einen Raman-Übergang zwischen zwei Hyperfeinzuständen. Dabei erfahren die betroffenen Atome eine Impulsänderung von $2\hbar k$. Durch geeignete Wahl der Laserpulsformen und Frequenzen ist es möglich, zum einen den Impulsübertrag auf stehende Atome zu vermeiden, und zum andern nur Geschwindigkeitsklassen anzuregen, deren gerichtete Impulsänderung zur Kühlung des Ensembles führt. Im Anschluss an den Raman-Übergang werden die Atome durch resonantes optisches Pumpen mit anschließender spontaner Emission wieder in den Ausgangszustand überführt, um einen weiteren Raman-Kühlzyklus anzuschliessen. Im Mittel wird beim Rückpumpen kein Impuls übertragen, da der Rückpumplaser aus mehreren gegenläufigen Richtungen eingestrahlt wird, so dass Absorptions- und Emissionsrichtung der ausgetauschten Photonen nicht festliegen. Im Idealfall bewirkt der Raman-
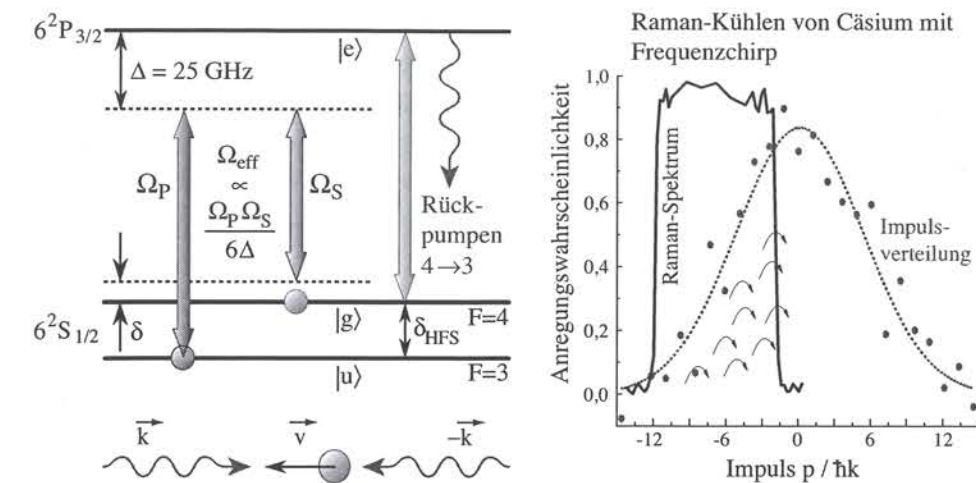
Abbildung 3.1: Raman-Kühlen von Cäsium. Raman-Pulse mit Impulsübertrag von $2\hbar k$ sind durch adiabatische Passage mit Frequenzchirp von -81 kHz bis 0 kHz auf Atome mit Impulsen von $-12 p_{rec}$ bis Null beschränkt. Rückpumpen mit mittlerem Impulsübertrag Null erlaubt ein Wiederholen.

Übergang nur für Atome mit Impuls $p < -2\hbar k$ eine auf den Nullpunkt gerichtete Impulsänderung, während bereits ruhende Atome keine Änderung erfahren, um ein Aufheizen zu vermeiden. In der Praxis wurde dies zunächst mit Sequenzen von Raman-π-Pulsen erreicht [32–35], deren Verstimmung von Puls zu Puls variiert, um die Geschwindigkeitsverteilung der Atome nach und nach zu komprimieren. Wir konnten zeigen, dass sich im effektiven Zwei-Niveau System jede π-Pulssequenz durch eine adiabatische Passage ersetzen lässt. Wie in Abschnitt 2.3 diskutiert, streicht zu diesem Zweck die Raman-Verstimmung δ über einen fest vorgegeben Frequenzbereich, $\delta_{begin} \dots \delta_{end}$. Da die gegenläufigen Raman-Pulse eine differentielle Dopplerverschiebung von $\delta_{Doppler} = 4\pi v/\lambda$ bewirken, sind nur Atome im Geschwindigkeitsbereich von $v_{begin} = \delta_{begin}\lambda/(4\pi)$ bis $v_{end} = \delta_{end}\lambda/(4\pi)$ einem Frequenzchirp über die Resonanz ausgesetzt und erfahren somit eine Raman-Anregung verbunden mit einem Impulsübertrag. Atome ausserhalb dieses Geschwindigkeitsintervals sind davon ausgenommen. Abbildung 3.1 zeigt, dass ein solcher Puls in der Lage ist, fast alle Atome mit negativem Impuls mit einer Wahrscheinlichkeit von nahezu 100% anzuregen.

Eine dreidimensionale Kühlung von Atomen in einem konservativen Potential ist möglich, indem die gegenläufigen Raman-Pulse entlang einer Achse eingestrahlt werden, die an die drei Schwingungsgrundmoden des Fallenpotentials koppelt. Wir konnten dies mit Cäsiumatomen in einer 300 μK tiefen optischen Dipolkraftfalle zeigen, die von zwei sich kreuzenden Strahlen von 80 μm Taille und 5 W Leistung eines Nd:YAG-Lasers gebildet wird (Abb. 3.2(a)). Die Polarisationen der Strahlen stehen senkrecht aufeinander, so dass keine interferenzbedingte Modulation des Potentials erfolgt. Abbildung 3.2(b) zeigt, dass das Fallenpotential im Kreuzungspunkt der beiden Strahlen tief genug ist, um Atome darin zu halten. Genau dies ist auch in der Absorptionsabbildung 3.2(c) zu erkennen: Aus
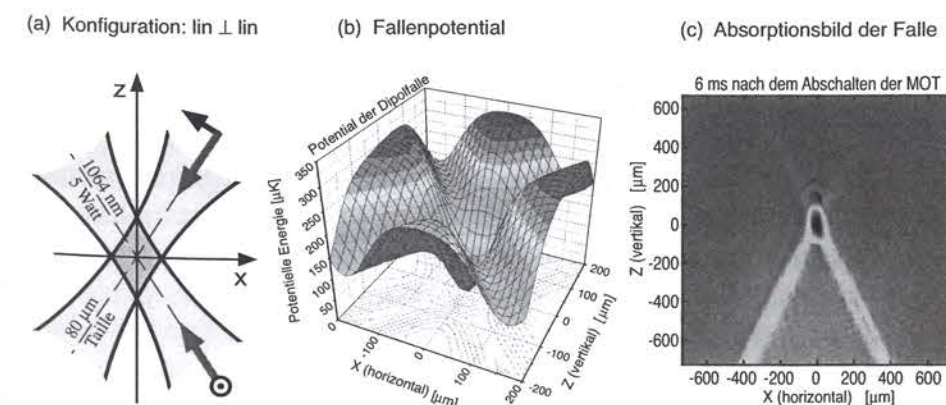

Abbildung 3.2: Optische Dipolkraftfalle. **(a)** Senkrecht zueinander polarisierte Fallenlaser kreuzen in einer senkrechten Ebene. **(b)** Attraktives Fallenpotential. **(c)** Absorptionsbild gefangener Atome.

einer magnetooptischen Falle wurden 10^7 Cäsiumatome in die Dipolkraftfalle geladen. Nach 6 ms befinden sich die meisten Atome noch im Kreuzungsgebiet der Nd:YAG Laserstrahlen. Nur ein kleiner Teil bleibt nicht im Fallenpotential und fällt entlang der beiden Strahlen nach unten. Das Absorptionsbild wurde mit einem resonanten Laserstrahl aufgenommen, der durch die Atomwolke hindurch auf eine CCD-Kamera fällt. Die Atome absorbieren einen Teil des Lichts, so dass deren ortsabhängige Dichte zur Modulation der transmittierten Intensität und somit zu einem Bild der Atomwolke führt.
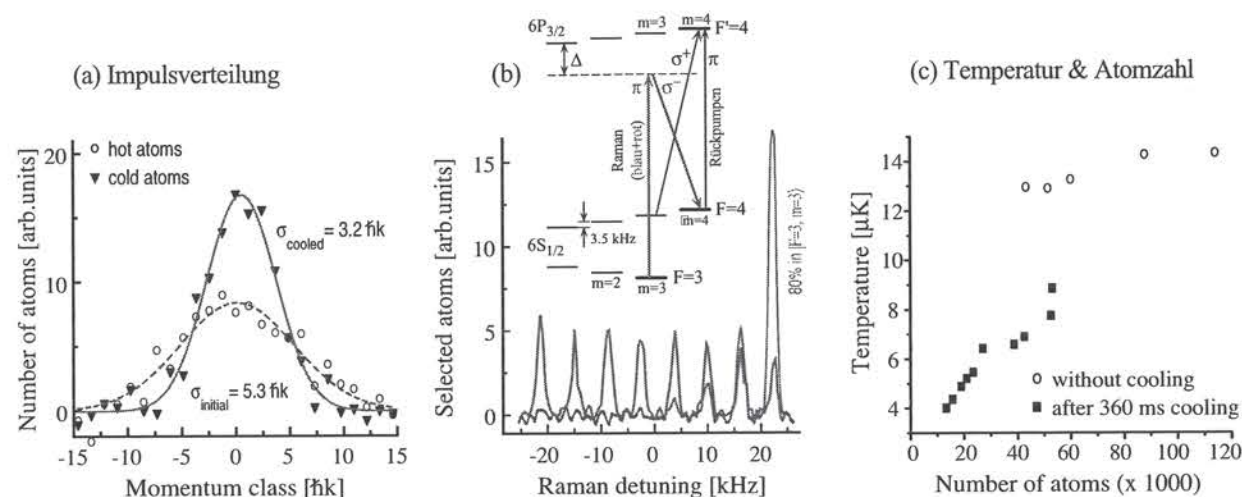

Abbildung 3.3: Raman-Kühlung. (a) Impulsverteilung der Atome vor und nach der Kühlung, gemessen mit geschwindigkeitsselektiven Raman-Pulsen. (b) Spinpolarisation und gleichzeitige Kühlung der Atome durch geschickte Wahl der Polarisationsrichtungen. In einem Magnetfeld von 9 mG spalten die Zeeman-Linien im Raman-Spektrum auf. Gezeigt sind Spektren vor und nach der Kühlung (blau bzw. rot). 80% der Atome konnten in ein Zeeman-Niveau gebracht werden. (c) Temperatur der spinpolarisierten Atome ohne und mit Raman-Kühlung nach 360 ms. Die erreichte Endtemperatur hängt stark von der Atomzahl ab.

Abbildung 3.3(a) zeigt, dass durch wiederholte Anwendung der Pulssequenz die Breite der Impulsverteilung von $\sigma_{initial} = 5.3\hbar k$ auf $\sigma_{final} = 3.2\hbar k \,\hat{=}\, 640$ nK reduziert wird. Zur weiteren Erhöhung der Phasenraumdichte haben wir während der Kühlung den atomaren Drehimpulses ausgerichtet, indem wir die Polarisationen der beiden Raman-Pulse so gewählt haben, dass die Atome bevorzugt in ein einziges Zeeman-Niveau gelangen. Abbildung 3.3(b) zeigt die Zeeman-Linien im Raman-Spektrum vor und nach der Kühlung. Zu Beginn sind die Atome noch auf alle Niveaus verteilt, während sich im Anschluss 80% im Zeeman-Zustand $|F = 3, m = 3\rangle$ befinden. Die Temperatur des Ensembles fällt während der 360 ms langen Kühlsequenz von $14\,\mu$K auf $4\,\mu$K ab und gleichzeitig sinkt die Atomzahl von 100 000 auf unter 20 000 (Abb. 3.3(c)). Dies ist weit entfernt von den Temperaturen im Nanokelvin Bereich, die bei der Kühlung freier Atome erzielt wurden. Begründet ist diese Diskrepanz durch den Anstieg der Atom- und damit auch optischen Dichte mit fallender Temperatur. Damit geht eine verstärkte Mehrfachstreuung und Reabsorption der während des Rückpumpens dissipierten Photonen einher, die zur Aufheizung der Atomwolke führt und der Kühlung entgegenwirkt. Auch der beobachtete Zusammenhang zwischen Atomzahl und Endtemperatur ist dadurch bedingt. In diesem Experiment limitiert die Reabsorption die erreichbare kleinste Phasenraumdichte auf $n\lambda^3 \approx 10^{-3}$ [36].
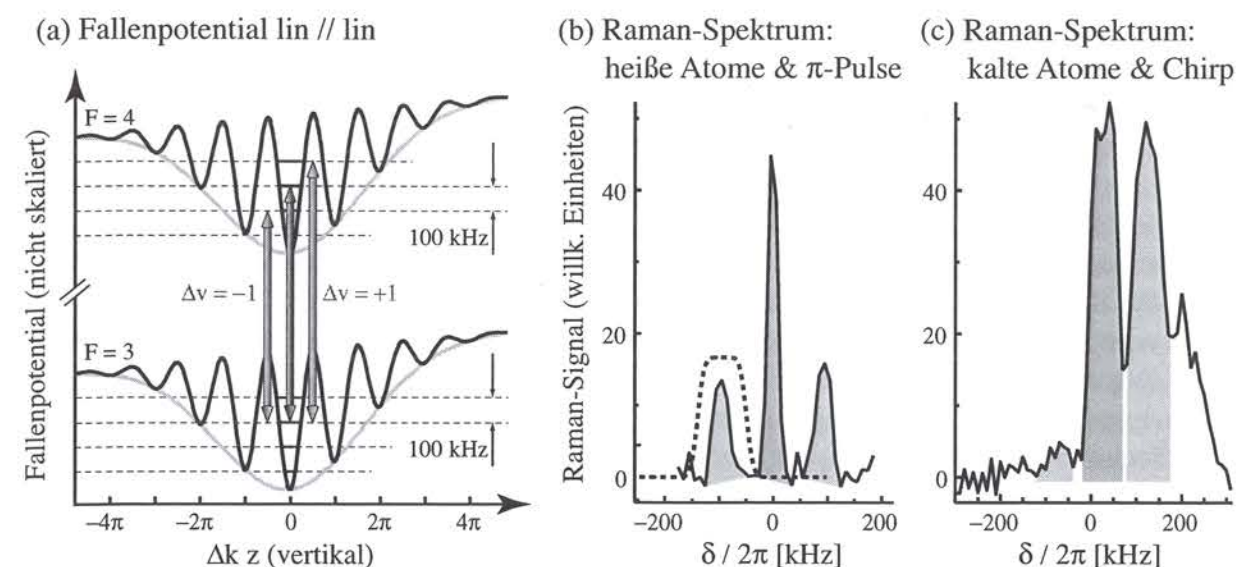
Abbildung 3.4: Raman-Seitenband Kühlung. (a) Parallel polarisierte Dipolfallenstrahlen führen zur Intensitätsmodulation entlang der Vertikalen mit entsprechend steilen Potentialtöpfen. Der Vibrationsniveauabstand von 100 kHz kann mit gegenläufigen Raman-Pulsen aufgelöst werden (b). Im Spektrum ist der Träger (grau) sowie das rote und blaue Seitenband sichtbar. Amplitude und Dauer der Pulse sind hier so gewählt, dass der Träger mit einem π-Puls angeregt wird. Zur Seitenbandkühlung dienen frequenzgechirpte Pulse (gestrichelt), die mit einer adiabatischen Passage das rote Seitenband (mit $\Delta v = -1$) anregen. (c) Nach der Kühlung sind 95% der Atome im Vibrationsgrundzustand, und das rote Seitenband ist nicht mehr sichtbar. Frequenzgechirpte Pulse gewährleisten hier eine gleich hohe Anregungswahrscheinlichkeit für die beiden Seitenbänder und den Träger.

3.2   Raman-Seitenbandkühlen und Fockzustandspräparation

Das bisher diskutierte Raman-Kühlverfahren nutzt den Dopplereffekt zur Selektion von Geschwindigkeitsklassen und erfordert daher Pulse, die im Vergleich zur Schwingungsperiode der Atome in der Falle kurz sind. Im umgekehrten Fall, d.h. mit Raman-Pulsen deren Dauer die Schwingungsperiode deutlich übersteigt, ist es möglich Übergänge zwischen Vibrationsniveaus aufzulösen und gezielt anzusprechen. Analog zur Seitenbandkühlung gefangener Ionen [37–40] ist es in Dipolkraftfallen möglich, Raman-Übergänge zur gezielten Seitenbandkühlung neutraler Atome einzusetzen [24, 41–43]. In einer Dimension konnten wir dies experimentell demonstrieren. Dazu haben wir die Polarisationen der in Abb. 3.2(a) gezeigten Dipolfallenstrahlen parallel zueinander gewählt. Die Strahlen bilden einen Winkel $\alpha = \pm 53°$ zur Horizontalen und interferieren im Kreuzungsgebiet, so dass entlang der Vertikalen ein optisches Gitter mit einer Periode von $\lambda_{YAG}/(2\sin\alpha) = 665$ nm resultiert. Jeder Bauch der Stehwelle stellt eine eigene Dipolfalle dar, deren vertikale Schwingungsfrequenz $\omega_{trap} = 2\pi \times 100$ kHz beträgt. Abbildung 3.4(a) zeigt Raman-Übergänge zwischen den Hyperfeinzuständen $F = 3$ und $F = 4$, die mit einer gezielten Änderung des Vibrationszustands einhergehen. Bei resonanter Anregung (auf der Trägerfrequenz) ändert sich der Schwingungszustand nicht ($\Delta v = 0$), während um ω_{trap} rot bzw. blau verstimmte Raman-Pulse nur das rote bzw. blaue Seitenband anregen und die Vibrationsquantenzahl entweder erniedrigen ($\Delta v = -1$) oder erhöhen ($\Delta v = +1$). Nach dem Laden der Dipolfalle sind alle Vibrationszustände besetzt, so dass im Raman-Spektrum (Abb. 3.4(b)) neben dem Träger zunächst beide Seitenbänder sichtbar sind. Diese erscheinen klein im Vergleich zum Träger, da die eingestrahlte Intensität nur für $\Delta v = 0$ zu einem Raman-

π-Puls führt, nicht aber für $\Delta v = \pm 1$.

Seitenbandkühlung im optischen Gitter haben wir mit frequenzgechirpten Raman-Pulsen realisiert, deren Anregungsspektrum in Abb. 3.4(b) gestrichelt eingezeichnet ist. Der Frequenzchirp erlaubt eine effektive Anregung des roten Seitenbandes, obwohl dessen genaue Lage aufgrund der Anharmonizität der Potentiale und der Variation der Schwingungsfrequenz von Potentialtopf zu Potentialtopf leicht variiert. Im Gegensatz zur Anregung mit π-Pulsen ist dieser Prozess zudem nicht von den Zeeman-Niveaus der Atome abhängig, denn die adiabatische Passage regt diese bei hinreichend großer Rabifrequenz alle mit gleicher Wahrscheinlichkeit an. Mit jeder Anregung des roten Seitenbands wird die Vibrationsquantenzahl um eins erniedrigt, so dass der Prozess mehrmals zu wiederholen ist, um den Schwingungsgrundzustand zu erreichen. Dazu ist es notwendig, zwischen den Raman-Pulsen jeweils einen Rückpumppuls einzustrahlen, der die Atome nach $F = 3$ zurückbringt. Nach einer Sequenz von 20 Pulsen ist im Raman-Spektrum kein rotes Seitenband mehr erkennbar (Abb. 3.4(c)). Dies bedeutet, dass sich fast alle Atome im Vibrationsgrundzustand, $v = 0$, befinden, und die Vibrationsquantenzahl nicht weiter erniedrigt werden kann. Zur besseren quantitativen Auswertung haben wir zur Aufnahme dieses Spektrums frequenzgechirpte Pulse verwendet, so dass das gemessene Signal nur von der Besetzung der Zustände, aber nicht von den jeweiligen Rabi-Frequenzen abhängt. Daher sind Träger und blaues Seitenband gleich stark, und aus dem Verhältnis von rotem und blauen Seitenband lässt sich direkt auf eine Grundzustandsbesetzung von 95(2)% schließen.

Neben dem Verschwinden des roten Seitenbands schlägt sich die Kühlung der Atome auch in ihrer Impulsverteilung nieder. Um dies zu beobachten schalten wir die Dipolfalle plötzlich ab, so dass sich die Atomwolke in alle Richtungen ausbreiten kann. Senkrecht zur Vertikalen, d.h. entlang x und y, sind die Atome thermisch verteilt und nach einer Flugzeit τ hat die Wolke eine Ausdehnung mit $\sigma_{x,y}(\tau) = \tau\sqrt{k_B T/m}$. In Richtung der Vertikalen befinden sich die Atome alle im selben Vibrationszustand, $|v\rangle$, woraus bei Vernachlässigung der anfänglichen Ausdehnung nach der Flugzeit τ die Atomdichte $n_v(z,\tau) \propto |\langle p = m*z/\tau|v\rangle|^2$ resultiert, d.h. die anfängliche Impulsverteilung überträgt

sich 1:1 in eine expandierende Dichteverteilung entlang z. Im Grundzustand ist die Impulsverteilung gaußförmig, $n_0(p) \propto |\langle p|v = 0\rangle|^2 = \exp(-p^2/2p_0^2)/(p_0\sqrt{2\pi})$, mit $p_0 = \sqrt{\hbar\omega_{trap}m/2}$, so daß man nach einer Expansionszeit von $\tau = 6\,\text{ms}$ die in Abb. 3.5(a) gezeigte anisotrope Dichteverteilung erhält. Die Dichte der Atome in diesem Absorptionsbild ist proportional zu $\ln(I_t/I_0)$, wobei I_0 die einfallende und I_t die transmittierte Intensität bezeichnet. Abbildung 3.5(c) zeigt die zugehörige integrale Dichte entlang der Vertikalen. In [43] haben wir zudem gezeigt, dass die Atome aus dem Vibrations-Grundzustand gezielt in andere Vibrations-Fockzustände versetzt werden können. Dazu haben wir im Anschluss an die Kühlung in den Grundzustand ein einziges Mal das blaue Seitenband mit einem frequenzgechirpten Puls adiabatisch angeregt. Dies transferiert die Atome aus $v = 0$ in den ersten angeregten Vibrationszustand, $v = 1$. In Abb. 3.5(b+d) ist zu erkennen, dass dies eine dramatische Auswirkung auf die Impulsverteilung hat. Diese ist mit $n_1(p) \propto |\langle p|v = 1\rangle|^2 = p^2\exp(-p^2/2p_0^2)/(p_0^3\sqrt{2\pi})$ nicht mehr gaußförmig, sondern weist zwei Maxima bei $\pm\sqrt{2}p_0$ auf. In der Dichteverteilung der Atome im Anschluss an eine Flugzeit von $\tau = 10\,\text{ms}$ ist dies deutlich zu erkennen. Dies zeigt, dass gezieltes Anregen von Raman-Seitenbandübergängen in Dipolfallen nicht nur eine Kühlung der Atome in den Grundzustand ermöglicht, sondern prinzipiell auch ein Besetzen beliebiger Vibrations-Fockzustände des Fallenpotentials.

Aufbauend auf den hier vorgestellten Arbeiten zur Seitenbandkühlung konnten C. Salomon und Mitarbeiter gequetschte Zustände und Superpositionszustände der Bewegung erzeugen [44], und zudem Atome zu einem nicht entarteten kalten zweidimensionalen Gas abkühlen [45]. In der Gruppe von S. Chu gelang schließlich eine Erweiterung des Raman-Seitenband Kühlverfahrens auf drei Dimensionen [46].

Die hier vorgestellten Kühlverfahren waren der erste Schritt hin zur rein optischen Bose-Einstein Kondensation von Alkaliatomen in Dipolkraftfallen. In Kombination mit einer Verdampfungskühlung der Atome wurde dies inzwischen von M. D. Barrett und Mitarbeitern [47] für Rubidium und von T. Weber und Mitarbeitern [48] für Cäsium gezeigt.
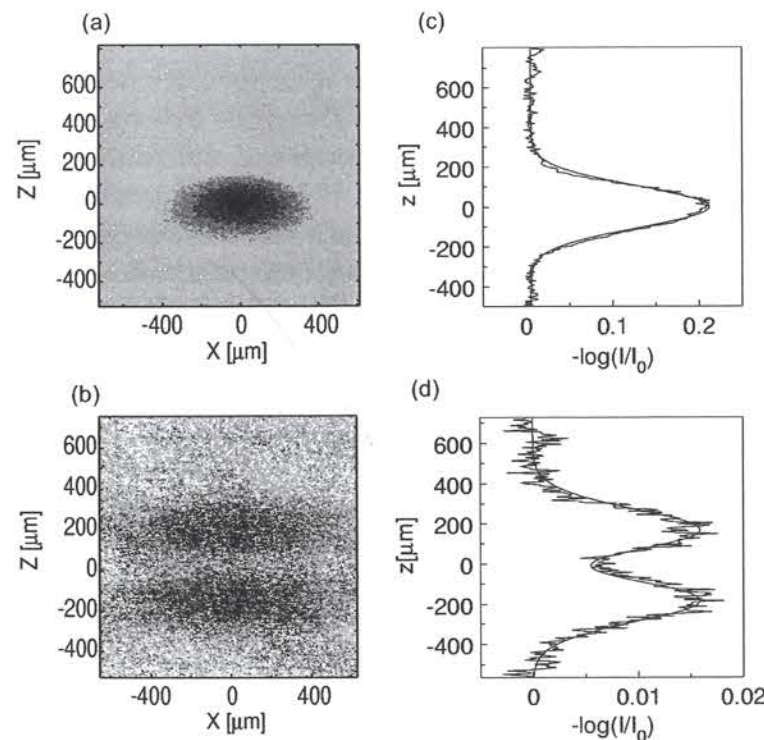

Abbildung 3.5: Impulsverteilung der Atome nach der Seitenbandkühlung. (a) Absorptionsbild der in den Vibrationsgrundzustand gekühlten Atome, aufgenommen nach einer Flugzeit von 6 ms nach dem Abschalten der Dipolfalle. (b) Impulsverteilung der Atome nach Besetzen des Vibrationszustands $v = 1$ der Dipolfalle durch Seitenbandkühlung in den Grundzustand, gefolgt von einer einmaligen Anregung des blauen Seitenbandes. Die Flugzeit bis zur Aufnahme des Absorptionsbildes beträgt hier 10 ms. (c+d) Integrale Impulsverteilung entlang der Vertikalen.

Kapitel 4

Schnittstelle zwischen Atom und Licht

Der gezielte Einsatz von Quanteneffekten bietet die Chance, verschränkte oder überlagerte Quantenzustände zur Informationsverarbeitung zu nutzen und mit neuartigen Algorithmen bisher unlösbare Fragestellungen anzugehen. Weltweit wird daher intensiv daran gearbeitet, wesentliche Elemente von Quantencomputern zu realisieren [49]. Dazu gehören insbesondere Schnittstellen zwischen verschiedenen Informationsträgern, wie z.B. Atomen und Licht. Abbildung 4.1 zeigt schematisch die prinzipielle Funktionsweise einer solchen Schnittstelle, die auf Effekten der Resonator-Quantenelektrodynamik [50, 51] beruht, um eine starke Kopplung eines Atoms an das Lichtfeld im Inneren eines optischen Resonators zu erreichen.

Wir haben eine solche Schnittstelle realisiert und gezeigt, dass diese zur gezielten Erzeugung einzelner Photonen geeignet ist. Der Energieaustausch zwischen einem einzelnen Atom und den Feldmoden eines optischen Resonators wird durch Laserpulse kontrolliert, die Raman-Übergänge im Atom treiben und dabei jeweils ein Photon im Resonator erzeugen, das diesen in einer vorgegebenen Richtung verlässt. Dieser Prozess ist unitär und somit prinzipiell umkehrbar, so dass Atome in verteilten Quantennetzwerken auch als Photonenempfänger dienen könnten [52, 53]. Zudem liegen die Eigenschaften der Photonen fest, was sie ununterscheidbar und für rein optische Quantengatter geeignet erscheinen lässt [54]. Somit ist ein Quantennetzwerk denkbar, in dem einzelne Atome als Quantenspeicher, Photonensender und Photonenempfänger fungieren und in dem die Quanteninformationsverarbeitung rein optisch erfolgt.
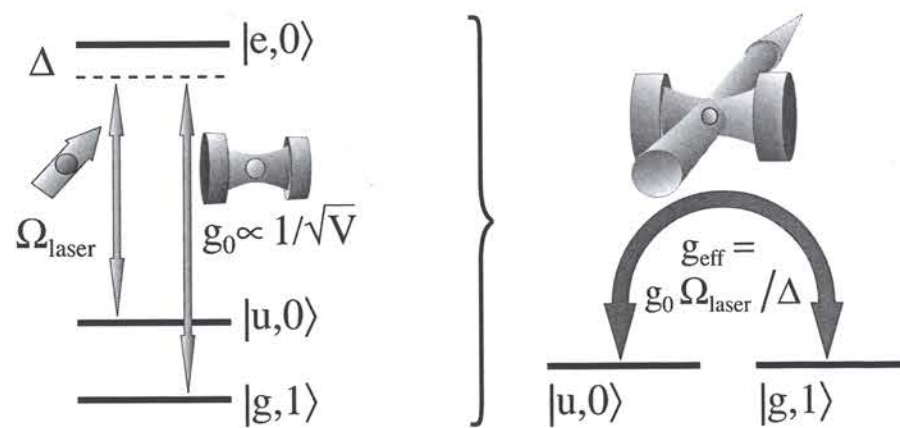

Abbildung 4.1: Atom-Licht Quantenschnittstelle: Die effektive Kopplungsstärke, g_{eff}, eines Atoms an das Feld im Inneren eines Resonators wird durch einen transversal eingestrahlten Laser kontrolliert. Dieser treibt Ramanübergänge im Atom, die mit einer Änderung der Photonenzahl einhergehen.
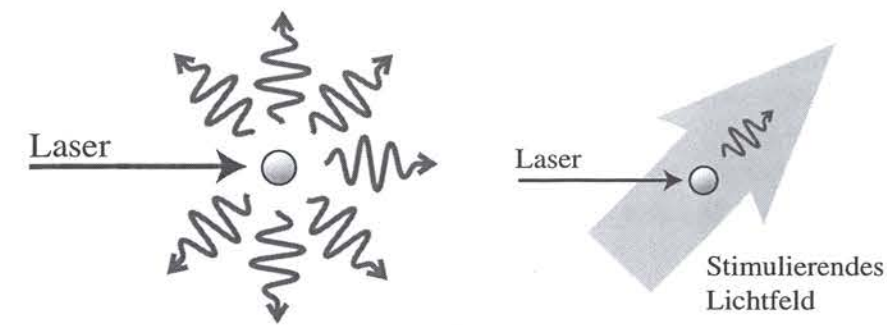
Abbildung 4.2: Einzelne Quantensysteme emittieren einzelne Photonen entweder mit großer Bandbreite spontan in alle Richtungen (links), oder stimuliert durch ein umgebendes Feld in eine einzige Feldmode fester Frequenz (rechts).

4.1 Atome und Photonen in Resonatoren hoher Finesse

Damit einzelne Photonen als Informationsträger in Quantencomputern und Quantennetzen eingesetzt werden können, müssen diese Eigenschaften aufweisen, die mit herkömmlichen Lichtquellen nicht zu realisieren sind. Zum einen sollten die Photonen ununterscheidbar sein, und zum anderen ist ein reversibler Erzeugungsprozess wünschenswert, der ein Zwischenspeichern von Photonen gestattet. Es ist leicht möglich, ein einzelne Atome oder Ionen als Quellen einzelner Photonen zu verwenden [55, 56], indem diese zur Fluoreszenz angeregt werden. Ohne weitere Maßnahmen wird ein Atom pro anregendem Laserpuls maximal ein Photon emittieren. Frequenz und Richtung liegen dabei jedoch nicht fest und variieren zufällig. Abbildung 4.2(links) illustriert dieses Verhalten. Im Gegensatz zur spontanen Emission liegen bei stimulierten Emissionsprozessen Frequenz und Richtung der Photonenemission fest, da sie durch das stimulierende Lichtfeld um das Atom vorgegeben werden (Abb. 4.2(rechts)). Stimulierte Emissionsprozesse führen z.B. dazu, dass ein Laser monochromatisches Licht in nur eine Richtung abstrahlt. Im Hinblick auf die Realisierung einer Einzelphotonenquelle stellt eine große Zahl von Photonen im stimulierenden Feld jedoch einen schwerwiegenden Nachteil dar, da sie es unmöglich macht, einzelne zusätzliche Photonen zu diskriminieren. Abhilfe schafft in unserem Fall der Einsatz eines optischen Resonators, der von zwei gegenüberstehenden Spiegeln hoher Reflektivität geformt wird. Bei hinreichend kleinem Modenvolumen ist das Vakuumfeld des lichtlosen Resonators bereits in der Lage, Photonenemissionen zu stimulieren. Dieser nach Purcell benannte Effekt [57] führt nicht nur zu einer Erhöhung der spontanen Emissionsrate in die Resonatormode, sondern erlaubt auch das Stimulieren von Ramanübergängen mit dem Vakuumfeld. Abb. 4.3 zeigt den in unseren Experimenten eingesetzten Resonator sowie das Energieniveauschema der an den Resonator gekoppelten ^{85}Rb-Atome. Im Resonator wird ein Atom von einem Laser angeregt, der den Pumpzweig eines Raman-Übergangs mit Λ-förmiger Niveauanordnung treibt, während der andere Zweig des Übergangs resonant zur betreffenden Mode des Resonators ist. Somit kann ein einzelnes Atom kohärent ein Photon in den Resonator abstrahlen. Der Energieaustausch mit dem Lichtfeld im Resonator beruht im Fall starker Kopplung auf einer adiabatischen Passage in Kombination mit stimulierter Raman-Streuung, wobei die Atom-Resonator Kopplung die Rolle eines stimulierenden Lichtfelds einnimmt, das den Übergang zwischen $|e, n-1\rangle$ und $|g, n\rangle$ mit der Rabifrequenz $\Omega_S = 2g_0\sqrt{n}$ treibt, wobei g_0 die Atom-Resonator Kopplungskonstante ist, und $|n-1\rangle$ und $|n\rangle$ Photonenzahlzustände des Resonators bezeichnen. Die Zeitentwicklung dieses gekoppelten Systems wird durch den Hamiltonoperator

$$\hat{H} = \hbar \left[\omega_u \hat{\sigma}_{uu} + \omega_e \hat{\sigma}_{ee} + \omega_g \hat{\sigma}_{gg} + \omega_c \left(\frac{1}{2} + \hat{a}^\dagger \hat{a} \right) - g_0 (\hat{\sigma}_{eg} \hat{a} + \hat{a}^\dagger \hat{\sigma}_{ge}) - \frac{1}{2}\Omega_P (\hat{\sigma}_{eu} + \hat{\sigma}_{ue}) \right] \quad (4.1)$$

beschrieben, wobei $\hat{a}^\dagger$ und $\hat{a}$ Photonen in der Resonatormode erzeugen bzw. vernichten. Betrachtet man die drei Zustände $|u, n-1\rangle$, $|e, n-1\rangle$ und $|g, n\rangle$, so sind diese in Rotating-Wave Approxi-
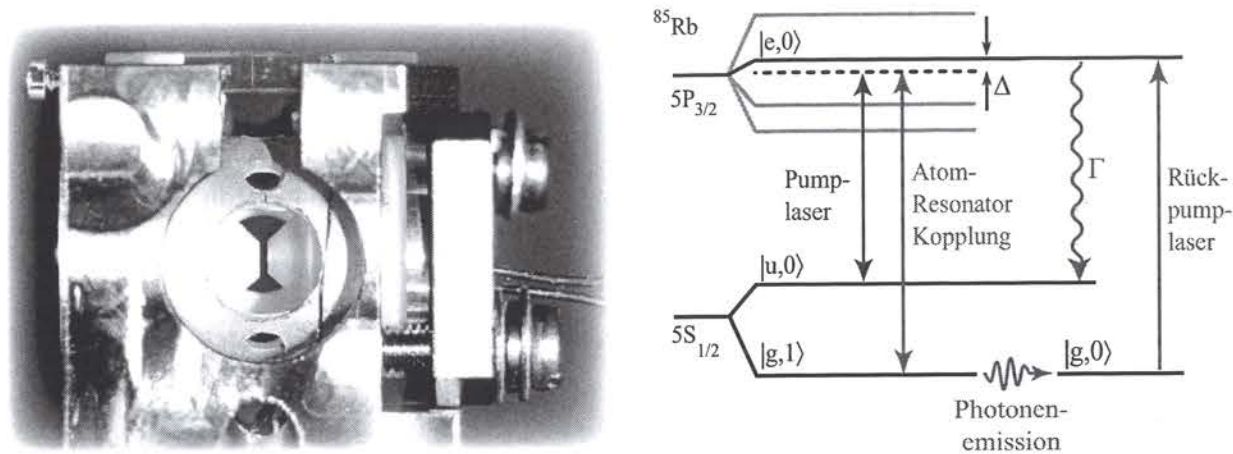
Abbildung 4.3: **(links):** Optischer Resonator hoher Finesse mit einer Finesse von $F = 60000$ und einem Spiegelabstand von $0,5\,mm$. Durch die Öffnung im zylindrischen Piezorohr im Zentrum der Abbildung sind die beiden kegelförmigen Spiegel zu erkennen. **(rechts):** Im ^{85}Rb-Atom treiben Pumplaser und Atom-Resonator Kopplung einen Raman-Übergang von $|u, 0\rangle$ nach $|g, 1\rangle$ zur Photonenerzeugung. Ein weiterer Laser pumpt das Atom nach erfolgter Emission in den Ausgangszustand zurück und erlaubt, den Prozess zu wiederholen.

mation (RWA) entartet, solange keine Kopplung vorliegt. Mit endlichen Kopplungsstärken, Ω_P und g_0, spalten diese jedoch in drei neue Eigenzustände des Hamiltonoperators (4.1) auf. Einer dieser Eigenzustände,

$$|\phi_n^0\rangle = \left[\Omega_P|u, n-1\rangle - 2g_0\sqrt{n}|g, n\rangle\right]/\sqrt{4ng_0^2 + \Omega_P^2}, \qquad (4.2)$$

ist erneut ein Dunkelzustand, der wie in Kapitel 2.3 beschrieben zum adiabatischen Besetzungstransfer und somit zur kontrollierten Kopplung von Atom und Resonator verwendet werden kann.

4.2 Vakuumstimulierte Raman-Streuung

Zunächst haben wir experimentell gezeigt, dass das Vakuumfeld im Inneren eines Resonators in der Lage ist, den in Abb. 4.3 gezeigten Raman-Übergang zu stimulieren [58]. Dazu haben wir eine Wolke von Rubidiumatomen in einer magnetooptischen Falle auf wenige Mikrokelvin abgekühlt und im Zustand $|u\rangle \equiv |5S_{1/2}, F = 3\rangle$ präpariert. Diese ultrakalten Atome fallen nach dem Abschalten der Falle mit einer Geschwindigkeit von 2 m/s zwischen den Spiegeln eines lichtleeren Resonators hindurch, der mit dem Übergang von $|e\rangle \equiv |5P_{3/2}, F = 3\rangle$ nach $|g\rangle \equiv |5S_{1/2}, F = 2\rangle$ resonant ist. Während sich die Atome durch den Resonator bewegen, strahlen wir kontinuierlich einen Laser von der Seite ein, der den Übergang von $|u\rangle$ nach $|e\rangle$ treibt. Die experimentelle Anordnung ist in Abb. 4.4(links) skizziert. Im gekoppelten Atom-Resonator System erzeugt jeder Raman-Übergang von $|u, 0\rangle$ nach $|g, 1\rangle$ ein Photon im Resonator, das anschließend durch einen der Spiegel emittiert wird. Abbildung 4.4(rechts) zeigt die Zahl der emittierten Photonen als Funktion der Verstimmungen von Laser und Resonator von den jeweiligen atomaren Resonanzlinien. Emissionsmaxima treten immer auf, wenn beide Verstimmungen identisch sind. Dies zeigt, dass der Raman-Prozess vom Vakuumfeld des Resonators stimuliert wird [31, 58]. Um Verluste durch Zerfall des kurzlebigen Zustands $|e, 0\rangle$ zu vermeiden, treiben wir den Übergang mit einer antiintuitiven zeitlichen Abfolge der beiden Wechselwirkungen, indem wir den anregenden Laserstrahl von der Resonatorachse weg nach unten verschieben, so dass jedes Atom zuerst an den lichtlosen Resonator koppelt. Dieser hat zwar keine unmittelbare Wirkung auf den anfangs besetzten Zustand $|u, 0\rangle$, doch die starke Kopplung be-
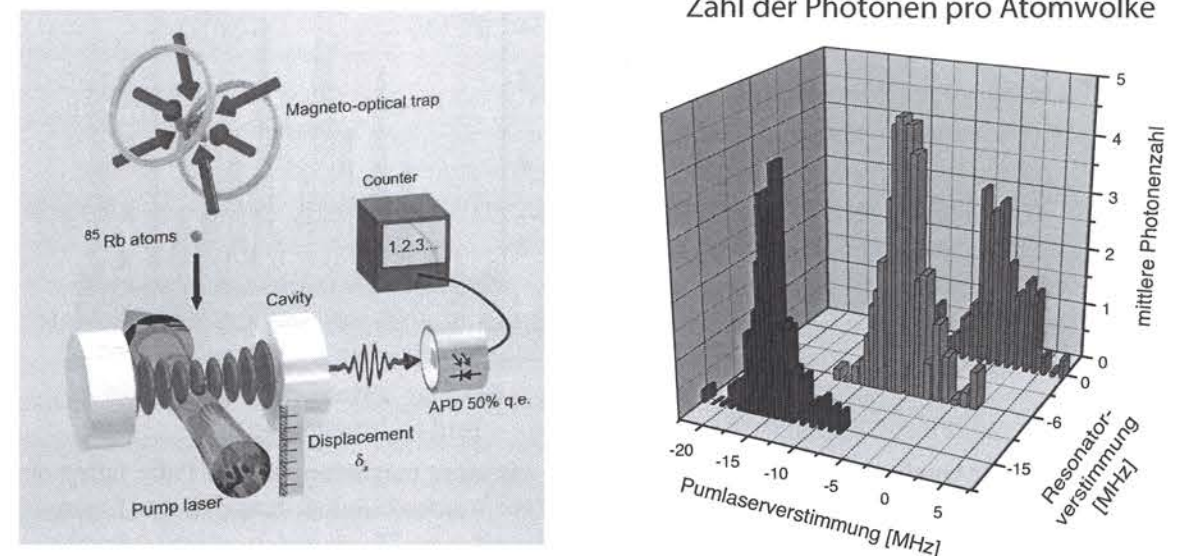

Abbildung 4.4: **(links):** Experimenteller Aufbau zur vakuumstimulierten Raman-Streuung. Die Atome werden zunächst in einer magnetooptischen Falle präpariert und fallen anschließend durch den Resonator. **(rechts):** Raman-Anregungsspektren. Emittierte Photonenzahl als Funktion der Resonator- und Pumplaserverstimmung von der atomaren Resonanz.

wirkt, dass dieser vollständig auf den Dunkelzustand $|\phi_1^0\rangle$ projiziert. Die Wechselwirkung mit dem Licht des verschobenen Pumplaserstrahls setzt verzögert ein. Geschieht dies langsam genug, dann wird der Raman-Prozess adiabatisch getrieben und ein Photon wird im Resonator erzeugt, ohne den kurzlebigen Zustand $|e, 0\rangle$ zu besetzen. Optimal ist, den Laserstrahl gegenüber dem Resonator um die Breite seiner eigenen Strahltaille nach unten abzusenken [59, 60].

Aufgrund des adiabatisch getriebenen Ramanübergangs kann in dieser Anordnung jedes Atom maximal ein Photon erzeugen. Die Photonenstatistik des emittierten Lichts ist jedoch Poissonsch, da in dieser Anordnung die zufällige Ortsverteilung der Atome in der fallenden Atomwolke auf die Verteilung der Photonen übertragen wird. Nicht-klassisches Licht, das deutliches Antibunching zeigt, erhält man erst durch gezieltes Auslösen mehrerer einzelner Photonemissionen während sich ein Atom im Resonator befindet. Dies ist im nächsten Abschnitt beschrieben.

4.3 Einzelne Photonen auf Knopfdruck

Mit einer kleinen Modifikation eignet sich die beschriebene Technik bestens, um einzelne Photonen auf kontrollierte Art und Weise zu erzeugen [62–64]. Anstelle des kontinuierlich eingestrahlten Pumplasers verwenden wir hierzu Laserpulse, die die Emission einzelner Photonen auslösen. Abbildung 4.5 (links) skizziert den experimentellen Aufbau. Eine Wolke von ^{85}Rb-Atomen fällt aus einer magnetooptischen Falle heraus durch einen optischen Resonator hoher Finesse. Das Vakuumfeld des Resonators stimuliert die Photonenemission, so dass Frequenz und Emissionsrichtung der Photonen festliegen. Während sich ein Atom im Resonator befindet, ist es einer Sequenz von Laserimpulsen ausgesetzt, die den Ramanübergang adiabatisch treiben und einzelne Photonemissionen triggern. Die Photonen verlassen den Resonator durch den Spiegel mit höherer Transmission und gelangen über einen Strahlteiler zu zwei Detektoren. Letzteres entspricht der Anordnung von Hanbury-Brown und Twiss [61] zur Messung der Intensitätskorrelation des emittierten Lichts.
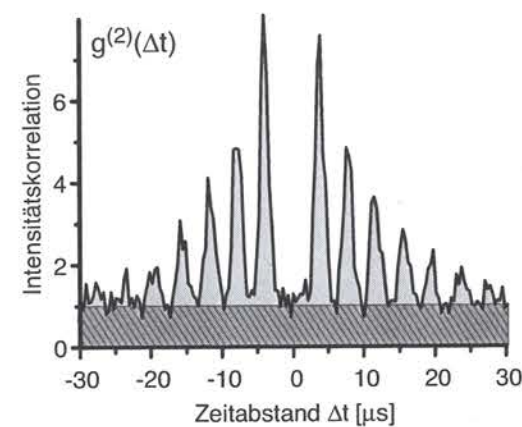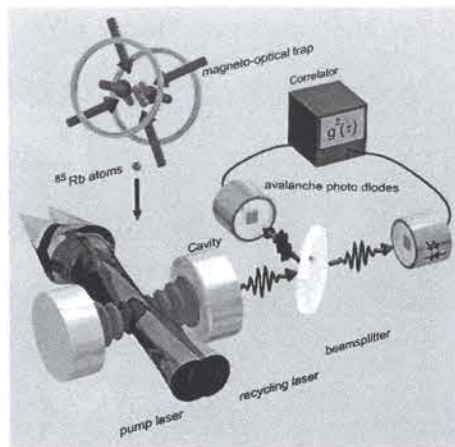
Abbildung 4.5: (links): Quelle einzelner Photonen: Atome aus einer magnetooptischen Falle fallen durch die TEM$_{00}$ Mode eines optischen Resonators hoher Finesse. Dort werden sie einer Sequenz von Laserpulsen ausgesetzt, die die Emission einzelner Photonen triggern. Zwei Avalanche-Photodioden erlauben die Messung der **rechts** gezeigten Intensitätskorrelation zweiter Ordnung, $g^{(2)}(\Delta t)$, des emittierten Photonenstroms nach Hanbury-Brown und Twiss [61]. Bei dem hier eingestellten geringen Fluss von 3.4 Atomen/ms durch den Resonator sind Mehratom-Effekte in der Korrelationsfunktion nicht sichtbar.

Im Energieniveauschema der Atome (Abb. 4.3 (rechts)) ist zu erkennen, dass zusätzlich zum Pumplaser noch ein weiterer Laser zum Einsatz kommt, der das Atom nach erfolgter Photonenemission zurück in den Ausgangszustand versetzt, so dass vom selben Atom mehrere sukzessive Photonen ausgehen können. Abbildung 4.5 (rechts) zeigt die Intensitätskorrelation $g^{(2)}(\Delta t)$ des emittierten Lichts. Diese spiegelt die Häufigkeit wieder, mit der Photonen im Zeitabstand Δt auf die beiden Detektoren treffen. Auffällig ist, dass die Maxima der Korrelationsfunktion einer Gaußförmigen Einhüllenden folgen, deren Dauer die 20 μs Durchflugzeit der Atome durch den Resonator widerspiegelt. Dies ist darauf zurückzuführen, dass Korrelationen zwischen Photonen ein-und-desselben Atoms nur innerhalb der Durchflugzeit auftreten können. Zudem ist zu erkennen, dass der Abstand zwischen den Maxima durch die Taktrate der Triggerpulse gegeben ist. Dies bedeutet, dass Photonen nur während der Triggerpulse emittiert werden. Besonders bemerkenswert ist jedoch das vollständige Fehlen eines Maximums im Korrelationssignal bei $\Delta t = 0$. Dies zeigt, dass innerhalb eines Triggerpulses keine weiteren Photonen vom selben Atom emittiert werden können und somit auch, dass ein einzelnes gekoppeltes Atom-Resonator System eine ideale Einzelphotonenquelle darstellt.

Aus der statistischen Analyse des gesamten Datenstroms kann lässt sich zudem schließen, dass die experimentelle Anordnung nichtklassisches Licht emittiert, obwohl $g^{(2)}(0) \approx 1$. Letzteres ist auf die Poissonverteilung der fallenden Atome und auf Detektorrauschen zurückführen, die beide in das Korrelationssignal eingehen [65]. Eine quantitative Analyse, die dem nichtstationären Charakter der Quelle durch Konditionierung des Signals auf die Anwesenheit von Atomen Rechnung trägt [66, 67], lässt sich bewerkstelligen indem die emittierten Photonen selbst als Signal aufgefasst werden, das die Anwesenheit von Atomen anzeigt. Auf diese Art haben wir die die statistische Analyse auf Triggerpulse beschränkt, die einer Photonendetektion unmittelbar benachbart sind. Abbildung 4.6 stellt die derart konditionierte Korrelationsfunktion, $g^{(2)}(\Delta i)$, der zugehörigen unkonditionierten Korrelationsfunktion, $g^{(2)}(\Delta t)$, gegenüber. Zur Berechnung des konditionierten Signals sind die Pulse durchnummeriert und wir betrachten nur die Zahl der Korrelationen als Funktion der Pulsnummer-Differenz, Δi (diese tritt an Stelle des Zeitabstands Δt). Mit $g^{(2)}(\Delta i = 0) = 0,41(6)$ und $g^{(2)}(\Delta i \neq 0) = 1,00(9)$ ist die Photonenstatistik bei Anwesenheit eines Atoms eindeutig sub-Poissonsch. Im Fall eines kleineren Atomflusses, wie in Abb. 4.5 (rechts), erhalten wir sogar
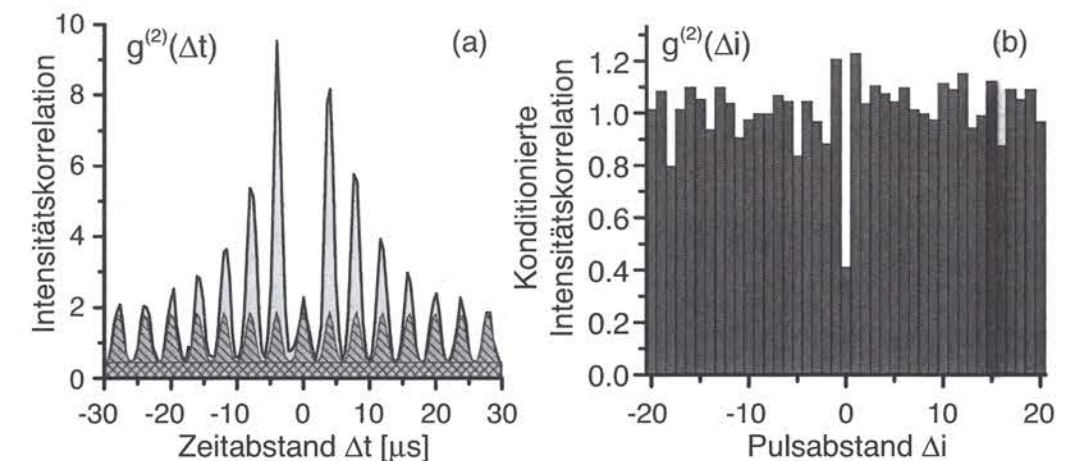
Abbildung 4.6: (a): Intensitätskorrelation $g^{(2)}(\Delta t)$ bei einem Fluss von 10 Atomen/ms durch den Resonator. Mehratombeiträge führen zu einem kleinen Korrelationspeak bei $\Delta t = 0$. **(b):** Konditioniert auf die Anwesenheit eines Atoms zeigt die zugehörige Intentensitätskorrelation $g^{(2)}(\Delta i)$ Antibunching. Korrelationen innerhalb der Triggerpulse sind hier zusammengefasst, und Δi bezeichnet die Differenz zwischen Pulsnummern.

$g^{(2)}(\Delta i = 0) = 0,25(11)$. Dies zeigt, dass der Resonator bei Anwesenheit eines Atoms nichtklassisches Licht mit $g^{(2)}(0) < 1$ emittiert, und dass ein gekoppeltes Atom-Resonator System zuverlässig als deterministische Einzelphotonenquelle arbeitet.

Anzumerken ist, dass ein einzelnes Atom innerhalb der Wechselwirkungszeit mit der Resonatormode im Prinzip bis zu sechs aufeinander folgende Photonen erzeugen kann. Somit lassen sich mit unserer experimentellen Anordnung einfache Experimente zur optischen Quanteninformationsverarbeitung angehen, die mit einer kleinen Zahl von Photonen auskommen. Eine Skalierung zu einem optischen Quantenprozessor, wie von E. Knill und Mitarbeitern vorgeschlagen [54], erfordert jedoch weit mehr gleichzeitig verfügbare einzelne Photonen. Diese könnten z.B. von mehreren permanent gekoppelten Atom-Resonator Systemen generiert werden. Der Weg zu einem derartigen System ist im nächsten Abschnitt skizziert.

4.4   Permanente Atom-Resonator Kopplung

Aufgrund der beschränkten Wechselwirkungszeit der fallenden Atome mit der Mode des optischen Resonators ist es weder möglich, einen ununterbrochenen Bit-Strom einzelner Photonen zu generieren, noch können einzelne Atome zur permanenten Speicherung von Quantenbits eingesetzt werden. Insbesondere sind Experimente zur Kopplung und Verschränkung mehrerer Atome innerhalb eines Resonators [68–71], bzw. zur Quantenkommunikation zwischen entfernten Atome in separaten Resonatoren [52, 53], aufgrund dieser Einschränkung nur schwer durchführbar. Abhilfe schaffen permanent gekoppelte Atom-Resonator Systeme, in denen ein einzelnes Atom gezielt in einen Resonator gebracht und dort festgehalten wird. Dieses Ziel wird weltweit von mehreren Gruppen verfolgt und erste Erfolge wurden bereits erzielt: Experimente von H. J. Kimble (Caltech) und G. Rempe (Garching) haben gezeigt, dass es möglich ist, einzelne Atome in der Feldmode eines optischen Resonators einzufangen und zu kühlen [72, 73]. R. Blatt (Innsbruck) und H. Walther (Garching) ist es gelungen, ein einzelnes Ion gezielt in einen optischen Resonator zu führen und damit die Mode des Resonators mit sub-λ Präzision abzutasten [74, 75]. D. Meschede (Bonn) und P. Grangier (Orsay) ha-
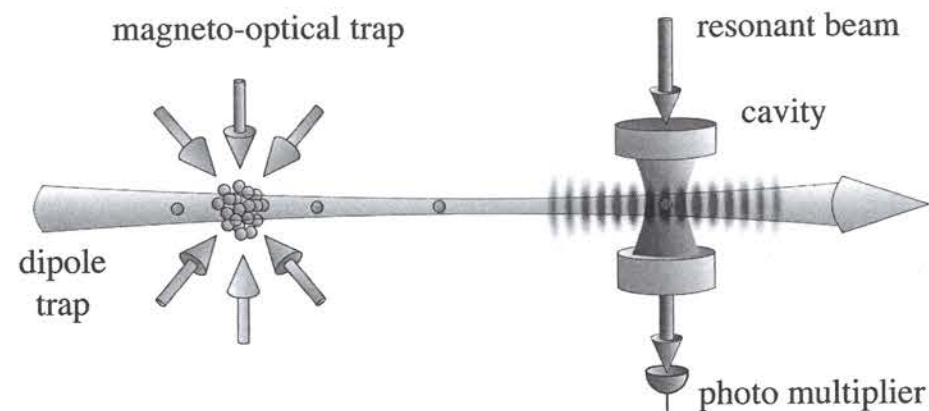
Abbildung 4.7: Kombination einer magnetooptischen Falle (MOT) mit zwei Dipolkraftfallen. Die erste Dipolfalle mit langer Rayleighlänge dient dazu, Atome von der MOT in das Modenvolumen eines Resonators zu führen. Dort werden sie anschließend in den Bäuchen einer Stehwellen-Dipolfalle festgehalten.
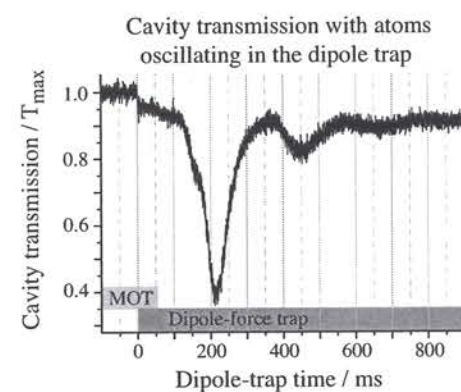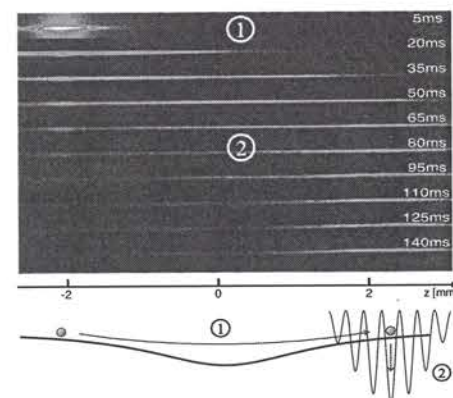

Abbildung 4.8: **(a):** Absorptionsbilder des Atomtransports in der Dipolfalle über eine Strecke von 4 mm (Einsichtsgebiet der Kamera) und dem anschließenden Festhalten der Atome in einer Stehwellen-Dipolfalle. **(b):** Modulation der Resonatortransmission durch die Oszillation von Atomen in der führenden Dipolkraftfalle über eine Distanz von 12 mm.

ben gezeigt, dass sich Dipolkraftfallen zur Manipulation und Positionierung einzelner neutraler Atome hervorragend eignen [76,77], und M. Chapman (Atlanta) [78] und uns ist es vor kurzem gelungen, einzelne Atome mit Hilfe einer vom Resonator unabhängigen Dipolkraftfalle in einen optischen Resonator zu führen, und die Atome aufgrund der Normalmodenaufspaltung in der Transmission des Resonators zu beobachten.

Abbildung 4.7 skizziert unseren experimentellen Aufbau. Eine Wolke kalter Rubidium Atome wird aus einer magnetooptischen Falle in eine horizontal verlaufende Dipolfalle transferiert, die von einem einzelnen kontinuierlichen Strahl eines Yb:YAG Lasers (1030 nm, 5 Watt, 1 cm Rayleigh Länge) gebildet wird. Der Fokus dieses Strahls liegt zwischen MOT und Resonator, so dass die Atome zwischen den beiden 12 mm entfernten Positionen hin- und her oszillieren. Sobald die Atomwolke in den Resonator gelangt, ändern wir die Geometrie der Dipolfalle adiabatisch in eine Stehwellenfalle, die von zwei gegenläufigen Strahlen desselben Yb:YAG Lasers geformt wird. Die Atome werden dabei in den Bäuchen der stehenden Welle gefangen, und können im Prinzip mehrere Sekunden im Modenvolumen des Resonators gehalten werden.

Der Atomtransport und die Oszillation der Atome sind in Abb. 4.8 zu sehen. Die Sequenz von Absorptionsbildern der Atomwolke (links) zeigt, dass die Atome innerhalb von 80 ms eine halbe Oszillationsperiode, von links nach rechts, durchlaufen. Danach erfolgt der Wechsel von der rein führenden Fallengeometrie zur stehenden Welle, so dass die augenblickliche Position der Atome eingefroren wird, da diese in den 1 mK tiefen Bäuchen der stehenden Welle gefangen bleiben. Die
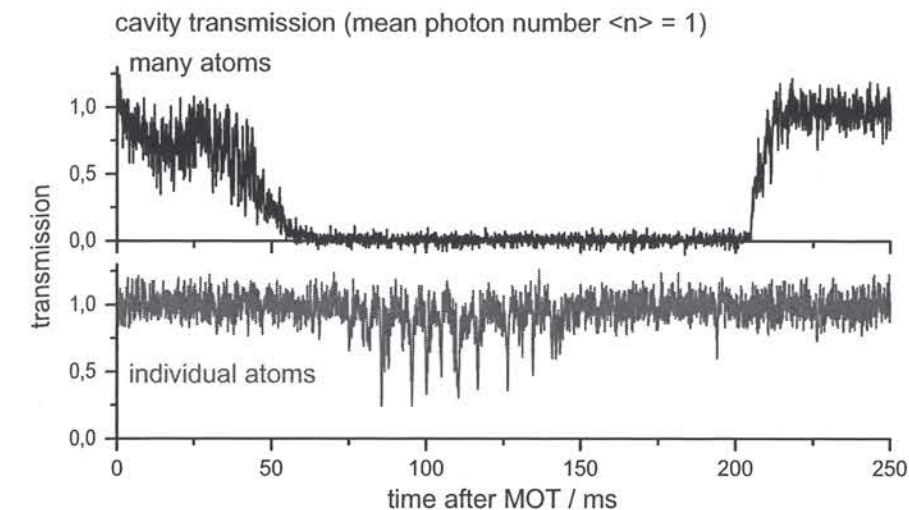
Abbildung 4.9: Resonatortransmission während des Durchflugs zweier Atomwolken unterschiedlicher Dichte. Die diskreten Einbrüche der Transmission (individual atoms) deuten auf die Wechselwirkung einzelner Atome mit dem Resonator hin.

rechte Seite von Abb. 4.8 zeigt die Transmission des Resonators als Funktion der Zeit, während sich Atome im Potential der führenden Dipolfalle bewegen (ein Wechsel zur stehenden Welle findet hier nicht statt). Der Resonator und der einfallende Laser sind in Resonanz mit dem $(5^2S_{1/2}(F = 3) \longleftrightarrow 5^2P_{3/2}(F' = 4))$ Übergang des ^{85}Rb. Gelangen N Atome in den Resonator, dann spaltet dessen Resonanzlinie um $g\sqrt{N}$ auf, und die Transmission des resonanten Lichts fällt stark ab. Der Resonator dient in diesem Fall als Atomdetektor, der erlaubt die Bewegung der Atome in der Dipolfalle in situ zu beobachten. Nach dem Umladen der Atome in die führende Dipolfalle (bei t=60 ms) führt deren Oszillation im Fallenpotential zu drei sukzessiven Einbrüchen der Resonatortransmission bei t={210 / 450 / 670} ms. Die scheinbare Aperiodizität und der starke Verlust von Atomen sind zum einen auf die Anharmonizität des Potentials und die damit verbundene Aufweitung der Atomwolke zurückzuführen, und zum anderen pumpt das Licht im Resonator mehr und mehr Atome aus dem anfänglich besetzten Zustand $5^2S_{1/2}(F = 3)$ in den anderen Hyperfeinzustand $5^2S_{1/2}(F = 2)$. Dieser Zustand koppelt nicht an den Resonator, so dass diese Atome das Transmissionsverhalten nicht mehr beeinflussen.

Eine einfache Abschätzung zeigt, dass der 500 μm lange Resonator (mit einer Finesse von 62000, $(g, \kappa, \gamma)/2\pi = (5, 2.4, 3)$ MHz und einer Kooperativität von $2C_0 = g^2/\kappa\gamma = 3.5$) bereits auf ein einziges Atom mit einem empfindlichen Transmissionsrückgang reagieren sollte. Ein solches Verhalten lässt Abb. 4.8 jedoch nicht erkennen, da dort die mittlere Photonenzahl im Resonator zu groß ist. Erst durch Absenken der mittleren Photonenzahl auf $\langle n \rangle \approx 1$ ist der Durchflug einzelner Atome durch die Resonatormode in Form diskreter Einbrüche der Transmission erkennbar, wie Abb. 4.9 zeigt. Die mittlere Dauer der Transmissionseinbrüche beträgt 400 μs und genügt, um das Eintreffen eines Atoms im Resonator abzuwarten und getriggert auf die Detektion des Atoms von der führenden Dipolfalle in die Geometrie der Stehwellen-Dipolfalle zu wechseln. Wir haben beobachtet, dass es auf diese Art möglich ist, ein einzelnes Atom mehrere Sekunden im Modenvolumen des Resonators zu halten. Dies wollen wir in Zukunft nutzen, um Atome untereinander zu verschränken oder um Quantenzustände zwischen Atomen (bzw. Atomen und Licht) zu übertragen. Im nächsten Kapitel werden erste Schritte in diese Richtung diskutiert.

Kapitel 5

Quanteninterferenz und Verschränkung

Dieses Kapitel geht über die reine Quantenzustandskontrolle und Manipulation hinaus. Ausgehend von einzelnen Photonen, die von einem stark gekoppelten Atom-Resonator System emittiert werden, haben wir Interferenzeffekte höherer Ordnung zeitaufgelöst betrachtet. Es ist uns gelungen, eine Quantenschwebung unabhängiger einzelner Photonen aufzulösen, und wir konnten diesen neuen Effekt nutzen, um eine Atom-Photon Verschränkung zu realisieren [79, 80].

5.1   Zwei-Photonen Interferenz

Eine Vielzahl faszinierender Experimente, die den nichtklassischen Charakter von Licht zeigen, basieren auf der Quanteninterferenz einzelner Photonen [81]. Fallen zwei unabhängige einzelne Photonen gleichzeitig auf einen Strahlteiler, so verlassen sie diesen stets als Photonenpaar, vorausgesetzt sie sind nicht unterscheidbar. Dieses klassisch nicht erklärbare Phänomen wurde zuerst mit Photonen aus einer parametrischen Frequenzkonversion gezeigt [82] und wird heute benutzt, um die Ununterscheidbarkeit unabhängiger einzelner Photonen nachzuweisen [83]. Mit Photonen aus einem gekoppelten Atom-Resonator System haben wir jetzt erstmals die Möglichkeit, den Quanteninterferenzprozess zeitaufgelöst zu betrachten.

Eine detaillierte theoretische Beschreibung der zeitaufgelösten Zwei-Photonen Quanteninterferenz findet sich in [79]. Kernaussage dieser Analyse ist, dass zwei Photonen, die auf die Eingänge 1 und 2 eines Strahlteilers mit den jeweiligen Modenfunktionen $\zeta_1(t)$ und $\zeta_2(t)$ auftreffen, mit der Wahrscheinlichkeit

$$P_{joint}(t_0, \tau) = \frac{1}{4}|\zeta_1(t_0 + \tau)\zeta_2(t_0) - \zeta_2(t_0 + \tau)\zeta_1(t_0)|^2. \tag{5.1}$$

in beiden Ausgängen des Strahlteilers zu den Zeiten t_0 und $t_0 + \tau$ detektiert werden. Daraus folgt unmittelbar, dass identische Photonen (mit $\zeta_1(t) \equiv \zeta_2(t)$) niemals in verschiedene Ausgänge des Strahlteilers gelangen. Unterscheiden sich die Photonen jedoch, so ist dies nur für $\tau = 0$ der Fall, d.h. die Photonen sind zwar niemals gleichzeitig in beiden Ausgängen des Strahlteilers zu finden, können aber, bedingt durch das Auseinanderlaufen der Modenfunktionen mit $|\tau|$, mit zunehmender Wahrscheinlichkeit in getrennte Ausgänge gelangen.

Als Beispiel betrachten wir zwei δt-lange Fourier-limitierte gaußförmige Ein-Photon Pulse, die gleichzeitig auf den Strahlteiler treffen und deren Trägerfrequenzen sich um $\Delta = \omega_2 - \omega_1$ unterscheiden. In diesem Fall führt die Integration von Gl.(5.1) über t_0 zu einer Wahrscheinlichkeit von

$$P_{2h\nu}(\tau) = \frac{1 - \cos(\Delta \times \tau)}{2\delta t\sqrt{\pi}} \times \exp(-(\tau/\delta t)^2) \tag{5.2}$$
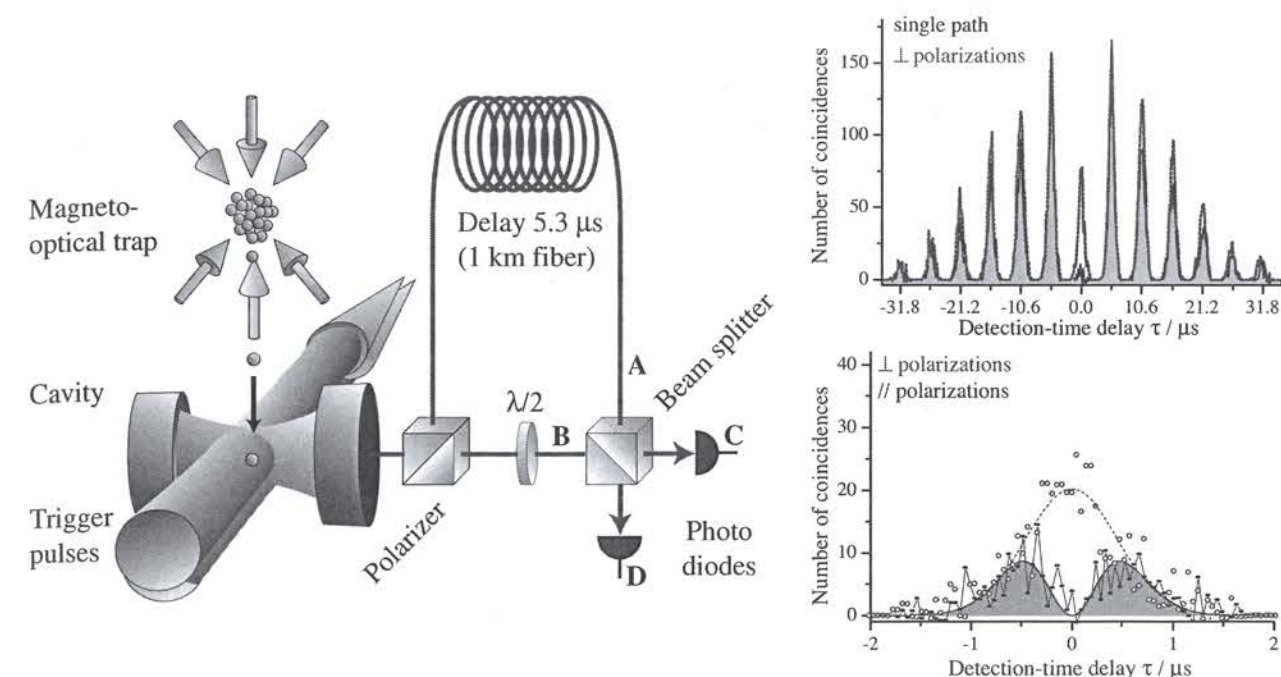
Abbildung 5.1: Quanteninterferenz einzelner Photonen. Unpolarisierte Photonen werden von einem polarisierenden Strahlteiler zufällig entlang zwei möglicher Pfade zum zweiten Strahlteiler geschickt. Ein Pfad verzögert ein Photon so lange, bis es gleichzeitig mit dem nachfolgenden Photon (im anderen Pfad) auf den Strahlteiler trifft. Wir messen die Zahl der Koinzidenzen zwischen den beiden Photodioden als Funktion der Zeitdifferenz der Detektionen: Mit nur einem Pfad ist dies eine Hanbury-Brown&Twiss Messung der Photonenstatistik, die Antibunching zeigt (oben, blau). Sind beide Pfade offen, treffen Photonen gleichzeitig auf den Strahlteiler. Stehen deren Polarisationen senkrecht zueinander, kommt es nicht zur Interferenz (oben und unten, rot gestrichelt). Die Photonen interferieren erst, wenn ihre Polarisationen parallel stehen, und im Zentrum des mittleren Peaks zeigt sich ein Zwei-Photonen Interferenzdip (unten, blau).

beide Photonen mit einem Zeitabstand τ in verschiedenen Ausgängen zu detektieren. Neben der Oszillation dieser Wahrscheinlichkeit mit der Differenzfrequenz Δ ist hervorzuheben, dass die Oszillation stets bei $\tau = 0$ startet. Daraus folgt, dass die Wahrscheinlichkeit für Photonenkoinzidenzen zwischen den Strahlteilerausgängen immer Null beträgt, auch falls Δ fluktuiert und inhomogen verbreitet ist. Im speziellen Fall einer verschwindenden mittleren Frequenzdifferenz, $\bar{\Delta} = 0$, und einer inhomogenen Bandbreite $\delta\omega$ ist die Wahrscheinlichkeit beide Photonen in verschiedenen Ausgängen des Strahlteilers zu detektieren

$$P_{inh}(\tau) = \frac{1 - \exp(-(\delta\omega \times \tau/2)^2)}{2\delta t\sqrt{\pi}} \times \exp(-(\tau/\delta t)^2). \tag{5.3}$$

Daraus ist ersichtlich, dass die inhomogene Verbreiterung des Photonenspektrums zu einem Dip in der zwei-Photonen Detektionswahrscheinlichkeit mit einer Breite von $2/\delta\omega$ führt (halbe Breite bei 1/e Tiefe). Unabhängig von der Bandbreite erreicht das Minimum des Dips in P_{inh} immer Null, so dass trotz inhomogener Verbreiterung eine perfekte Zwei-Photonen Interferenz realisiert werden kann, indem man durch einen zeitlichen Filter nur Ereignispaare selektiert, deren Detektionszeitabstand der Bedingung $|\tau| \ll 2/\delta\omega$ genügt.

Die experimentelle Anordnung ist in Abb. 5.1 gezeigt. Aufeinanderfolgende Photonen werden von einem ersten Strahlteiler zufällig entlang zwei möglicher Pfade geschickt, die beide zu einem zweiten 50:50 Strahlteiler führen. Ein Pfad enthält eine 1 km lange optische Faser, woraus eine Lauf-

zeitdifferenz von $5.3\,\mu s$ zwischen den Pfaden resultiert. Von zwei Photonen, die mit einem entsprechenden Zeitabstand nacheinander emittiert werden, wählt das erste mit einer Wahrscheinlichkeit von 50 % den langen Pfad und das zweite mit gleicher Wahrscheinlichkeit den kurzen Pfad. Daher treffen in einem von vier Fällen die Wellenpakete beider Photonen gleichzeitig auf den zweiten Strahlteiler, so dass an dessen Ausgang Quanteninterferenzphänomene beobachtet werden können.

Abbildung 5.1 zeigt die Zahl der gemessenen Koinzidenzen, $K(\tau)$, zwischen den beiden Detektoren am Ausgang des zweiten Strahlteilers als Funktion des Zeitabstands τ zwischen den Detektionen. Wir haben diese Messung mit unterschiedlichen relativen Polarisationen der beiden Photonen durchgeführt, um die Auswirkung der Quanteninterferenz zu verdeutlichen. Im ersten Fall stehen die Polarisationen senkrecht zueinander, so dass die Photonen nicht interferieren. Sie werden zufällig auf beide Detektoren verteilt, und der Verlauf von $K(\tau)$ im zentralen Peak um $\tau = 0$ spiegelt die gaussförmige Einhüllende der Photonenwellenpakete $\propto \exp(-(\tau/\delta t)^2)$ wider. Im zweiten Fall stehen die Polarisationen parallel zueinander und es kommt zur Interferenz, so dass bei absolut identischen Photonen das gesamte Koinzidenzsignal um $\tau = 0$ verschwinden sollte. Wie erwartet, zeigt die Messung einen tiefen Einbruch endlicher Breite bei $\tau = 0$, der auf Null hinuntergeht. Die Breite des Einbruchs ist jedoch zu gering, um das gesamte Koinzidenzsignal auszulöschen. Diese Abweichung vom idealen Verhalten schreiben wir einer inhomogenen Verbreiterung des Photonenspektrums zu. Aus einem Fit des nach Gl. (5.3) erwarteten Verlaufs an das gemessene Signal ergibt sich eine inhomogene Linienbreite von $\delta\omega/2\pi = 690\,\text{kHz}$, bzw. eine halbe $1/e$ Breite des Einbruchs von $460\,\text{ns}$, die die mittlere Dephasierungszeit widerspiegelt. Zu dieser Dephasierung trägt eine Kombination mehrerer Mechanismen bei, die im Experiment nicht vollkommen ausgeschaltet werden konnten. Insbesondere sind dies nicht-adiabatische Übergänge im Atom und eine Durchmischung der Zeemanzustände durch statische Magnetfelder und Magnetfeldfluktuationen während der Photonenerzeugung sowie akustische und thermische Fluktuationen der 1 km langen optischen Faser, die sich auf die Phase der transmittierten Photonen übertragen. Es handelt sich offensichtlich um eine rein technische Limitierung, denn die Kohärenzzeit übersteigt die Lebensdauer des Resonators und die Lebensdauer angeregter Atome bereits um eine Größenordnung, so dass diese als prinzipiell limitierende Faktoren ausgeschlossen werden können.

Innerhalb der Dephasierungszeit können nacheinander erzeugte Photonen jedoch als identisch angesehen werden, so dass mit Einsatz eines zeitlichen Filters prinzipiell optische Quantengatter realisiert werden können. Zudem bietet die Kopplung von Atomen und Licht die Möglichkeit, Photonen und Atome zu verschränken und dies innerhalb der Dephasierungszeit nachzuweisen. Dies ist im folgenden Abschnitt erläutert.

5.2 Atom-Photon Verschränkung

Das korrelierte Verhalten zweier entfernter Quantensysteme ist eines der erstaunlichsten Phänomene, das von der Quantenmechanik korrekt beschrieben wird. Dieser als Verschränkung bekannte Effekt findet zwar keine klassische Erklärung [84], wird aber zunehmend in aktuellen Experimenten eingesetzt. Diese Anstrengungen gipfelten vor einigen Jahren in der erfolgreichen Teleportation von Lichtfeldern [85–87]. Demgegenüber stellt die mehrfach vorgeschlagene Verschränkung entfernter massiver Teilchen [88–92] und deren Teleportation [93–95] eine neue Herausforderung dar. Erst vor kurzem ist es der Gruppe um C. Monroe gelungen, eine Polarisationsverschränkung zwischen einem Ion und einem Photon zu demonstrieren [96], während wir zeigen konnten, dass die in unserem System beobachtete Zwei-Photonen Quantenschwebung [80] eine transiente Verschränkung eines Atoms mit einem Photonenzahlzustand impliziert.
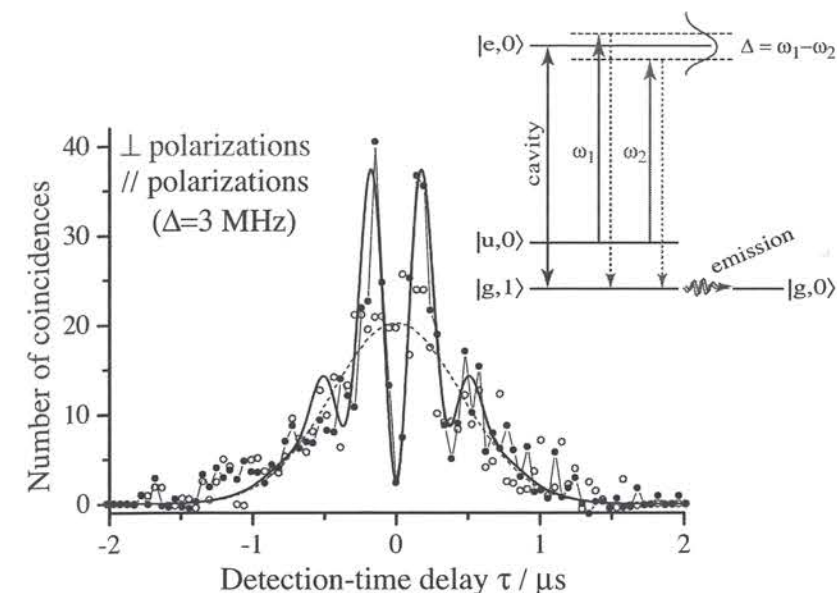
Abbildung 5.2: Quantenschwebung im Koinzidenzsignal. Die Photonenquelle erzeugt abwechselnd einzelne Photonen unterschiedlicher Frequenz (siehe Niveauschema). Diese treffen gleichzeitig auf den Strahlteiler und führen bei paralleler Polarisation zu einer Schwebung im Koinzidenzsignal (durchgezogen). Bei $\tau = 0$ liegt die Sichtbarkeit der Schwebung bei über 90%. Zum Vergleich ist das Koinzidenzsignal senkrecht polarisierter Photonen gezeigt (gestrichelt).

Wir beschreiben dazu das stark gekoppelte Atom-Resonator System mit einem vereinfachten Modell. Bei der Erzeugung der Photonen durch eine adiabatische Passage sind nur die Zustände $\{|u,0\rangle, |e,0\rangle, |g,1\rangle\}$ involviert, wobei $|0\rangle$ und $|1\rangle$ die Photonenzahlzustände des Resonators bezeichnen. Der Dunkelzustand und der Grundzustand,

$$|e'\rangle \equiv (g|u,0\rangle - \Omega|g,1\rangle)/N.N. \quad \text{und} \quad |g'\rangle \equiv |g,0\rangle \qquad (5.4)$$

spannen dabei den Unterraum auf, der zur vollständigen Beschreibung genügt. Das System verbleibt im Zustand $|e'\rangle$ bis ein Photon den Resonator verlässt. Erst in diesem Moment geht das System in den Grundzustand $|g'\rangle$ über.

Hervorzuheben ist, dass in unserer Anordnung ein Photon, das entlang des kurzen Weges zum Strahlteiler läuft, streng genommen nicht genügend Raum hat, um in voller Länge zu existieren. Sein Photonenwellenpaket hat eine Dauer von $2\,\mu s$, aber die kurze Strecke vom Resonator zum zweiten Strahlteiler legt es in nur $50\,\text{ns}$ zurück. Daher ist der Zustand dieses Strahlteilereingangs mit den möglichen Zustände des Atom-Resonator Systems, $|e'\rangle$ und $|g'\rangle$, zu beschreiben.

Die Laufzeit entlang des langen Pfades beträgt hingegen $5,3\,\mu s$, so dass der Zustand des anderen Strahlteilereingangs durch die beiden möglichen Photonenzahlzustände der Faser, $|0\rangle$ und $|1\rangle$ ausgedrückt werden kann.

Im Folgenden beschränken wir uns auf Situationen, in denen zwei Photonen nacheinander emittiert, in der richtigen Reihenfolge auf beide Pfade verteilt und zudem beide nachgewiesen werden. Nur Photonenpaare, auf die diese Bedingungen zutreffen, tragen zum gemessenen Signal bei. Andere Fälle werden nicht betrachtet.

Eine Schritt-für Schritt Analyse des Interferenzprozesses zeigt, dass unter diesen Bedingungen die Messung des ersten Photons eine Atom-Photon Verschränkung induziert. Mit der Messung des zweiten Photons wird die Verschränkung anschliessend interferometrisch nachgewiesen und gleichzeitig (d.h. per Postselektion) sichergestellt, das obige Bedingungen erfüllt sind.

Die Ausgangssituation mit einem Photon in der Faser und einem angeregten Atom-Resonator System beschrieben wird durch

$$|\Psi_{initial}\rangle = |e'\rangle|1\rangle.$$

Mit der Detektion eines ersten Photons zum Zeitpunkt t_0 wird ein Anregungsquant aus dem System

genommen. Da jedoch nicht bekannt ist, welches Photon detektiert wird, projiziert dies das verbleibende System in den verschränkten Zustand

$$|\Psi_{cond}(t_0)\rangle = (|e',0\rangle \pm |g',1\rangle)/\sqrt{2}. \tag{5.5}$$

Dies ist ein messungsinduzierter maximal verschränkter Zustand zwischen dem gekoppelten Atom-Resonator System (im Zustand $|e'\rangle$ oder $|g'\rangle$) einerseits, und der Feldmode der Faser (im Zustand $|0\rangle$ oder $|1\rangle$) andererseits. Die relative Phase der beiden Teile hängt davon ab, welchen Weg das detektierte Photon am Ausgang des Strahlteilers eingeschlagen hat. Um den Grad der Verschränkung und die Kohärenzzeit zu messen, genügt es die Detektion eines zweiten Photons abzuwarten, während man die Phasendifferenz zwischen den beiden Teilen von $|\Psi_{cond}\rangle$ systematisch variiert. Letzteres wird erreicht durch eine kleine Frequenzdifferenz Δ zwischen den beiden nacheinander erzeugten Photonen[1]. Wird das zweite Photon zum Zeitpunkt $t_0 + \tau$ detektiert, dann baut sich zwischen beiden Teilen des verschränkten Zustands ein relativer Phasenunterschied von $\delta\phi(\tau) = \Delta\tau$ auf, so dass der Zustand des Systems im Produktraum rotiert zu

$$|\Psi_{cond}(t_0 + \tau)\rangle = (|e',0\rangle \pm e^{i\Delta\tau}|g',1\rangle)/\sqrt{2}.$$

Unmittelbar vor der Detektion des zweiten Photons muss das Atom seine Anregung an die Mode des kurzen Pfades abgeben, so dass das Atom-Resonator System vom den Photonenzuständen separiert werden kann,

$$|\Psi_{cond}(t + \tau)\rangle \longrightarrow |g'\rangle \otimes (|1,0\rangle \pm e^{i\Delta\tau}|0,1\rangle)/\sqrt{2}.$$

Dies entspricht dem Zustand eines klassischen Mach-Zehnder Interferometers, in dem ein einzelnes Photon entlang zwei möglicher Pfade zum zweiten Strahlteiler gelangt. Welchen Weg das Photon am Ausgang einschlägt hängt von der Phasendifferenz der Pfade ab, die in diesem Fall $\Delta\tau$ beträgt. Daher erwarten wir am Ausgang des Strahlteilers ein Schwebungssignal in der Korrelationsfunktion der Detektoren, $K(\tau)$, das mit der Differenzfrequenz Δ oszilliert.

Abbildung 5.2 zeigt die Zahl der gemessenen Korrelationen zwischen beiden Detektoren als Funktion der Zeitdifferenz τ zwischen den Detektionen des ersten und des zweiten Photons. Die Differenzfrequenz zwischen aufeinanderfolgenden Triggerpulsen beträgt 3 MHz, so dass die relative Phase der beiden Teile von $|\Psi_{cond}\rangle$ nach der Detektion des ersten Photons mit $\Delta = \pm 3$ MHz auseinanderläuft. Dies führt zu der ausgeprägten Oszillation des Korrelationssignals, die deutlich über das gestrichelt gezeigte Referenzlevel nicht interferierender Photonen hinausschwingt. Der Grad der Verschränkung zwischen Atom-Resonator System und der Feldmode der Faser ist durch die Sichtbarkeit des Quantenschwebungssignals, $V_{quant} = (K_{max} - K_{min})/(K_{max} + K_{min})$, gegeben. Für $\tau \longrightarrow 0$ liegt diese bei 90% (innerhalb der Fehler), und dies bedeutet das die Verschränkung unmittelbar nach Detektion des ersten Photons nahezu perfekt ist. Wie im vorigen Abschnitt beträgt auch hier die Lebensdauer des Schwebungssignals (und damit die Kohärenzzeit) 460 ns, begrenzt durch die mittlere Dephasierung des Systems.

Bemerkenswert ist, dass die Messung des ersten Photons die anfängliche Phasendifferenz (bei $\tau = 0$) festlegt. Diese beträgt entweder 0 oder π, je nachdem welchen Weg das Photon nach dem Strahlteiler nimmt. Daraus folgt zwingend, dass die Quantenschwebung mit der ersten Photonendetektion in Phase ist. In der Kreuzkorrelation der Ausgänge des Strahlteilers erwartet man daher ein Schwebungssignal mit einer Sichtbarkeit von 100%. Dies unterstreicht den Quantencharakter des Experiments, da eine derart hohe Sichtbarkeit klassisch nicht erklärt werden kann. Lässt man z.B.

---

[1]Dazu dient eine Frequenzdifferenz zwischen den klassischen Laserpulsen, die die Photonenerzeugung treiben. Aufgrund der Energieerhaltung überträgt sich diese auf die Frequenz der erzeugten Photonen
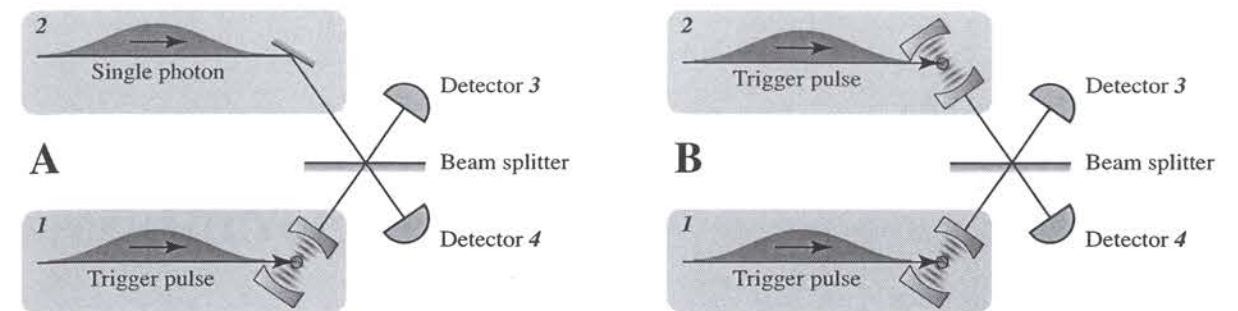
Abbildung 5.3: Anordnungen zur Verschränkung. **(A)** Situation im Experiment. Ein Photon läuft entlang einer langen Faser (Strahlteilereingang 2), das andere kommt direkt vom Resonator (Eingang 1). Die erste Photodetektion verschränkt die Feldmode der Faser mit dem Zustand des Atoms. **(B)** Äquivalente Situation mit zwei separaten Resonatoren. Hier würde eine erste Photodetektion die Zustände der Atome verschränken.

kohärente Felder gleicher Amplitude und einer Frequenzdifferenz Δ interferieren, dann führt dies im besten Fall zu einer Schwebung mit einer Sichtbarkeit von 100% an jedem einzelnen Ausgang des Strahlteilers. Die Detektion eines einzelnen Photons wirkt sich jedoch nicht auf die relative Phasenlage aus, so dass das Kreuzkorrelationssignal der beiden Ausgänge des Strahlteilers durch das Faltungsintegral

$$K(\tau) \propto \int dt_0 \sin^2(t_0\Delta/2)\cos^2((t_0 + \tau)\Delta/2) \propto 1 - 0.5\cos(\tau\Delta)$$

gegeben ist, und mithin nur eine Sichtbarkeit der Schwebung von maximal $V_{coherent} = 50\%$ aufweisen kann.

In Abbildung 5.3 ist skizziert, dass sich das Photon in der 1 km langen Faser im Prinzip auch durch ein zweites, identisches Atom-Resonator System ersetzen lässt. Physikalisch ist ein solches System vollkommen äquivalent zum jetzigen Aufbau, mit dem Unterschied , dass dessen Ausgangszustand,

$$|\Psi_{initial}\rangle = |e_1'\rangle|e_2'\rangle,$$

mit der ersten Detektion eines Photons in den verschränkten Atom-Atom Zustand

$$|\Psi_{cond}(t_0)\rangle = (|e_1'g_2'\rangle \pm |g_1'e_2'\rangle)/\sqrt{2}$$

projiziert würde. Eine derartige messungsinduzierten Verschränkung zweier unabhängiger Atom-Resonator Systeme wurde in leicht verschiedenen Varianten in einer Vielzahl theoretischer Arbeiten diskutiert [88–95, 97, 98]. Unser Experiment bildet ein solches System zweier unabhängiger Resonatoren nach, die beiden Teilsysteme sind jedoch nicht räumlich, sondern zeitlich voneinander getrennt. Dies impliziert, dass die verschränkten Systeme nicht gleichzeitig existieren, so dass es nicht einfach ist diese spezielle Form der Verschränkung zur Quanteninformationsverarbeitung zu nutzen. Dennoch ist die beobachtete Quantenschwebung ein experimenteller Beweis, dass eine Verschränkung massiver Teilchen in getrennten Resonatoren möglich ist.

Kapitel 6

Relevanz für die Quanteninformationsverarbeitung

Aufbauend auf den hier vorgestellten Arbeiten konnten vor kurzem auch andere Gruppen zeigen, dass durch Vakuum-stimulierte Raman-Streuung einzelne Atome zur kontrollierten Erzeugung einzelner Photonen in der Lage sind [64, 99]. Der zugrunde liegende physikalische Prozess ist unitär und somit prinzipiell umkehrbar, so dass sich ein einzelnes Atom auch zur kontrollierten Absorption einzelner Lichtquanten eignen sollte. Es sollte daher prinzipiell möglich sein, mit diesem Prozess den Quantenzustand eines ersten Atoms auf ein zweites Atom in einem weit entfernten Resonator zu übertragen [52]. Mit Hilfe von Photonen als Übermittler von Quanteninformation wäre somit die Vernetzung von weit entfernt gelegenen Quantencomputern möglich.

Ebenso ist auf Basis unserer Entwicklung die Realisierung eines Quantengatters – eines Grundbausteins eines zukünftigen Quantencomputers – vorstellbar. Von zwei Atomen innerhalb eines Resonators kann eines durch den hier vorgestellten Prozess gezielt seinen Quantenzustand auf das Lichtfeld im Resonator übertragen. Solange das Licht im Resonator verbleibt, kann es das andere Atom im Resonator beeinflussen und damit dessen Quantenzustand verändern. Dies entspricht einem Zwei-Qubit Quantengatter, das auf die Zustände der Atome wirkt [68, 100, 101]. Um dies zu bewerkstelligen, sind die Atome mit einer geeigneten Vorrichtung, wie z.B. einer optischen Dipolkraftfalle, im Resonator festzuhalten. Alternativ bietet die Ununterscheidbarkeit der Photonen die Möglichkeit, in einem rein optischen Netzwerk Quantenoperationen mittels linearer Elemente zu realisieren [54]. Die Quantenoperationen basieren in diesem Fall auf der Interferenz mehrerer Photonen, die entlang verschiedener Pfade in das System gelangen. Die Kombination atomarer und/oder optischer Quantengatter mit dem oben diskutierten Quantennetzwerk ermöglicht im Prinzip den Aufbau eines skalierbaren Quantencomputers.

Zuletzt ist es uns gelungen, die messungsinduzierte Verschränkung eines massiven Teilchens (Rubidium Atom) mit einem Photon experimentell nachzuweisen. Dies lässt den Schluss zu, dass auf gleiche Art auch mehrere Atome in getrennten Atom-Resonator Systemen verschränkt werden können. Eine Erweiterung dieses Schemas hin zur Teleportation bzw. zum Verschränkungs-Austausch (Entanglement Swapping) zwischen Atomen und Photonen ist naheliegend, und scheint ein vielversprechender Ansatz zur Realisierung eines Quanten-Repeaters.

Literaturverzeichnis

[1] A. E. Siegman. *Lasers*. University Science Books, Sausalito, California, 1986.

[2] C. Cohen-Tannoudji, J. Dupont-Roc, and G. Grynberg. *Photons and Atoms*. J. Wiley & Sons, 1997.

[3] C. Cohen-Tannoudji, J. Dupont-Roc, and G. Grynberg. *Atom-Photon Interactions*. J. Wiley, Chichester, 1998.

[4] W. Demtröder. *Laserspektroskopie*. Springer, Berlin, Heidelberg, 2000.

[5] N. V. Vitanov, M. Fleischhauer, B. W. Shore, and K. Bergmann. Coherent manipulation of atoms and molecules by sequential laser pulses. *Adv. At. Mol. Opt. Phys.*, 46:55–190, 2001.

[6] H. J. Metcalf and P. van der Straten. *Laser Cooling and Trapping*. Springer, New York, 1999.

[7] D. Leibfried, B. DeMarco, V. Meyer, D. Lucas, M. Barrett, J. Britton, W. M. Itano, B. Jelenkovic, C. Langer, T. Rosenbrand, and D. J. Wineland. Experimental demonstration of a robust, high-fidelity geometric two ion-qubit phase gate. *Nature*, 422:412–415, 2003.

[8] F. Schmidt-Kaler, H. Häffner, M. Riebe, S. Gulde, G. P. T. Lancaster, T. Deuschle, C. Becher, C. F. Roos, J. Eschner, and R. Blatt. Realization of the Cirac-Zoller controlled-NOT quantum gate. *Nature*, 422:408–411, 2003.

[9] J. Gruska. *Quantum Computing*. McGraw-Hill, UK, 1999.

[10] D. Bouwmeester, A. Ekert, and A. Zeilinger, editors. *The Physics of Quantum Information*. Springer, Berlin, 2000.

[11] T. Beth and G. Leuchs, editors. *Quantum Information Processing*. Wiley-VCH, Berlin, 2003.

[12] L. Allen and J. H. Eberly. *Optical Resonance and Two-Level Atoms*. J. Wiley & Sons, NY, 1975.

[13] B. W. Shore. *The Theory of Coherent Atomic Excitation*. J. Wiley & Sons, 1990.

[14] K. Bergmann and B. W. Shore. Coherent population transfer. In H. L. Dai and R. W. Field, editors, *Molecular dynamics and stimulated emission pumping*, pages 315–373. World Scientific, Singapore, 1995.

[15] K. Bergmann, H. Theuer, and B. W. Shore. Coherent population transfer among quantum states of atoms and molecules. *Rev. Mod. Phys.*, 70:1003–1026, 1998.

[16] A. Kuhn, S. Steuerwald, and K. Bergmann. Coherent population transfer in NO with pulsed lasers: The consequences of hyperfine structure, Doppler broadening and electromagnetically induced absorption. *Eur. Phys. J. D*, 1:57–70, 1998.

[17] A. Messiah. *Quantum Mechanics*, volume 2, chapter 17. J. Wiley & Sons, NY, 1958.

[18] A. Abragam. *The Principles of Nulcear Magnetism.* Oxford University Press, Oxford, 1961.

[19] M. M. T. Loy. Self-induced rapid adiabatic passage. *Phys. Rev. Lett.*, 32:814–817, 1974.

[20] M. M. T. Loy. Observation of two-photon optical nutation and free-induction decay. *Phys. Rev. Lett.*, 36:1454–1457, 1976.

[21] M. M. T. Loy. Two-photon adiabatic inversion. *Phys. Rev. Lett.*, 41:473–475, 1978.

[22] L. P. Yatsenko, B. W. Shore, T. Halfmann, and K. Bergmann. Source of metastable H(2s) atoms using the Stark chirped rapid-adiabatic-passage technique. *Phys. Rev. A*, 60:R4237–R4240, 1999.

[23] A. Kuhn, H. Perrin, W. Hänsel, and C. Salomon. Three dimensional Raman cooling using velocity selective rapid adiabatic passage. In K. Burnett, editor, *OSA TOPS on Ultracold Atoms and BEC*, volume 7, pages 58–65. OSA, 1996.

[24] H. Perrin, A. Kuhn, I. Bouchoule, and C. Salomon. Sideband cooling of neutral atoms in a far-detuned optical lattice. *Europhys. Lett.*, 42:395–400, 1998.

[25] S. E. Harris. Electromagnetically induced transparency with matched pulses. *Phys. Rev. Lett.*, 70:552–555, 1993.

[26] S. E. Harris. Electromagnetically induced transparency. *Phys. Today*, 50(7):36, 1997.

[27] L. V. Hau, S. E. Harris, Z. Dutton, and C. H. Behroozi. Light speed reduction to 17 metres per second in an ultracold atomic gas. *Nature*, 397:594–598, 1999.

[28] M. D. Lukin, S. F. Yelin, and M. Fleischhauer. Entanglement of atomic ensembles by trapping coherent photon states. *Phys. Rev. Lett.*, 84:4235–4238, 2000.

[29] M. Fleischhauer and M. D. Lukin. Dark-state polaritons in electromagnetically induced transparency. *Phys. Rev. Lett.*, 84:5094–5097, 2000.

[30] D. F. Phillips, A. Fleischhauer, A. Mair, R. L. Walsworth, and M. D. Lukin. Storage of light in atomic vapor. *Phys. Rev. Lett.*, 86:783–786, 2001.

[31] A. Kuhn, M. Hennrich, T. Bondo, and G. Rempe. Controlled generation of single photons from a strongly coupled atom-cavity system. *Appl. Phys. B*, 69:373–377, 1999.

[32] M. Kasevich and S. Chu. Laser cooling below a photon recoil with three-level atoms. *Phys. Rev. Lett.*, 69:1741, 1992.

[33] J. Reichel, O. Morice, G. M. Tino, and C. Salomon. Sub-recoil Raman cooling of Cesium atoms. *Europhys. Lett.*, 28:477, 1994.

[34] J. Reichel, F. Bardou, M. Ben Dahan, E. Peik, S. Rand, C. Salomon, and C. Cohen-Tannoudji. Raman cooling of Cesium below 3 nK: New approach inspired by Lévy flight statistics. *Phys. Rev. Lett.*, 75:4575, 1995.

[35] H. J. Lee, C. S. Adams, M. Kasevich, and S. Chu. Raman cooling of atoms in an optical dipole trap. *Phys. Rev. Lett.*, 76:2658, 1996.

[36] H. Perrin, A. Kuhn, I. Bouchoule, T. Pfau, and C. Salomon. Raman cooling of spin polarized Cesium atoms in a crossed dipole trap. *Europhys. Lett.*, 46:141–147, 1999.

[37] W. Neuhauser, M. Hohenstatt, P. Toschek, and H. Dehmelt. Optical-sideband cooling of visible atom cloud confined in parabolic well. *Phys. Rev. Lett.*, 41:233–236, 1978.

[38] C. A. Blockley and D.F. Walls. Cooling of a trapped ion in the strong-sideband regime. *Phys. Rev. A*, 47(3):2115–2127, 1993.

[39] R.L. de Matos Filho and W. Vogel. Second-sideband laser cooling and nonclassical motion of trapped ions. *Phys. Rev. A*, 50(3):R1988–R1991, 1994.

[40] C. Monroe, D. M. Meekhof, B. E. King, S. R. Jefferts, W. M. Itano, and D. J. Wineland. Resolved-sideband Raman cooling of a bound atom to the 3D zero-point energy. *Phys. Rev. Lett.*, 75:4011, 1995.

[41] S. E. Hamann, D. L. Haycock, G. Klose, P. H. Pax, I. H. Deutsch, and P. S. Jessen. Resolved-sideband Raman cooling to the ground state of an optical lattice. *Phys. Rev. Lett.*, 80:4149, 1998.

[42] V. Vuletić, C. Chin, A. J. Kerman, and S. Chu. Degenerate Raman sideband cooling of trapped cesium atoms at very high atomic densities. *Phys. Rev. Lett.*, 81:5768–5771, 1998.

[43] I. Bouchoule, H. Perrin, A. Kuhn, M. Morinaga, and C. Salomon. Neutral atoms prepared in Fock states of a 1d harmonic potential. *Phys. Rev. A*, 59:R8–R11, 1999.

[44] M. Morinaga, I. Bouchoule, J.-C. Karam, and C. Salomon. Manupulation of motional quantum states of neutral atoms. *Phys. Rev. Lett.*, 83:4037–4040, 1999.

[45] I. Bouchoule, M. Morinaga, and C. Salomon. Cesium gas strongly confined in one dimension: Sideband cooling and collisional properties. *Phys. Rev. A*, 65:033402, 2002.

[46] A. J. Kerman, V. Vuletić, C. Chin, and S. Chu. Beyond optical molasses: 3D Raman sideband cooling of atomic Cesium to high phase-space density. *Phys. Rec. Lett.*, 84:439–442, 2000.

[47] M. D. Barrett, J. A. Sauer, and M. S. Chapman. All-optical formation of an atomic Bose-Einstein condensate. *Phys. Rev. Lett.*, 87:010404, 2001.

[48] T. Weber, J. Herbig, M. Mark, H.-C-Nägerl, and R. Grimm. Bose-Einstein condensation of Cesium. *Science*, 299:232, 2002.

[49] D. DiVincenzo. Real and realistic quantum computers. *Nature*, 393:113–114, 1998.

[50] E. T. Jaynes and F. W. Cummings. Comparison of quantum and semiclassical radiation theories with application to the beam maser. *Proc. IEEE*, 51:89–109, 1963.

[51] S. Haroche and D. Kleppner. Cavity quantum electrodynamics. *Phys. Today*, pages 24–30, January 1989.

[52] J. I. Cirac, P. Zoller, H. J. Kimble, and H. Mabuchi. Quantum state transfer and entanglement distribution among distant nodes in a quantum network. *Phys. Rev. Lett.*, 78:3221–3224, 1997.

[53] S. van Enk, J. I. Cirac, P. Zoller, H. J. Kimble, and H. Mabuchi. Quantum state transfer in a quantum network: A quantum optical implementation. *J. Mod. Opt.*, 44:1727, 1997.

[54] E. Knill, R. Laflamme, and G. J. Milburn. A scheme for efficient quantum computing with linear optics. *Nature*, 409:46–52, 2001.

[55] H. J. Kimble, M. Dagenais, and L. Mandel. Photon antibunching in resonance fluorescence. *Phys. Rev. Lett.*, 39:691–695, 1977.

[56] F. Diedrich and H. Walther. Nonclassical radiation of a single stored ion. *Phys. Rev. Lett.*, 58:203–206, 1987.

[57] E. M. Purcell. Spontaneous emission probabilities at radio frequencies. *Phys. Rev.*, 69:681, 1946.

[58] M. Hennrich, T. Legero, A. Kuhn, and G. Rempe. Vacuum-stimulated Raman scattering based on adiabatic passage in a high-finesse optical cavity. *Phys. Rev. Lett.*, 85:4872–4875, 2000.

[59] A. Kuhn and G. Rempe. Optical cavity qed: Fundamentals and application as a single-photon light source. In Martini F. De and C. Monroe, editors, *Experimental Quantum Computation and Information*, volume 148, pages 37–66. IOS-Press, 2002.

[60] M. Hennrich, A. Kuhn, and G. Rempe. Counter-intuitive vacuum-stimulated Raman scattering. *J. Mod. Opt.*, 50:936–942, 2003.

[61] R. Hanbury-Brown and R. Q. Twiss. A test of a new type of stellar interferometer on Sirius. *Nature*, 178:1046–1448, 1956.

[62] A. Kuhn, M. Hennrich, and G. Rempe. Deterministic single-photon source for distributed quantum networking. *Phys. Rev. Lett.*, 89:067901, 2002.

[63] A. Kuhn, M. Hennrich, and G. Rempe. Strongly-coupled atom-cavity systems. In T. Beth and G. Leuchs, editors, *Quantum Information Processing*, pages 182–195. Wiley-VCH, Berlin, 2003.

[64] J. McKeever, A. Boca, A. D. Boozer, R. Miller, J. R. Buck, A. Kuzmich, and H. J. Kimble. Deterministic generation of single photons from one atom trapped in a cavity. *Science*, 303:1992–1994, 2004.

[65] H. J. Kimble. Comment on "Deterministic single-photon source for distributed quantum networking". *Phys. Rev. Lett.*, 90:249801, 2003.

[66] A. Kuhn, M. Hennrich, and G. Rempe. A reply to the comment by Harry J. Kimble. *Phys. Rev. Lett.*, 90:249802, 2003.

[67] M. Hennrich, T. Legero, A. Kuhn, and G. Rempe. Photon statistics of a non-stationary periodically driven single-photon source. *New Journal of Physics*, 6:86, 2004.

[68] A. Beige, D. Braun, B. Tregenna, and P. L. Knight. Quantum computing using dissipation to remain in a decoherence-free subspace. *Phys. Rev. Lett.*, 85:1762–1765, 2000.

[69] C. Marr, A. Beige, and G. Rempe. Entangled state preparation via dissipation-assisted adiabatic passages. *Phys. Rev. A*, 68:033817, 2003.

[70] A. Beige, H. Calbe, and P. L. Knight. Dissipation-assisted quantum computation in atom-cavity systems. *SPIE proceedings*, 5111:370, 2003.

[71] J. K. Pachos and A. Beige. Decoherence-free dynamical and geometrical entangling phase gates. *Phys. Rev. A*, 69:033817, 2004.

[72] J. McKeever, J. R. Buck, A. D. Boozer, A. Kuzmich, H.-C. Nägerl, D. M. Stamper-Kurn, and H. J. Kimble. State-insensitive cooling and trapping of single atoms in an optical cavity. *Phys. Rev. Lett.*, 90:133602, 2003.

[73] T. Fischer, P. Maunz, P. W. H. Pinkse, T. Puppe, and G. Rempe. Feedback on the motion of a single atom in an optical cavity. *Phys. Rev. Lett.*, 88:163002, 2002.

[74] A. B. Mundt, A. Kreuter, C. Becher, D. Leibfried, J. Eschner, F. Schmidt-Kaler, and R. Blatt. Coupling a single atomic quantum bit to a high finesse optical cavity. *Phys. Rev. Lett.*, 89:103001, 2002.

[75] G. R. Guthörlein, M. Keller, K. Hayasaka, W. Lange, and H. Walther. A single ion as a nanoscopic probe of an optical field. *Nature*, 414:49–51, 2001.

[76] S. Kuhr, W. Alt, D. Schrader, M. Müller, V. Gomer, and D. Meschede. Deterministic delivery of a single atom. *Science*, 293:278–280, 2001.

[77] N. Schlosser, G. Reymond, I. Protsenko, and P. Grangier. Sub-poissonian loading of single atoms in a microscopic dipole trap. *Nature*, 411:1024–1027, 2001.

[78] J. A. Sauer, K. M. Fortier, M. SW. Chang, C. D. Hamley, and M. S. Chapman. Cavity qed with optically transported atoms. *Phys. Rev. A*, 69:051804(R), 2004.

[79] T. Legero, T. Wilk, A. Kuhn, and G. Rempe. Time-resolved two-photon quantum interference. *Appl. Phys. B*, 77:797–802, 2003.

[80] T. Legero, T. Wilk, M. Hennrich, G. Rempe, and A. Kuhn. Quantum beat of two single photons. *Phys. Rev. Lett.*, 93:070503, 2004.

[81] L. Mandel. Quantum effects in one-photon and two-photon interference. *Rev. Mod. Phys.*, 71:S274–S282, 1999.

[82] C. K. Hong, Z. Y. Ou, and L. Mandel. Measurement of subpicosecond time intervals between two photons by interference. *Phys. Rev. Lett.*, 59:2044–2046, 1987.

[83] C. Santori, D. Fattal, J. Vučković, G. S. Solomon, and Y. Yamamoto. Indistinguishable photons from a single-photon device. *Nature*, 419:594–597, 2002.

[84] A. Einstein, B. Podolsky, and N. Rosen. Can quantum-mechanical description of physical reality be considered complete? *Phys. Rev.*, 47:777–780, 1935.

[85] D. Bouwmeester, J.-W. Pan, K. Mattle, M. Eibl, H. Weinfurter, and A. Zeilinger. Experimental quantum teleportation. *Nature*, 390:575–579, 1997.

[86] D. Boschi, S. Branca, F. de Martini, L. Hardy, and S. Popescu. Experimental realization of teleporting an unknown pure quantum state via dual classical and Einstein-Podolsky-Rosen channels. *Phys. Rev. Lett.*, 80:1121–1125, 1998.

[87] A. Furusawa, J. L. Sørensen, S. L. Braunstein, C. A. Fuchs, H. J. Kimble, and E. S. Polzik. Unconditional quantum teleportation. *Science*, 282:706–709, 1998.

[88] C. Cabrillo, J. I. Cirac, P. García-Fernández, and P. Zoller. Creation of entangled states of distant atoms by interference. *Phys. Rev. A*, 59:1025–1033, 1999.

[89] S.-B. Zheng and G.-C. Guo. Efficient scheme for two-atom entanglement and quantum information processing in cavity QED. *Phys. Rev. Lett.*, 85:2392–2395, 2000.

[90] J. Hong and H.-W. Lee. Quasideterministic generation of entangled atoms in cavities. *Phys. Rev. Lett.*, 89:237901, 2002.

[91] X.-L. Feng, Z.-M. Zhang, X.-D. Li, S.-Q. Gong, and Z.-Z. Xu. Entangling distant atoms by interference of polarized photons. *Phys. Rev. Lett.*, 90:217902, 2003.

[92] D. E. Browne, M. B. Plenio, and S. F. Huelga. Robust creation of entanglement between ions in spatially separate cavities. *Phys. Rev. Lett.*, 91:067901, 2003.

[93] J. I. Cirac and A. S. Parkins. Schemes for atomic-state teleportation. *Phys. Rev. A*, 50:R4441–R4444, 1994.

[94] S. Bose, P. L. Knight, M. B. Plenio, and V. Vedral. Proposal for teleportation of an atomic state via cavity decay. *Phys. Rev. Lett.*, 83:5158–5161, 1999.

[95] S. Lloyd, M. S. Shahriar, J. H. Shapiro, and P. R. Hemmer. Long distance, unconditional teleportation of atomic states via complete Bell state measurements. *Phys. Rev. Lett.*, 87:167903, 2001.

[96] B. B. Blinov, D. L. Moehring, L.-M. Duan, and C. Monroe. Observation of entanglement between a single trapped atom and a single photon. *Nature*, 428:153–157, 2004.

[97] M. B. Plenio, S. F. Huelga, A. Beige, and P. Knight. Cavity-loss-induced generation of entangled atoms. *Phys. Rev. A*, 59:2468–2575, 1999.

[98] L.-M. Duan and H. J. Kimble. Efficient engineering of multiatom entanglement through single-photon detections. *Phys. Rev. Lett.*, 90:253601, 2003.

[99] W. Lange, M. Keller, and H. Walther. private communication. 2004.

[100] T. Pellizari, S. A. Gardiner, J. I. Cirac, and P. Zoller. Decoherence, continuous observation, and quantum computing: A cavity QED model. *Phys. Rev. Lett.*, 75:3788–3791, 1995.

[101] A. Rauschenbeutel, G. Nogues, S. Osnaghi, P. Bertet, M. Brune, J.-M. Raimond, and S. Haroche. Coherent operation of a tunable quantum phase gate in cavity QED. *Phys. Rev. Lett.*, 83:5166–5169, 1999.
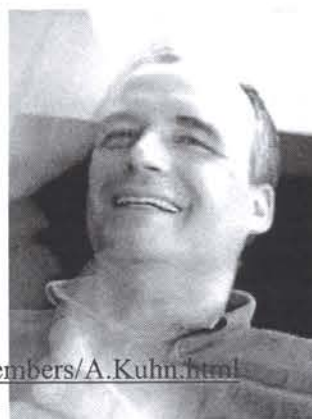
Anhang

A.1 Lebenslauf

Dr. Axel Kuhn

Geburtsdatum: 17. März 1964 in Worms

Hochschuladresse: Max-Planck-Institut für Quantenoptik
Hans-Kopfermann-Str. 1
85748 Garching
Telefon: +49 (0) 89 - 32905 264
Fax: +49 (0) 89 - 32905 395
E-Mail: Axel.Kuhn@mpq.mpg.de
Homepage: http://www.mpq.mpg.de/qdynamics/members/A.Kuhn.html

Privatadresse: Untere Isarau 1
85356 Freising   Telefon: +49 (0) 8161 – 872271

Familienstand: Verheiratet mit Fanny Gutjahr (seit 1998);
Drei Kinder: Joscha (1996), Noah (1998), Miro (2001)

Wissenschaftlicher Werdegang:

Studium

1984-1990   Studium der Physik und Informatik der Universität Kaiserslautern

Diplomarbeit bei Prof. Dr. K. Bergmann, Universität Kaiserslautern

1990   Physik Diplom

Diplomarbeit: *Experimentelle Implementierung des STIRAP-Verfahrens zur Schwingungsanregung von Molekülen*

Promotion

1990 – 1995   Doktorarbeit am FB Physik der Universität Kaiserslautern unter der Anleitung von Prof. Dr. K. Bergmann

1995   Promotion, Universität Kaiserslautern

Dissertation: *Kohärente optische Phänomene bei Anregung kleiner Moleküle mit Nanosekunden-Pulsen*

Beschäftigungen und Forschungsaufenthalte

1986 – 1994   Wissenschaftliche Hilfskraft am FB Physik der Universität Kaiserslautern

1990 – 1995   Anstellung als Doktorand am FB Physik der Universität Kaiserslautern

1995 – 1997   Feodor-Lynen Stipendiat der Alexander-von-Humboldt Stiftung

1995 – 1997   PostDoc an der École Normale Supérieure (Paris, Frankreich) bei Prof. Dr. C. Cohen-Tannoudji. Experimentelle Arbeiten zur *„Raman- und Raman-Seitenbandkühlung neutraler Atome in optischen Dipolkraftfallen"*.

1998 – 1999   Teilprojektleiter und Mitarbeiter der Arbeitsgruppe von Prof. Dr. G. Rempe an der Fakultät für Physik der Universität Konstanz. Vorarbeiten zur *„Kontrollierten Emission einzelner Photonen aus einem stark gekoppelten Atom-Resonator System"*.

1999 –   Teilprojektleiter und Mitarbeiter der Abteilung Quantendynamik von Prof. Dr. G. Rempe am Max-Planck-Institut für Quantenoptik, Garching. Arbeiten zur *„Quanteninformationsverarbeitung mit neutralen Atomen in optischen Resonatoren hoher Finesse"*.

1. Publications in Scientific Journals

G. Z. He, A. Kuhn, S. Schiemann and K. Bergmann: Population transfer by stimulated Raman scattering with delayed pulses and by the stimulated-emission pumping method: a comparative study. J. Opt. Soc. Am. B **7**, 1960-1969 (1990)

G. Ziegler, S. V. K. Kumar, H.-G. Rubahn, A. Kuhn, B. Sun and K. Bergmann: Angularly resolved rotational energy transfer in highly vibrationally excited states: $Na_2(v=31)$-Ne. J. Chem. Phys. **94**, 4252-4259 (1991)

A. Kuhn, G. W. Coulston, G.Z. He, S. Schiemann and K. Bergmann: Population transfer by stimulated Raman scattering with delayed pulse using spectrally broad light. J. Chem. Phys. **96**, 4215-4223 (1992)

B. W. Shore, K. Bergmann, A. Kuhn, S. Schiemann and J. Oreg: Laser--induced population transfer in multistate systems: A comparative study. Phys. Rev. A **45**, 5297-5300 (1992)

S. Schiemann, A. Kuhn, S. Steuerwald and K. Bergmann: Efficient coherent population transfer in NO-molecules using pulsed lasers. Phys. Rev. Lett. **71**, 3637-3640 (1993)

A. Kuhn, H. Perrin, W. Hänsel, and C. Salomon: Three dimensional Raman cooling using velocity selective rapid adiabatic passage. OSA TOPS vol. 7, ed. K. Burnett, 58-65 (1996)

U. Ernst, J. Schuster, F. Schreck, A. Marte, A. Kuhn, and G. Rempe: Free Expansion of a Bose-Einstein Condensate in an Ioffe-Pritchard Magnetic Trap. Appl. Phys. B **67,** 719-722 (1998)

A. Kuhn, S. Steuerwald, and K. Bergmann: Coherent Population Transfer in NO with Pulsed Lasers: The Consequences of Hyperfine Structure, Doppler Broadening and Electromagnetically Induced Absorption. Eur. Phys. J. D **1**, 57-70 (1998)

H. Perrin, A. Kuhn, I. Bouchoule, and C. Salomon: Sideband cooling of neutral atoms in a far-detuned optical lattice. Europhys. Lett. **42**, 395-400 (1998)

I. Bouchoule, H. Perrin, A. Kuhn, M. Morinaga, and C. Salomon: Neutral atoms prepared in Fock states of a one-dimensional harmonic potential. Phys. Rev. A **59, R**8-11 (1999)

H. Perrin, A. Kuhn, I. Bouchoule, T. Pfau, and C. Salomon: Raman Cooling of Spin-Polarized Cesium Atoms in a Crossed Dipole Trap. Europhys. Lett. **46**, 141-147 (1999)

A. Kuhn, M. Hennrich, T. Bondo, and G. Rempe: Controlled Generation of Single Photons from a Strongly Coupled Atom-Cavity System. Appl. Phys. B **69**, 373-377 (1999)

M. Hennrich, T. Legero, A. Kuhn and G. Rempe: Vacuum-Stimulated Raman Scattering based on Adiabatic Passage in a High-Finesse Optical Cavity. Phys. Rev. Lett. **85**, 4872-4875 (2000)

A. Kuhn, M. Hennrich, T. Legero and G. Rempe: Photons made by vacuum-stimulated Raman scattering in an optical cavity. OSA TOPS vol. **57**, QELS 2001 Tech. Digest, 223-224 (2001)

A. Kuhn, M. Hennrich and G. Rempe: Deterministic Single-Photon Source for Distributed Quantum Networking. Phys. Rev. Lett. **89**, 067901 (2002)

Sept. 1997 (poster)

H. Perrin, A. Kuhn, I. Bouchoule, and C. Salomon: Sideband Cooling of Neutral Atoms in a Far-Detuned Optical Lattice. European Quantum Electronics Conference (EQEC), Glasgow, Scotland, Sept. 14-18, 1998 **(invited talk)**

T. Bondo, M. Hennrich, A. Kuhn, and G. Rempe: A Novel Scheme for the Detection of a Single Atom. Verhandl. DPG (VI) **34**, 406, 1999 (poster)

A. Kuhn, T. Bondo, M. Hennrich, and G. Rempe: Kontrollierte Erzeugung einzelner Photonen in einem optischen Resonator höchster Finesse. Verhandl. DPG (VI) **34**, 549, 1999 (talk)

A. Kuhn, M. Hennrich, and G. Rempe: Controlled Emission of Single Photons from a High-Finesse Optical Cavity. EURESCO Conference on Quantum Optics, Mallorca, Spain, October 2-7, 1999 (poster)

A. Kuhn, M. Hennrich, T. Legero and G. Rempe: Controlled Single-Photon Emission from a Strongly Coupled Atom-Cavity System. Fundamentals on Quantum Optics V, Kühtai, Austria, January 16-21, 2000 (poster)

M. Hennrich, T. Legero, T. Bondo, A. Kuhn, and G. Rempe: Zustandsselektiver Nachweis einzelner Rubidium Atome. Verhandl. DPG (VI) **35**, 1089, 2000 (poster)

A. Kuhn, M. Hennrich, T. Legero, and G. Rempe: Photons one-by-one: a novel scheme based on strong atom-cavity coupling. Quantum Communication Measurement & Computing (QCM&C), Capri, Italy, July 3-8, 2000 (poster)

A. Kuhn, M. Hennrich, T. Legero, and G. Rempe: Controlled Single-Photon Emission from a Strongly Coupled Atom-Cavity Sytem. International Quantum Electronics Conference (IQEC), Nice, France, Sept. 10-15, 2000 (talk)

M. Hennrich, T. Legero, A. Kuhn and G. Rempe: Vacuum-Stimulated Photon Emission Based on Strong Atom-Cavity Coupling. EURESCO Conference on Quantum Optics, Mallorca, Spain, October 14-19, 2000 (poster)

T. Legero, M. Hennrich, S. Nußmann, A. Kuhn and G. Rempe: Single-atom multi-photon entanglement mediated by a high-finesse cavity. ECAMP VII, 7th European conference on atomic and molecular physics, Verhandl. DPG (VI) 36, 5/191, 2001 (poster)

M. Hennrich, T. Legero, A. Kuhn and G. Rempe: Pulsed generation of photons by vacuum-stimulated Raman scattering. ECAMP VII, 7th European conference on atomic and molecular physics, Verhandl. DPG (VI) 36, 5/193, 2001 (poster)

A. Kuhn, M. Hennrich, T. Legero and G. Rempe: Photons generated by vacuum-stimulated Raman scattering. ECAMP VII, 7th European conference on atomic and molecular physics, Verhandl. DPG (VI) 36, 5/198, 2001 (group report)

M. Hennrich, T. Legero, A. Kuhn and G. Rempe: Vacuum stimulated photon generation in a high finesse optical cavity. Euroconference on Quantum interference and cryptographic keys: novel physics and advancing technologies, CARGESE CORSICA April 7-13, 2001 (poster)

A. Kuhn, M. Hennrich, T. Legero and G. Rempe: Vacuum-Stimulated Raman Scattering in an

Optical Cavity - A New Scheme to Generate Single Photons. Workshop on solid state quantum computing, 26.-29. April 2001, Warsaw, Poland **(invited talk)**

A. Kuhn, M. Hennrich, T. Legero and G. Rempe: Photons made by vacuum-stimulated Raman scattering in an optical cavity. Quantum Electronics and Laser Science Conference (QELS), Baltimore (USA), May 2001 **(invited talk)**

A. Kuhn, M. Hennrich, T. Legero and G. Rempe: Photons produced by vacuum-stimulated Raman scattering in a high-finesse optical cavity. International Conference on Quantum Information IQCI, Rochester, NY (USA), June 2001 (poster)

A. Kuhn, M. Hennrich and G. Rempe: Vacuum-stimulated photon bursts from a coupled atom-cavity system. European Comission QIPC workshop, 28.-31.October 2001, Torino, Italy (talk)

M. Hennrich, T. Legero, A. Kuhn and G. Rempe: Photons generated by stimulated emission into the vacuum field of a high-finesse optical cavity. EURESCO Conference on Quantum Optics, 6.-11. October 2001, San Feliu de Guixols, Spain (poster)

M. Hennrich, A. Kuhn and G. Rempe: Photon antibunching and bunching in a strongly coupled atom-cavity system. DPG AMOP-Frühjahrstagung Osnabrück, March 2002, Verhandl. DPG VI, 37 (2) (talk)

A. Kuhn, M. Hennrich and G. Rempe: Triggered Emission of Narrowband Single-Photon Sequences. DPG AMOP-Frühjahrstagung Osnabrück, March 2002, Verhandl. DPG VI, 37 (2) (group report)

T. Legero, S. Kudera, A. Kuhn and G. Rempe: A High-Finesse Cavity as a Beamsplitter in a Mach-Zehnder interferometer. DPG AMOP-Frühjahrstagung Osnabrück, March 2002, Verhandl. DPG VI, 37 (2) (poster)

A. Kuhn, M. Hennrich and G. Rempe: Triggered Emission of Narrowband Single-Photon Sequences from Strongly Coupled Atom-Cavity Systems. EURESCO Conference on Quantum Information/Quantum Entanglement, March 23-28, 2002, San Feliu de Guixols, Spain (poster)

A. Kuhn, M. Hennrich and G. Rempe: Single Photons on Demand. Second Annual QUEST meeting, July 8-10, 2002, Gif sur Yvette, France (talk)

M. Hijlkema, S. Nußmann, B. Weber, A. Kuhn and G. Rempe: Towards deterministic atom-cavity coupling. Second Annual QUEST meeting, July 8-10, 2002, Gif sur Yvette, France (talk)

A. Kuhn, M. Hennrich and G. Rempe: Indistinguishable Narrowband Single-Photon Pulses on Demand for All-Optical Quantum Information Processing. International Conference on Quantum Information: Conceptual Foundations, Developments and Perspectives, July 2002, Oviedo, Spain **(invited talk)**

A. Kuhn, M. Hennrich, M. Hijlkema, P. Krok, T. Legero, S. Nußmann, F. Rohde, B. Weber, T. Wilk, and G. Rempe: Single Photons for Distributed Quantum Networking. 3rd European QIPC Workshop, 15th-18th September 2002, Dublin (poster)

A. Kuhn, M. Hennrich, M. Hijlkema, P. Krok, T. Legero, S. Nußmann, F. Rohde, B. Weber, T. Wilk, and G. Rempe: Elements of Quantum Networks. DPG AMOP-Frühjahrstagung Hannover, March 2003, Verhandl. DPG (VI) 38, 6/119 (group report)

M. Hennrich, A. Kuhn, and G. Rempe: From Antibunching to Bunching in Cavity QED. DPG AMOP-Frühjahrstagung Hannover, March 2003, Verhandl. DPG (VI) 38, 6/127 (talk)

T. Legero, T. Wilk, A. Kuhn, and G. Rempe: Quantum Interference of Independently Generated Single Photons. DPG AMOP-Frühjahrstagung Hannover, March 2003, Verhandl. DPG (VI) 38, 6/127 (talk)

S. Nussmann, M. Hijlkema, B. Weber, F. Rohde, A. Kuhn, and G. Rempe: Towards Deterministic Control of Atom-Cavity Coupling. DPG AMOP-Frühjahrstagung Hannover, March 2003, Verhandl. DPG (VI) 38, 6/137 (talk)

P. Krok, A. Kuhn, and G. Rempe: Towards the Storage of Single Photons Using Elecromagnetically Indiced Transparency. DPG AMOP-Frühjahrstagung Hannover, March 2003, Verhandl. DPG (VI) 38, 6/153 (poster)

A. Kuhn, M. Hennrich, M. Hijlkema, P. Krok, T. Legero, S. Nußmann, F. Rohde, B. Weber, T. Wilk, and G. Rempe: Elementary Quantum-Network Links and Nodes. CLEO-Europe/EQEC 23th-27th June 2003, Munich (talk)

T. Legero, T. Wilk, M. Hennrich, A. Kuhn, and G. Rempe: Second-Order Interference of Two Independent Photons. CLEO-Europe/EQEC 23th-27th June 2003, Munich (poster)

M. Hijlkema, S. Nußmann, B. Weber, F. Rohde, A. Kuhn, and G. Rempe: Towards Deterministic Control of Atom-Cavity Coupling. CLEO-Europe/EQEC 23th-27th June 2003, Munich (poster)

A. Kuhn, M. Hennrich, M. Hijlkema, P. Krok, T. Legero, S. Nußmann, F. Rohde, B. Weber, T. Wilk, and G. Rempe: Photonic Quantum Network Links and Nodes. QIPC Workshop 14th-18th July 2003, Oxford (talk)

A. Kuhn, M. Hennrich, T. Legero, T. Wilk, and G. Rempe: Single Photons for Quantum Networking from a Coupled Atom-Cavity System. ESF Conference on Quantum Optics, 28th September – 2nd October 2003, Grenada, Spain **(invited talk)**

A. Kuhn: Quantum Networking with Single Photons from Coupled Atom-Cavity Systems. 304th Heraeus Seminar on "Elementary Quantum Processors", 12th – 15th October 2003, Bad Honnef **(invited talk)**

A. Kuhn: Entanglement between Single Atoms and Light. Kolloquium des DFG-Schwerpunktprogramms Quanteninformationsverarbeitung, 29th – 30th January 2004, Bad Honnef **(invited talk)**

A. Kuhn: Cavity-QED in the QGATES project of the EU/QIPC programme, QIPC Review meeting, Bratislava, Slovakia, 16th-18th February 2004 (talk)

A. Kuhn: Quantum information processing with single photons, Final meeting of the European RTN QUEST, 6th-12th March 2004, La Thuile, Italy **(invited talk)**

B. Weber, S. Nußmann, M. Hijlkema, F. Rohde, A. Kuhn, and G. Rempe: Deterministic control of atom-cavity coupling. DPG AMOP-Frühjahrstagung Munich, March 2004, Verhandl. DPG (VI) 39, 7/113 (talk)

T. Wilk, T. Legero, M. Hennrich, A. Kuhn, and G. Rempe: Time-bin entangled photons from a cavity-QED source. DPG AMOP-Frühjahrstagung Munich, March 2004, Verhandl. DPG (VI) 39, 7/127 (poster)

M. Hennrich, A. Kuhn, and G. Rempe: One- and N-atom lasers. DPG AMOP-Frühjahrstagung Munich, March 2004, Verhandl. DPG (VI) 39, 7/144 (poster)

B. Weber, S. Nußmann, M. Hijlkema, F. Rohde, A. Kuhn, and G. Rempe: Deterministic control of atom-cavity coupling. DPG AMOP-Frühjahrstagung Munich, March 2004, Verhandl. DPG (VI) 39, 7/113 (talk)

T. Legero, T. Wilk, M. Hennrich, A. Kuhn, and G. Rempe: Entanglement of a single photon with an atom-cavity system. DPG AMOP-Frühjahrstagung Munich, March 2004, Verhandl. DPG (VI) 39, 7/155 (group report)

A. Kuhn: Quantum information processing with single photons from cavity-QED systems. CLEO/IQEC, May 18th-20th, 2004, San Francisco, USA **(invited talk)**

6. Lectures

„Photons one by one: Vacuum-Stimulated Raman Scattering in an optical Cavity", Atomic Physics Colloquium, Universität Bonn, Germany, 16.01.2001

„Photons from Vacuum-Stimulated Raman Scattering in an Optical Cavity", Atomic Physics Seminar, SUNY, Stony Brook, USA, 04.05.2001

„Erzeugung einzelner Photonen durch vakuumstimulierte Ramanstreuung", Laser Physics Seminar, Universität Kaiserslautern, Germany, 18.05.2001

„Photons Produced by Vacuum–Stimulated Raman–Scattering in an Optical Cavity", Laser Seminar, MPI für Quantenoptik, Garching, Germany, 19.06.2001

„Triggered Emission of Narrowband Single-Photon Sequences", Ecole Normale Supérieure, Paris, France, 22.02.2002

„Single-Photon Pulses on Demand", Institut d'Optique, Orsay, France, 25.02.2002

„Emission déclenchée de photons solitaires", Université Paris 13, Villetaneuse, France, 26.02.2002

„Single Photons on Demand", Prof. Klaas Bergmann's 60th Birthday Colloquium, Universität Kaiserslautern, 14.6.2002

„Single Photons for Distributed Quantum Networking", Universität Heidelberg, Quantenoptik, Atom- & Neutronenphysik-Seminar, 30.4.2003

„Single Photons for Distributed Quantum Networking", Universität Darmstadt, Institut für angewandte Physik, 1.7.2003

„Photonic Quantum Network Links and Nodes", Imperial College London (Blackett Laboratories), 18.7.2003

„Single photons for quantum networking and information processing",
Universität Regensburg, 4.12.2003

„Quantum information processing with single photons from cavity-QED systems",
Universität Stuttgart, Quantenforum, 19.2.2004

„Single photons from cavity-QED systems for optical quantum information processing",
Universität Wien, 3.5.2004

„Transition from antibunching to bunching in cavity-QED",
California Institute of Technology, Pasadena, CA, USA, 24.5.2004

7. Forthcoming Conferences and Lectures

„Atom-photon interaction under control",
Summerschool and Workshop of the SFB 631, September 13th-17th, 2004 (**tutorial**)

Organization of the MIQOP 2004 workshop on "Microcavities in Quantum Optics",
Ringberg Castle, Lake Tegernsee, Germany, September 21th – 24th, 2004

8. Supervision of Diploma Theses

Wolfgang Hänsel: Raman-Kühlen von Cäsiumatomen in einer gekreuzten Dipolfalle. Juni 1996 (Ecole normale supérieure, Paris & Universität Konstanz)

Torsten Bondo: Laser induced fluorescence detection of single atoms. August 1999 (Universität Konstanz & Københavns Universitet)

Stefan Kudera: Aufbau eines optischen Resonators als Eingangsstrahlteiler in einem Mach-Zehnder Interferometer. Juli 2002 (TUM)

Bernhard Weber: Transport von Atomen in einer optischen Dipolfalle. November 2002 (TUM)

Patrizia Krok: Elektromagnetisch induzierte Transparenz in ^{85}Rb. Juni 2003 (TUM)

Felix Rohde: Ein optischer Resonator hoher Finesse als Atomdetektor. Juni 2003 (TUM)

Holger Specht: Erzeugung spinverschränkter Atom/Photon Paare.

9. Supervision of PhD Theses

Hélène Perrin: Refroidissement d'atomes de Césium confinés dans un piège dipolaire très désaccordé. June 1998 (École Normale Supérieure, LKB, Paris, France)

Isabelle Bouchoule: Refroidissement Raman par bandes latérales d'atomes dans un réseau optique. October 2000 (École Normale Supérieure, LKB, Paris, France)

Markus Hennrich: Kontrollierte Erzeugung einzelner Photonen in einem optischen Resonator hoher Finesse. January 2004 (Technische Universität München & MPQ)

Thomas Legero: (Zeitaufgelöste Interferenz vierter Ordnung und Verschränkung einzelner Atome mit Licht)

Stefan Nussmann: (Neutralatom-Quantengatter)

Markus Hijlkema: (Cavity mediated atom-atom entanglement)

Tajana Wilk: (Experimente mit einzelnen Photonen)

Bernhard Weber: (Experimente zur Quanteninformationsverarbeitung mit Neutralatomen in Resonatoren hoher Finesse)

10. Teaching: Coordination of Proseminars and Supervision of Talks

SS 1998,   Proseminar „Kühlen und Speichern von Atomen mit Licht" (Universität Konstanz), supervised talks:

1. Subrecoil Kühlung: Ramankühlung, Levy Flights
2. Laserkühlung in Ionenfallen
3. Dipolfalle, magnetische Fallen, RF Fallen, elektrooptische Fallen
4. Wellenleiter für Atome: Hohlfaser, TEM01 Moden
5. Blochoszillationen, Wannier Stark Leiter

WS 1999/00   Coordination of the proseminar „Einführung in die Quantenoptik" (TUM) supervised talks:

1. Photonen und Atome
2. Schrödinger Katzen

SS 2000   Coordination of the proseminar „Präzisionsexperimente in der Physik" (TUM) supervised talk: Zerstörungsfreie Quantenmessungen

WS 2000/01,   Coordination of the proseminar „Atomoptik" (TUM) supervised talk: Lichtkühlung ohne Grenzen

SS 2001,   Coordination of the proseminar „Quanteninformation" (TUM) supervised talk: Einzelne Photonen

WS 2001/02,   Coordination of the proseminar „Quanteninformation" (TUM) supervised talk: Resonatoren als Quantenschnittstellen

WS 2003/04,   Coordination of the proseminar „Quanteninformation" (TUM)

SS 2004,   Coordination of the proseminar „Atomoptik" (TUM)

11. Teaching: Supervision and Elaboration of Exercises accompanying Lectures

WS 1999/00   Übungen zur Vorlesung „Moderne Optik 1" (G. Rempe)

SS 2000   Übungen zur Vorlesung „Moderne Optik 2" (G. Rempe)

WS 2000/01   Übungen zur Vorlesung „Quantenoptik 1" (G. Rempe)

WS 2002/03   Übungen zur Vorlesung „Quantenoptik 1" (G. Rempe)

12. Teaching: Lectures (given in place of Prof. Dr. G. Rempe)

SS 1998   Grundkurs Physik IV (ca. 50% of all lectures)

WS 1998/99   Laser Physik   (3-4 lectures)

WS 2002/03   Quantenoptik 1   (1 lecture)

13. Proposals and Research Projects

DFG- Focussed research programme „Quanteninformationsverarbeitung"

1999-2000	Quantenschalter und kontrollierte Erzeugung einzelner Photonen 1 (funded)
2001-2002	Quantenschalter und kontrollierte Erzeugung einzelner Photonen 2 (funded)
2003-2004	Multi-Photon Quantum Network Links and Nodes 3 (funded)

DFG - Sonderforschungsbereich

SFB 631   Festkörperbasierte Quanteninformationsverarbeitung (participation, funded)

EU-Programme QIPC in the 5th framework

2000-2002   Quantum based information processing and transfer using single atoms and photons (QUBITS) (participation, funded)

2003-2005   Quantum gates and elementary scalable processors using deterministically addressed atoms (QGATES) (scientist-in-charge, funded)

n.a.   Quantum network links and nodes with atoms, ions and photons (QuLAN) (project coordination and participation, no funding obtained in FP5)

Member of the QUIPROCONE network of excellence.

EU-Programme QIPC in the 6th framework

Member of the QUIPROCONE network of excellence (no funding obtained).

Member of the ADOPT-Q network of excellence (under evaluation)

EU-IHP Programme in the 5th framework

2000-2004   Quantum entangled states of trapped particles (QUEST) (participation, funded)

EU-IHP Programme in the 6th framework

2004-2007   Controlled Quantum Coherence and Entanglement in Sets of Trapped Particles (ConQuest) (scientist-in-charge, funded)

2004-   Engineering and Manipulation of Quantum States of Matter and Light (EMQUAST) (scientist-in-charge, under evaluation)

A.2 Publikationen

Verzeichnis der angefügten Veröffentlichungen:

- A. Kuhn, H. Perrin, W. Hänsel, and C. Salomon. Three dimensional Raman cooling using velocity selective rapid adiabatic passage. In K. Burnett, editor, *OSA TOPS on Ultracold Atoms and BEC*, volume 7, pages 58–65. OSA, 1996.

- U. Ernst, J. Schuster, F. Schreck, A. Marte, A. Kuhn and G. Rempe. Free Expansion of a Bose-Einstein Condensate in an Ioffe-Pritchard Magnetic Trap. *Appl. Phys. B*, 67:719–722, 1998.

- A. Kuhn, S. Steuerwald, and K. Bergmann. Coherent population transfer in NO with pulsed lasers: The consequences of hyperfine structure, Doppler broadening and electromagnetically induced absorption. *Eur. Phys. J. D*, 1:57–70, 1998.

- H. Perrin, A. Kuhn, I. Bouchoule, and C. Salomon. Sideband cooling of neutral atoms in a far-detuned optical lattice. *Europhys. Lett.*, 42:395–400, 1998.

- I. Bouchoule, H. Perrin, A. Kuhn, M. Morinaga, and C. Salomon. Neutral atoms prepared in Fock states of a 1d harmonic potential. *Phys. Rev. A*, 59:R8–R11, 1999.

- H. Perrin, A. Kuhn, I. Bouchoule, T. Pfau, and C. Salomon. Raman cooling of spin polarized Cesium atoms in a crossed dipole trap. *Europhys. Lett.*, 46:141–147, 1999.

- A. Kuhn, M. Hennrich, T. Bondo, and G. Rempe. Controlled generation of single photons from a strongly coupled atom-cavity system. *Appl. Phys. B*, 69:373–377, 1999.

- M. Hennrich, T. Legero, A. Kuhn, and G. Rempe. Vacuum-stimulated Raman scattering based on adiabatic passage in a high-finesse optical cavity. *Phys. Rev. Lett.*, 85:4872–4875, 2000.

- A. Kuhn, M. Hennrich, and G. Rempe. Deterministic single-photon source for distributed quantum networking. *Phys. Rev. Lett.*, 89:067901, 2002.

- A related comment by H. J. Kimble. *Phys. Rev. Lett.*, 90:249801, 2003 – and a reply to this comment. A. Kuhn, M. Hennrich, and G. Rempe. *Phys. Rev. Lett.*, 90:249802, 2003.

- A. Kuhn and G. Rempe. Optical cavity qed: Fundamentals and application as a single-photon light source. In F. De Martini and C. Monroe, editors, *Experimental Quantum Computation and Information*, volume 148, pages 37–66. IOS-Press, 2002.

- A. Kuhn, M. Hennrich, and G. Rempe. Strongly-coupled atom-cavity systems. In T. Beth and G. Leuchs, editors, *Quantum Information Processing*, pages 182–195. Wiley-VCH, Berlin, 2003.

- M. Hennrich, A. Kuhn, and G. Rempe. Counter-intuitive vacuum-stimulated Raman scattering. *J. Mod. Opt.*, 50:936–942, 2003.

- T. Legero, T. Wilk, A. Kuhn, and G. Rempe. Time-resolved two-photon quantum interference. *Appl. Phys. B*, 77:797–802, 2003.

- M. Hennrich, T. Legero, A. Kuhn, and G. Rempe. Photon statistics of a non-stationary periodically driven single-photon source. *New Journal of Physics*, 6:86, 2004.

- T. Legero, T. Wilk, M. Hennrich, G. Rempe, and A. Kuhn. Quantum beat of two single photons. *Phys. Rev. Lett.*, 93:070503, 2004.

- M. Hennrich, A. Kuhn, and G. Rempe. Transition from antibunching to bunching in cavity QED. *Phys. Rev. Lett.*, 94:053604, 2005.

- T. Bondo, M. Hennrich, T. Legero, A. Kuhn, and G. Rempe. Time-resolved and state-selective detection of individual free atoms. In preparation.

Three Dimensional Raman Cooling using Velocity Selective Rapid Adiabatic Passage

Axel Kuhn, Hélène Perrin, Wolfgang Hänsel and Christophe Salomon

Laboratoire Kastler Brossel, École Normale Supérieure, 24 rue Lhomond, 75231 Paris Cedex 05, France

ABSTRACT

We present a new and efficient implementation of Raman cooling of trapped atoms. It uses Raman pulses with an appropriate frequency chirp to realize a velocity selective excitation through a rapid adiabatic passage. This method allows to address in a single pulse a large number of non zero atomic velocity classes and it produces a nearly unity transfer efficiency. We demonstrate this cooling method using cesium atoms in a far-detuned crossed dipole trap. Three-dimensional cooling of 1×10^5 atoms down to 2 μK is performed in 100 ms. In this preliminary experiment the final atomic density is 1.3×10^{12} at/cm^3 (within a factor of 2) and the phase-space density increase over the uncooled sample is 20. Numerical simulations indicate that temperatures below the single photon recoil temperature should be achievable with this method.

KEY WORDS

Trapped atoms, Laser cooling, Ultracold atoms, Coherent optical effects

I. INTRODUCTION

The recent observation of Bose-Einstein condensation in dilute alkali vapors was a major advance in the field of atom cooling and trapping [1,2]. The quantum degeneracy threshold was reached by evaporative cooling of the atomic sample in a magnetic trap. Despite the tremendous success of these experiments, one can see two important drawbacks to this method for future applications of these Bose condensates: (i) the strong magnetic field gradients required for the evaporation and their time dependence are not easily compatible with the high precision measurements of, for instance, cold atoms frequency standards and atom interferometers. (ii) The evaporation is relatively slow (tens of seconds), requires a very low rate of inelastic collisions and leads to a substantial loss of atoms (typically a factor 100). A possible route to solve both of these problems is to trap the atoms with optical fields and to apply to the trapped atoms the subrecoil cooling methods first developped for free atoms. Optical fields are easily switched on and off and, if properly designed, subrecoil cooling presents a priori no loss of atoms. Recently Raman cooling of trapped Na atoms has produced a sample at 1 μK= 0.42 T_R, where $T_R = \hbar^2 k^2/Mk_B$ is the single photon recoil temperature [3]. This is a factor 320 increase in phase-space density but still a factor 300 short of the condensation threshold.

In this paper, we present a new Raman method for subrecoil cooling of trapped atomic samples and our efforts to reach the quantum degeneracy on atomic cesium by purely optical methods. Contrarily to previous demonstrations of Raman cooling, we use velocity selective Raman pulses in which both the amplitude and the frequency are changed in a controlled way. This produces a velocity selective rapid adiabatic passage which is very efficient (transfer efficiency close to one) and which can excite simultaneously a large number of velocity classes.

This paper is organized as follows: we first recall the main elements of Raman cooling (section II). We then describe the Rapid Adiabatic Passage (RAP), its velocity selectivity, and optimization of the frequency chirp to reach an efficiency close to one (section III). The effect of the pulse rate in the cooling sequence and of the atomic motion in a crossed dipole trap is studied using a numerical simulation of the cooling process for cesium atoms (section IV). The experimental setup is described in section V. The loading of the crossed dipole trap from a Magneto Optical Trap (MOT) and the results of Raman cooling using the RAP method are given in section VI.

II. RAMAN COOLING SCHEME

Raman cooling was first proposed for subrecoil cooling of free atoms in one dimension [4]. It has recently been used to cool cesium atoms down to a 1D temperature of 3 nK= $T_R/70$ [6]. Since in subrecoil cooling schemes, the temperature decreases with increasing interaction times [7,6], the extension of the method to trapped atoms is very attractive because of the potentially long storage time [3]. In addition, in an harmonic trap, the phase space density scales as T^{-3}. In the trap, the cooling can be performed along a single axis, because, under certain circumstances, the motion of the atoms couples all three degrees of freedom [3]. As we will show in section IV, this coupling causes new effects which lead to a different cooling strategy than for free atoms.

The principle of the cooling mechanism is shown in fig.1 in the case of cesium atoms. Two counter-propagating Raman pulses excite the atoms from $F = 3$ to $F = 4$ in the ground state $6^2S_{1/2}$ and push them by $2\hbar k$ towards zero velocity. One chooses the pulse shapes and detunings in a proper way to avoid excitation of atoms at rest and to select only the desired velocity class.

Subsequently, the excited atoms are brought back to the initial level $F = 3$ by pumping them to the excited $6^2P_{3/2}$ state which decays by spontaneous emission with a rate $\Gamma = 2\pi \times 5.3$ MHz. We have chosen the $F = 3$ level in the excited state which decays with a branching ratio of 2/3 to the initial state. To avoid a systematic momentum transfer by this repumping process, the laser shines on the atoms in a molasses geometry. This repumping process communicates between two and four photons of random directions. There is no average momentum change in this process, but this dissipative random walk is required to reach sub-recoil temperatures. In addition, it produces some heating in the directions perpendicular to the Raman axis. One has to take this into account to optimize the cooling sequence (see section IV).
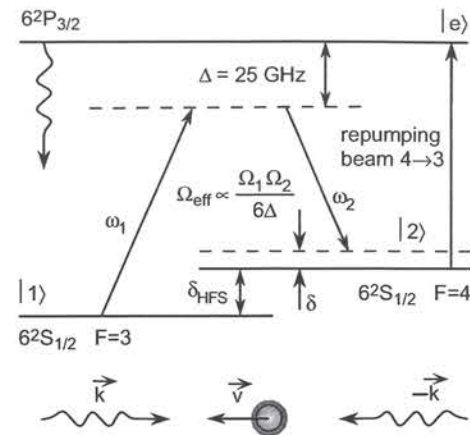
FIG. 1. Raman excitation scheme and subsequent repumping to $F = 3$ by excitation of $F = 4 \longrightarrow 3$.

Usually, the initial momentum distribution is much larger than $\hbar k$ and the cooling relies on a repetition of the Raman- and repumping pulses. In fig.2, we show an *ideal* Raman excitation profile on the left-hand side. It provides an excitation probability of 'one' for all atoms at $p < -2\hbar k$ and tends towards zero around $p = 0$. Traditionally, such an ideal excitation profile was replaced by a sequence of Π-pulses at different detunings [3–6], starting at large Raman detuning δ and compressing the velocity distribution by a reduction of δ from pulse to pulse.

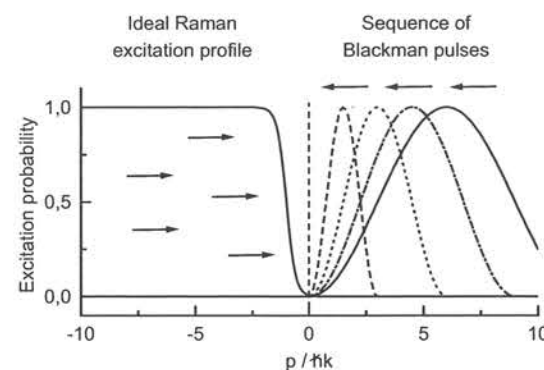

FIG. 2. Idealized Raman excitation profile (shown for $p < 0$) and traditionally realized pulses (for $p > 0$).

On free atoms, the direction of the Raman pulses is changed from pulse to pulse to cool both wings of the initial velocity distribution. In a three dimensional trap, there is no need to alternate the Raman beam directions because the atoms oscillate in the harmonic potential. However, the dissipative repumping process and the oscillatory motion may bring some atoms to high velocities that are no more affected by the Raman pulse with the smallest detuning. Therefore, the sequence has to be restarted at higher detuning to re-collect these atoms. In fact, one single Raman pulse affects only a small fraction of the velocity distribution (especially the narrow band pulses at small δ). There are also some technical disadvantages of such a sequence. One has to fulfill the Π-pulse condition for each of them, and the pulse duration has to be adapted to δ to avoid the excitation of atoms at rest.

Most of the disadvantages of such a Π-pulse sequence vanish if one provides pulses with an ideal excitation profile in momentum space. In the following section, we demonstrate the usefulness of the well known rapid adiabatic passage (RAP) to tailor the desired Raman excitation profile.

III. RAPID ADIABATIC PASSAGE

The first successful combination of stimulated Raman scattering involving adiabatic passage in a Λ-type three level system by Bergmann [9] was based on time delayed Raman pulses with fixed frequencies. The excitation probability of such a scheme reflects the Fourier transform of the applied pulses. The same holds for the previous Raman cooling schemes using coinciding Blackman [4] or square pulses [6] with fixed frequencies at large detuning Δ.

In the latter case, the simplification of the three level system to an effective two level system is justified if $\Delta \gg |\Omega_{1,2}|$. In our method, we further allow the Raman detuning δ_{eff} to be time dependent. The interaction Hamiltonian is then

$$H_{\text{eff}}(t) = -\frac{\hbar}{2} \begin{pmatrix} 0 & \Omega_{\text{eff}}(t) \\ \Omega_{\text{eff}}^*(t) & 2\delta_{\text{eff}}(t) \end{pmatrix}. \tag{1}$$

It describes the evolution of $|\Psi\rangle$ in the basis of the initial level $|1\rangle$ and final level $|2\rangle$, the intermediate level being eliminated. In this effective two level system, it is clear that rapid adiabatic passage (RAP), as described by Loy [8], can be employed when the Raman detuning δ_{eff} is chirped across the resonance.

If one takes into account the different magnetic sublevels m_F, the effective Rabi frequency and detuning read

$$\Omega_{\text{eff}} = \frac{\Omega_1 \Omega_2}{6\Delta} \sqrt{1 - \left(\frac{m_F}{4}\right)^2} \tag{2a}$$

$$\delta_{\text{eff}} = \delta + \frac{\delta_{\text{HFS}}^2(\Omega_1^2 - \Omega_2^2) + \Delta\,\delta_{\text{HFS}}(\Omega_1^2 + \Omega_2^2)}{4\Delta(\Delta^2 - \delta_{\text{HFS}}^2)} \tag{2b}$$

At this point, we note that it is impossible to have the same Π-pulse condition for all magnetic sublevels, because the effective Rabi frequencies depend on m_F. In addition, because of the differential light shift, the effective detuning δ_{eff} depends on Ω.

In a dressed state picture, the eigenstates of the two state Hamiltonian read

$$|a^+\rangle = \cos\phi|1\rangle - \sin\phi|2\rangle$$
$$|a^-\rangle = \sin\phi|1\rangle + \cos\phi|2\rangle \qquad \tan\phi = \frac{\sqrt{\Omega^2 + \delta^2} - \delta}{\Omega}, \tag{3}$$

with the corresponding eigenfrequencies

$$\omega^\pm = -\frac{\delta}{2} \pm \frac{1}{2}\sqrt{\Omega^2 + \delta^2} \tag{4}$$

Both the mixing angle ϕ and the eigenfrequencies $\omega^\pm$ are a function of the Raman detuning δ. If δ sweeps across the resonance, ϕ turns from $\pi/2$ to 0 (which is valid for $\Omega \ll \delta$ in the wings of a Raman pulse), and by consequence $|a^-\rangle$ evolves from $|1\rangle$ to $|2\rangle$. In fig.3, the corresponding avoided crossing at $\delta = 0$ is shown.
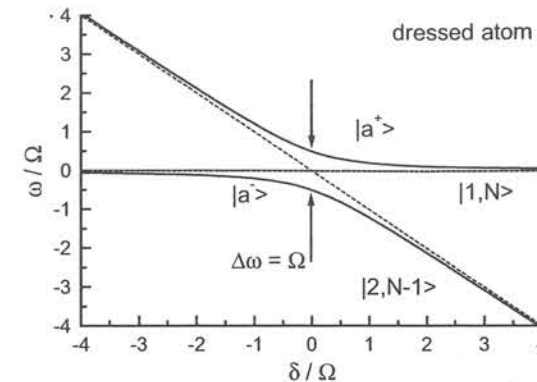

FIG. 3. Avoided crossing at $\delta = 0$

If the extend of the frequency chirp is limited, only the atoms which experience such a crossing due to their Doppler shifted resonance frequency are excited by the Raman pulse. Even atoms which do not experience a crossing follow $|a^-\rangle$ adiabatically, but the dressed state returns to the initial state $|1\rangle$ in the end of the pulse.
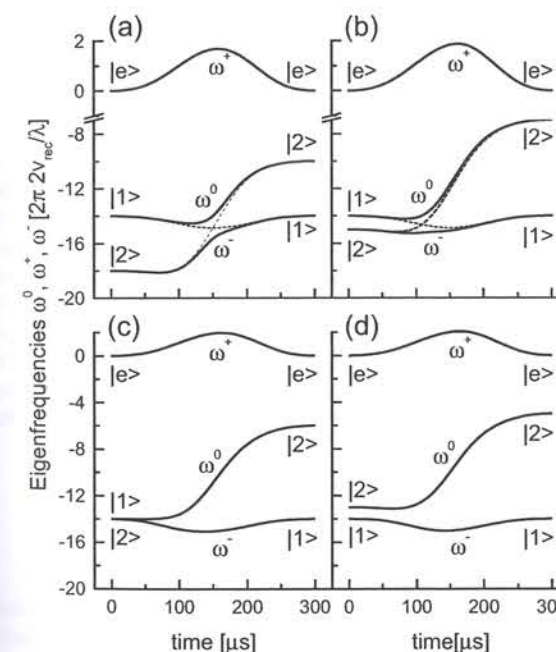

FIG. 4. Energies of the dressed levels (solid lines) in response to a frequency chirped Blackman pulse with a duration of 300 μs and a pulse area $\int \Omega(t)dt = 3\pi$. The dashed lines represent the energies of the uncoupled states. The chirp extends from $\delta = -24\,kv_{\text{rec}}$ to $\delta = -6\,kv_{\text{rec}}$. Due to the Doppler shift $\delta_{\text{eff}} = \delta_{\text{chirp}} + 2kv$ of the counter-propagating Raman beams, atoms in the velocity interval $-12 \lesssim v/v_{\text{rec}} \lesssim -3$ are affected. The evolution is shown for four different initial velocities – (a): $v/v_{\text{rec}} = -7.5$; (b): $v/v_{\text{rec}} = -4$; (c): $v/v_{\text{rec}} = -3$; (d): $v/v_{\text{rec}} = -2$.

In fig.4, the evolution of the eigenfrequencies of a real three level system is shown for a fixed frequency chirp and different Doppler shifts. (a) shows a crossing right in the center of the chirp, (b) shows that there is still an avoided crossing when the Doppler shift is close to the border of (but within) the

chirp. If the Doppler shift coincides with the detuning in the end (c), $|a^+\rangle$ and $|a^-\rangle$ become degenerate and both states are equally populated. (d) shows that there is no more avoided crossing if the Doppler shifted resonance is not within the chirp, i.e. there is no Raman excitation in such a case and no momentum exchange takes place. In fact, the extend of the chirp determines the range of velocities which are excited.

A. Shape of the δ chirp

To insure that the state vector $|\Psi\rangle$ follows the dressed state $|a^-\rangle$ adiabatically throughout the interaction, the adiabaticity criterion (see [10])

$$\left|\langle a^+|\frac{d}{dt}|a^-\rangle\right| \ll |\omega^+ - \omega^-| = \sqrt{\Omega^2 + \delta^2}, \tag{5}$$

needs to be fulfilled. It is most stringent in the vicinity of the crossing, where it can be expressed as

$$\left|\frac{d}{dt}\delta\right| \ll \Omega^2. \tag{6}$$
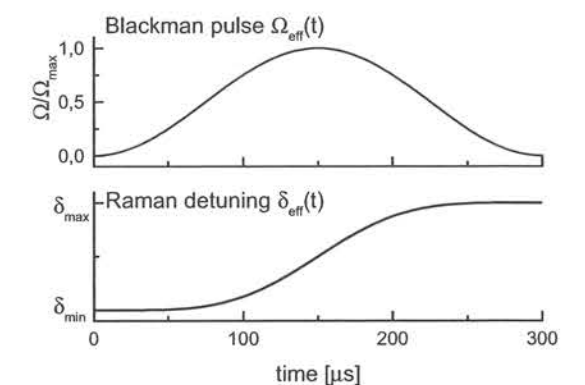
FIG. 5. Form of the Blackman shaped Raman pulse (upper part) and the superimposed frequency chirp (lower part).

Due to the different atomic velocities, the exact position of the crossing within the chirp is not known. Therefore, the chirp has to be shaped like

$$\delta(t) \propto \int \Omega^2(t)dt, \tag{7}$$

to insure the same adiabaticity condition for all atoms. The chirp thus reflects the pulse shape and is fast at high Rabi frequencies and slow at small Ω. Fig.5 shows the shape of the Raman pulse together with the optimized chirp.

B. Efficiency and Selectivity

A straightforward numerical simulation of the RAP excitation was done solving the time-dependent Schrödinger equation. We show the resulting transfer efficiency as a function of the atomic velocities (i.e. the Doppler shift) for different pulse amplitudes in fig.6.

FIG. 6. Transfer efficiency of frequency chirped Raman pulses in comparison with the excitation profile of a non-chirped Blackman pulse. All pulses have a duration of 300 μs and are chirped by $\Delta\delta = 2\pi \times 74$ kHz, which extends over 9 v_{rec}. The start frequency is shifted from resonance in order to avoid exciting atoms at rest. Also shown is the power law dependence of the excitation profiles near $p = 0$.

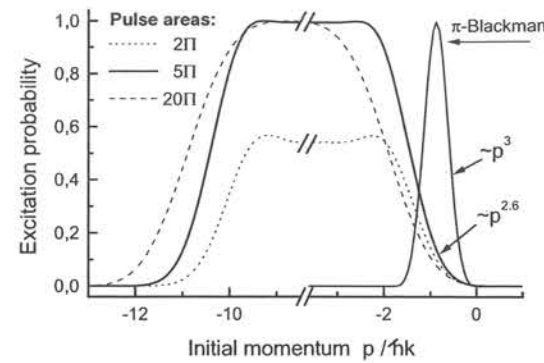The simulation shows that a box-like excitation profile is realized with such pulses, but it reveals at the same time that the border of the profile is not as steep as the one achieved with a Blackman pulse of same duration.

Once the recoil limit $p \lesssim \hbar k$ is reached, a description of the cooling process using Lévy flight statistics [11] shows that there is an ideal exponent α for the excitation probability $P_{exc} \propto v^\alpha$ around $v = 0$. It depends on the dimension D of the cooled atomic ensemble and

$$\frac{D}{\alpha} = \mu \lesssim 1 \qquad (8)$$

is the optimal choice for free atoms [6]. There is no real 'zero' in the excitation profile of the chirped Raman pulses and one has to choose an arbitrary cut-off to determine the origin. If one chooses $P_{exc} t_{trap} \Gamma_{cool} = 0.25$ as condition to determine this origin (i.e. a probability of 25% to excite atoms at rest during the trapping time t_{trap}). We obtain for a typical cooling time $t_{trap} = 200$ ms, a cooling pulse rate $\Gamma_{cool} = 0.5$ ms and pulse parameters of fig.6:

$$\alpha_{RAP} \simeq 2.6. \qquad (9)$$

In this case, D/α is slightly greater than one, which is not the optimum choice to enter far in the subrecoil region. By contrast, a Blackman pulse without frequency chirp has a first minimum in its excitation profile where $\alpha_{BM} \simeq 3.3$ is well determined. Therefore, a combination of both profiles, a chirped Blackman at large detuning and a narrow fixed frequency Blackman pulse might turn out to be the optimum choice.

IV. COOLING SEQUENCE

In three dimensional Raman Cooling, one has to be aware that the re-thermalization after each pulse has to take place. We call Γ_{therm} this thermalization rate and Γ_{couple} the rate of coupling of the atomic motion to the Raman axis. If the pulse rate Γ_{cool} in the cooling sequence is larger than both of these rates, i.e. if

$$\Gamma_{cool} > \max(\Gamma_{therm}, \Gamma_{couple}), \qquad (10)$$

the coupling of the atomic motion perpendicular to the Raman axis to this same axis becomes ineffective. In such a case, the ensemble is cooled in one dimension at the expense of heating the other degrees of freedom due to the dissipative repumping process.
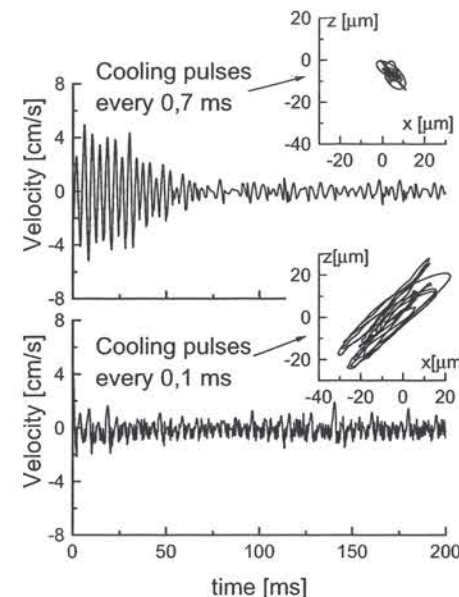

FIG. 7. Time evolution of the velocity component along the Raman axis for different pulse rates Γ_{cool}. Projections of the corresponding trajectories (between 100 ms and 200 ms) in the plane containing the vertical and the Raman axis are shown in the insets.

The Monte Carlo simulation of single atom trajectories in fig.7 demonstrates this effect. We have calculated 3D classical trajectories with random initial positions and velocities and have chosen a simplified excitation profile for the Raman pulses:

$$P_{exc}(p) = \begin{cases} 1 & p < -3\hbar k \\ |p/3\hbar k|^2 & \text{for} \quad -3\hbar k \le p \le 0 \\ 0 & p > 0 \end{cases} \qquad (11)$$

In the simulation, every Γ_{cool}^{-1} the atom can be excited according to P_{exc}. Once a Raman excitation takes place, the repumping process is simulated by adding three momenta $\hbar k$ of random directions.

For the different cooling rates shown in fig.7, the velocity component along the Raman axis decreases in all cases. However, a closer look to the trajectory for the high cooling rate $\Gamma_{cool}^{-1} = 0.1$ ms reveals that the other degrees of freedom are not cooled efficiently.

The energy loss due to the different cooling rates in fig.8 underline this effect. After 100 ms, an equilibrium is reached in case of a high pulse rate, i.e. the heating of the perpendicular motion is balanced by the combination of cooling and coupling to the Raman axis. The 'temperature' of 9 μK is rather high in this case (there is no thermal distribution – we express the average energy in terms of a 'temperature'). On the other hand, the low cooling rate $\Gamma_{cool}^{-1} = 0.7$ ms allows an effective coupling of the atomic motion to the Raman axis.
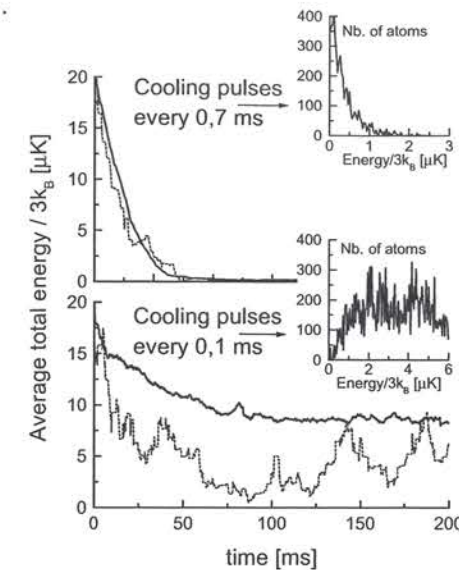

FIG. 8. Total energy loss for different pulse rates Γ_{cool}. The solid lines show the average over 100 atoms, the dashed lines correspond to single trajectories. In the insets are shown the energy distributions in the steady-state.

A simulation of the temperature obtained after a typical cooling time $t_{trap} = 200$ ms is shown in fig.9 as function of Γ_{cool}^{-1}. Due to the limited cooling time, there is an optimum choice $\Gamma_{cool}^{-1} = 0.7$ ms for which the temperature reaches 0.2 μK, i.e. the recoil temperature for cesium. At lower pulse rates, the number of pulses is too small to bring the temperature further down. We have observed that for cooling times longer than 200 ms, the temperature still decreases below 200 nK.
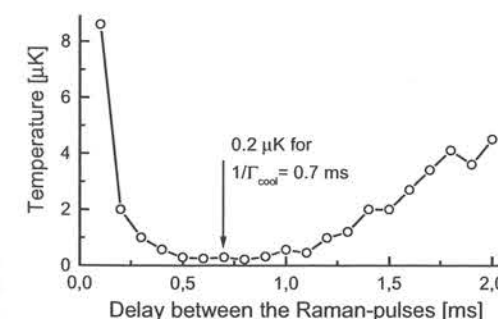
FIG. 9. Temperature reached after 100 ms Raman cooling as a function of the pulse rate.

V. EXPERIMENTAL SETUP

A. YAG and Raman beams

Atoms are loaded in the crossed dipole trap from a vapor cell magneto optical trap (MOT) [13]. The beam configuration of the red detuned dipole trap is shown in fig.10. We use a 1064 nm TEM$_{00}$ Nd:YAG laser which is split into two arms having each a power of 7 W. These two beams cross in their focal points with a common waist $w_0 = 80$ μm. Both of them

propagate in a vertical plane and make an angle of $\pm 37°$ with the vertical.
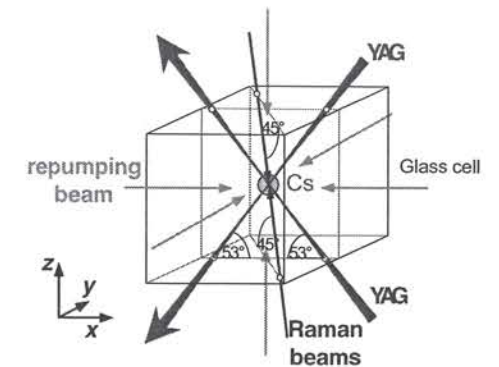
FIG. 10. Configuration of the dipole and Raman beams.

The attractive potential (see fig.11) is caused by the ground state light shift

$$\Delta E = \frac{\hbar \Omega_{YAG}^2(\vec{r})}{4\Delta_{YAG}} \qquad (12)$$

and corresponds to a well depth of 150 μK. With these laser parameters, gravity is compensated only in the intersection volume of the two beams. Because of the large detuning of the YAG laser, the maximum photon scattering rate at the center of the trap is 3 s^{-1}. The calculated oscillation frequencies near the bottom of the potential are

$$\nu_x = 458 \text{ Hz} \qquad \nu_y = 577 \text{ Hz} \qquad \nu_z = 350 \text{ Hz}, \qquad (13)$$

where x and y design the directions in the horizontal plane, y being perpendicular to both of the dipole beams, and z the vertical axis.
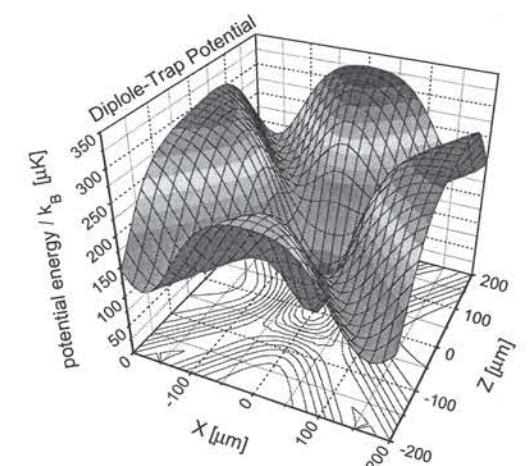
FIG. 11. Cut of the dipole trap potential in the plane of the beams.

The Raman cooling beams are spatially filtered using optical fibers and propagate along the (1,1,1) direction referred to the eigen-axes of oscillation in the dipole trap. This provides an effective coupling of the one dimensional cooling to all degrees of freedom of the atomic motion. The waist of the

Raman beams is on the order of ~ 1 mm and their power is up to 35 mW. For a detuning $\Delta = 2\pi \times 25$ GHz, the maximum effective Rabi frequency is $\Omega_{\rm eff} = 4 \times 10^5$ rad.s^{-1}. The two beams are issued from two diode lasers whose frequency difference is phase-locked to a stable frequency source at the 9.2 GHz Cesium hyperfine frequency [5,6]. The shape, central frequency and frequency chirp of the pulses are achieved using acousto-optic modulators. The Raman tranfer from $F = 3$ to $F = 4$ is followed by a repumping pulse, resonant with the $F = 4 \longrightarrow F'= 3$ transition which returns the atoms to $F = 3$. This repumping laser illuminates the atoms in a six beam molasses geometry (fig.10).

B. Detection

We measure the atom number, the velocity distribution of the trapped atoms and the size of the cloud: the number of atoms and the velocity distribution are deduced from fluorescence measurements while the size is obtained by absorption imaging [2]. After switching off the YAG beams, we turn on a σ^+ polarized probe beam tuned to the $F = 4 \longrightarrow F'= 5$ transition which overlaps the dipole trap. It is slightly red detuned and in a standing wave configuration. 2% of the fluorescence light is collected with a lens on a calibrated photodiode. For measuring the momentum distribution, we use velocity selective Raman transition [12]. We transfer a narrow velocity class from $F = 3$ to $F = 4$ with a 200 μs Blackman Π–pulse. The fluorescence of these selected atoms is then recorded as above. By scanning the Raman detuning δ we obtain the full momentum distribution, with a resolution of about $\hbar k/2$.

The absorption image is obtained on a CCD camera by shining a 15 μs probe beam pulse on the trapped atoms in the $(1,1,0)$ direction (in the horizontal plane). The probe is typically detuned by -1.5Γ from resonance. The trap is imaged with a magnification of 4 on the CCD. The image appears as the ratio between a picture with atoms and a reference picture without atoms. The absorption picture gives the size of the trap with a resolution of about 8μm and an independant measure of the number of atoms.

VI. EXPERIMENTAL RESULTS

A. Loading the Dipole Trap

Cesium atoms are first collected for 1 s in the MOT from the background gas at 10^{-9} mbar. In order to capture the largest possible number of atoms, the YAG trap and the MOT overlap in time for about 100 ms. Within this time, the MOT is contracted by doubling the magnetic field gradient to 30 Gauß/cm and reducing the intensity of the MOT beams by a factor of 20 to 1 mW/cm^2. The detuning of the beams is increased to $-10\ \Gamma$ for a short period (~ 5 ms) to further cool the atoms before switching the MOT off. Absorption images recorded 10 ms and 100 ms after switching off the MOT are shown in fig.12. After 10 ms the atoms initially at the intersection of the YAG beams remain trapped while the others fall preferentially along the YAG beams. After 100 ms, 10^5 atoms (1% of the number of atoms in the MOT) remain in

the crossed dipole trap with a density of 3×10^{11} atoms/cm^3 (within a factor 2) and an initial temperature of 6 μK.
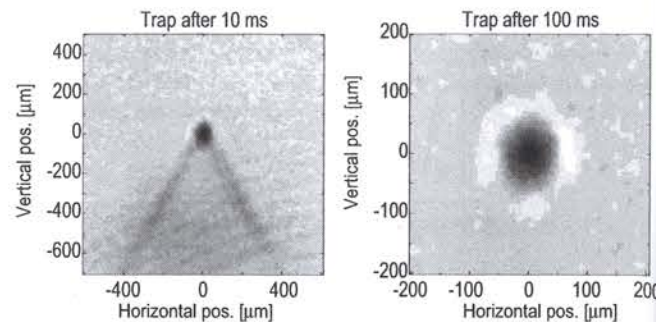

FIG. 12. Absorption images of cesium atoms in the crossed trap in the lin$\perp$lin configuration of the YAG beams. After 100 ms, 10^5 atoms remain in the 'harmonic' trap and form a cloud of Gaussian shape with $\sigma_{x,y} \simeq 24$ μm, $\sigma_z \simeq 30$ μm.

We have observed that the loading of the YAG trap and the shape of the atomic cloud was strongly dependent of the polarization of the YAG beams. When the two YAG beams have linear and parallel polarizations, the number of trapped atoms is about 5 times higher than in the case of orthogonal polarizations. The shape of the cloud (fig.13) is also very different as it displays a 'X' pattern.
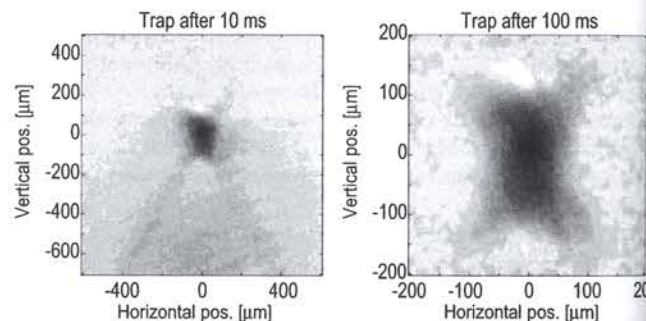

FIG. 13. Absorption images in the lin$\parallel$lin configuration of the YAG beams. The X shape of the trap which contains 5×10^5 atoms is due to an intensity modulation along the vertical (see text).

We attribute this effect as being due to the intensity interference pattern along the vertical when the two polarizations are parallel. This produces horizontal planes of micro-wells on the scale of the YAG wavelength ($\lambda_{\rm YAG}/2\sin 53°$). The atoms are trapped in these planes of intensity maxima and the effective trapping volume is larger. An interesting application of this interference effect might be to enhance the loading efficiency of the YAG trap. After loading with parallel polarizations we could rotate the polarization of one of the beams during the cooling phase to collect these atoms in the bottom of the harmonic trap.

When the YAG beams have linear and orthogonal polarizations, there is no intensity modulation but there is a polarization lattice along z which leads to a modulation of the light shift potential. It is easy to show that both of the cesium D1 and D2 transitions (at 894 nm and 852 nm respectively) contribute to the light shift in a way which depends on the local polarization. The amplitude of the modulation is proportional to the frequency difference between the D1 and D2

lines and is opposite for the $F = 3$ and $F = 4$ hyperfine states. It represents about $\pm 10\%$ of the total depth of the potential. Because our YAG laser has several longitudinal modes, this polarization lattice may fluctuate in time and produce an unwanted heating.

B. Realization of the Raman excitation profile

To realize the optimal excitation profile, we first note that the effective detuning of the Raman transition depends on the power of the Raman beams as given by eq.(2b).
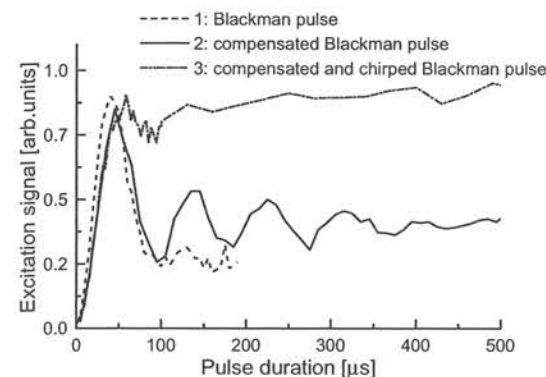

FIG. 14. Excitation rate as a function of the pulse duration; intensity is kept constant; (1) Blackman pulse without light shift compensation; (2) Blackman pulse with light shift compensation; (3) chirped Blackman pulse for rapid adiabatic passage (including light shift compensation).

For $\Delta > \delta_{\rm HFS}$ it is not possible to cancel the light shift term in eq.(2b), so that the instantaneous resonance frequency is shifted proportionally to the instantaneous intensity of the pulse. This leads to an imperfect π-pulse condition and to a damping of Rabi oscillations when using Blackman pulses as shown in fig.14, curve 1.

In order to solve this problem, we actively compensate the light shift by chirping the detuning during the Blackman pulse. Several periods of the Rabi oscillation become then visible (fig.14, curve 2). The effective Rabi frequency can be measured by this method and for instance fig.14 gives $\Omega_{\rm eff} = 7 \times 10^4$ rad/s. The 'damping' of the oscillation is mostly due to the interference between the various m-dependent Rabi frequencies (See eq.(2a)). In the case of the pulses used for the rapid adiabatic passage which are frequency chirped, we add the compensation of the light shift to the RAP chirp. In such conditions and with a frequency chirp symetric around resonance (fig.14, curve 3), the excitation probability remains close to one for a pulse area greater than 3π.

We then tested the efficiency of the rapid adiabatic passage with copropagating Raman beams for which there is no velocity selectivity. The transfer efficiency as a function of Raman detuning δ is presented in fig.15 for a 200 μs long Blackman pulse chirped from -81 kHz to 0, $\Delta = 2\pi \times 25$ GHz and for various intensities. The agreement with theory (fig.6) is excellent. Note the high transfer efficiency (90%) and the square shape of the excitation profile for the pulse of area 5.7Π which we will use in the Doppler sensitive case for Raman cooling (next section).
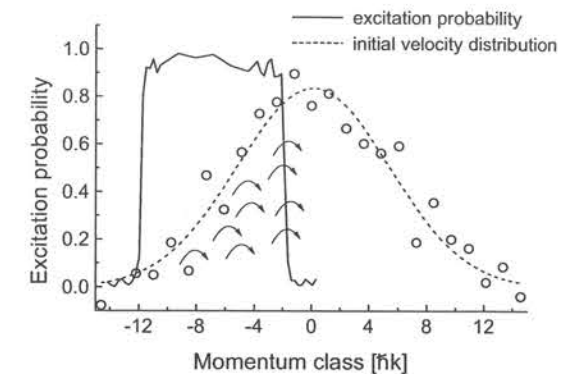
FIG. 15. Excitation probability as a function of detuning for 200 μs Blackman pulses chirped from -81 kHz to 0; the three curves correspond to three different pulse areas.

C. Raman cooling sequence

For Raman cooling, we use the Raman beams in the counter-propagating geometry. The transition probability of fig.15 becomes a Doppler sensitive excitation profile: for an atom with velocity v along the Raman beams, $\delta_{\rm eff} = \delta + 2kv$.
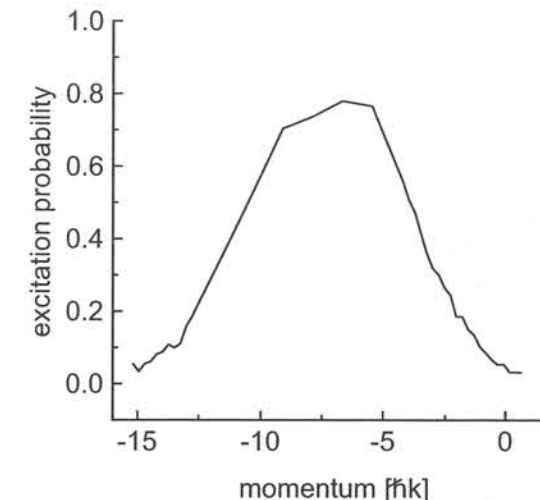
FIG. 16. Measured initial momentum distribution in the crossed dipole trap ($T = 5.6$ μK) and Doppler selective excitation profile for a 200 μs long chirped Blackman pulse.

We carefully adjust the initial detuning and the pulse spectral width in order to avoid any excitation at zero velocity. Fig.16 shows the momentum dependent excitation profile of a 200 μs Blackman pulse chirped over 81 kHz together with the initial momentum distribution. We optimize the cooling sequence to get the narrowest momentum distribution after a fixed time (70 ms). We find that the temperature of the cooled atoms is larger if the pulse rate is too high. This observation is in agreement with the simple simulation described in section IV. The optimal cooling sequence was: a 300 μs Blackman pulse exciting the atoms with momentum between $-12\hbar k$ and $-3\hbar k$, followed by a 100 μs repumping pulse. The total time between two cooling pulses was then 400 μs, which

corresponds to 7 to 10 pulses per oscillation period. This sequence was repeated 170 times.

D. Results

The result of the Raman cooling is shown in fig.17: before cooling, the momentum distribution along the Raman axis is gaussian with a $\sigma = 5.3\hbar k$ dispersion. We were able to cool the atomic sample down to $\sigma = 3.2\hbar k$. This corresponds to a temperature of $T = 2.0\ \mu$K. Since the areas of the two momentum distributions are equal, there is no atom loss during the cooling process.
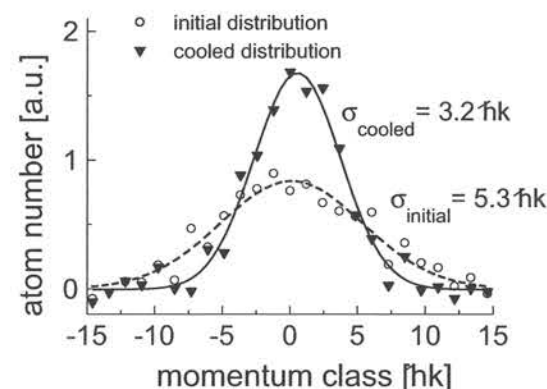
FIG. 17. Momentum distribution before and after Raman cooling.

The momentum dispersion along one axis was reduced by a factor $\eta = 1.65$. The increase in phase space density, proportional to η^6 for atoms trapped in an harmonic potential, is a factor 20. We also checked that the cooling was effective in 3 dimensions by taking absorption pictures of the trap before and after cooling with the CCD camera. The density of the cooled atoms is 1.3×10^{12} cm^{-3} with an uncertainty of a factor 2.

E. Limitations and prospects

For longer cooling sequences, we did not reach a temperature smaller than 2 μK. Nor was the temperature lower when we added a second, longer, pulse in order to excite atoms with momentum between $-3\hbar k$ and $-1\hbar k$. We suspect that Raman cooling is in competition with a residual heating mechanism due to a time dependent interference betwen the YAG beams inducing fluctuations of the trapping potential. A possible solution to this problem is to alternate in time the two YAG trapping beams at a rate much higher than the oscillation frequencies. Our numerical simulations indicate that, after suppression of this heating, temperatures near the single photon recoil temperature should be accessible. Such a value would be near the Bose-Einstein condensation threshold, if we neglect possible density limitations due to photon multiple scattering [14,15]. A second interesting development is to initiate evaporative cooling from the high density already obtained in this dipole trap [16].

[1] M.H.Anderson, J.R.Ensher, M.R.Matthews, C.E.Wieman and E.A.Cornell, Science 269, 198 (1995)
[2] K.B.Davis, M.-O.Mewes, M.R.Andrews, N.J. van Druten, D.S.Durfee, D.M.Kurn, and W.Ketterle, Phys.Rev.Lett. 75, 3969 (1995)
[3] H.J.Lee, C.S.Adams, M.Kasevich and S.Chu, Phys.Rev.Lett. 76, 2658 (1996)
[4] M.Kasevich and S.Chu, Phys.Rev.Lett. 69, 1741 (1992)
[5] J.Reichel, O.Morice, G.M.Tino and C.Salomon, Europhys.Lett. 28, 477 (1994)
[6] J.Reichel, F.Bardou, M. Ben Dahan, E.Peik, S.Rand, C.Salomon and C.Cohen-Tannoudji, Phys.Rev.Lett. 75, 4575 (1995)
[7] A.Aspect, E.Arimondo, R.Kaiser, N.Vansteenkiste and C.Cohen-Tannoudji, Phys.Rev.Lett. 61, 826 (1988)
[8] M.M.T.Loy, Phys.Rev.Lett. 32, 814 (1974)
[9] U.Gaubatz, P.Rudecki, S.Schiemann and K.Bergmann, J.Chem.Phys. 92, 5363 (1990)
S.Schiemann, A.Kuhn, S.Steuerwald and K.Bergmann, Phys.Rev.Lett. 71, 3637 (1993)
[10] A.Messiah, 'Mécanique Quantique,' Vol.2, Chap.17, Dunod, Paris (1959)
[11] F.Bardou, J.P.Bouchaud, O.Emile, A.Aspect and C.Cohen-Tannoudji, Phys.Rev.Lett. 75, 4575 (1995) P.Lévy, 'Théorie de l'Addition des Variables Aléatoires,' Gautier-Villars (1954)
[12] M.Kasevich and S.Chu, Phys.Rev.Lett. 67, 181 (1991)
[13] C.Monroe, W.Swann, H.Robinson et C.Wieman, Phys.Rev.Lett. 65, 1571 (1990)
[14] M.Olshanii, Y.Castin and J.Dalibard, Proc. Laser Spectr. XII, 7 (1995)
[15] J.I.Cirac, M.Lewenstein and P.Zoller, Europhys.Lett. 35, 647 (1996)
[16] C.S.Adams, H.J.Lee, N.Davidson, M.Kasevich and S.Chu, Phys.Rev.Lett. 74, 3577 (1995)

Free expansion of a Bose–Einstein condensate from an Ioffe–Pritchard magnetic trap

U. Ernst[1], J. Schuster[1], F. Schreck[2], A. Marte[1], A. Kuhn[1], G. Rempe[1,*]

[1] Fakultät für Physik, Universität Konstanz, Fach M701, D-78457 Konstanz, Germany
[2] Present address: Laboratoire Kastler Brossel, École Normale Supérieure, Paris, France

Abstract. The free expansion of a Bose–Einstein condensate of about 10^5 rubidium-87 atoms released from an Ioffe–Pritchard magnetic trap is investigated experimentally. The expansion dynamics depend only on the trap frequencies, which are determined independently. The data are in good agreement with the expected expansion of a condensate, and are clearly distinct from the behaviour of a classical gas in the hydrodynamic regime.

PACS: 03.75.Fi; 05.30.Jp; 32.80.Pj

The observation of Bose–Einstein condensation (BEC) in dilute alkali vapours three years ago [1–3], initiated enormous activities, both experimentally and theoretically, with the goal to study the properties of a weakly interacting degenerate quantum gas [4, 5]. Here, we are interested in the dynamics of a coherent atomic ensemble. In particular, we will focus on the time-dependent expansion properties of a Bose–Einstein condensate which is produced in and subsequently released from our Ioffe–Pritchard magnetic trap [6]. Experimentally, the unique properties of the density distribution after the expansion can be used to identify the BEC phase transition and to distinguish the condensed fraction of atoms from its non-condensed counterpart. The time-dependent expansion after a sudden change of the trapping potential has been studied theoretically in [7–10], but a detailed comparison with experimental data has only been published in [6, 10]. In [10], agreement between experiment and theory was found to be rather poor for the case of the JILA experiment, and the aspect ratio of the MIT condensate could only be estimated from published false-colour images. The data reported in the present paper extend our previous work [6] and allow for a quantitative comparison between experiment and theory.

Following the notation of [9], we now summarize the theoretical results which are relevant for the experiment described below. Using a mean-field approach, the single-particle wave function of the condensate is described by the Gross–Pitaevskii equation

$$\mu \Phi(r) = \left[-\frac{\hbar^2}{2m}\Delta + U(r) + Ng|\Phi(r)|^2 \right] \Phi(r). \quad (1)$$

Here, μ is the chemical potential, g is related to the s-wave scattering length a by $g = 4\pi\hbar^2 a/m$, and $U(r)$ is the potential used to trap the atomic gas. For the Ioffe–Pritchard configuration, this potential is harmonic but anisotropic, $U(r) = \frac{1}{2}\sum_i m\omega_i^2 r_i^2$, where $\omega_1 = \omega_2 = \omega_\perp$ and $\omega_3 = \omega_\parallel$ are the single-particle oscillation frequencies along the radial and axial direction, respectively.

In the Thomas–Fermi regime, the mean-field energy arising from collisions between the particles dominates the kinetic energy which can therefore be neglected in (1). In this case, the confining potential $U(r)$ of the atoms in the trap is balanced by the mean-field energy,

$$g\rho(r) = Ng|\Phi(r)|^2 = \begin{cases} \mu - U(r) & \text{for } \mu \geq U(r) \\ 0 & \text{otherwise} \end{cases}, \quad (2)$$

where $\rho(r)$ is the spatial density in the gas. Consequently, any cut through $\rho(r)$ has the form of an inverted parabola, whereas the surfaces of equal density are ellipsoids.

The trap is switched off at $t = 0$, i.e. $U(r) = 0$ for $t \geq 0$. However, the mean-field energy remains and gives rise to an expansion of the atomic ensemble, i.e. the mean-field energy is converted into kinetic energy of the atoms. From a classical point of view, this acceleration is due to a force $F(r, t) = -\nabla(g\rho(r, t))$, which depends on the gradient of the mean-field energy. As was derived in [8–10] from a classical and a quantum mechanical treatment, the dynamics of the expansion is contained in the evolution of three time-dependent scaling parameters λ_1, λ_2, and λ_3, obeying the initial condition $\lambda_1 = \lambda_2 = \lambda_3 = 1$. In particular, the condensate remains elliptical, still featuring its truncated parabolic density profile.

The Ioffe–Pritchard trap used in our experiment is anisotropic, with the axial frequency, $\omega_\parallel$, being smaller than the radial frequency, $\omega_\perp$. In this case, the widths of the condensate along the axial and radial directions are given by $W_\parallel$ and $W_\perp$, respectively, with $W_\parallel$ being larger than $W_\perp$. Consequently, the condensate is cigar shaped with an aspect ratio

$W_\perp/W_\parallel = \epsilon$, where $\epsilon = \omega_\parallel/\omega_\perp < 1$ is the ratio of the trap frequencies. After switching off the trap, the aspect ratio is given by

$$\eta(t) = \frac{W_\perp(t)}{W_\parallel(t)} = \frac{\lambda_\perp(t)}{\lambda_\parallel(t)}\epsilon . \tag{3}$$

Note that it depends only on the two scaling parameters $\lambda_\perp = \lambda_1 = \lambda_2$ and $\lambda_\parallel = \lambda_3$, which evolve according to

$$\frac{d^2}{d\tau^2}\lambda_\perp = \frac{1}{\lambda_\perp^3 \lambda_\parallel} \quad \text{and} \quad \frac{d^2}{d\tau^2}\lambda_\parallel = \frac{\epsilon^2}{\lambda_\perp^2 \lambda_\parallel^2} . \tag{4}$$

Here $\tau = \omega_\perp t$ is a dimensionless time variable. The two equations can be solved analytically for $\epsilon \ll 1$. To lowest order in ϵ, the result is

$$\lambda_\perp(\tau) = \sqrt{1+\tau^2} ,$$

$$\lambda_\parallel(\tau) = 1 + \epsilon^2 \left[\tau \arctan\tau - \ln\sqrt{1+\tau^2} \right] . \tag{5}$$

Obviously, $\lambda_\perp$ increases much faster than $\lambda_\parallel$. Therefore the shape of the condensate changes from a prolate (cigar-shaped) distribution to an oblate (pancake-like) distribution after a time $\tau \approx 1/\epsilon$.

Note that ϵ is neglected in the equation for $\lambda_\perp$, because the radial expansion is fast. However, the second-order term in ϵ is needed for $\lambda_\parallel$ in order to take into account any axial expansion in this model. Note also that the aspect ratio is independent of the number, N, of atoms in the condensate.

We now discuss our experiments which are performed in the magnetic trap described in [6]. Briefly, a gas of ^{87}Rb atoms is trapped and cooled in a UHV chamber with two magneto-optical traps. The atoms are then loaded into the magnetic trap and cooled by means of radio-frequency-induced evaporation. Condensation starts at a critical temperature $T_c \approx 550$ nK. We have realized pure condensates with more than 10^5 atoms at peak densities of 4×10^{14} atoms/cm^3.

It is obvious from the theory outlined above that the trap frequencies play a crucial role in the experiment. We have therefore carefully measured the axial frequency, $\omega_\parallel$, by monitoring the oscillation of an atomic cloud in the trap. This is achieved by placing the atoms initially off-centre with respect to the minimum of the magnetic trapping potential. The oscillation is stopped at a variable time delay by linearly ramping down the current through the coils within 200 μs. This turns off the trap on a timescale short compared with the inverse oscillation frequencies (see below). At this moment, an absorption picture of the cloud is taken. The position of the cloud centre is plotted versus time in Fig. 1. The data are fitted by a sinusoidal function, with amplitude, frequency, and phase as fit parameters. The axial frequency is found to be $\omega_\parallel = 2\pi \times (24.5 \pm 0.7)$ Hz.

The radial frequency is too fast to be monitored in the same way. Instead, the cloud is heated by modulating the magnitude of the magnetic bias field in the centre of the trap, thereby modulating the radial frequency. We first cool the atomic cloud by rf-induced evaporation to 2 μK. At this temperature, the size of the cloud is small so that the anharmonicity of the trapping potential can be neglected. Next, an ac magnetic field with adjustable frequency is applied along
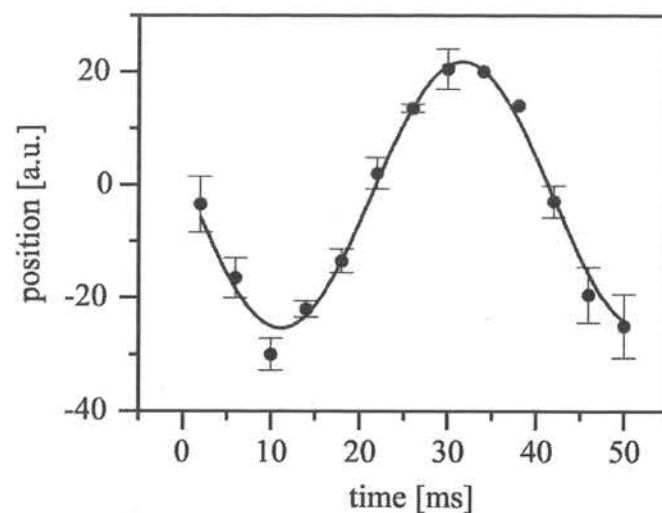

Fig. 1. Oscillation of the atomic cloud along the symmetry axis of the dc magnetic trap, induced by placing the atoms initially off-centre

the axial direction while the radio frequency is kept on at a constant value. This limits the effective trap depth to a sufficiently small value so that resonantly excited atoms with enough energy can escape from the trap. After the trap is suddenly switched off, the number of remaining atoms is measured. This is achieved by pumping the atoms to a dark hyperfine state and recording the laser-induced fluorescence with a photo-multiplier, which is calibrated by a frequency-resolved absorption technique. The total fluorescence signal is proportional to the number of atoms. Results for various modulation frequencies are shown in Fig. 2. When the resonance condition is met, the radial oscillation is excited and the trap is depleted. By fitting an inverted Lorentzian to the data, we find $\omega_\perp = 2\pi \times (246.8 \pm 0.2)$ Hz.

Next, Fig. 3 shows the radial density profile of a condensate 12 ms after release from the trap. A near-resonant absorption technique is used, so that the displayed profile represents the integral of the density distribution $\rho(r)$ along the
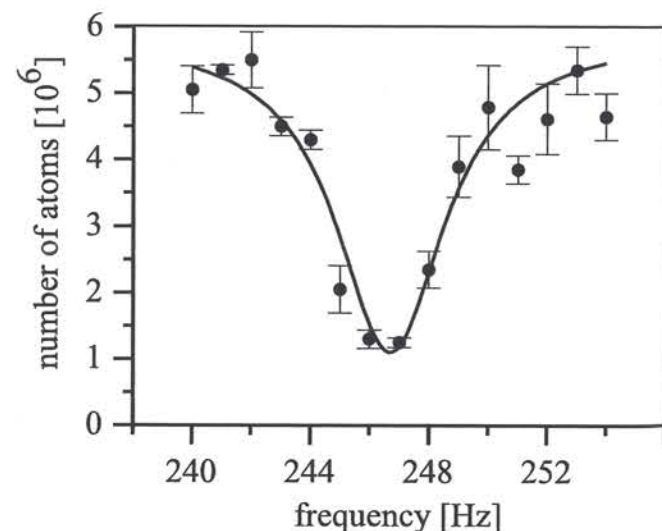

Fig. 2. Resonant excitation of the radial oscillation by means of an auxiliary ac magnetic field. The resonance manifests itself as a decrease of the number of trapped atoms
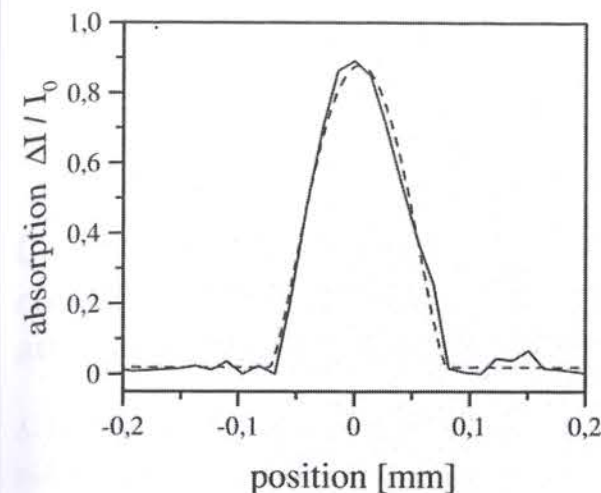

Fig. 3. Radial absorption profile of the condensate after a 12-ms-long free expansion featuring its inverted parabolic shape. The profiles are taken from normalized absorption images and therefore represent the integrated atomic absorption $\Delta I/I_0$ along the observation direction, where I_0 is the intensity of the incoming light and ΔI is the difference between I_0 and the transmitted intensity. The *dashed line* is a fit to the experimental data

observation direction. The width can easily be obtained by fitting an integrated truncated parabola to the experimental data. For example, a full width of $W_\perp = 150$ μm is obtained for the profile displayed in Fig. 3. Similar plots are obtained for the axial direction.

The time-dependent aspect ratio of the expanding cloud is obtained from a series of measurements like that shown in Fig. 3, for both the axial and the radial directions. Note, however, that the condensate falls a considerable distance during the 100-μs-long exposure time. For example, after 30 ms gravity has accelerated the condensate to a mean velocity of 0.3 m/s. The atoms therefore move a distance of 30 μm along
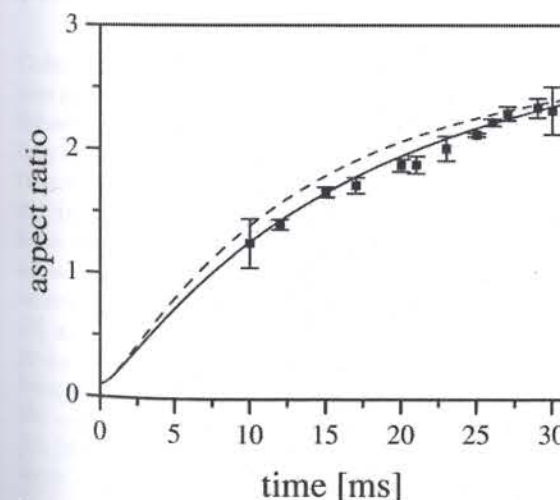

Fig. 4. Aspect ratio of the freely expanding condensate as a function of time. The *solid squares* represent the experimental data, which are corrected for the gravity-induced motion along the vertical direction. The *solid curve* is taken from [9], i.e. from (3) and (5) and shows the expected expansion of a Bose–Einstein condensate. The free expansion of a classical gas in the hydrodynamic regime, as described by (7) taken from [11], is also shown as a *dashed curve*. Both curves are corrected to include the effect of our observation angle, and are plotted without any free parameter

the vertical direction during the exposure time. Because the symmetry axis of the trap and the direction of observation are both horizontal, the measured radial width is broadened by this motional effect. The experimental data were therefore corrected by simply subtracting the relevant flight distances from the measured radial widths. Results for the aspect ratio are plotted as solid squares in Fig. 4. Each data point is obtained by averaging over two realisations, with error bars representing shot-to-shot fluctuations.

To allow for a direct comparison between our experimental results and the theoretical prediction, we also take into account that the condensate is not observed exactly perpendicular to its symmetry axis, but under an angle of 76°. Although small, this difference of $\alpha = 14°$ has a significant effect for longer expansion times, where the condensate has the shape of a pancake. In this regime, the axial width of the condensate's absorption image has two contributions: one from $W_\parallel$ and the other from $W_\perp$. However, the radial width, $W_\perp$, remains unchanged. Therefore, the observed aspect ratio is always smaller than expected from (3) and (5). Assuming a hard-core ellipsoid for the condensate, the effect of the projection can easily be included in the theoretical model by considering

$$\eta_\alpha(t) = \frac{\eta(t)}{\sqrt{\cos^2\alpha + \eta^2(t)\sin^2\alpha}} , \tag{6}$$

instead of $\eta(t)$, which is the aspect ratio for $\alpha = 0°$ from (3). The result is shown as a solid line in Fig. 4. Note that no adjustable parameters are used for the comparison between experimental data and theoretical prediction.

The evolution of the aspect ratio as a function of time observed in the experiment agrees well with the theoretical prediction. However, to use the expansion dynamics as a signature of Bose–Einstein condensation, a more detailed investigation is required, since also a classical gas can show a behaviour which is close to that of an expanding condensate. This would be the case for a gas in the hydrodynamic regime, where the density is so high that the mean free path of the particles is much smaller than the sample size. It has been shown by Kagan et al. [11] that the dynamics of such a dense gas are also described by scaling laws, with scaling parameters obeying the differential equations

$$\frac{d^2}{d\tau^2}\lambda_\perp = \frac{1}{\lambda_\perp^{7/3}\lambda_\parallel^{2/3}} \quad \text{and} \quad \frac{d^2}{d\tau^2}\lambda_\parallel = \frac{\epsilon^2}{\lambda_\perp^{4/3}\lambda_\parallel^{5/3}} . \tag{7}$$

The resulting evolution of the aspect ratio is shown as a dashed line in Fig. 4. It resembles the expansion of a Bose–Einstein condensate. However, the data clearly proof that an expanding condensate is observed in the experiment.

It is worth noting that the data shown here cannot be explained by invoking Heisenberg's position-momentum uncertainty relation alone, i.e. by the dispersion of a free atomic wave packet initially localised in the magnetic trap. Without the repulsive force associated with the mean-field energy, a Bose–Einstein condensate would expand much slower than actually observed in the experiment and the aspect ratio would asymptotically reach a value $1/\sqrt{\epsilon}$.

We emphasize that no asymptotic limit of the aspect ratio is reached in our experiment. However, the long-term behaviour of the expanding condensate is of general interest,

because a simple physical picture implies that all the mean-field energy is converted to kinetic energy of the atoms. Consequently, a stationary aspect ratio must be reached. The existence of an asymptotic limit is also evident from the differential equations (4). However, the value for this aspect ratio cannot be deduced from these equations. In particular, the assumption of a constant η is only consistent with $\eta(t) = 1$, i.e. a spherically expanding condensate. In general, the asymptotic limit can only be found by numerically integrating (4). For the parameters of our experiment, the result is $\eta(\infty) \simeq 6.7$ (i.e. $\eta_\alpha(\infty) \simeq 3.55$ for $\alpha = 14°$), which differs from the prediction of (5), $\eta(\infty) = 2/(\pi\epsilon) = 6.4$, obtained in lowest order. Experimentally, no such limit has been observed so far and it remains a challenging task of future experiments to record the free expansion of a Bose–Einstein condensate for very long time intervals.

References

1. M.H. Anderson, J.R. Ensher, M.R. Matthews, C.E. Wieman, E.A. Cornell: Science **269**, 198 (1995)
2. C.C. Bradley, C.A. Sackett, J.J. Tollett, R.G. Hulet: Phys. Rev. Lett. **75**, 1687 (1995)
3. K.B. Davis, M.-O. Mewes, M.R. Andrews, N.J. van Druten, D.S. Durfee, D.M. Kurn, W. Ketterle: Phys. Rev. Lett. **75**, 3969 (1995)
4. For a recent review of the experimental work, see, e.g., H.-J. Miesner, W. Ketterle: Solid State Commun. **107**, 629 (1998)
5. For a recent review of the theoretical work, see, e.g., A.S. Parkins, D.F. Walls: Phys. Rep. **303**(1), 1 (1998) and F. Dalfovo, S. Giorgini, L.P. Pitaevskii, S. Stringari: Rev. Mod. Phys., to appear (1999)
6. U. Ernst, A. Marte, F. Schreck, J. Schuster, G. Rempe: Europhys. Lett. **41**, 1 (1998)
7. M. Holland, J. Cooper: Phys. Rev. A **53**, R1954 (1996)
8. Yu. Kagan, E.L. Surkov, G.V. Shlyapnikov: Phys. Rev. A **54**, 1753R (1996)
9. Y. Castin, R. Dum: Phys. Rev. Lett. **77**, 5315 (1996)
10. F. Dalfovo, C. Minniti, S. Stringari, L. Pitaevskii: Phys. Lett. A **227**, 259 (1997)
11. Yu. Kagan, E.L. Surkov, G.V. Shlyapnikov: Phys. Rev. A **55**, R18 (1997)

Coherent population transfer in NO with pulsed lasers: the consequences of hyperfine structure, Doppler broadening and electromagnetically induced absorption

A. Kuhn[a], S. Steuerwald, and K. Bergmann[b]

Fachbereich Physik der Universität Kaiserslautern, Postfach 3049, 67653 Kaiserslautern, Germany

Abstract. Coherent population transfer between vibrational levels of the NO molecule induced by the interaction of two delayed laser pulses, also referred to as stimulated Raman scattering involving adiabatic passage (STIRAP), is studied experimentally in a molecular beam and in the bulk. The consequences of hyperfine splitting and Doppler broadening are discussed in detail. Unlike in previous studies of this kind, transfer occurs simultaneously between more than one group of non degenerate levels. In a molecular beam or in the bulk, the transfer efficiency of STIRAP exceeds that obtained by Stimulated Emission Pumping (SEP) by a factor of 3.6 or 15, respectively. We estimate the absolute transfer efficiency T in the beam to be $T \approx 60\%$, while $T \approx 18\%$ is found in the bulk. In both cases, this is 60% of the maximum value expected from numerical studies. Possible reasons for this discrepancy are discussed. Finally we show that the absorption of a pump pulse in a weakly absorbing medium is significantly enhanced by the presence of a copropagating Stokes pulse when the Rabi frequency Ω_S of the latter is smaller than the width of the Doppler profile $\Delta\nu_D$. The relation of this observation to the phenomenon of Electromagnetically Induced Transparency (EIT), which is observed for $\Omega_S \gg \Delta\nu_D$, is also discussed.

PACS. 33.80.Wz Other multiphoton processes – 33.80.-b Photon interactions with molecules – 42.65.Dr Stimulated Raman scattering; CARS

1 Introduction

Coherent population transfer by a stimulated Raman process involving adiabatic passage (STIRAP) is now an established technique for manipulating the population distribution in atoms and molecules [1]. After the first demonstration with continuous lasers [2] and the subsequent implementation with pulsed lasers [3–5] numerous applications have been proposed or demonstrated. New elements for atom optics [6–8] were developed, applications to atom interferometry [9,10] and laser cooling were reported [11–13] and a concept to use this method to prepare and probe the state of the radiation field in optical cavities has been proposed [14]. The technique was also used to study the collision dynamics of vibrationally excited molecules [15,16]. With some modification the method was furthermore applied for spectroscopic studies [17].

In its simplest form, the STIRAP technique is implemented for a three state system [2,18,19]. Initially state 1 carries the population. The objective is to transfer all the population to a state 3. This is done by suitably timed

coupling of an intermediate state 2, typically a state in a different electronic level, to the states 1 and 3 by radiation from a pump laser and a Stokes laser, respectively. Nearly complete population transfer is achieved provided the interaction begins with the Stokes laser and ends with the pump laser. The laser frequencies may be detuned from the resonance with the transition to the intermediate level. However, the two–photon resonance must be maintained. With these conditions met, the system is prepared in a superposition state (called trapped state, discovered in 1976 [20]) with contributions from the bare states 1 and 3, but no contribution from bare state 2. In the adiabatic limit level 2 is not populated in the course of the transfer process and radiative losses from the intermediate state 2 are efficiently suppressed.

The timing of the interactions is done either by pulsing the radiation or, when molecular beams in combination with continuous lasers are used, by spatially shifting the axes of the lasers. In the latter case the particles are exposed to a time dependent radiative coupling as they cross the laser beams. The losses during the transfer process are small, if the evolution is (nearly) adiabatic. Adiabatic evolution depends on several conditions. Firstly, the pulse area of the interaction must be sufficiently large [1,2,21], i.e. $\Omega_0 \Delta\tau \gg 1$, where $\Omega_0 = \sqrt{\Omega_{P0}^2 + \Omega_{S0}^2}$ and Ω_{P0}, Ω_{S0} are

[a] current address: Lab. Kastler Brossel, Ecole Normale Supérieure 24 Rue Lhomond, 75231 Paris Cedex 05, France
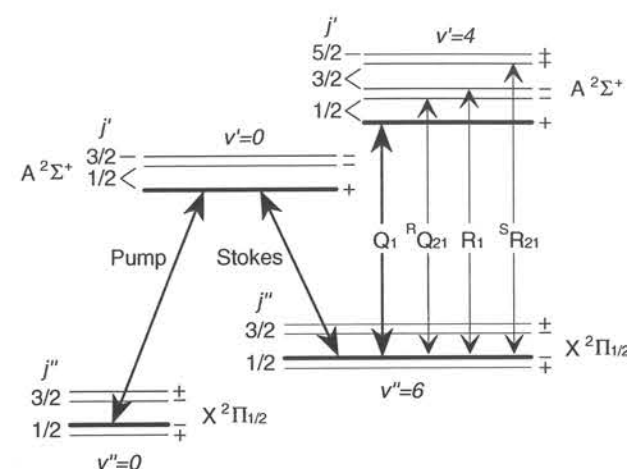[b] e-mail: bergmann@rhrk.uni-kl.de

Fig. 1. The level scheme for the NO molecule, relevant for the transfer and the detection.

Fig. 2. Details of the level scheme for NO, relevant for the transfer, including the hyperfine structure. Since only the amount of M_F is shown, all the levels are doubly degenerate. The levels are numbered from 1 to 9, for convenient reference in the text.

the peak Rabi frequencies of the pulses [22], which measure the coupling strength induced by the lasers; $\Delta\tau$ is the relevant interaction time. Secondly, the frequency fluctuations during the interaction with the atom or molecule with both lasers must be small [3]. Also, deviations from a smooth pulse shape are detrimental. Therefore special care must be taken when implementing the method with pulsed lasers, which usually exhibit inferior coherence properties. In fact, nearly transform limited radiation is required for successful application of the STIRAP technique [4].

Early studies [23] and recent theoretical [24–26] and experimental [27] work has carried the method beyond three level systems. It was found [27] that efficient transfer in multilevel systems can be achieved, subject to some restrictions with regard to the choice of the polarization, frequency and power of the lasers. Also, the consequences of detuning from the two–photon resonance have been analyzed [3,19,28].

In the present work, we expand on previously reported results on coherent population transfer with pulsed lasers applied to the NO molecule [4] as well as on some aspects relevant for population transfer in multilevel systems [27]. We consider in particular the consequences of the hyperfine structure of the molecular levels and the consequences of Doppler broadening.

2 Background

2.1 Some spectroscopic and experimental details

Figure 1 shows the relevant transitions in NO including the level splitting due to Λ-doubling, which is characteristic for molecules in a Π-state. We consider the transfer from the Λ-component with negative parity [29–31] of the lowest rotational state ($j'' = 1/2$) of the vibrational level $v'' = 0$ in the $^2\Pi_{1/2}$ electronic ground state to the ($j'' = 1/2, v'' = 6$) level. The intermediate level is ($j' = 1/2, v' = 0$) in the $A^2\Sigma^+$ electronic state. The
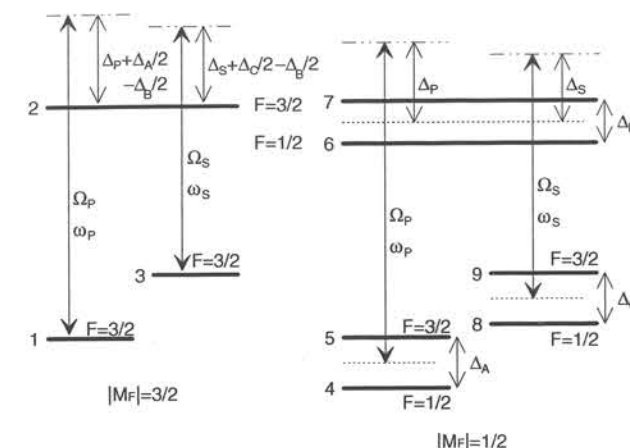
wavelength of the pump and Stokes laser is 226 nm and 300 nm, respectively. This coupling leads to the population of only one parity component in the $v'' = 6$ level. The population of this level is monitored by fluorescence induced by excitation to the $v' = 4$ level *via* a Q_1 or $^SR_{21}$ transition. Collisional transfer to the adjacent level of different parity is monitored by R_1 or $^RQ_{21}$ transitions.

Pulsed radiation with nearly transform limited bandwidth is obtained by pulse amplification of cw radiation [4] with a typical energy of 1 mJ for each of the pulses. The pulse width was $\Delta\tau = 3.0$ ns according to $E(t) = E_0 \exp[-(t/\Delta\tau)^2]$ while the power spectrum had a width (FWHM) of $\Delta\nu_{FL} = 125$ MHz. Very high lying vibrational levels (*e.g.* $v'' \geq 20$) can be populated when coupling occurs to the B–state, which requires radiation with $\lambda < 200$ nm [32]. A spatially smooth intensity profile is needed in the region where the laser and molecular beams cross, in order to assure the validity of the condition for adiabatic evolution near the laser beam axes. Therefore the radiation was spatially filtered, at considerable expense in pulse energy. Typically 0.1 mJ/pulse was delivered to the molecular beam.

2.2 The hyperfine structure

The nuclear spin of $^{14}N^{16}O$ is $I = 1$ leading to levels with total spin of $F = 1/2$ and $3/2$, see Figure 2. Therefore, what is shown in Figure 1 as a three state system encompasses actually 18 states. Such hyperfine splitting could be detrimental for efficient population transfer since the laser frequencies may not be in two–photon resonance with all radiatively coupled pairs of initial and final levels. However, for linear polarization, when $\hat{E}_P$ is parallel to $\hat{E}_S$ (this state of polarization was used throughout this experiment), the system decomposes into four independent systems, one each for $m_F = \pm 1/2$ and $m_F = \pm 3/2$. The latter two are three state systems while the former consist

---

$$H_6 = -\frac{\hbar}{2} \begin{pmatrix} -2\Delta_P + \Delta_A & 0 & \Omega_{46} & \Omega_{47} & 0 & 0 \\ 0 & -2\Delta_P - \Delta_A & \Omega_{56} & \Omega_{57} & 0 & 0 \\ \Omega_{64} & \Omega_{65} & \Delta_B & 0 & \Omega_{68} & \Omega_{69} \\ \Omega_{74} & \Omega_{75} & 0 & -\Delta_B & \Omega_{78} & \Omega_{79} \\ 0 & 0 & \Omega_{86} & \Omega_{87} & -2\Delta_S + \Delta_C & 0 \\ 0 & 0 & \Omega_{96} & \Omega_{97} & 0 & -2\Delta_S - \Delta_C \end{pmatrix} \quad (2.2)$$
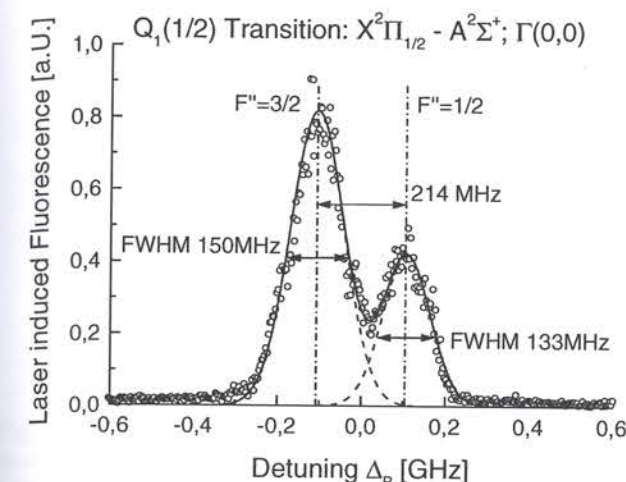

Fig. 3. Laser-induced fluorescence of the $Q_1(1/2)$ level of the X–A -transition. The hyperfine splitting of the ground state is well resolved. The gaussian fit to the profiles reveals a difference in the width of 17 MHz, which is close to the hyperfine splitting of 15 MHz in the upper state. This difference is related to the variation of the linestrength for transitions between (F, m_F)-states, given in Table 1 of the appendix. The ratio of the transition strength $F'' \longrightarrow F' = 1/2$ and $F'' \longrightarrow F' = 3/2$ is 1:8 for $F'' = 1/2$ but 4:5 for $F'' = 3/2$. Therefore, the profile of the peak labeled $F'' = 1/2$ is dominated by the transitions to only one hyperfine component of the upper level, while transitions to both hyperfine levels contribute nearly equally to the peak labeled $F'' = 3/2$, giving rise to a broadening equivalent to the upper state hyperfine splitting.

of six states each. They reduce to effective three level systems since the hyperfine splitting in the electronic ground state is 214 MHz [33] and is spectrally resolved, see Figure 3. The hyperfine splitting in the intermediate state of 15 MHz [34] is small compared to the laser linewidth. The precise value of the difference frequency of the pump and Stokes laser radiation determines between which pairs of levels $(F, |m_F| = 1/2)$ the transfer occurs. Following the numbering shown in Figure 2, transfer may occur between one of the states 4 and 5 to one of the states 9 and 8. When the two–photon resonance is established for the pair of states 4 and 8, the same is true for the pair 5 and 9, since the difference $\Delta_A - \Delta_C$ (see Fig. 3) of the hyperfine splitting in the levels $v'' = 0$ and $v'' = 6$ is negligibly small.

In cases (not encountered here) where the hyperfine splitting in the X-state is not fully resolved additional complications may arise, since transfer from any one of the thermally populated levels 4 and 5 may be transferred

to any one of the levels 8 and 9. Such a situation was not encountered in previous studies. In the recent work involving multilevel systems, the initial state was always a single quantum state [27], or the initial level consisted of degenerate quantum states [2].

2.3 The Hamiltonian and dressed state eigenvalues

With reference to the detunings, defined in Figure 2, the Hamiltonian (in rotating wave approximation) [22] for the three-state system, relevant for the $|m_F| = 3/2$ states is

$$H_3 = -\frac{\hbar}{2} \begin{pmatrix} -2\Delta_P - \Delta_A & \Omega_{12} & 0 \\ \Omega_{21} & -\Delta_B & \Omega_{23} \\ 0 & \Omega_{32} & -2\Delta_S - \Delta_C \end{pmatrix}, \quad (2.1)$$

while the six-state Hamiltonian, relevant for the $|m_F| = 1/2$ states reads

see equation (2.2) above.

The Rabi frequencies and their dependence on the quantum numbers are explicitly given in Appendix B. It is instructive to inspect the variation of the dressed state eigenvalues for various ratios of the Rabi frequencies and the hyperfine splitting. However, one can not adapt the approach used in [27] because only diabatic crossings arise.

Figure 4 shows the variation of the dressed state eigenvalues for four Rabi frequencies Ω_0 with $\Omega_0/2$ much larger, slightly larger, equal or smaller than the ground state hyperfine splitting. The calculation was done for parallel linear laser polarizations with the laser frequencies tuned to the two-photon resonance for the 4, 8 and 5, 9 pairs of levels. Initially, when only the Stokes laser is present, the system evolves along the horizontal (thick) lines correspond to the trapped states which are, at early times, identical to the initially populated levels 4 and 5. For large Rabi frequencies (Fig. 4a and 4b) a crossing of eigenvalues occurs at early times when the pump laser intensity is zero (or very small). At this time the trapped states have not acquired yet a contribution from the level 8 resp. 9, and the coupling with the states that correlate asymptotically to state 6 resp. 7 is zero. Therefore the crossing is not avoided (or only very weakly avoided) and the system follows the horizontal paths. The dressed states corresponding to these paths correlate to state 8 resp. 9 at late times. The situation is equivalent at the second crossing and thus complete transfer to states 8 and 9 is possible.

For small Rabi frequencies (Fig. 4d), there is no crossing of eigenstates and adiabatic transfer from 4 to 8
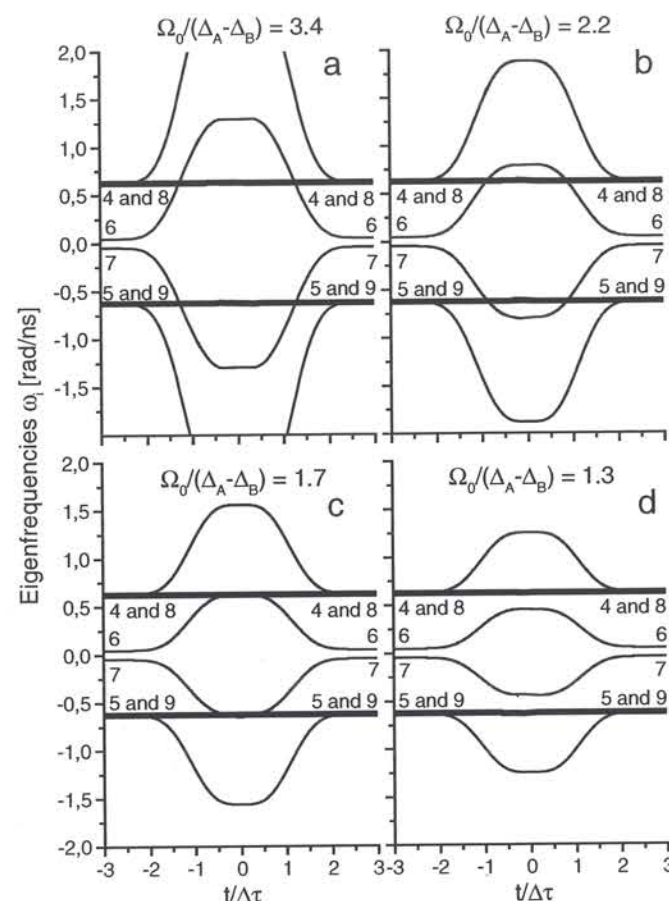
Fig. 4. Evolution of the dressed state eigenvalues of the Hamiltonian (Eq. 2.2), for various ratios of the Rabi frequency and the hyperfine splitting of the ground state level. The horizontal thick line is the adiabatic path for the transfer. The numbers of the bare states (see Fig. 2) which correlate with the eigenvalues at very early and very late times are also given.

(or 5 to 9) is possible, provided the conditions for adiabatic following are met.

Only in the intermediate case (Fig. 4c) where the Rabi frequency matches the hyperfine splitting, the eigenvalues become degenerate near $t = 0$. At this time, the trapped states are superpositions of states 4 and 8 (resp. 5 and 9) and some population will be transferred to the states which asymptotically correlate to 6 resp. 7, from where they will be lost by spontaneous emission.

3 Population transfer in a molecular beam

3.1 Numerical results

Unlike for Na$_2$ and Ne* used in previous studies with cw lasers, the electronic lifetime of the NO A–state (200 ns) is long compared to the overall interaction time of 10–20 ns. Therefore, radiative losses from the intermediate state are small during the interaction time with the laser pulses and

numerical calculations based on the Schrödinger equation (rather than on the Liouville equation) are adequate. However, any population which reached the intermediate state due to nonadiabatic coupling during the transfer process will later on be lost by spontaneous emission.

The state vector prior to the arrival of the laser pulses is

$$|\Psi(\text{early})\rangle = \frac{1}{\sqrt{3}}(e^{i\phi_1}|1\rangle + e^{i\phi_4}|4\rangle + e^{i\phi_5}|5\rangle). \quad (3.1)$$

It should be emphasized again, that unlike in our previous studies, more than one non-degenerate quantum state is initially populated. The state vector (3.1) is propagated to

$$|\Psi(\text{late})\rangle = \sum_n (c_{n1}e^{i\phi_1} + c_{n4}e^{i\phi_4} + c_{n5}e^{i\phi_5})|n\rangle \quad (3.2)$$

with $|\Psi(t)\rangle = \hat{T}_t|\Psi(t=0)\rangle$, leading to

$$|\Psi(t)\rangle = \frac{1}{\sqrt{3}}(e^{i\phi_1}\hat{T}_t|1\rangle + e^{i\phi_4}\hat{T}_t|4\rangle + e^{i\phi_5}\hat{T}_t|5\rangle). \quad (3.3)$$

Levels 1, 4 and 5 are each doubly degenerate. They are thermally populated lacking any fixed relative phases amongst them. Therefore the population in state $|n\rangle$ is given by

$$\langle\Psi(t)|n\rangle\langle n|\Psi(t)\rangle = c_{n1}^*c_{n1} + c_{n4}^*c_{n4} + c_{n5}^*c_{n5} \quad (3.4)$$

since cross terms vanish.

The transfer efficiency obtained from numerical simulation studies is shown in Figure 5. The panel (a) represents the transfer efficiency as a function of the pump– and Stokes laser detuning on a gray-coded scale. Along the diagonal, the two-photon resonance ($\Delta_P = \Delta_S$) is maintained while the frequencies are detuned from the one-photon resonance ($\Delta_0 \neq 0$). The solid line in Figure 5b shows the transfer efficiency "along the diagonal" ($\Delta_P = \Delta_S$) as Δ_0 is changed. The dashed line shows the two photon line shape, "perpendicular to the diagonal", *i.e.* for $\Delta_P = -\Delta_S$.

The panels (c) and (d) show the related fluorescence intensity. Because the upper state lifetime is long compared to the laser pulse duration, most of the fluorescence is emitted after the population transfer is completed. The pronounced dark resonance, associated with efficient population transfer is obvious from panel (c). Panel (d) shows a horizontal cut (Stokes laser tuned while the pump laser frequency remains on resonance, $\Delta_P = 0$) through the structure of panel (c). The details of the lineshape depend on the pump laser detuning Δ_P and are similar to the Fano profiles [35] which were also observed by Neusser [17].

The transfer efficiency is slightly reduced for $\Delta_S = \Delta_P$, which is even more pronounced when only the transfer from state 4 to state 8, shown in Figure 6, is considered. The loss on resonance is caused by the coupling to states which correlate to level 6 and 7, as discussed in the previous section. Figures 6a and 6b show the transfer from 4 to 8, while the transfer from 4 to 9, which requires tuning of the Stokes laser frequency by 214 MHz, is shown in Figures 6c and 6d. For the latter the relevant Rabi frequencies are smaller (see Appendix), and the condition for adiabatic following is no longer satisfied.
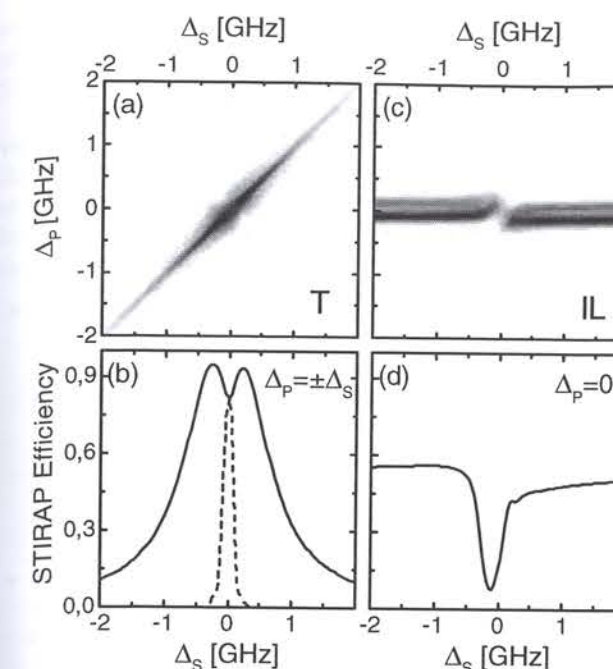
Fig. 5. Numerical simulation of the transfer efficiency (T) shown in (a) and excitation of the intermediate level (IL) shown in (c) as a function of the detunings Δ_P and Δ_S, respectively, in the beam. The solid line (b) shows the transfer efficiency along the contour $\Delta_P = \Delta_S$ (Raman resonance), while the dashed line refers to $\Delta_P = -\Delta_S$. For $\Delta_P = 0$ a pronounced dark resonance is observed (d). The center of the dark resonance is shifted from zero by 107 MHz in the latter panel, because the detunings are measured with reference to the middle between the ground state hyperfine levels (see Fig. 2).

Fig. 6. Numerical Simulation of the transfer in the beam from level 4 to 8 ((a) and (b)) or level 4 to 9 ((c) and (d)) with the frequencies adjusted accordingly (see also the caption of Fig. 5).

3.2 Experimental results

The overall features of the coherent population transfer in NO, observed in the simulation studies discussed in the previous section are well reproduced in the experiment. The population transfer and the related dark resonance is shown in Figure 7 as a function of Stokes and pump laser detuning. The maximum of the Stokes pulse preceded that of the pump pulse by 3 ns. The pump and Stokes laser energies (and beam diameters) were $E_P = 17~\mu J$ (2 mm) and $E_S = 340~\mu J$ (4 mm), respectively. The corresponding peak Rabi frequencies for $\Delta m = 0$ transitions (and beam diameters) from the magnetic sublevels $m = \pm 1/2$ are both $\Omega_0 = 2\pi~330$ MHz (neglecting the hyperfine splitting, see also appendix A as well as Table 2). With $\Delta\tau = 3$ ns, this leads to $\Omega_0\Delta\tau \approx 6.3$, falling short of the desirable value of $\Omega_0\Delta\tau > 10$.

Figure 7a shows the population in the final state, measured by probe laser induced fluorescence. The signal along the diagonal is related to the STIRAP process. The horizontal structure seen for $\Delta_P = 0$ ($\Delta_S \neq 0$) results from those molecules which are excited to the intermediate level by the pump laser and which decay during the short time interval of 300 ns set for detection about 1 μs after the STIRAP pulse sequence. This fluorescence is a small fraction of the time integrated total fluorescence

shown in panel (c), representing the decay from the intermediate level after the excitation to all accessible vibronic levels. Since the simulation studies are based on the Schrödinger equation, the total loss out of the system by spontaneous emission is included, while the population of the initial or final levels by spontaneous emission is not. Therefore the horizontal structure of Figure 7a is not seen in Figures 5a, 6a and 6c.

The transfer efficiency along the ridge of the diagonal structure is displayed in the lower left panel. The maximum transfer efficiency is observed, as expected, very close to the one-photon resonance. The two photon lineshape (recorded for $\Delta_P = -\Delta_S$, *i.e.* along a line which is perpendicular to the "STIRAP-ridge") is also shown.

3.3 STIRAP signature and transfer efficiency

Figure 8 shows the variation of the fluorescence induced by the probe laser as the delay between the pump and Stokes laser is changed from about $\Delta T = -8$ ns (Stokes laser precedes the pump laser) to about $\Delta T = +10$ ns (pump laser precedes the Stokes laser). The maximum of the transfer efficiency near $\Delta T = -3.5$ ns is significantly higher than that for $\Delta T = +2.5$ ns, which is a typical signature of the STIRAP process. For large positive delay, the transfer is caused by Stimulated Emission Pumping (SEP). Obviously, the STIRAP signal exceeds the SEP signal by more than a factor of three.

Experimental determination of the absolute transfer efficiency requires a calibration procedure. When cw lasers
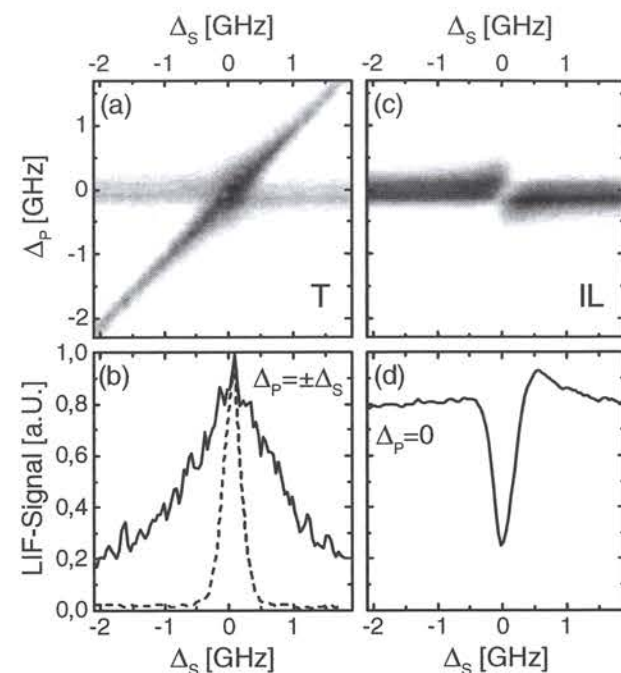
Fig. 7. Experimentally determined transfer efficiency (T) in the beam as a function of the Stokes laser and pump laser detunings shown in (a) and the fluorescence from the intermediate level (IL) shown in (c). Cuts along $\Delta_P = \Delta_S$ ((b), solid line, Raman resonance), $\Delta_P = -\Delta_S$ ((b), dashed line), or for $\Delta_P = 0$ ((d), exhibiting the dark resonance) are also shown. The horizontal structure seen in (a) shows that the spontaneous emission of the population from the intermediate level still contributes to the fluorescence signal. Most of these molecules do not reach the final level and therefore this process is not included in the numerical studies (Fig. 5).
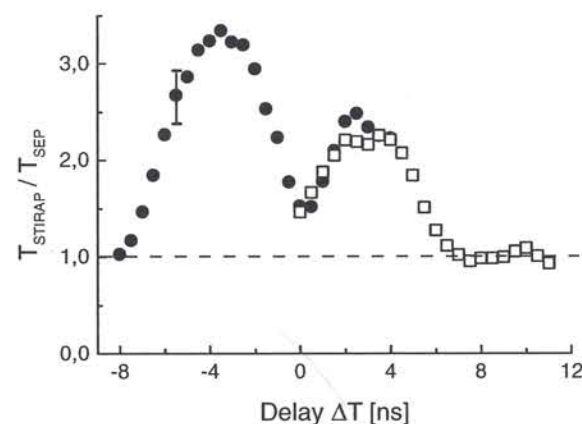
Fig. 8. Experimentally determined ratio T_{STIRAP}/T_{SEP} of the population transfer efficiency T *in the beam* as a function of the delay between the pulses (STIRAP-signature). Negative delay corresponds to the STIRAP configuration (Stokes pulse precedes the pump pulse) while positive delay relates to the SEP configuration (pump pulse precedes Stokes pulse). The results from two different runs are combined. The transfer observed at large positive delay is used to calibrate the absolute transfer efficiency.

are used for the transfer *via* an electronic state, the radiative lifetime of which is short compared to the interaction time with the laser, the normalization procedure is straightforward and unambiguous [2, 27]. Under those circumstances the pump laser alone will deplete all the population of the initial state by optical pumping. The fraction of the population, which reaches the final state by spontaneous emission is determined from the known transition strength. Thus, the ratio of the laser-induced fluorescence out of the final state for the STIRAP transfer to the fluorescence when only the pump laser is present provides an accurate measure of the transfer efficiency.

The attempt to use the pump laser induced spontaneous emission to the final state for calibration fails here, because pump laser induced Rabi oscillations occur which are not damped during the interaction time. Therefore the fraction of molecules residing in the electronic state after the pump laser pulse is over depends sensitively on the pulse area $\Omega_{P0}\Delta\tau$. In fact, it may range between zero and 100%. However if $\Omega_{P0}\Delta\tau \gg 1$, and pulse-to-pulse fluctuations are large enough, on the average 50% of the molecules will be in the excited state at the end of the pump pulse. Thus 50% of the molecules (rather than 100%) will radiatively decay, the fraction of molecules reaching the final state is again known and can be used for the calibration, as demonstrated in the recent work on SO_2 [5]. Here, we adopt a different approach. When the pump laser precedes the Stokes laser with no overlap between the two but the delay ΔT is still small compared to the radiative lifetime, molecules are first excited to the intermediate state by the pump laser and then transferred to the final state by stimulated emission pumping. If the pulse areas of both lasers are large enough and the signal is accumulated for a sufficiently large number of pulses, the pulse-to-pulse fluctuations will average over the Rabi oscillations and a known fraction of the molecules will be found in the final state.

For this experiment the collimation of the molecular beam is such that the residual Doppler width related to the motion perpendicular to the molecular beam axis is small compared to the laser linewidth. Therefore the detuning of the laser frequencies from their respective transition frequencies is the same for all the molecules in the beam and the consequences of the hyperfine splitting for the normalization procedure need to be carefully considered. In the Stimulated Emission Pumping (SEP) configuration ($\Delta T > 6$ ns, see Fig. 8), the molecules are excited to the intermediate level by a pump laser induced one-photon process, in which the hyperfine structure of the initial state is resolved, *i.e.* only the population of one hyperfine component is transferred to the intermediate state. Here we tune the pump laser frequency to the $F'' = 3/2$ level which carries 2/3 of the total population accessible for coherent population transfer. The fraction of 25% of that population, *i.e.* 16.7% of the total population of the initial $j'' = 1/2$ level, will be transferred to the final level in the SEP process. The STIRAP process will transfer the population of both levels $F'' = 1/2$ and $3/2$ since the Raman resonance for transitions out of these levels is the

same. Since the STIRAP signal exceeds that one obtained with SEP by a factor of 3.6, the transfer efficiency of the STIRAP process is 60%.

There are several possible causes which may have prevented us from reaching a transfer efficiency closer to unity than actually observed. We first mention two aspects which, at first glance, seem to contribute to the difficulties. Closer inspection shows, that they can't be the major cause of the problem:

- the line strength factors, see Table 3, vary by nearly one order of magnitude with m_F and at first glance it may seem that the mean Rabi frequency overestimates the value of $\Omega\Delta\tau$ for transfer out of same levels and thus non adiabatic coupling may have been stronger than expected. However, when the line strength factors are summed over the $F' = 1/2$ and $F' = 3/2$ levels in the upper state, which are not resolved, the effective linestrength factors are independent of m_F;
- the bandwidth of the laser were larger than measured when the data in the SEP regime was taken, transfer out of the $F = 1/2$ level would have been possible. The higher transfer efficiency in the SEP regime would increase the transfer efficiency in the STIRAP regime accordingly. We emphasize, however, that saturation broadening does not occur for excitation with coherent pulses, *i.e.* for radiation with transform limited bandwidth (see Append. C).

The lower than expected transfer efficiency could have been caused by the following:

- despite spatial filtering, the profile of the laser beams may have been less uniform than anticipated. This would locally lead to an effective Rabi frequency smaller than estimated;
- depending on the alignment of the Nd:YAG laser, the pump pulse could have been of asymmetric shape. If, for instance, the fall time is longer than the rise time, the ratio Ω_S/Ω_P would not approach zero as needed. Therefore, some of the population in the dark state would coherently return to the initial levels. On the other hand, for large negative delay (Stokes precedes pump, with no overlap expected), an asymmetric pulse shape would lead to a transfer signal which is larger than expected from pump laser induced fluorescence (Franck-Condon pumping). Such enhanced transfer is indeed observed for $\Delta T = -8$ ns, see Figure 8.

4 Population transfer in Doppler broadened media

Here we consider the feasibility of efficient population transfer in the bulk. We show that Doppler broadening is detrimental to the success of STIRAP when exciting high lying vibrational states of the NO molecule, but that it might be applied successfully in other cases with a small energy difference between initial and final levels.

We examined NO at a pressure of $p = 0.1$ mbar and at room temperature. For $T = 300$ K, we have $kT/\omega_c \approx 0.1$
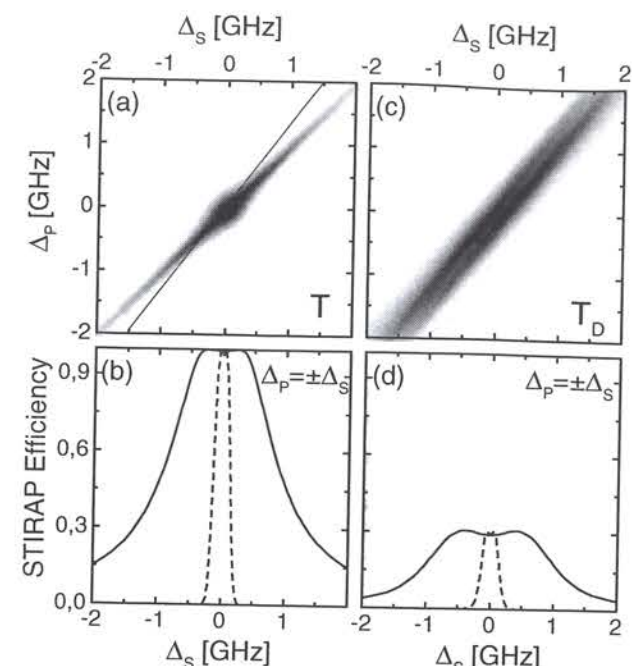
Fig. 9. Comparison of the results of numerical simulation studies of the transfer efficiency in the beam (T, shown in (a) and (b)) and in the bulk (T_D shown in (c) and (d)) for $\Omega_0\Delta\tau = 9$ and $\Delta\tau = 3$ ns. The cuts along the Raman resonance ($\Delta_P = \Delta_S$, solid lines, see also thin line in (a)) and perpendicular to it ($\Delta_P = -\Delta_S$, dashed lines) are also shown.

and only the vibrational state $v'' = 0$ of the electronic ground state $X^2\Pi$ carries significant population. There is, however, a broad rotational distribution with its maximum at $j'' = 10.5$. In the experiments we use $j'' = 5.5$.

4.1 Numerical results

The transfer efficiency $T_0(\Omega_P, \Omega_S, \Delta_P, \Delta_S)$ depends on the Rabi frequencies and the detunings. In a Doppler broadened medium, the effective detuning depends on the velocity component along the direction of the laser beam

$$\Delta_P^{eff} = \Delta_P + v/\lambda_P \qquad \Delta_S^{eff} = \Delta_S + v/\lambda_S. \qquad (4.1)$$

The overall transfer efficiency

$$T_D(\Delta_P, \Delta_S) = \int f(v)T_0(\Delta_P + v/\lambda_P, \Delta_S + v/\lambda_S)dv \qquad (4.2)$$

is obtained by integration over the velocity distribution

$$f(v)dv = \frac{1}{\bar{v}_x\sqrt{\pi}} e^{-(v/\bar{v}_x)^2} dv. \qquad (4.3)$$

Results are shown in Figure 9 for $\bar{v}_x = 408$ m/s, $\lambda_P = 226$ nm and $\lambda_S = 300$ nm, in comparison with those for a collimated molecular beam ($\bar{v}_x = 0$). Obviously, the Doppler broadening reduces the overall transfer efficiency
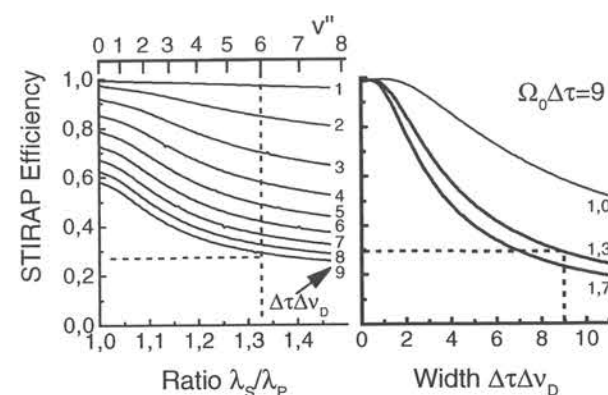
Fig. 10. Simulation of the STIRAP transfer efficiency in Doppler broadened media as a function of the ratio λ_S/λ_P and the product $\Delta\tau\Delta\nu_{Doppler}$. The relevant λ_S/λ_P ratios for the population of specific vibrational levels v'' in the NO molecule are indicated. Here we have $\lambda_P = 226$ nm and $v'' = 6$ is excited with $\Delta\tau\Delta\nu_{Doppler} = 9$, therefore a transfer efficiency of 29% is expected.

to less than 1/3 as compared to the beam results. It is, however, significantly higher than for SEP, see below.

For $\lambda_P = \lambda_S$, the two photon resonance is maintained independent of the detuning due to the Doppler shift. The integration (Eq. (4.2)) is then along the two photon resonance line (the diagonal in Fig. 9). With increasing velocity, the frequencies are detuned further from the resonance with the intermediate level, and a higher Rabi frequency is needed to guarantee adiabatic following.

For $\lambda_P \neq \lambda_S$, the Doppler broadening is significantly more detrimental, since the Doppler shift of the pump and Stokes laser is only partially compensated. With increasing velocity, the system will tune off the two photon resonance, and adiabatic following is no longer possible. The integration (Eq. (4.2)) is along a path which is tilted with respect to the diagonal, see Figure 9.

The dependence of the efficiency $T_D(\Delta_P = \Delta_S = 0)$ on the ratio λ_S/λ_P and the product $\Delta\tau\Delta\nu_{Doppler}$, where $\Delta\nu_{Doppler}$ is the Doppler width, is depicted in Figure 10. Almost complete inversion of a three level system can be achieved for $\lambda_S/\lambda_P \longrightarrow 1$ and/or for higher peak Rabi frequencies (not available for this experiment).

The STIRAP efficiency for excitation of $v'' = 6$ would increase to 85% when the product $\Delta\tau\Delta\nu_{Doppler}$ is reduced by a factor 5. This could be achieved either by cooling or by using shorter pulses. If the pulse length decreases the pulse energy must increase in order to maintain the pulse area.

4.2 Experimental results

The transfer efficiency T_D from $(v'' = 0, j'' = 5.5)$ to $(v'' = 6, j'' = 5.5)$ *via* $v' = 0$ in the A-state in the bulk is shown in Figure 11 as the time delay of the pulses is changed. The STIRAP signature is again clearly seen.

From the laser pulse energies ($E_P = 60\ \mu J$, $E_S = 300\ \mu J$) and the beam diameters ($D_P = D_S = 3$ mm), we estimate the Rabi frequencies to be

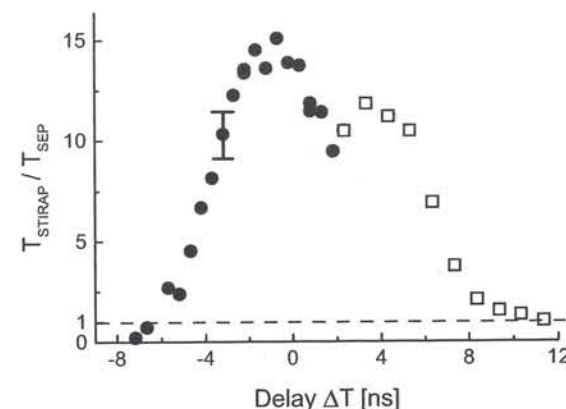**Fig. 11.** Experimentally determined ratio T_{STIRAP}/T_{SEP} of the population transfer efficiency T *in the bulk* as a function of the delay between the pulses (STIRAP-signature). Negative delay corresponds to the STIRAP configuration (Stokes pulse precedes the pump pulse) while positive delay relates to the SEP configuration (pump pulse precedes Stokes pulse). The results from two different runs are combined. The transfer observed at large positive delay is used to calibrate the absolute transfer efficiency.

$\Omega_{P0} = \Omega_{S0} = 2\pi\ 480$ MHz, averaged over the magnetic sublevels of NO.

Figure 11 shows a dramatic enhancement of the transfer efficiency in the STIRAP regime as compared to the SEP regime. This enhancement is significantly larger in the bulk than in the beam. In the bulk, only a small fraction of the molecules, essentially given by the ratio of the laser linewidth over the Doppler linewidth ($\approx 4.7\%$), participates in the SEP process (concerning the absence of power broadening in this experiment, see append. C). Since partial Doppler compensation occurs in the STIRAP process, a larger fraction of the molecules is addressed in this case.

Detection of the molecules in $v'' = 6$ is done by laser induced fluorescence. The bandwidth of the excimer laser pumped dye laser used in this case was large compared to the Doppler width. Therefore the detection efficiency is independent of the velocity of the molecules. The hyperfine splitting is more than one order of magnitude smaller than the Doppler width and can be neglected here. Therefore the SEP process reaches an efficiency of

$$E_{SEP} \approx 0.25 \times 4.7\% = 1.2\%. \qquad (4.4)$$

The transfer efficiency of the STIRAP process is 15 times larger than for SEP, *i.e.* $E_{STIRAP} = 18\%$. As in the beam experiments, this is only 60% of the value expected from the calculation.

5 Stokes laser induced absorption in a Doppler broadened medium

Pulse propagation effects in absorbing media have recently attracted much interest [36–39]. Harris and coworkers [40] as well as others (see *e.g.* [41]) demonstrated the phenomenon of Electromagnetically Induced Transparency
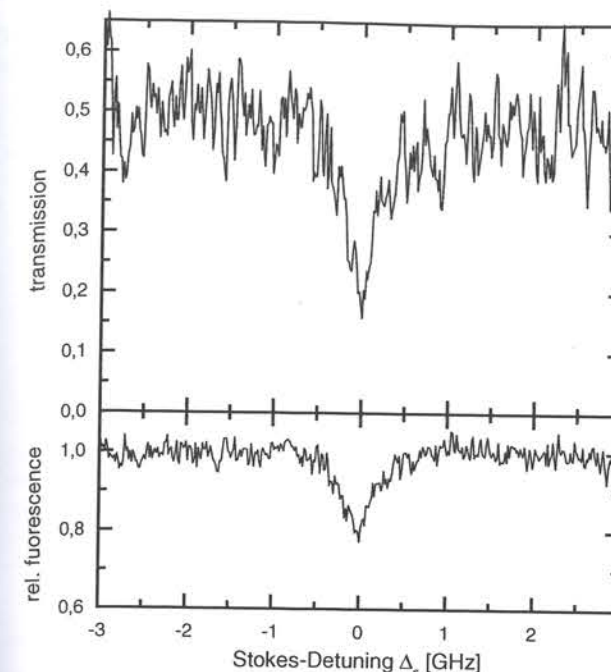
Fig. 12. Transmission of the pump pulse embedded in the Stokes pulse (*i.e.* zero delay), upper panel, and laser induced fluorescence from the intermediate level, lower panel, as a function of the Stokes laser detuning Δ_S. The pump laser was tuned to resonance $\Delta_P = 0$ while the Rabi frequencies were $\Omega_{P0} \approx 2\pi\ 140$ MHz and $\Omega_{S0} \approx 2\pi\ 370$ MHz.

(EIT) in lead vapor. In their experiment, strongly absorbing lead vapor was made transparent for pump laser radiation when its pulse envelope was embedded in the envelope of a powerful Stokes pulse. The Rabi frequency of the latter was $\Omega_S > 2\pi\ 160$ GHz and thus much larger than the Doppler width. Therefore a Doppler shift has only a negligible effect. Here we show that a related mechanism, which leads to EIT when $\Omega_S \gg \Delta\nu_D$, results in Electromagnetically Induced Absorption (EIA) when we have $\Omega_S \leq \Delta\nu_D$. The connection of EIT and STIRAP is discussed in some more detail in [42].

5.1 Experimental results

In the experiment, we observe the transmission of a pump laser pulse ($\Omega_P = 2\pi\ 140$ MHz) after propagation through a 300 mm long cell containing NO at $T = 300$ K. A pressure of 0.4 mbar was chosen to adjust the absorption of the pump pulse resonant with the $Q_1(5.5)$ line of the $\gamma(0,0)$ band to 50%.

We compare the absorption of the pump laser pulse ($\Delta\tau_P = 2.7$ ns) with and without copropagating Stokes laser pulse ($\Delta\tau_S = 3.1$ ns, $\Omega_S = 2\pi\ 370$ MHz, no time delay). Figure 12 shows the transmission of the pump laser as the Stokes laser frequency is tuned. On two photon resonance, the transmission drops from 50% to about 15%. This confirms that the pump laser pulse is indeed more strongly absorbed when embedded in a copropagating resonant Stokes laser pulse. In parallel, we also observe a
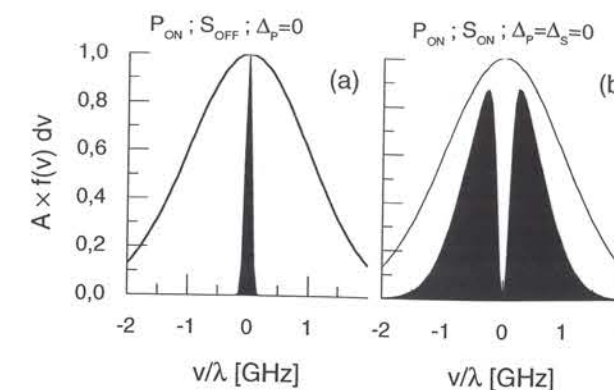
Fig. 13. Velocity distribution of the molecules in the cell (solid lines). The fraction of molecules contributing to absorption is shaded, with the pump laser alone (tuned to resonance) and the pump laser together with the Stokes laser (tuned to the Raman resonance) are shown on the left and right side, respectively. With the Stokes laser present, molecules with $v \approx 0$ do not absorb the pump laser radiation anymore (EIT). However, otherwise inactive molecules in a large range of velocities $|v| > 0$ may contribute (EIA). The net result is a significantly enhanced absorption.

significant reduction of the fluorescence from the intermediate level about half way along the absorption path. This signifies that the absorption due to resonant one photon excitations of the intermediate level is reduced, whereas the enhanced overall absorption must be a result of two photon processes, *i.e.* Raman excitations to $v'' = 6$.

5.2 Induced transparency *vs.* absorption

Figure 13a shows the range of velocity which leads to a Dopplershift of no more than the laser bandwidth. These molecules (a fraction of about 5%) contribute to the absorption. With the Stokes laser present and tuned to resonance, pump laser radiation can not be absorbed by molecules with $v \approx 0$. This group of molecules experiences electromagnetically induced transparency, like in the experiments by Harris. In those experiments, the range over which absorption is eliminated is of the order of 150 GHz and thus covers all of the Doppler width. In our experiments, however, the Rabi frequency is of the order of the Doppler width and molecules in a large range of velocities are tuned, because of their Doppler shifted frequencies, into resonance with the components of the Stark doublet (the fraction of molecules is shown in Fig. 13b). The net effect is a strongly enhanced absorption.

In order to observe the EIA process discussed here, one typically needs a medium with an initial transmission of about 50% which can be reduced to a much smaller value when the Stokes laser pulse is present.

It is interesting to see, that it is the magnitude of $\Omega_S/\Delta\nu_D$ which controls the consequences of the presence of the Stokes laser; EIT is observed for $\Omega_S/\Delta\nu_D \gg 1$, while $\Omega_S/\Delta\nu_D \leq 1$ leads to EIA. Obviously, there is a value of $\Omega_S/\Delta\nu_D$ for which the Stokes laser has no effect on the transmission of the pump laser.
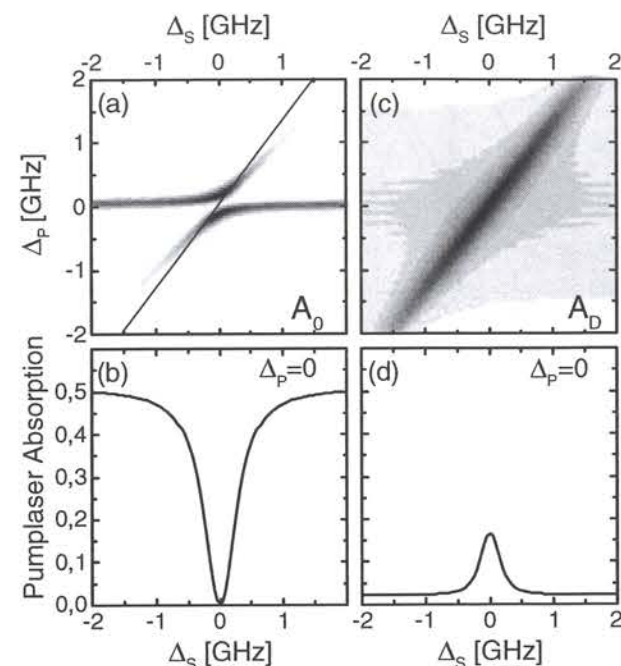
Fig. 14. Comparison of the pump laser absorption under the influence of the Stokes laser in the beam (A_0 shown in (a)) and in the bulk (A_D shown in (c)). The lower panels show the absorption for $\Delta_P = 0$ as a function of Δ_S. In the beam ((b), no Doppler broadening), the absorption vanishes at the Raman resonance. In the bulk ((d), Doppler broadening), the absorption reaches a maximum when $\Delta_P = \Delta_S = 0$. The integration path used to determine $A_D(\Delta_P = \Delta_S = 0)$ is indicated in (a).

In Figure 14, the pump laser absorption without Doppler broadening (left hand side) is compared to the absorption of a Doppler broadened medium (right hand side) as a function of pump- and Stokes laser detuning. The parameters for the numerical simulation correspond to the experimental conditions (see section 5.1). It is seen that the absorption drops to zero without Doppler broadening but raises up to 16% in the Doppler broadened medium. Due to the dynamic Stark shift, the peaks of the absorbing Stark doublet are shifted towards the Raman resonance line $\Delta_P = \Delta_S$. The path of the Doppler integral, indicated in Figure 14a, runs almost parallel to this line, thus increasing the number of molecules participating in the absorption process. The ratio λ_S/λ_P determines the direction of the integration path and controls the relative contribution of EIT and EIA. For the parameters used here, the medium becomes transparent for $\lambda_S/\lambda_P \leq 0.7$.

6 Summary and conclusion

We have expanded our previous studies of coherent population transfer to a vibrationally excited level of the NO molecule. In particular we have analyzed the consequences of hyperfine splitting and Doppler broadening for the transfer efficiency.

In previous STIRAP studies, the initial level consisted of a single quantum state or of a group of degenerate sub-

levels. Here we transfer simultaneously population from two groups of non-degenerate levels to two such groups in the vibrationally excited state. Since the hyperfine splitting is larger than the bandwidth of the laser and both radiation fields are linearly polarized parallel to each other, complications, such as demonstrated and analyzed by Martin *et al.* [27], do not occur. We have also discussed, in some detail, the normalization procedure needed to determine the absolute transfer efficiency. A discrepancy between the expected and observed efficiencies is found, the reason for which has not yet been identified unambiguously.

We have also studied population transfer in the bulk with a Rabi frequency Ω_0 smaller than the Doppler width $\Delta\nu_D$. The STIRAP transfer efficiency is more than an order of magnitude larger than that obtained by Stimulated Emission Pumping (SEP), since a partial compensation of the Doppler shift occurs in the coherent two photon process, allowing a larger fraction of molecules to participate in the transfer.

Finally we considered the effect of a Stokes laser pulse copropagating with a pump laser pulse in a weakly absorbing medium. While the phenomena of Electromagnetically Induced Transparency (EIT) is observed when $\Omega_S \gg \Delta\nu_D$, we observe an enhanced absorption (EIA), since $\Omega_S \leq \Delta\nu_D$, since the number of molecules which are able to absorb a photon increases due to the Stark shift and splitting at resonance. Thus, the EIT or the EIA phenomena could be used to open or close, respectively, a light path in a laser controlled optical gate.

Appendix A: Rabi frequencies

The population of a two level system exposed to coherent, resonant radiation oscillates between the levels with the Rabi frequency $\Omega = \mu \cdot E/\hbar$, where E is the amplitude of the radiation field. Evaluation of the dipole matrix element μ is a non trivial task because of the large manifold of rotational sublevels and the mixtures of Hunds cases a and b in the $X^2\Pi$ state of NO. Therefore, we compile the necessary information in this appendix.

A.1 Dipole moments of NO

The coupling schemes in the A and X states of NO are different. This leads to different sets of quantum numbers, (v', j', m', k') and (v'', j'', m'', Ω) respectively, which specify the rovibronic substates. The parity splitting in the X state and the hyperfine splitting are not considered in equations (A.1 and A.2). The squared dipole moment of

Table 1. Hönl-London factors and dipole matrix elements for the various pump and Stokes transitions of the NO $\gamma(0,0)$ and $\gamma(0,6)$ bands, assuming linear polarization ($\Delta m = 0$) for $j'' = 1/2$ and $j'' = 3/2$.

j''	Transition	Line	HLF	$\mu_{0,0}[10^{-31}$ Asm] $\pm 1/2$	$\pm 3/2$	$\mu_{0,6}[10^{-31}$ Asm] $\pm 1/2$	$\pm 3/2$	$\leftarrow m''$
1/2	$^2\Sigma^+$	Q_1	0.667	2.135	–	0.968	–	
		Q_{21}	0.667	2.135	–	0.968	–	
	$\updownarrow$	R_1	0.333	1.510	–	0.684	–	
	$^2\Pi_{1/2}$	R_{21}	0.333	1.510	–	0.684	–	
3/2	$^2\Sigma^+$	P_1	0.362	1.573	–	0.713	–	
		P_{21}	0.306	1.447	–	0.656	–	
	$\updownarrow$	Q_1	1.112	0.872	2.616	0.395	1.186	
	$^2\Pi_{1/2}$	Q_{21}	1.022	0.836	2.508	0.379	1.137	
		R_1	0.616	1.590	1.298	0.721	0.588	
		R_{21}	0.582	1.545	1.262	0.701	0.572	
	$^2\Sigma^+$	P_{12}	0.972	2.578	–	1.169	–	
		P_2	1.028	2.652	–	1.202	–	
	$\updownarrow$	Q_{12}	0.756	0.719	2.157	0.326	0.978	
	$^2\Pi_{3/2}$	Q_2	0.846	0.761	2.282	0.345	1.034	
		R_{12}	0.184	0.869	0.709	0.394	0.322	
		R_2	0.218	0.946	0.772	0.429	0.350	

a specific A $\longrightarrow$ X transition reads [43]

$$\begin{aligned}
\mu^2 &= |\langle A, v', j', m', k'|d_q|X, v'', j'', m'', \Omega\rangle|^2 \\
&= \mu_{el}^2 \, \text{FCF}_{v'v''} \, |\langle j', m', k'|d_q|j'', m'', \Omega\rangle|^2 \\
&= \mu_{el}^2 \, \text{FCF}_{v'v''} \begin{pmatrix} j' & 1 & j'' \\ m' & -\Delta m & m'' \end{pmatrix}^2 |\langle j', k'|d_q|j'', \Omega\rangle|^2,
\end{aligned} \quad (A.1)$$

where d_q is the dipole operator ($q = 0$ for excitation with linearly polarized light) and $|\langle j', k'|d_q|j'', \Omega\rangle|^2$ is equivalent to the Hönl-London Factor (HLF).

The Einstein coefficients $A_{v'v''}$ for individual vibrational transitions $v'' \longrightarrow v'$, needed to determine the electronic and vibrational contribution to the dipole moment μ, are known [44]

$$\mu_{vib}(v'; v'') = \mu_{el}\sqrt{FCF_{v'v''}} = \sqrt{\frac{A_{v'v''}3h\varepsilon_0\lambda^3}{16\pi^3}}. \quad (A.2)$$

The algorithm to calculate the HLF for a mixed coupling scheme is given in [45]. It relies on the ratio γ of spin-orbit coupling coefficient A to the rotational constant B. With A and B from [46] using the fact that B is only weakly dependent on v'', we use here an average value of $\gamma = 74.5$.

The renormalized Hönl-London factors for the $^2\Sigma^+ \longrightarrow {}^2\Pi_{1/2}$ transitions with $j'' = 1/2$ and $j'' = 3/2$ are given explicitly in Table 1. Using the Einstein coefficients from [44]

$$A_{0,0} = 1.002 \times 10^6 \, \text{s}^{-1} \longrightarrow \mu_{0,0} = 6.406 \times 10^{-31} \, \text{Asm}$$

$$A_{0,6} = 8.801 \times 10^4 \, \text{s}^{-1} \longrightarrow \mu_{0,6} = 2.904 \times 10^{-31} \, \text{Asm}$$

and linear polarized light ($\Delta m = 0$), the dipole matrix elements of the NO $\gamma(0,0)$ and $\gamma(0,6)$ bands were calculated and are also given in Table 1.

Table 2. Rabi frequencies of the pump- and Stokes transitions for several pulse energies W with $R = 1.5$ mm beam radius and pulse duration $\Delta\tau = 3$ ns. Ω_P and Ω_S are scaling with $\Omega^0 \sqrt{W[\mu J]}$ where $\Omega_P^0 = 2\pi \, 54.2$ MHz and $\Omega_S^0 = 2\pi \, 24.7$ MHz.

$W[\mu J]$	$\Omega_P/2\pi$ [MHz]	$\Omega_S/2\pi$ [MHz]
1	54.2	24.7
5	121	55
10	172	78
50	383	174
100	542	247

A.2 Laser fieldstrengths

Assuming laser pulses of gaussian envelope $E(t) = E_0 \exp(-(t/\Delta\tau)^2)$, an homogeneous intensity distribution within a circular area of radius R and a pulse energy W, the electric field amplitude E_0 at the center of the pulse is given by

$$E_0 = \sqrt{\frac{W \, 2\sqrt{2}}{\pi^{3/2} R^2 c \varepsilon_0 \Delta\tau}}. \quad (A.3)$$

Typical Rabi frequencies for the pump- and Stokes transitions ($j'' = 1/2$) ($^2\Pi_{1/2}(v'' = 0) \longrightarrow {}^2\Sigma^+(v' = 0)$ with $\mu = 2.135 \times 10^{-31}$ Asm, and $^2\Sigma^+(v' = 0) \longrightarrow {}^2\Pi_{1/2}(v'' = 6)$ with $\mu = 0.968 \times 10^{-31}$ Asm, respectively) are given in Table 2. The Stokes pulse energy needs to be a factor of five larger than the corresponding pump pulse energy to equalize both Rabi frequencies.

Appendix B: Relative transition strengths

For a full treatment the consequences of hyperfine splitting need to be considered. We determine the dipole moments for transitions between levels in the X-state with quantum

$$H_6 = -\frac{\hbar}{2} \begin{pmatrix} -2\Delta_P + \Delta_A & 0 & \frac{1}{3}\Omega_P & \sqrt{8/9}\Omega_P & 0 & 0 \\ 0 & -2\Delta_P - \Delta_A & \sqrt{8/9}\Omega_P & \frac{1}{3}\Omega_P & 0 & 0 \\ \frac{1}{3}\Omega_P & \sqrt{8/9}\Omega_P & \Delta_B & 0 & \frac{1}{3}\Omega_S & \sqrt{8/9}\Omega_S \\ \sqrt{8/9}\Omega_P & \frac{1}{3}\Omega_P & 0 & -\Delta_B & \sqrt{8/9}\Omega_S & \frac{1}{3}\Omega_S \\ 0 & 0 & \frac{1}{3}\Omega_S & \sqrt{8/9}\Omega_S & -2\Delta_S + \Delta_C & 0 \\ 0 & 0 & \sqrt{8/9}\Omega_S & \frac{1}{3}\Omega_S & 0 & -2\Delta_S - \Delta_C \end{pmatrix} \quad (B.4)$$

Table 3. Relative transition strengths S_q in units of $|\langle j', k'|d|j'', \Omega\rangle|^2$ for linear polarization $q = 0$ (see Eq. (B.1 and B.2)) with $j'' = j' = 1/2$ and $I = 1$.

| | | X | | | | F''=1/2 | |
		F''=3/2					
A	M_F	3/2	1/2	-1/2	-3/2	1/2	-1/2
	3/2	9/54	-	-	-	-	-
F'=	1/2	-	1/54	-	-	8/54	-
3/2	-1/2	-	-	1/54	-	-	8/54
	-3/2	-	-	-	9/54	-	-
F'=	1/2	-	8/54	-	-	1/54	-
1/2	-1/2	-	-	8/54	-	-	1/54

numbers $(v'', \Omega, I, j'', F'', M_F'')$ and the A–state with quantum numbers $(v', k', I, j', F', M_F')$. The electronic and vibrational contributions may be separated according to ([22], Chap. 21)

$$\mu_{dip} = \mu_{el}\sqrt{FCF(v',v'')} \quad (B.1)$$
$$\times \langle k',I,j',F',M_F'|d_q|\Omega,I,j'',F'',M_F''\rangle$$
$$= \mu_{el}\sqrt{FCF(v',v'')}\, HLF(j',k',j'',\Omega)$$
$$\times (-1)^{j''+I+2F'-M_F'+1} \times \begin{pmatrix} F' & 1 & F'' \\ -M_F' & \Delta M & M_F'' \end{pmatrix}$$
$$\times \sqrt{(2F''+1)(2F'+1)} \times \begin{Bmatrix} j' & 1 & F' \\ F'' & I & j'' \end{Bmatrix}.$$

The ratios of the relative transition strength factors

$$S_q = |\langle k',I,j',F',M_F'|d_q|\Omega,I,j'',F'',M_F''\rangle|^2 \quad (B.2)$$

to the Hönl-London factors $HLF(j',k',j'',\Omega)$, calculated from equation (B.1), are given in Table 3. With these relations the Hamiltonians in equations (2.1 and 2.2) read explicitly

$$H_3 = -\frac{\hbar}{2} \begin{pmatrix} -2\Delta_P - \Delta_A & \Omega_P & 0 \\ \Omega_P & -\Delta_B & \Omega_S \\ 0 & \Omega_S & -2\Delta_S - \Delta_C \end{pmatrix} \quad (B.3)$$

and see equation (B.4) *above*

where the coupling strength is given with reference to the Rabi frequencies in the three–state system, $\Omega_{12} = \Omega_P$ and $\Omega_{32} = \Omega_S$.

Appendix C: Coherent population return

The dynamics of the interaction of coherent radiation with a two level system is well known [22]. Here, we explain

why a strong pulse of coherent radiation with smooth envelope does not lead to substantial saturation broadening. The understanding of this phenomenon is important for the normalization procedure of the transfer efficiency in a three level system.

Pulsed laser excitation with large pulse area and an interaction time much shorter than the lifetime of the excited state leads to Rabi oscillations. Figure 15 shows the population of the upper state after the interaction with a gaussian pulse or a pulse with a rectangular shape, both of them having the pulse area $\int \Omega(t)dt = \sqrt{\pi}\Omega_{12}\Delta\tau$. The half width at $1/e$ with respect to the maximum of the former is $\Delta\tau$, while the duration of the latter is $\sqrt{\pi}\Delta\tau$. For on resonance tuning ($\Delta = 0$), the variation of the excitation probability is the same for both pulses. However, for $\Delta \neq 0$ the excitation dynamics is dramatically different. While substantial saturation broadening is observed for excitation with a pulse of rectangular shape, such broadening is not observed for a gaussian pulse.

The eigenstates of the Hamiltonian of the system

$$\hat{H}' = -\frac{\hbar}{2} \begin{pmatrix} -\Delta & \Omega(t) \\ \Omega^*(t) & \Delta \end{pmatrix} \quad (C.1)$$

are written in the basis of the bare states $|1\rangle$ and $|2\rangle$

$$|a^+\rangle = \cos\Theta|1\rangle - \sin\Theta|2\rangle \qquad |a^-\rangle = \sin\Theta|1\rangle + \cos\Theta|2\rangle \quad (C.2)$$

where

$$\tan\Theta = \frac{\Omega}{\sqrt{\Omega^2+\Delta^2}+\Delta} = \frac{\sqrt{\Omega^2+\Delta^2}-\Delta}{\Omega} \quad (C.3)$$

and the corresponding eigenvalues are

$$\omega^\pm = \pm\frac{1}{2}\sqrt{\Omega^2+\Delta^2}.$$

For $\Delta \neq 0$, we have $\tan\Theta = 0$ at very early and very late times ($\Omega(t) \ll |\Delta|$). Therefore $|\langle a^+|1\rangle| = 1$ at early and late times and no population remains in state $|2\rangle$ at the end of the pulse, provided the evolution is adiabatic, i.e. $|\dot{\Theta}| \ll |\omega^\pm|$. This phenomenon is known as "Complete Population Return" (CPR) [47]. For Gaussian pulses, the condition for adiabatic evolution is well satisfied and only little population is transferred from the initially populated state $|a^+\rangle$ to the state $|a^-\rangle$. Some of the population which reaches the latter will be in state $|2\rangle$ at the end of the interaction. For a Gaussian pulse excitation will only be observed for $\Delta < 1/\Delta\tau$.
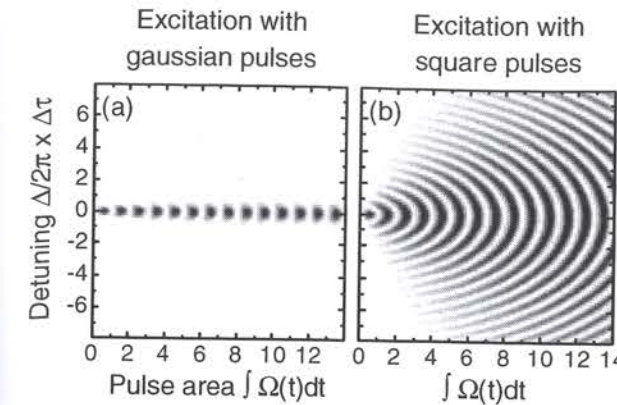
Fig. 15. Comparison of the excited state population in a two level system for gaussian pulses (a) and square pulses (b) of same pulse areas (square pulse duration $\sqrt{\pi}\Delta\tau$), as a function of the Rabi frequency Ω_{12} and laser detuning Δ_{12}.

The sudden increase of the Rabi frequency in case of the rectangular pulse leads to strong nonadiabatic coupling of the states $|a^+\rangle$ and $|a^-\rangle$ at the beginning and the end of the interaction. In the beginning the angle Θ increases suddenly to a value determined by the Rabi frequencies and the population in $|1\rangle$ is distributed accordingly to the dressed $|a^+\rangle$ and $|a^-\rangle$ states. At the end, the phase relation $\omega^+ t$ between the dressed states determines how the population projects back onto the bare states. Averaging over this relative phase, the final population in the upper state

$$\overline{|\langle 2|\Psi(t>0)\rangle|^2} = 2\sin^2\phi\,\cos^2\phi\,\overline{\sin^2(\omega^+t)} \quad (C.4)$$
$$= \frac{\Omega^2}{2(\Omega^2+\Delta^2)},$$

shows the expected Lorentzian line profile with full width at half maximum $\Delta_{FWHM} = \Omega$.

Appendix D: Dependence on the pulse shape

The envelope $E(t)$ of laser pulses often derivates from a gaussian shape. Here we examine the detrimental effect of asymmetry of the pulse shape. Such an asymmetry could be caused by a slow decay of the inversion in the Nd:YAG rod or nonlinear effects in the pulse amplifiers or the doubling crystals. Also Nd:YAG lasers with an internal phase conjugate mirror exhibit an intrinsic asymmetric pulse with a fast rise time and a slow decay.

For the purpose of demonstration, we assume the asymmetric pulse shape shown in Figure 16. The tails prevent the increase of the mixing angle to $\Theta = 90°$ as needed for complete transfer. Figure 16 shows the simulated time evolution of the population due to such pulses. Although at $t \approx 3$ ns, the population is transferred almost completely to the final level, a large fraction of it returns to the initial state. Furthermore, we note that the small
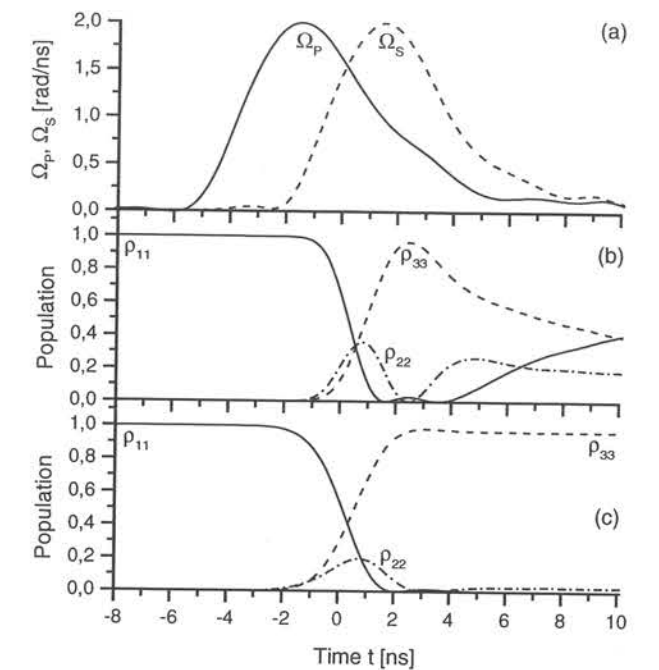
Fig. 16. Comparison of the population evolution (b) during the STIRAP excitation using a pulse envelope with tails (a) to the evolution using gaussian shaped pulses (c). The maxima of the Rabi frequencies $\Omega_{S,P}^0 = 2\pi$ 320 MHz were chosen to fit the measured two photon linewidths.

Rabi frequencies in the tail do not assure adiabatic following and some population is lost by non-adiabatic coupling.

It is interesting to note that the determination of a pulse shape for most efficient transfer by the optimal control theory [48] leads to asymmetric forms. However, the optimal shape of the Stokes laser shows a slower rise and a faster fall, while the optimal shape of the pump laser is one with a faster rise and a slower fall.

References

1. K. Bergmann, B.W. Shore, in *Molecular Dynamics and Spectroscopy by Stimulated Emission Pumping*, edited by H.L. Dai and R.W. Field (World Scientific, Singapore, 1995) pp. 315–373.
2. J.R. Kuklinski, U. Gaubatz, F.T. Hioe, K. Bergmann, Phys. Rev. A **40**, 6741–6744 (1989); U. Gaubatz, P. Rudecki, S. Schiemann, K. Bergmann, J. Chem. Phys. **92**, 5363–5376 (1990).
3. A. Kuhn, G.W. Coulston, G.Z. He, S. Schiemann, K. Bergmann, W.S. Warren, J. Chem. Phys. **96**, 4215–4223 (1992).
4. S. Schiemann, A. Kuhn, S. Steuerwald, K. Bergmann, Phys. Rev. Lett. **71**, 3637–3640 (1993).
5. T. Halfmann, K.Bergmann, J. Chem. Phys. **104**, 7068–7072 (1996).
6. P. Marte, P. Zoller, J.L. Hall, Phys. Rev. A **44**, R4118–4121 (1991).
7. L.S. Goldner, C. Gerz, R.J. Spreeuw, S.L. Rolston, C.I. Westbrook, W.D. Phillips, P. Marte, P. Zoller, Phys. Rev. Lett. **72**, 997–1000 (1994).

8. J. Lawall, M. Prentiss, Phys. Rev. Lett. **72**, 993–996 (1994).

9. M. Weitz, B.C. Young, S. Chu, Phys. Rev. Lett. **73**, 2563–2566 (1994).

10. P.D. Featonby, G.S. Summy, J.L. Martin, H. Wu, K.P. Zerie, C.J. Foot, K. Burnett, Phys. Rev. **A 53**, 373 (1996).

11. J. Lawall, F. Bardou, B. Saubamea, K. Shimizu, M. Leduc, A. Aspect, C. Cohen–Tannoudji, Phys. Rev. Lett. **73**, 1915–1918 (1994); J. Lawall, S. Kulin, B. Saubamea, N. Bigelow, M. Leduc, C. Cohen–Tannoudji, *Proceeding of the 4th Intl. Workshop on Laser Physics* (Moscow, August 1995); Laser Physics **6**, 153–158 (1996).

12. T. Esslinger, F. Sander, M. Weidemüller, A. Hemmerich, T.W. Hänsch, Phys. Rev. Lett. **76**, 2432 (1996).

13. A. Kuhn, H. Perrin, W. Hänsel, C. Salomon, OSA TOPS on Ultracold Atoms and BEC, Vol.7, edited by K. Burnett, 58–65 (1996); S. Kulin, B. Saubamea, E. Peik, J. Lawall, T.W. Hijmans, M. Leduc, C. Cohen–Tannoudji, Phys. Rev. Lett. **78**, 4185 (1997).

14. R. Walser, J.I. Cirac, P. Zoller, Phys. Rev. Lett. **77**, 2658 (1996).

15. P. Dittmann, F.P. Pesl, J. Martin, G.W. Coulston, G.Z. He, K. Bergmann, J. Chem. Phys. **97**, 9472–9475 (1992).

16. M. Külz, M. Keil, A. Kortyna, B. Schellhaaß, J. Hauck, K. Bergmann, D. Weyh, W. Meyer, Phys. Rev. **A 53**, 3324–3334 (1996).

17. R. Sussmann, R. Neuhauser, H.J. Neusser, J. Chem. Phys **100**, 4784–4789 (1994); R. Sussmann, R. Neuhauser, H.J. Neusser, J. Chem. Phys. **103**, 3315 (1995); R. Neuhauser, R. Sussmann, H.J. Neusser, Phys. Rev. Lett. **74**, 3141–3144 (1995).

18. J. Oreg, F.T. Hioe, J.H. Eberly, Phys. Rev. A **29**, 690–697 (1984).

19. M.P. Fewell, B.W. Shore, K. Bergmann, Austr. J. Phys. **50**, 281–308 (1997).

20. G. Alzetta, A. Gozzini, L. Moi, G. Orriols, Nuovo Cimento **B36**, 5 (1976); E. Arimondo, G. Orriols, Lett. Nouv. Cim. **17**, 333 (1976).

21. S. Stenholm, *Foundations of Laser Spectroscopy* (J. Wiley&Sons, NY 1984).

22. B.W. Shore, *The theory of coherent atomic excitation* (J. Wiley& Sons, NY 1990).

23. G.W. Coulston, K. Bergmann, J. Chem. Phys. **96**, 3467–3475 (1992).

24. A. Vardi, M. Shapiro, J. Chem. Phys. **104**, 5490–5496 (1996).

25. B.W. Shore, J. Martin, M. Fewell, K. Bergmann, Phys. Rev. **A 52**, 566–582 (1995).

26. J. Martin, B.W. Shore, K. Bergmann, Phys. Rev. **A 52**, 583–593 (1995).

27. J. Martin, B.W. Shore, K. Bergmann, Phys. Rev. **A 54**, 1556–1569 (1996).

28. C.E. Carroll, F.T. Hioe, J. Phys. **A19**, 2061–2073 (1986); B.W. Shore, K. Bergmann, J. Oreg, Z. Phys. **D 23**, 33–39 (1992); M.V. Danileiko, V.I. Romanenko, L.P.Yatsenko, Opt. Comm. **109**, 462–466 (1994).

29. E. Hill, J.H. van Vleck, Phys. Rev. **32**, 250–272 (1928).

30. R.S. Mulliken, Rev. Mod. Phys. **3**, 89–115 (1931).

31. R. de Vivie, S.D. Peyerimhoff, J. Chem. Phys. **90**, 3660–3670 (1989).

32. X. Yang, E.H. Kim, A.M. Wodtke, J. Chem. Phys. **96**, 5111 (1992).

33. F.A. Blum, K.W. Nill, A.R. Calwa, T.C. Harman, Chem. Phys. Lett. **15**, 144–146 (1972); D. Feller, E.D. Glendening, E.A. McCullough Jr., R.J. Miller, J. Chem. Phys. **99**, 2829–2839 (1993).

34. T. Bergeman, R.N. Zare, J. Chem. Phys. **61**, 4500–4514 (1974); R.J. Miller, W.L. Glab, B.A. Bushaw, J. Chem. Phys. **91**, 3277–3279 (1989).

35. U. Fano, Phys. Rev. **124**, 1866–1878 (1961).

36. S.E. Harris, J.E. Field, A. Imamoğlu, Phys. Rev. Lett. **64**, 1107–1110 (1990); S.E. Harris, Phys. Rev. Lett. **70**, 552–555 (1993); S.E. Harris, Phys. Rev. Lett. **72**, 52–55 (1994); S.E. Harris, J.J. Macklin, Phys. Rev. **A 40**, 4135–4137.

37. J.H. Eberly, M.L. Pons, H.R. Haq, Phys. Rev. Lett. **72**, 56–59 (1994).

38. M. Fleischhauer, Phys. Rev. Lett. **72**, 989–992 (1994).

39. F.T. Hioe, R. Grobe, Phys. Rev. Lett. **73**, 2559–2562 (1994); R. Grobe, F.T. Hioe, J.H. Eberly, Phys. Rev. Lett. **73**, 3183–3186 (1994); A. Kasapi, M. Jain, G.Y. Yin, S.E. Harris, Phys. Rev. Lett. **74**, 2447–2450 (1995).

40. K.J. Boller, A. Imamoğlu, S.E. Harris, Phys. Rev. Lett. **66**, 2593–2596 (1991); J.E. Field, K.H. Hahn, S.E. Harris, Phys. Rev. Lett. **67**, 3062–3065 (1991).

41. Yong-qing Li, Shao-zheng Jin, Min Xiao, Phys. Rev. A **51**, R1754–1757 (1995).

42. K. Bergmann, H. Theuer, B.W. Shore, Rev. Mod. Phys. (submitted).

43. C. Cohen–Tannoudji, B. Diu, F. Laloë, *Quantum mechanics*, Vol. 2, Chap. 10 (Hermann, Paris and J.Wiley&Sons, NY 1977).

44. L.G. Piper, L.M. Cowles, J. Chem. Phys. **85**, 2419–2422 (1986).

45. L.T. Earls, Phys. Rev. **48**, 423–424 (1935).

46. R. Engleman Jr., P.E. Rouse, J. Molec. Spectr. **37**, 240 (1971); R. Engleman Jr., P.E. Rouse, H.M. Peek, V.D. Baiamonte, Los Alamos Scientific Lab. Report LA–4364 UC–34 physics TID–4500, July 1970.

47. N.V. Vitanov, J. Phys. B **28**, L19–L22 (1995); N.V. Vitanov, P.L. Knight, J. Phys. B **28**, 1905–1920 (1995).

48. V. Malinovsky, D. Tannor, Phys. Rev. A (in press).

Sideband cooling of neutral atoms in a far-detuned optical lattice

H. Perrin, A. Kuhn(*), I. Bouchoule and C. Salomon

Laboratoire Kastler Brossel, École Normale Supérieure
24 rue Lhomond, 75231 Paris Cedex 05, France

Abstract. – Sideband laser cooling using stimulated Raman transitions is performed on trapped cesium atoms. The confinement is produced by a far–off-resonance dipole trap consisting of two crossed YAG beams which, by interference, create a one-dimensional optical lattice. In a pure intensity lattice, we measure a 1D temperature of $T = 6$ µK corresponding to a mean quantum vibrational number of about $\langle n_v \rangle = 0.75$. In a polarization gradient lattice, the final temperature is $T = 3.6$ µK corresponding to $\langle n_v \rangle \simeq 2.4$.

Sideband laser cooling has become a very efficient method to prepare ions in the vibrational ground state $v = 0$ of a harmonic trap of frequency ω_v [1]-[4]. The resolved sideband regime is obtained when the width of the excited state of the two-level system is much smaller than ω_v. This condition is conveniently fulfilled when using Raman transitions between two long-lived states [5]. In the Lamb-Dicke regime, the rms size of the fundamental vibrational state Δx is much smaller than $\lambda/2\pi$, where λ is the wavelength of the cooling transition. In this regime a two-level ion excited from the n_v vibrational level in the ground state to $n_v - 1$ in the excited state decays mostly into $n_v - 1$ in the ground state. Using this method, Monroe *et al.* [4] prepared an ion in the ground state of a three-dimensional trap 92% of the time. The ability to prepare ions in this pure, minimum uncertainty, quantum state has enabled spectacular advances such as the preparation of Fock states or Schrödinger cat states [6].

In the case of neutral atoms, it is much more difficult to realize a single potential well satisfying the Lamb-Dicke condition. However, this condition can be fulfilled using optical lattices [7]. Sisyphus cooling has long been studied in nearly resonant lattices and atoms have been cooled in three dimensions to a mean vibrational number $\langle n_v \rangle = 1/(e^{\hbar\omega_v/k_B T} - 1) \sim 1$ [8]. In such a case cooling and trapping are intimately coupled as the same lasers are responsible for both. Selection of atoms in $n_v = 0$ has recently been performed in a 3D far detuned lattice [9].

(*) Present address: Fakultät für Physik der Universität Konstanz, Germany.
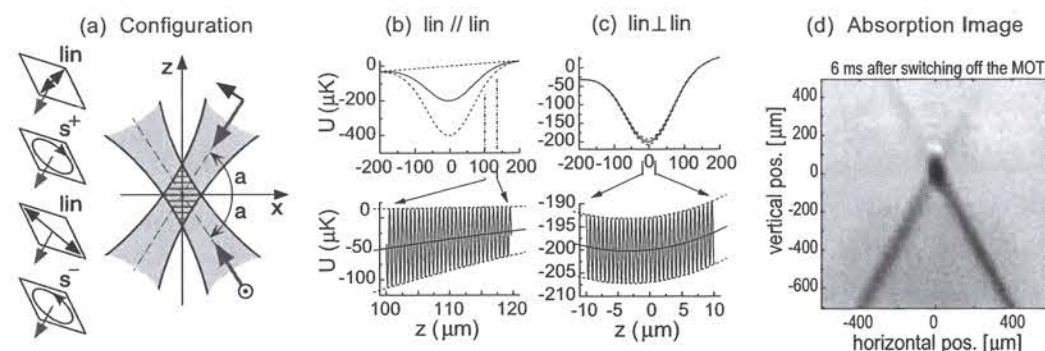
Fig. 1. – Configuration of the dipole trap beams and the resulting polarization with respect to the quantization axis aligned along the down-going YAG beam in the lin $\perp$ lin case (a). The period of this modulation is $\lambda/(2\sin\alpha) = 665$ nm. Trap potential for parallel polarizations of the YAG beams (b), and orthogonal polarizations (c), displayed for $m = 3$. In (b) the potential is independent of the magnetic sublevel. (d) Absorption picture of the trap 10 ms after loading from a MOT in the lin $\perp$ lin case. Untrapped atoms fall along the YAG beams whereas atoms in the intersection volume of both beams remain trapped for up to 1-2 seconds.

In this letter we demonstrate efficient sideband cooling of cesium atoms in a 1D far–off-resonance lattice. We use stimulated Raman transitions between the two hyperfine ground states, which act as an effective two-level system with a narrow width [5], [10]. In contrast to near-resonance Sisyphus cooling, the dissipation induced by the lattice beams is totally negligible. Vibrational sidebands are resolved and co-propagating Raman beams with frequency difference tuned to the red sideband are used to induce Doppler-insensitive transitions to extract energy from the system. Cooling is performed by a sequence of pulses in the time domain which are matched to the energy width of the sideband and dissipation of energy is provided by an independent repumping process. Our cesium sample is confined in three dimensions in a crossed dipole trap and the 1D lattice simply results from their interference. A time-of-flight method in two-dimensional absorption imaging provides a direct measurement of the velocity distribution in the lattice direction and in a direction orthogonal to it. We show in two simple cases that, depending on the choice of the trapping beam polarizations, the sideband cooling mechanism is quite different from the ion case and new processes occur. In the first case, we observe a 1D temperature of 6 µK corresponding to a mean quantum vibrational number of $\langle n_{\rm v} \rangle = 0.75$, i.e. 57% of the atoms are in the $n_{\rm v} = 0$ state. In the second case, we get a temperature of 3.6 µK and $\langle n_{\rm v} \rangle \simeq 2.4$.

Our experiments proceed as follows: cesium atoms are collected for 1 s in a magneto-optical trap (MOT) from the background gas at 10^{-9} mbar and loaded into a red-detuned crossed dipole trap with a peak density of a few 10^{12} at/cm^3 [11]. This trap consists of two TEM$_{00}$ Nd:YAG laser beams with a power of 5 W each which cross in their focal points with a common waist $w_0 = 80$ µm. They propagate in a vertical (x, z)-plane and make an angle of $\alpha = \pm 53°$ with the horizontal axis x (fig. 1a). The attractive potential is given by the ground-state light shift $\Delta E = \hbar \Omega^2_{\rm YAG}(\mathbf{r})/4\Delta_{\rm YAG}$, where $\Omega_{\rm YAG}$ is the Rabi frequency of the light field and $\Delta_{\rm YAG}$ is defined by $3/\Delta_{\rm YAG} = 1/\Delta_1 + 2/\Delta_2$. Here Δ_i is the detuning between the YAG laser frequency and the D_i line of Cs. Since Δ_i is much larger than the excited-state and ground-state hyperfine splitting, the Hamiltonian reduces to an effective Hamiltonian $H_{\rm eff}$ acting on a $J = 1/2$ manifold. Therefore, $H_{\rm eff}$ is the sum of a scalar term and a term equivalent to a fictitious magnetic field which depends on the local polarization of the light.
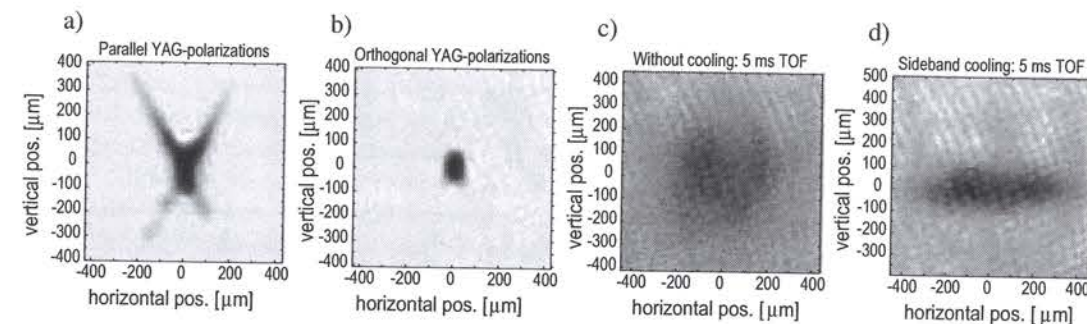
Fig. 2. – Absorption pictures of the atom cloud recorded 100 ms after the MOT has been switched off for parallel (a) and orthogonal (b) polarizations of the dipole trap beams. In the lin $\perp$ lin configuration, the trap contains about $2 \cdot 10^5$ atoms. Absorption pictures after 5 ms time of free flight before (c) and after (d) sideband cooling with lin $\perp$ lin polarizations of the dipole trap beams.

With $\Delta_{\rm YAG} = -2\pi \times 64$ THz, the photon scattering rate is less than $3\,{\rm s}^{-1}$ and can be neglected. The lifetime of the trap is about one second, due to collisions with the background gas. Both of the beams are linearly polarized: One polarization is always orthogonal to the (x, z)-plane while the other is either parallel or orthogonal to the former. The trapping potential strongly depends on this choice, as illustrated in fig. 1 and fig. 2.

With parallel polarizations (lin $\parallel$ lin along y), the YAG intensity is modulated in the z-direction with a period $a = \lambda/(2\sin\alpha) = 665$ nm. In this case, all $|F, m_{\rm F}\rangle$ states see the same trapping potential modulated between zero and a maximal value $U_\parallel$ varying as the Gaussian shape of the beams, $U^{\rm max}_\parallel/k_{\rm B} = 400(100)$ µK at the centre (fig. 1b). The calculated vertical oscillation frequency in a micro-well is $\nu_\parallel = 180$ kHz in the centre, whereas the horizontal oscillation frequencies are only about 300 Hz. When the MOT is switched off, atoms located far from the centre remain trapped in either one of the YAG beams because the interference with the wing of the other beam is sufficient to compensate gravity. This explains the "X" shape of the trap seen in the absorption image (fig. 2a).

When the polarizations of the YAG beams are orthogonal (lin $\perp$ lin case), there is no intensity modulation on the wavelength scale but the polarization of the total light field is modulated. Since the fine structure of the Cs $6p$ state is non-negligible with respect to the detuning of the YAG laser, the D1 and D2 transitions (at 894 nm and 852 nm, respectively) contribute differently to the light shift, which therefore depends on the local polarization. It is the sum of a scalar term $U_\perp$ (with $U^{\rm max}_\perp/k_{\rm B} = 200$ µK) and a term modulated along z (period a) that is formally equivalent to a magnetic field along the axis orthogonal to the polarization of the two YAG beams. This axis is chosen as the quantization axis. The effect of this effective field is opposite in the two hyperfine states due to opposite gyromagnetic factors. The amplitude of the modulation is $\pm 3.5\%$ of $U_\perp$ for the extreme magnetic sublevels $m = \pm 3$ (see fig. 1c). When the modulation is smaller than $k_{\rm B}T$, the global shape of the trap is unaffected and is Gaussian (fig. 2b). Finally, we emphasize that the effective trap depth is only $U^{\rm max}_\perp/2$ as atoms may escape along one of the YAG beams.

Sideband cooling is performed using two-photon Raman transitions between the $F = 3$ and $F = 4$ hyperfine states [11], [12]. Copropagating Raman pulses are used, so that the Doppler shift is negligible. Both beams propagate along the $-z$ direction with linear polarizations always orthogonal to each other. With respect to the quantization axis, they couple the $|3, m\rangle$ state with the $|4, m'\rangle$ state where $m' - m = -1, 0$ or 1. Their detuning from the D2 line $\Delta = -2\pi \times 25$ GHz is large compared to the hyperfine structure of the excited state. Their
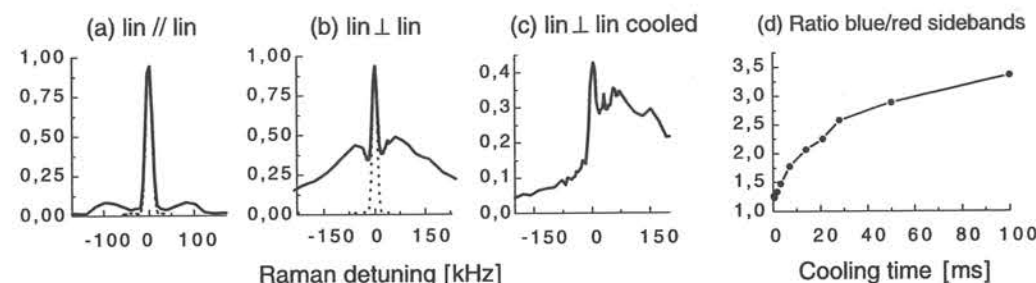
Fig. 3. – Raman spectra of uncooled atoms in the lin ∥ lin (a) and lin ⊥ lin (b) case. (c): Raman spectrum after 100 ms of sideband cooling in the lin ⊥ lin case. Note the different scales in (b) and (c). The dotted line in the panels (a-b) is the corresponding spectrum on free atoms. (d): Ratio of the blue to the red sideband as a function of the cooling time (lin ⊥ lin case).

frequency difference is $\Delta_{HFS} + \delta$, where δ is the Raman detuning and $\Delta_{HFS} = 2\pi \times 9.2$ GHz. The cooling process consists of a sequence of Raman pulses followed by repumping pulses (resonant with the D2 $F = 4 \longrightarrow F' = 3$ transition) which return the atoms to the $F = 3$ state. To avoid a systematic momentum transfer, the repumping is done with three standing waves along x, y, z. The sideband cooling relies on the large energy spacing ΔE between the vibrational levels of the micro-wells in the z-direction. These levels are resolved with the Raman transition and for $\delta < 0$, the atoms are forced into lower-lying vibrational levels in $F = 4$. The copropagating Raman pulses are selective only in internal state and in energy but do not induce any momentum change. The elementary cooling cycle is completed with a 20 μs repumping pulse and the atoms lose an energy of about $|\hbar\delta|$ on average.

The Raman spectra shown in fig. 3 depict, as a function of δ, the fraction of atoms transferred to $F = 4$ by a Raman probe pulse, and measured by state-selective laser induced fluorescence. To avoid Rabi oscillations of saturated lines, the Raman transfer is obtained with a rapid adiabatic passage by chirping δ during the pulse over a range $\Delta\delta$ [11]. If the chirp is sufficiently slow, the atoms follow adiabatically a dressed state and are transferred to the other hyperfine state as soon as the effective detuning crosses a resonance. The Raman probe is a 1 ms pulse chirped over $\Delta\delta = 16$ kHz which determines the energy resolution.

In the lin ∥ lin case for the YAG beams we do not expect transitions between atomic states with different vibrational energies in the micro-wells since the potential is independent of the internal state. Two wave functions with different vibrational quantum numbers are orthogonal and a change of the vibrational level is forbidden in the Raman transitions. However, a typical Raman spectrum (fig. 3a) consists of three peaks, a central "Rayleigh" peak when the Raman detuning is zero and two lateral "Stokes" and "anti-Stokes" peaks when the Raman detuning is about $\pm\nu_\parallel$. The position of these two peaks depends on the YAG power P_{YAG} and scales as $\sqrt{P_{YAG}}$ like the oscillation frequency. The maximum oscillation frequency deduced from these spectra is 130 kHz, somewhat smaller than the calculated one. The height of the sidebands is very sensitive to the intensity of the Raman beams: it is almost zero if we select with a π Blackman pulse, whereas with chirped Raman pulses it keeps increasing while the central peak is saturated. The width of the sidebands reflects the inhomogeneity of the oscillation frequency across the trapped cloud (see fig. 1b and fig. 2a). The sideband cooling sequence in the lin ∥ lin case uses a 100 μs Blackman pulse [13] chirped from $\delta = -80$ kHz to $\delta = -96$ kHz centered on the anti-Stokes transition of fig. 3a, followed by a 20 μs repumping pulse. When repeating this sequence 754 times, the temperature along z decreases from 14(2) μK to 6(1) μK, while the horizontal temperature slightly raises from

17(3) μK to 20(3) μK. These temperatures are extracted by a time-of-flight technique from absorption images [14]. Assuming a thermal distribution, one finds about 57(5)% of the atoms in the vibrational ground state for $\nu_\parallel = 100$ kHz. We believe that the surprising observation of sidebands is due to a small defect in the polarization of the YAG beams: for instance, the resulting potentials in $F = 3$ and $F = 4$ could differ by a few percent and two different vibrational states in the $F = 3$ and $F = 4$ manifolds would no longer be orthogonal. Therefore, the transition probabilities depend strongly on the YAG polarizations: experimentally, changing by one degree the polarization direction of one YAG beam alters the amplitude of the sidebands by a factor 2–3.

In the lin ⊥ lin case, the situation is quite different; transitions between different vibrational states are always allowed since the modulated potentials are different for $|F = 3, m\rangle$ and for $|F = 4, m'\rangle$ and the external wave functions are thus no longer orthogonal. The modulation amplitude of the potential is proportional to m, with opposite signs for $F = 3$ and $F = 4$. This induces a spatial shift of the structure by half a period $(a/2)$ between the two hyperfine states. Raman transitions fulfill the rule $\Delta m = \pm 1, 0$ with probabilities proportional to the squared overlap integral of the vibrational wave functions, i.e. the Franck-Condon factors (FCF).

Raman spectra display two broad peaks centered at about ± 70 kHz in addition to a narrow central peak (fig. 3b). The maximum oscillation frequencies deduced from the lin ∥ lin data are $\nu_\perp(m) = \nu_\parallel \times 0.15 \times \sqrt{|m|} = \sqrt{|m|} \times 20$ kHz. The detuning of the maxima of the sidebands is larger than the oscillation frequencies because transitions with $\Delta n_v = 1$ are less favored than those with $\Delta n_v > 1$ due to the FCF. We cool using a 300 μs Raman pulse chirped between -40 kHz and -56 kHz centered on the anti-Stokes peak, followed by a 20 μs repumping pulse. Two 5 ms time-of-flight absorption images are shown in fig. 2 (c) and (d), before and after 100 ms of sideband cooling (273 pulse pairs). The velocity distribution is clearly compressed along z while it is slightly broadened in the horizontal plane. The temperature in the z-direction drops from 18(0.5) μK to 3.6(0.5) μK, whereas in the horizontal plane it raises to 24(1) μK. After cooling, the red sideband almost disappears while the blue one increases with respect to the Rayleigh peak (fig. 3c and d). From the time evolution of the ratio of the two sidebands, we deduce typical cooling times in the 10–20 ms range. Note that the Raman spectra depict the convolution of the total energy distribution of the atoms in $F = 3$ with the transition probabilities to all the accessible levels in $F = 4$. Since the Raman transfer efficiency depends on the populations in the different m-sublevels which are not measured here, we cannot simply deduce the velocity distribution from the Raman spectra as in the case of trapped ions. The comparison of the final temperature of 3.6 μK with the potential well depth of ~ 10 μK which is an average over m ($m = 0, \pm 1, \pm 2, \pm 3$) shows that most of the atoms are bound in the modulated structure. Assuming equal populations in the magnetic sublevels and a thermal distribution, the mean vibrational number in the micro-wells is $\langle n_v\rangle = 2.4$.

The sideband cooling described here differs in several respects from the sideband cooling of trapped ions [1], [3]. Due to energy conservation, every red-detuned Raman pulse imposes a loss of external energy (linked to the external part of the wave function) in a $F = 3 \longrightarrow F = 4$ transition, i.e. the atoms are transferred to energetically lower-lying vibrational states, including states of higher vibrational quanta if $m' \neq m$. However, the FCFs are very small for transitions between tightly bound states if m does not change sign. This is due to the very weak overlap of the corresponding wavefunctions in the spatially shifted potentials. All potential wells in $F = 3$ coincide with local maxima of the potential surface in $F = 4$ for m's of same sign (and vice versa). Thus the FCFs are vanishingly small ($< 10^{-6}$) for atoms in the first two bound states with $|m| \geq 2$. Therefore, the disappearance of the red sideband does not imply that the atoms are accumulated in the vibrational ground states of the six modulated magnetic sublevels.

The same transition probabilities apply to the repumping process, but work in the opposite sense. It preferably heats the tightly bound atoms in $F = 4$ since they are located at the maxima of the respective potential in $F = 3$. It preferably cools atoms in highly excited levels which have a large FCF with tightly bound states in $F = 3$. However, the repumping back to $F = 3$ needs one or two emission cycles and m may change significantly, e.g. the probability for $|\Delta m| = 3$ is 2%. If m changes sign, transitions between tightly bound states become more favored. We observe experimentally that the balance between Raman cooling and repumping is reached when the red sideband almost disappears. First results of a quantum Monte Carlo simulation confirm that the red sideband disappears when the fraction of atoms bound in the modulated potential increases, in good agreement with our observations.

We believe that this method can be pushed further to cool atoms down to the vibrational ground state in a 1-, 2- or 3-dimensional lattice. In the lin $\parallel$ lin case, counter-propagating Raman beams will allow transitions between all vibrational states and transition probabilities between tightly bound states will not vanish, in contrast to the case studied here [15]. With the high oscillation frequencies produced here, heating due to photon multiple scattering during repumping at high optical thickness could be overcome [16].

***

REFERENCES

[1] WINELAND D. J. and DEHMELT H., Bull. Am. Phys. Soc., 20 (1975) 637.
[2] WINELAND D. J., ITANO W. M., BERGQUIST J. C. and HULET R. G., Phys. Rev. A, 36 (1987) 2220.
[3] DIEDRICH F., BERGQUIST J. C., ITANO W. M. and WINELAND D. J., Phys. Rev. Lett., 62 (1989) 403.
[4] MONROE C., MEEKHOF D. M., KING B. E., JEFFERTS S. R., ITANO W. M., WINELAND D. J. and GOULD P., Phys. Rev. Lett., 75 (1995) 4011.
[5] HEINZEN D. and WINELAND D. J., Phys. Rev. A, 42 (1990) 2977.
[6] MONROE C., MEEKHOF D. M., KING B. E. and WINELAND D. J., Science, 272 (1996) 1131.
[7] TAÏEB R., DUM R., CIRAC J., MARTE P. and ZOLLER P., Phys. Rev. A, 49 (1994) 4876.
[8] KASTBERG A., PHILLIPS W., ROLSTON S. and SPREEUW R., Phys. Rev. Lett., 74 (1995) 1542.
[9] MÜLLER-SEYDLITZ T., HARTL M., BREZER B., HÄNSEL H., KELLER C., SCHNETZ A., SPREEUW R., PFAU T. and MLYNEK J., Phys. Rev. Lett., 78 (1997) 1038.
[10] KASEVICH M. and CHU S., Phys. Rev. Lett., 67 (1991) 181.
[11] KUHN A., PERRIN H., HÄNSEL W. and SALOMON C., in OSA TOPS on Ultracold Atoms and BEC, edited by K. BURNETT, Vol. 7, 1996.
[12] REICHEL J., BARDOU F., BEN-DAHAN M., PEIK E., RAND S., SALOMON C. and COHEN-TANNOUDJI C., Phys. Rev. Lett., 75 (1995) 4575.
[13] KASEVICH M. and CHU S., Phys. Rev. Lett., 69 (1992) 1741.
[14] ANDERSON M. H., ENSHER J. R., MATTHEWS M. R., WIEMAN C. E. and CORNELL E. A., Science, 269 (1995) 198.
[15] In the 1D lin $\parallel$ lin case, we recently produced $\langle n_v \rangle = 0.1$. BOUCHOULE I. et al., in preparation.
[16] CIRAC J., LEWENSTEIN M. and ZOLLER P., Europhys. Lett., 35 (1996) 647.
[17] HAMANN S., HAYCOCK D., KLOSE G., PAX P., DEUTSCH I. and JESSEN P., preprint December 24, 1997.

Neutral atoms prepared in Fock states of a one-dimensional harmonic potential

I. Bouchoule, H. Perrin, A. Kuhn,* M. Morinaga, and C. Salomon
Laboratoire Kastler Brossel, Ecole Normale Supérieure, 24 rue Lhomond, 75231 Paris Cedex 05, France
(Received 18 September 1998)

We describe the preparation of Fock states of motion of cesium atoms trapped in potential wells of a far detuned optical lattice. Direct observation of the velocity distribution of the $|n=0\rangle$ and $|n=1\rangle$ Fock states is obtained by an absorption imaging technique. [S1050-2947(99)50701-4]

PACS number(s): 32.80.Pj, 03.75.−b

The quantum harmonic oscillator is one of the canonical models in physics. Noninteracting boson fields, such as photons, are described, for each mode, by a harmonic Hamiltonian $H = \hbar\omega(a^\dagger a + 1/2)$. The eigenstates of H are number states, $|n=0\rangle, |n=1\rangle, \ldots$, called Fock states. In cavity electrodynamics, the Fock state $|n=1\rangle$ has been produced [1]. For a particle trapped in a harmonic potential, the Fock state $|n\rangle$ consists of n quanta of vibrational excitation of the center-of-mass motion. $|n\rangle$ is nothing but the vibrational state of quantum number n. A system that has been extensively studied consists of a single ion confined in a harmonic potential. Sideband cooling in the Lamb-Dicke regime has been used to prepare the ion in the ground state of a three-dimensional trapping potential [2–5]. From this pure quantum state, a number of nonclassical states of motion (Fock states $n = 1, 2, \ldots$, Schrödinger cat states, etc.) have been prepared [6]. Recently sideband cooling has been extended to neutral atoms confined in optical lattices [7,8]. In each potential well of the lattice, the atoms experienced a harmonic potential and after two-dimensional sideband cooling the population of the vibrational ground state reached 98% [7].

In this paper, we present the preparation of $|n=0\rangle$ and $|n=1\rangle$ Fock states of motion of neutral atoms and a direct observation of the velocity distribution of $|n=1\rangle$. First, one-dimensional sideband cooling using Raman transitions is used to prepare 92(5)% of the atoms in the $n=0$ state. A properly chosen Raman pulse then transfers the atoms in the $n=1$ Fock state. Finally, the velocity distribution of $|n=1\rangle$ is recorded using a time-of-flight technique. In contrast to the ion experiments where the distribution over the Fock states was deduced from an analysis of Rabi oscillations, our straightforward method gives direct access to the square of the modulus of the wave function in velocity space.

We use the experimental setup described in [8]. Cesium atoms are trapped in a red detuned crossed dipole trap [Fig. 1(a)]. This trap consists of two TEM$_{00}$ neodymium-doped yttrium aluminum garnet (Nd:YAG) laser beams with a power of 5 W, each of which crosses at its focal points with a common waist $w_0 = 120 \mu m$. The two beams are linearly polarized along the same axis, propagate in a vertical plane, and make an angle of $\alpha = \pm 53°$ with the horizontal plane. Because the detuning of the YAG laser from the D_1 and the D_2 lines (about 64 THz) is much larger than all hyperfine

splittings, atoms in both hyperfine states $F=3$ and $F=4$ "see" the same scalar potential, proportional to the light intensity [8]. The photon scattering rate is less than 2.2 s^{-1} and can be neglected in our experiments. The lifetime of the trap is about one second, limited by collisions with the background gas.

The interference of the two YAG beams produces a modulation of the intensity along the vertical direction (z axis) with a period of $a = \lambda/(2\sin\alpha) = 665$ nm. Thus the trapping potential is modulated along z with a maximum depth of 200(20) μK at the center [Fig. 1(b)]. The vertical oscillation frequency in a microwell at the center of the trap is $\nu_{osc}^0 = 120$ kHz. This oscillation frequency decreases from ν_{osc}^0 to 0 for wells far from the center. To avoid a large dispersion of the oscillation frequencies, the trap is loaded from a small cloud of atoms having an rms width of 56 μm, leading to a dispersion of the oscillation frequencies of $\sim 8\%$. This is performed by first loading from a magneto-optical trap the crossed dipole trap with orthogonal polarization of the two YAG beams. In this case, there is no intensity modulation and the atoms are confined at the bottom of the potential [8]. After 50 ms, the intensity lattice is produced by turning in 10 ms the polarization of one of the YAG beams so that it is parallel to the other. In this way, about 150 horizontal planes are populated with ~ 650 atoms in each plane. The Gaussian shape of the YAG beams provides a weak horizontal confinement with oscillation frequencies around 200 Hz. The potential wells of the optical lattice are
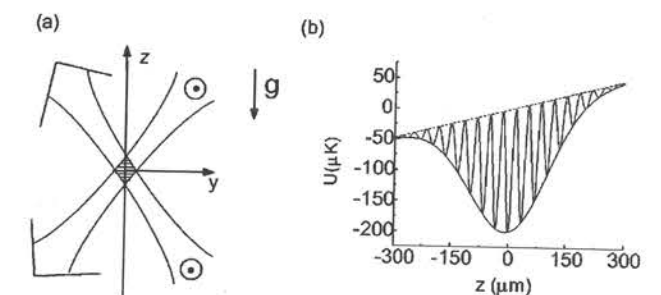
FIG. 1. (a) The dipole trap beams propagate in a vertical plane and have the same linear polarization. They create a far detuned optical lattice along z with a period of 665 nm as well as a weak confining potential in the horizontal plane. (b) Cut of the resulting trapping potential along z including the effect of gravity. The period of the modulation has been multiplied by 50. The vertical oscillation frequency in a microwell at the center of the trap is 120 kHz, whereas the horizontal oscillation frequencies are $\nu_y = 180$ Hz and $\nu_x = 220$ Hz.

*Present address: Fakultät für Physik der Universität Konstanz, Konstanz, Germany.
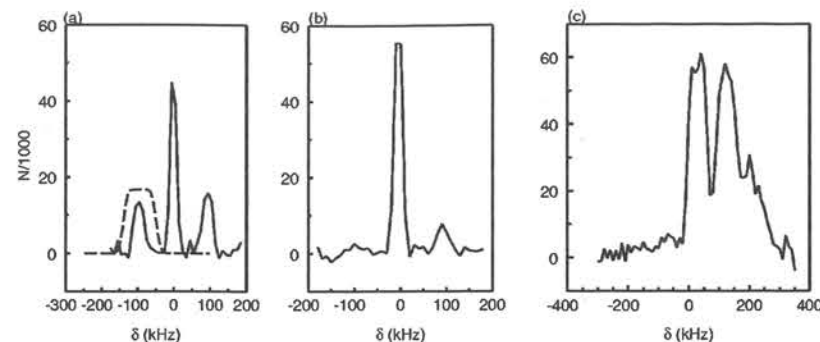
FIG. 2. Raman spectra (a) before cooling and (b),(c) after 20 cooling sequences. Plotted is the number of transferred atoms as a function of the Raman detuning δ. The Raman probing pulses for (a) and (b) are 150-μs-long Blackman pulses, in the low intensity limit for the sidebands. (a) The dotted line shows the excitation profile of the Raman cooling pulses. (b) The quasidisappearance of the red sideband and the decrease of the blue sideband indicate that most of the atoms are accumulated in the $n=0$ vibrational state. In (c), the Raman transition is performed by rapid adiabatic passage at high intensity (see text) so that the efficiency of the transfer is close to 1 for both sidebands and the central peak. From the ratio of the two sidebands we obtain $n_0=92(5)\%$.

deep enough so that, for the first 10 bound states, tunneling is negligible and the potential acts as a harmonic potential. As the initial temperature is 13 μK, about 30% of the atoms are in the fundamental vibrational state and the mean vibrational number is 3.2. The atoms are initially pumped into the $F=3$ hyperfine ground state.

The Lamb-Dicke factor of a single photon transition $\eta =k\Delta z_0$, where $k=7.4\times10^6$ m^{-1} is the wave vector of the D_2 transition and $\Delta z_0=20$ nm is the rms width of the fundamental ground state, is small ($\eta=0.14$). In this regime resolved sideband cooling will accumulate most of the atoms in the vibrational ground state [3,5].

Sideband cooling is performed using two-photon Raman transitions between the $F=3$ and $F=4$ hyperfine states [8,5,9]. Here, we use counterpropagating Raman beams so that a Raman transfer with a change of the vibrational level is allowed: the two-photon Raman coupling between vibrational states $|n\rangle$ and $|n'\rangle$ is $\langle n|e^{2ikZ}|n'\rangle \simeq\langle n|2i\eta(a+a^\dagger)n'\rangle$ for low n. Both beams propagate along the z axis with orthogonal linear polarizations. Their detuning from the D_2 line $\Delta=-30$ GHz is large compared to the hyperfine structure of the excited state. Their frequency difference is $\Delta_{HFS}+\delta$ where δ is the Raman detuning and $\Delta_{HFS}=9.2$ GHz is the frequency difference between the ground hyperfine states. With the intensity used for the cooling, the Raman spontaneous process rate is about 10^2 s^{-1} and the induced heating can be neglected here.

Information on the vertical motion of the atoms is provided by ''Raman spectra'' that depict the number of atoms transferred from $F=3$ to $F=4$ by a Raman probe pulse as a function of δ. The number of transferred atoms is measured, after the probe pulse, by the fluorescence induced by a laser resonant with the transition $6S_{1/2},F=4\rightarrow6P_{3/2},F'=5$. The Raman probe pulse is, for Figs. 2(a) and 2(b), a Blackman pulse [10] with an overall duration of 150 μs. The Raman spectrum [Fig. 2(a)] consists of three peaks. A central peak (carrier) at zero Raman detuning corresponds to a transfer to $F=4$ without change of vibrational level: $\Delta n=0$. Two sidebands at a Raman detuning $\delta=\pm\nu_{osc}\simeq\pm100$ kHz correspond to a transfer with a change of the vibrational level $\Delta n=\pm1$. The width of the sidebands is larger than that of the central peak because of the slight inhomogeneity of the oscillation frequency across the trapped atom cloud [see Fig.

1(b)]. In addition to Raman spectra, we perform two-dimensional absorption images on a charge-coupled-device camera with a horizontal probe beam. The probe is σ_+ polarized, tuned to the $F=4\rightarrow F'=5$ transition and turned on for 60 μs. First, an image taken just after the switching off of the YAG gives a measurement of the trap size. Second, images taken after a long free expansion of the atoms reflect the velocity distributions along z and x (time-of-flight method).

Our Raman cooling process consists of a sequence of Raman pulses tuned to the red sideband followed by a 20-μs repumping pulse (resonant with the $D_2F=4\rightarrow F'=4$ transition), which returns the atoms to the $F=3$ state. The Raman cooling pulse is a 500-μs-long Blackman pulse chirped from $\delta=-50$ kHz to $\delta=-140$ kHz covering the red sideband of Fig. 2(a). When repeating this sequence 20 times (in 10 ms), the rms width of the velocity distribution along z, measured by time of flight, decreases from 31(3) mm/s to 11(1) mm/s [Fig. 3(a)]. Within our experimental error, this value is equal to the rms width v_0 of the velocity distribution $|\langle v|n=0\rangle|^2$ of the Gaussian vibrational ground state: $v_0=\sqrt{h\nu_{osc}/(2m)}=12$ mm/s [Fig. 3 (c) smooth line]. During cooling, the horizontal temperature rises from 13 to 20 μK. On the Raman spectrum after cooling [Fig. 2(b)], the red sideband disappears as expected if all the atoms are in the ground state. The height of the blue sideband also decreases as expected if the atoms are pumped into lower n states, since the Rabi frequency of the $n\rightarrow n+1$ transition decreases as n decreases. From Fig. 2(b), it is in principle possible to infer the population of $|n=0\rangle$ [3,4], but the weakness of the red sideband makes this measurement imprecise.

To circumvent this limitation, we use a Raman probe pulse that has a transfer efficiency close to 1 for both sidebands and the central peak. This pulse is realized by slowly chirping its frequency ($d\delta/dt\simeq-60$ kHz/ms) in order to perform a rapid adiabatic passage between $F=3$ and $F=4$ as the detuning crosses a resonance [11]. The adiabatic condition is fulfilled with a Rabi frequency of $\sim2\pi\times13$ kHz for the transition $F=3,n=0\rightarrow F=4,n=1$. The pulse duration is 1 ms and the amplitude of the frequency chirp is 60 kHz so that it covers completely each of the sidebands but still resolves them [Fig. 2(c)]. The Raman spectrum of Fig. 2(c) depicts the number of atoms transferred to $F=4$ as a func-
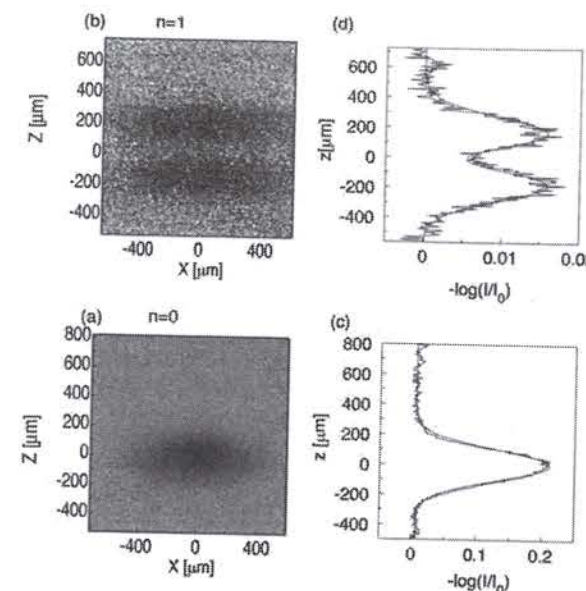
FIG. 3. Absorption images of Fock states (a) $|n=0\rangle$ and (b) $|n=1\rangle$ taken after a time of flight of (a) 6 ms and (b) 10 ms. Measured distributions along z are compared to the calculated ones in (c) and (d). The calculation assumes that all the atoms are in the corresponding Fock state and takes into account the initial size of the cloud along z measured independently (rms width of 56 μm).

tion of the initial detuning of this pulse. On this spectrum, the blue sideband has the same height as the central peak and the transfer efficiency is consistent with 1 within our 5% experimental error. On the other hand, the red sideband remains barely visible. As the blue (red) sideband corresponds to a transfer $n\rightarrow n+1$ ($n\rightarrow n-1$), all atoms contribute to the blue sideband, whereas only atoms that are in the excited vibrational levels (i.e., $n>0$) contribute to the red one. The ratio between the height of the red sideband and that of the blue sideband is equal to $1-n_0$, where n_0 is the fraction of atoms in the fundamental vibrational state. From Fig. 2(c) we obtain $n_0=92(5)\%$. Thus, we have prepared a sample of about 150 horizontal planes in which almost all atoms occupy the lowest quantum state of the vertical motion.

Once the atoms are cooled to the fundamental quantum state, it is straightforward to prepare any other Fock state of motion by a sequence of transfers performed on the sidebands or carrier. For instance, we prepare $|n=1\rangle$ as follows. Using a single Raman pulse tuned to the blue sideband, we transfer the atoms in the vibrational state $|n=1\rangle$ of $F=4$. Again, to achieve a transfer efficiency of ~1 we use a 1-ms Raman pulse frequency chirped over 60 kHz and centered at 90 kHz.

The velocity distribution of the vibrational state $n=1$ is

$$P(v)=|\langle v|n=1\rangle|^2=\frac{1}{\sqrt{2\pi}\,v_0^3}v^2\,e^{-v^2/2v_0^2}. \quad (1)$$

It displays two peaks at $\pm\sqrt{2}v_0$ and $P(v=0)=0$. The image taken after 10 ms of time of flight [Fig. 3(b)] indeed exhibits this double peak structure.

To make a quantitative comparison between observed and expected spatial distributions along z after a time of flight of duration t, we must take into account the finite initial size of the cloud. The expected spatial distribution $F_t(z)$ is

$$F_t(z)=\frac{1}{t}\int_{-\infty}^{\infty}F_0(z_0)\,P\left(\frac{z-z_0}{t}\right)dz_0, \quad (2)$$

where $F_0(z_0)$ is the initial spatial distribution which is Gaussian with an rms width of 56 μm, and $P((z-z_0)/t)=P(v)$ is given by Eq. 1. As shown in Fig. 3, the calculated distribution agrees well with the measured distribution, with no other adjustable parameter than the amplitude. Any higher Fock state could be prepared by applying a succession of Raman pulses that transfer the atoms into the other hyperfine state with an increase of the vibrational number of 1. For example, to produce the Fock state $|n=2\rangle$, a first Raman pulse on the blue sideband transfers the atoms in $F=4$ in $|n=1\rangle$ and then a Raman pulse on the red sideband brings them back to $F=3$ in $|n=2\rangle$.

Two directions could be explored for a future work. First, the manipulation of quantum states can be pushed further: a time-dependent coherent superposition of vibrational states could be produced and detected in the same manner as here. The quantum control of the single particle and the entanglement of several particles are essential ingredients for the realization of a quantum computer [12]. Second, it would be interesting to study the behavior of the trapped gas strongly confined in one dimension. For instance, after sideband cooling, the cloud is out of thermal equilibrium, the horizontal kinetic energy being larger than the vertical one. We have observed that the cloud thermalizes by collisions with a time constant of ~100 ms. Since the width of the vibrational ground state along z is 20 nm and the collisional cross section for Cs atoms in free space at $T=20$ μK is on the order of $(50\text{ nm})^2$ [13] how should the collisions be described? Finally, it would be interesting to search for a two-dimensional Bose-Einstein condensation in a harmonic trap [14] by cooling the horizontal motion of our trapped gas.

[1] X. Maitre, E. Hagley, G. Nogues, C. Wunderlich, P. Goy, M. Brune, J.M. Raimond, and S. Haroche, Phys. Rev. Lett. **79**, 769 (1997).

[2] D.J. Wineland and H. Dehmelt, Bull. Am. Phys. Soc. **20**, 637 (1975).

[3] D.J. Wineland, W.M. Itano, J.C. Bergquist, and R.G. Hulet, Phys. Rev. A **36**, 2220 (1987).

[4] F. Diedrich, J.C. Bergquist, W.M. Itano, and D.J. Wineland, Phys. Rev. Lett. **62**, 403 (1989).

[5] C. Monroe, D.M. Meekhof, B.E. King, S. R. Jefferts, W.M.

Itano, D.J. Wineland, and P. Gould, Phys. Rev. Lett. **75**, 4011 (1995).

[6] D.M. Meekhof, C. Monroe, B.E. King, W.M. Itano, and D.J. Wineland, Phys. Rev. Lett. **76**, 1796 (1996); C. Monroe, D.M. Meekhof, B.E. King, and D.J. Wineland, Science **272**, 1131 (1996).

[7] S. Hamann, D. Haycock, G. Klose, P.H. Pax, I. Deutsch, and P. Jessen, Phys. Rev. Lett. **80**, 4149 (1998).

[8] H. Perrin, A. Kuhn, I. Bouchoule, and C. Salomon, Europhys. Lett. **42**, 395 (1998).

[9] D. Heinzen and D.J. Wineland, Phys. Rev. A **42**, 2977 (1990).

[10] M. Kasevich and S. Chu, Phys. Rev. Lett. **67**, 181 (1991).

[11] A. Kuhn, H. Perrin, W. Hänsel, and C. Salomon, in *OSA TOPS on Ultracold Atoms and Bose Einstein Condensates*, edited by Keith Burnett (Optical Society of America, Washington, DC, 1996), Vol. 7.

[12] J.I. Cirac and P. Zoller, Phys. Rev. Lett. **74**, 4091 (1995).

[13] M. Arndt, M. Ben Dahan, D. Guery-Odelin, M.W. Reynolds, and J. Dalibard, Phys. Rev. Lett. **79**, 625 (1997).

[14] W. Ketterle and N.J. van Druten, Phys. Rev. A **54**, 656 (1996).

Raman cooling of spin-polarized cesium atoms in a crossed dipole trap

H. PERRIN, A. KUHN(*), I. BOUCHOULE, T. PFAU(*) and C. SALOMON

Laboratoire Kastler Brossel, École Normale Supérieure
24 rue Lhomond, 75231 Paris Cedex 05, France

Abstract. – We describe a Raman cooling scheme that allows for the simultaneous polarization and cooling of cesium atoms. Using efficient chirped Raman pulses, cesium atoms confined in a red-detuned crossed dipole trap are 80 % polarized and cooled to a temperature of 2.4 μK. After cooling, the phase-space density reaches 10^{-3}. We have strong evidence that this value is limited by multiple photon scattering within the atomic cloud.

Since the first observation of Bose-Einstein condensation in 1995 using evaporative cooling in a magnetic trap [1-3], important efforts have been made to achieve quantum degeneracy by all optical methods [4,5]. With current trap oscillation frequencies and atom number achievable with laser light, the onset of BEC requires temperatures below the single photon recoil temperature given by $k_B T_{rec} = m v_{rec}^2 = \hbar^2 k^2/m$ were k is the light wave number and m the atomic mass. There are two laser cooling methods that can reach ultra-low temperatures when applied to free atoms, namely velocity-selective coherent population trapping (VSCPT) [6,7] and Raman cooling [8-10]. Raman cooling of Na atoms confined in a dipole force trap has produced $T = 0.42 T_{rec}$ and a phase-space density of 6.5×10^{-3} [4]. Blue molasses [11] and Raman cooling [5] of Cs atoms confined in a dipole trap have produced phase-space densities of 10^{-3} and 2×10^{-4}, respectively. In these experiments, atoms were spread over all Zeeman substates. By contrast, gravitational Sisyphus cooling produced a sample of cold *polarized* rubidium atoms in a magnetic trap [12]. In this letter, we present a Raman cooling scheme that allows to *simultaneously* cool and polarize trapped cesium atoms in a weak bias magnetic field. Recently, a similar scheme was demonstrated on sodium atoms [13] and a temperature of $0.62 T_{rec}$ was obtained at a density of 4×10^{11} atoms/cm^3. In our experiments, we accumulate more than 80 % of the cesium atoms into the $|F = 3, m_F = 3\rangle$ stretched state at a temperature of 2.4 μK. The phase-space density reaches 10^{-3}, a factor $7 \times 80\% = 5.6$ larger than in the unpolarized case. This figure represents a four-order-of-magnitude gain over the phase-space density of a cesium magneto-optical trap (MOT) and a factor of 5 improvement over our
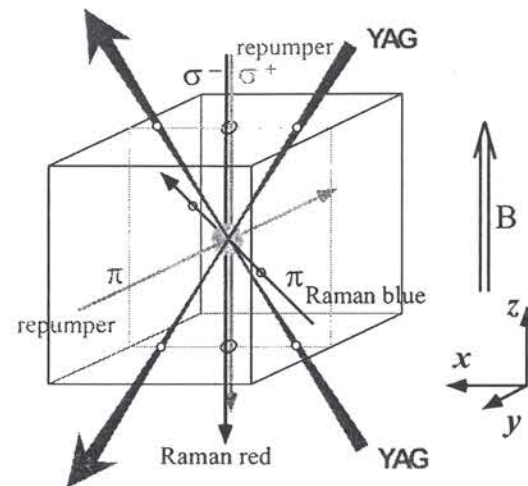
Fig. 1. – Configuration of the trapping YAG beams and the cooling beams. A small magnetic field (10 mG) along the vertical axis z provides our quantization axis. The YAG beams propagate in a vertical plane xz and make an angle of $\alpha = \pm 53°$ with the horizontal plane xy. The non degenerate eigenaxes of the resulting trap at the intersection of the beams are x, y and z. The Raman beams propagate respectively along $x - y$ and $-z$ and are π (resp. σ^-) polarized. The Raman transition is Doppler sensitive and induces a velocity change of $\sqrt{2}\,v_{rec}$ along the $\mathbf{x} - \mathbf{y} + \mathbf{z}$ direction. The repumping laser is present in two directions with polarizations σ^+ or π.

previous results. We demonstrate that this value is limited by a heating mechanism associated with multiple photon scattering within the atomic cloud.

In our experiments, cesium atoms are collected for 1 s in a vapor cell MOT [14]. They are then loaded into a crossed dipole trap (fig. 1) at a peak density of about 5×10^{11} atoms/cm^3. This trap consists of two TEM$_{00}$ Nd:YAG laser beams each having a power of $P_{YAG} = 5$ W and which cross in their focal points where the waist is $w_0 = 100$ μm (see fig. 1). They propagate in the vertical xz-plane and make an angle of $\alpha = \pm 53°$ with the horizontal axis x (fig. 1a). The attractive potential is given by the ground-state light shift $\Delta E = \hbar \Omega_{YAG}^2(\vec{r})/4\Delta_{YAG}$ where Ω_{YAG} is the Rabi frequency of the light field and Δ_{YAG} is defined by $3/\Delta_{YAG} = 1/\Delta_1 + 2/\Delta_2$. Here Δ_i is the detuning between the YAG laser frequency and the D_i line of Cs. With $\Delta_{YAG} = -2\pi \times 64$ THz, the photon scattering rate is less than 2 s^{-1}. The lifetime of the trap is about one second, limited by collisions with the background gas. The polarizations of both beams are linear and parallel to each other, i.e. orthogonal to the xz-plane. An interference pattern in the vertical direction is therefore produced with a period of 665 nm. In our previous work, we used this lattice to perform 1D Raman sideband cooling to the ground state [15, 16]. Here, by contrast, in order to produce a quasi-spherical trap, we use an acousto–optic modulator (AOM) to shift the frequency of one of the YAG beams by 100 MHz. The resulting interference pattern is moving at 33 m/s and the cold atoms are not able to follow this fast motion of the lattice. They see a time-averaged potential without this fine spatial structure. Its depth $U_{max}/k_B \sim 70$ μK is given by the AC-Stark shift of either one of the YAG beams. This potential depth corresponds to oscillation frequencies $\nu_x \sim 170$ Hz, $\nu_y = 5/4\,\nu_x \sim 210$ Hz, $\nu_z = 3/4\,\nu_x \sim 125$ Hz. Initially, a few 10^5 atoms are transferred from the MOT to the crossed dipole trap. The 1σ radius of the atomic cloud is $r = 28 \pm 5$ μm and its temperature is $T_0 = 14 \pm 2$ μK. This temperature is measured by an absorption imaging technique after a time of flight of 5 ms [1].
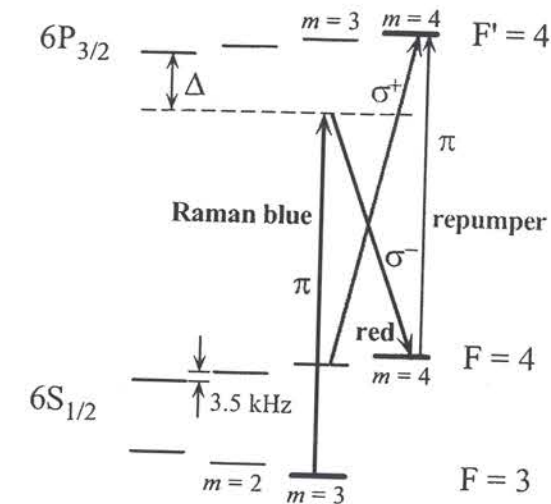
Fig. 2. – Principle of Raman cooling of polarized atoms. After each Raman transfer, the magnetic quantum number is increased by one. The repumping beam also contributes to polarize the atoms with its intense σ^+ component. The π component is necessary during cooling to pump the atoms in $|F = 4, m = 4\rangle$ back to $F = 3$.

In order to polarize and cool the atoms, we repeat a cycle consisting of a stimulated Raman transition between the two hyperfine ground states changing the magnetic quantum number by $+1$ followed by a repumping pulse which brings the atoms back to the initial hyperfine state. A small magnetic field ($B = 10$ mG) along the vertical axis z prevents from spin flips and provides a natural quantization axis. The Raman beams have the following configuration (fig. 1): the blue Raman beam propagates in the horizontal direction $\mathbf{x} - \mathbf{y}$ and polarized along z and the red Raman beam propagates along $-z$ and is σ^- polarized. After absorption of a π photon in the blue Raman beam and stimulated emission of a σ^- photon in the red Raman beam, an atom is transferred from $|6S_{1/2}, F = 3, m\rangle$ to $|6S_{1/2}, F = 4, m+1\rangle$ (fig. 2). Note that the Raman transfer is velocity selective with a Raman kick $\sqrt{2}\,v_{rec}$ (v_{rec} is the single photon recoil velocity, 3.5 mm/s for cesium) along the $\mathbf{x} - \mathbf{y} + \mathbf{z}$ axis, which will be referred to as the Raman axis. This kick has a non-zero projection on each of the three eigenaxes of the trap, thus allowing Raman cooling in three dimensions. The detuning of the Raman beams from the D_2 line, $\Delta = -2\pi \times 25$ GHz, is much larger than the hyperfine structure of the excited state. Their frequency difference is $\Delta_{HFS} + \delta$ where δ is the Raman detuning and $\Delta_{HFS} = 2\pi \times 9.2$ GHz is the splitting between the $|6S_{1/2}, F = 3\rangle$ and $|6S_{1/2}, F = 4\rangle$ hyperfine states of the cesium atom. The repumping laser is tuned to the D2 $F = 4 \longrightarrow F' = 4$ transition and is split into two beams, a σ^+ polarized saturating beam ($s = 1$) propagating along $-z$ and a much weaker π polarized beam ($s = 10^{-3}$) propagating in the horizontal plane. The repumping process thus also contributes to polarize the atoms. This π–beam is not needed for polarizing the atoms but is necessary during Raman cooling for pumping the atoms out of the $|F = 4, m = 4\rangle$ state.

With this configuration of Raman beams, a Raman pulse is velocity selective and its effective Raman detuning depends on m and the value of the bias field. To excite a broad velocity class with a transfer efficiency close to 100 %, the detuning of the Raman pulse is chirped [5]. For a given m, the chirp range determines the velocity classes which are adiabatically transferred to the other hyperfine state. First, we use the following sequence of Raman + repumping pulses to optically pump the atoms in the $|6S_{1/2}, F = 3, m = 3\rangle$ state: With $B = 10$ mG,
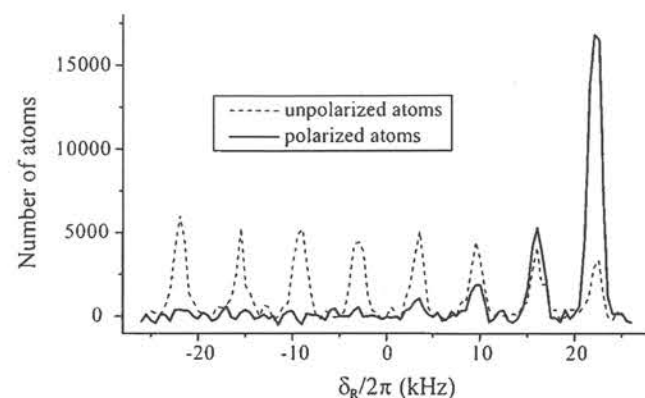
Fig. 3. – Raman spectra before (dashed line) and after (full line) 15 repetitions of the polarizing sequence. The right peak corresponds to the $|F = 3, m = 3\rangle \longrightarrow |F = 4, m = 4\rangle$ transition. The Raman pulse is a Blackman pulse which satisfies the π condition for the two extreme peaks. The population in $|F = 3, m = 3\rangle$ in this spectrum is 80 %.

the detuning δ of a 400 μs Raman pulse is chirped from +15 kHz to −44 kHz to excite $|F = 3, m = -3\rangle$ atoms with an initial velocity between −5.3 v_{rec} and +4.9 v_{rec} along the Raman axis. Atoms in $|F = 3, m = +3\rangle$ are excited if their velocity is between −12.5 v_{rec} and −2.3 v_{rec}. More generally, the Raman transfer from $|6S_{1/2}, F = 3, m\rangle$ to $|6S_{1/2}, F = 4, m + 1\rangle$ for an atom with an initial velocity $(u - \sqrt{2}/2) v_{\text{rec}}$ along the Raman axis occurs when $\delta = 5.8 u + 3.5 \times (2m + 1)$ kHz. This Raman pulse is followed by a 250 μs repumping pulse and the polarization sequence is repeated 15 to 20 times. In contrast to ref. [13], where a large bias magnetic field (430 mG) was used to resolve the Doppler broadened Raman transitions of various m_F substates, our method operates with a much weaker bias field allowing efficient simultaneous excitation of all m_F states with a single chirped Raman pulse.

To measure the atomic polarization, we plot the number of atoms transferred from $F = 3$ to $F = 4$ by a Raman Blackman pulse [17] as a function of the Raman detuning δ. This number is measured by the fluorescence light induced by a probe laser tuned to the $F = 4 \to F' = 5$ transition at 852 nm. This plot (a Raman spectrum) is produced with copropagating Raman beams. The red Raman beam is now aligned with the blue Raman beam and has a linear polarization orthogonal to z (see fig. 1). The Raman transition is then Doppler insensitive and is only selective in internal energy. The resulting spectrum (fig. 3) consists of eight peaks, each peak corresponding to the two degenerate transitions $|F = 3, m\rangle \longrightarrow |F = 4, m + 1\rangle$ and $|F = 3, m + 1\rangle \longrightarrow |F = 4, m\rangle$ except for the extreme peaks which give the transfer efficiency from $|F = 3, m = -3\rangle$ to $|F = 4, m = -4\rangle$ and from $|F = 3, m = 3\rangle$ to $|F = 4, m = 4\rangle$. The population of the different magnetic sublevels is inferred from the relative height of the peaks. After 15 repetitions of the polarizing cycle, about 80 % of the atoms are polarized in the $|F = 3, m = 3\rangle$ state, most of the others being in the $m = 2$ state. The repumping process is responsible for a slight depolarization because the atoms may absorb several π polarized photons before being pumped back to $F = 3$. Depolarization may also occur because of misalignment of the Raman beams with respect to the geometry imposed by the magnetic field. The final situation thus results from the equilibrium between polarizing and depolarizing processes [18].

Once the atoms are in the $|F = 3, m = 3\rangle$ state, Raman cooling is performed using the beam configuration of fig. 1. With respect to the quantization axis, the Raman beams couple
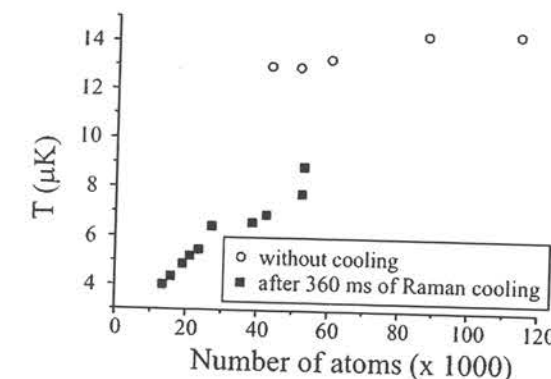
Fig. 4. – Temperature in the crossed dipole trap as a function of the atom number, without cooling (open circles) or after 360 ms of Raman cooling (closed squares). The number of atoms and the temperature are inferred from a time-of-flight measurement after cooling. Note that the temperature does not depend on the atom number without Raman cooling.

the $|F = 3, m = 3\rangle$ state with the $|F = 4, m = 4\rangle$ state. The atoms with a velocity component opposite to the Raman axis and between 5.2 and 10.2 v_{rec} are excited using a 300 μs Blackman pulse chirped over 29 kHz [5]. Because of the accumulation of the atoms in $m = 3$, this pulse can be chosen more selective than the polarizing pulses. After each Raman transfer, the atoms are pumped back to the $|F = 3, m = 3\rangle$ state via the $|F' = 4, m' = 4\rangle$ excited state using a 400 μs pulse. As above, the atoms may be depolarized during the repumping process by cycling between $F = 4$ and $F' = 4$ before being pumped in $F = 3$. However, due to the systematic change $\Delta m = +1$ at each Raman transfer, the polarization remains stable around 80% during Raman cooling. The trap temperature and atom number are measured by time-of-flight absorption imaging. After 500 cooling cycles (360 ms), a temperature of 2.4 μK is obtained, corresponding to an rms velocity of 3.5 v_{rec}. The number of atoms in the $|F = 3, m = 3\rangle$ ground state is 2.5×10^4. With a mean oscillation frequency of 170 Hz, this corresponds to a peak density of $n_0 = 10^{12}$ atoms/cm^3 and a phase-space density of 10^{-3}. This result is a four-order-of-magnitude improvement with respect to a magneto-optical trap. Thanks to the polarization of the atoms, the final phase-space density is higher than the one previously obtained with Raman cooling of unpolarized atoms in the trap with counter-propagating Raman beams [5]. However, the single-photon recoil temperature is not reached although our Raman cooling method for polarized atoms could in principle lead to subrecoil temperatures [4, 13, 10].

We now give evidence that the atomic temperature is likely to be limited by photon reabsorption during the repumping process: a spontaneous photon resonant with the $F = 3 \longrightarrow F' = 4$ transition emitted during repumping can be scattered several times before it escapes the cloud, thus heating the atomic sample. This process becomes important at large values of the parameter $\beta = n_0 \sigma r$, where σ is the absorption cross section ($\sigma = 6\pi/k^2$) [19, 11]. To illustrate this effect, we performed another set of experiments. We measured the temperature obtained after a given Raman cooling sequence for different values of the initial atom number N_i and hence different values of β. To vary β, we simply wait before starting cooling in the trap: the number of trapped atoms decreases with time due to collisions with the background gas. β before cooling was varied between 2.8 and 1.1. The cooling sequence is the same as before. The final temperature deduced from time-of-flight measurement is plotted in fig. 4 as a function of the number of atoms N_f at the end of the cooling process. Without

cooling, the temperature does not depend on the atom number, except for a slight spontaneous evaporation for large values of N. On the contrary, the final temperature is an increasing function of N_f as we apply the cooling sequence: we obtain 8 μK for 5×10^4 atoms, whereas it decreases down to 4 μK for 1.5×10^4 atoms. We have also observed that the cooling process induces an additional loss of atoms, typically 30 % at 6 μK. We attribute this loss to hyperfine changing collisions [20,21]. A detailed study of the heating rate as a function of n_0 and r is beyond the scope of this paper. Additional evidence of the existence of reabsorption effects was obtained in another experiment with unpolarized atoms. It consisted of lowering the trapping potential, enforcing at the same time a slight evaporation of atoms [25]. A combination of Raman and evaporative cooling produced a temperature of 680 nK ($v_{rms} = 1.8\ v_{rec}$) for a sample of 2×10^4 unpolarized atoms at a density of 4.3×10^{11} at/cm^3 in the trap.

Cirac *et al.* and recently Castin *et al.* suggested to lower the repumping rate in order to limit the effect of photon reabsorption [22,23]. If the two-atom model of ref. [23] is valid for a dense atomic cloud, we expect the reabsorption to be significantly reduced for repumping rates lower than the Doppler width kv_{rms}. Preliminary experimental results show a slight dependence of the final temperature with the pumping rate. The observed effect remains modest, the final temperature decreasing from 3 to 2.4 μK as the pumping rate is lowered from 100 kHz to 5 kHz with the same cooling sequence. Note however that, in the case of cesium, because of the giant spin relaxation collisions of the $|F = m_F = 4\rangle$ state [24] additional loss terms appear at very low repumping rates.

In conclusion, we have demonstrated a cooling scheme which prepares cesium atoms in a single internal state at very low temperatures. Using appropriate Raman and microwave pulses, it should be possible to transfer the atoms in any other magnetic state. Applications include the study of collisions in atomic fountains [26], atom optics experiments and pre-cooling for shortening the evaporation time in Bose-Einstein condensation.

***

REFERENCES

[1] ANDERSON M., ENSHER J., MATTHEWS M., WIEMAN C. and CORNELL E., *Science*, **269** (1995) 198.
[2] DAVIS K., MEWES M.-O., ANDREWS M., VAN DRUTEN N., DURFEE D., KURN D. and KETTERLE W., *Phys. Rev. Lett.*, **75** (1995) 3969.
[3] BRADLEY C., SACKETT C. A., TOLLETT J. and HULET R., *Phys. Rev. Lett.*, **75** (1995) 1687.
[4] LEE H., ADAMS C., KASEVICH M. and CHU S., *Phys. Rev. Lett.*, **76** (1996) 2658.
[5] KUHN A., PERRIN H., HÄNSEL W. and SALOMON C., in *OSA TOPS on Ultracold Atoms and BEC* Vol. **7** (Keith Burnett ed.) 1996.
[6] ASPECT A., ARIMONDO E., KAISER R., VANSTEENKISTE N. and COHEN-TANNOUDJI C., *Phys. Rev. Lett.*, **61** (1988) 826.
[7] SAUBAMÉA B., HIJMANS T., KULIN S., RASEL E., PEIK E., LEDUC M. and COHEN-TANNOUDJI, C., *Phys. Rev. Lett.*, **79** (1997) 3146.
[8] KASEVICH M. and CHU S., *Phys. Rev. Lett.*, **69** (1992) 1741.
[9] REICHEL J., MORICE O., TINO G.M.and SALOMON C., *Europhys. Lett.*, **28** (1994) 477.

[10] REICHEL J., BARDOU F., BEN-DAHAN M., PEIK E., RAND S., SALOMON C. and COHEN-TANNOUDJI C., *Phys. Rev. Lett.*, **75** (1995) 4575.
[11] BOIRON D., MICHAUD A., FOURNIER J.M., SIMARD L., SPRENGER M., GRYNBERG G. and SALOMON C., WEYERS S., SZYMANIEC K., COGNET L. and CLAIRON A., *Phys. Rev. A*, **57** (1998) R4106.
[12] NEWBURY N., MYATT C., CORNELL E. and WIEMAN C., *Phys. Rev. Lett.*, **74** (1995) 2196.
[13] LEE H. J. and CHU S., *Phys. Rev. A*, **57** (1998) 2905.
[14] MONROE C., SWANN W., ROBINSON H. and WIEMAN C., *Phys. Rev. Lett.*, **65** (1990) 1571.
[15] PERRIN H., KUHN A., BOUCHOULE I. and SALOMON C., *Europhys. Lett.*, **42** (1998) 395.
[16] BOUCHOULE I., PERRIN H., KUHN A., MORINAGA M. and SALOMON C., *Pys. Rev.A*, **59** (1999) R8.
[17] KASEVICH M. and CHU S., *Phys. Rev. Lett.*, **67** (1991) 181.
[18] We have also accumulated more than 95% of the atoms in the $|F = 3, m = 3\rangle$ state as follows: Using copropagating Raman beams we transfer atoms in the other m-states into $F = 4$. Then, these atoms are pushed outside of the trap with a σ^+ polarized resonant laser tuned to the cycling $|F = 4\rangle \longrightarrow |F' = 5\rangle$ transition. However, when applying the cooling sequences, we noticed that the polarization after cooling degraded to 80%.
[19] BOIRON D., MICHAUD A., LEMONDE P., CASTIN Y., SALOMON C., WEYERS S., SZYMANIEC K., COGNET L. and CLAIRON A., *Phys. Rev. A*, **57** (96) R3734.
[20] SESKO D., WALKER T., MONROE C., GALLAGHER A. and WIEMAN C., *Phys. Rev. Lett.*, **63** (1989) 961.
[21] LEMONDE P., MORICE O., PEIK E., REICHEL J., PERRIN H., HÄNSEL W. and SALOMON C., *Europhys. Lett.*, **32** (1995) 555.
[22] CIRAC J., LEWENSTEIN M. and ZOLLER P., *Europhys. Lett.*, **35** (1996) 647.
[23] CASTIN Y., LEWENSTEIN M. and CIRAC J., *Phys. Rev. Lett.*, **80** (1998) 5305.
[24] SÖDING J., GUÉRY-ODELIN D., DESBIOLLES P., FERRARI G. and DALIBARD J., *Phys. Rev. Lett.*, **80** (1998) 1869.
[25] ADAMS C., LEE H. J., DAVIDSON N., KASEVICH M. and CHU S., *Phys. Rev. Lett.*, **74** (1995) 3577.
[26] GIBBLE K. and CHU S., *Phys. Rev. Lett.*, **70** (1993) 1771.

Controlled generation of single photons from a strongly coupled atom-cavity system

A. Kuhn, M. Hennrich, T. Bondo, G. Rempe*

Max-Planck-Institut für Quantenoptik, Postfach 1513, D-85740 Garching, Germany

Abstract. We propose a new method for the generation of single photons. Our scheme will lead to the emission of one photon into a single mode of the radiation field in response to a trigger event. This photon is emitted from an atom strongly coupled to a high-finesse optical cavity, and the trigger is a classical light pulse. The device combines cavity-QED with an adiabatic transfer technique. We simulate this process numerically and show that it is possible to control the temporal behaviour of the photon emission probability by the shape and the detuning of the trigger pulse. An extension of the scheme with a reloading mechanism will allow one to emit a bit-stream of photons at a given rate.

PACS: 32.80.Qk; 42.50.Ct; 42.65.Dr

Atoms, ions or photons in a superposition of different states are the basic building blocks of quantum information processing, quantum communication, or quantum cryptography, where they act as elementary quantum bits (qubits) [1]. Simple quantum-logic operations [2, 3] in future quantum-logic networks [4] and the transmission of quantum information from one place to another [5], such as the teleportation of a quantum state [6–8], are based on the entanglement of different qubits or even different types of qubits. In a quantum network, for example, single atoms or ions are entangled with individual photons. To generate such an entanglement in a controlled way, a triggered source for single photons will be needed.

So far, most schemes used for the generation of single photons rely on spontaneous emission events or on parametric down-conversion. However, these processes produce photons at more or less random times. Only recently, evidence for a single-photon turnstile device has been demonstrated by Kim et al. [9]. They employed the Coulomb blockade mechanism in a quantum dot to trigger the emission of a single photon, radiated in an essentially random direction. Here, we adopt a different approach. Our studies are based on proposals by Law et al. [10, 11], where a single atom strongly coupled to an optical cavity is used as the active medium generating the photon. The cavity defines the active mode and ensures photon emission into a well-defined direction. The main aspects of the proposed mechanism can be explained analytically, but numerical simulations are necessary to analyze the flexibility and the limits of the excitation process.

Figure 1 shows the excitation scheme for a single-photon emission on the energy scale of the atomic bare states. We consider a Λ-type three-level atom with two long-lived states, $|u\rangle$ and $|g\rangle$, typically two Zeeman or hyperfine states of the atomic ground state, and an electronically excited state, $|e\rangle$. The atom is inside a single-mode optical cavity, with states $|0\rangle$ and $|1\rangle$ denoting a cavity field with zero and one photon, respectively. The cavity frequency is close to the atomic transition frequency between states $|e\rangle$ and $|g\rangle$, but far off resonance from the $|e\rangle$ to $|u\rangle$ transition. Hence, only the product states $|e, 0\rangle$ and $|g, 1\rangle$ are coupled by the cavity mode. The coupling constant g is time independent for an atom at rest. Note that the cavity does not couple states with equal photon number, i.e. $|e, 0\rangle$ with $|u, 0\rangle$, and $|e, 0\rangle$ with $|g, 0\rangle$.

Initially, the system is prepared in state $|u, 0\rangle$. To trigger a photon emission, the atom is exposed to a light pulse
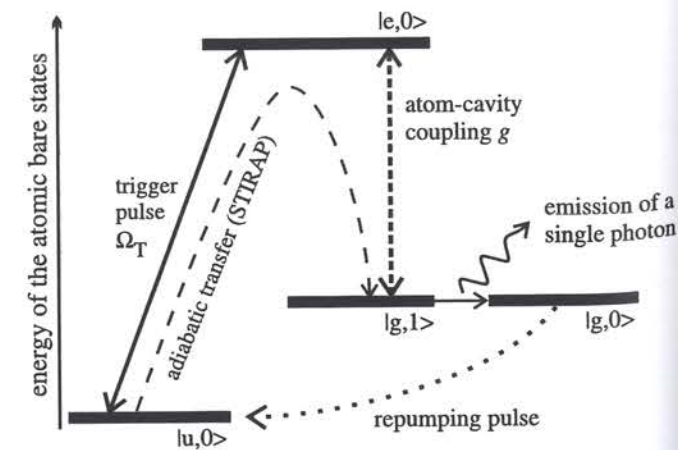

Fig. 1. Scheme of the atomic levels coupled by the trigger pulse, the cavity, and a possible repumping pulse

* Corresponding author.

crossing the cavity transverse to its axis. This pulse has Rabi frequency Ω_T and is near resonant with the transition between states $|u, 0\rangle$ and $|e, 0\rangle$, thereby coupling these states. Provided the trigger pulse rises sufficiently slowly, an adiabatic evolution of the atom-cavity system is assured. If the two-photon resonance condition is fulfilled, a STIRAP-type adiabatic passage [12, 13] takes place and a transition from $|u, 0\rangle$ to $|g, 1\rangle$ is realized. The process generates a single photon in the cavity mode, and the subsequent decay of the cavity field leads to the emission of a single-photon pulse. In the end, the state vector of the atom-cavity system is $|g, 0\rangle$, which is decoupled from any further interaction.

To analyze the excitation scheme in more detail, we assume a Raman-resonant excitation, where Δ is the common detuning of the trigger pulse and the cavity mode from the intermediate level $|e, 0\rangle$. The combined atom-cavity system is examined in the interaction picture. In the basis of the uncoupled states, $\{|u, 0\rangle, |e, 0\rangle, |g, 1\rangle\}$, the interaction Hamiltonian reads

$$H = -\frac{\hbar}{2}\begin{pmatrix} 0 & \Omega_T & 0 \\ \Omega_T^* & 2\Delta & 2g \\ 0 & 2g^* & 0 \end{pmatrix}, \tag{1}$$

where $2g$ is the cavity-induced resonant single-photon Rabi frequency on the $|e, 0\rangle \longleftrightarrow |g, 1\rangle$ transition. If the time dependence of the Hamiltonian is neglected, the state vector of the system, $|\Psi\rangle$, can be expressed as a time-independent superposition of the three eigenstates (or dressed states, see [14]) of Hamiltonian (1):

$$|a^0\rangle = \cos\Theta|u, 0\rangle - \sin\Theta|g, 1\rangle,$$
$$|a^+\rangle = \cos\Phi\sin\Theta|u, 0\rangle - \sin\Phi|e, 0\rangle + \cos\Phi\cos\Theta|g, 1\rangle,$$
$$|a^-\rangle = \sin\Phi\sin\Theta|u, 0\rangle + \cos\Phi|e, 0\rangle + \sin\Phi\cos\Theta|g, 1\rangle, \tag{2}$$

where the mixing angles Θ and Φ are given by

$$\tan\Theta = \frac{\Omega_T}{2g} \quad \text{and} \quad \tan\Phi = \frac{\sqrt{4g^2 + \Omega_T^2}}{\sqrt{4g^2 + \Omega_T^2 + \Delta^2} - \Delta}, \tag{3}$$

with Ω_T and g assumed to be real. The corresponding eigenfrequencies are

$$\omega^0 = 0 \quad \text{and} \quad \omega^{\pm} = \frac{1}{2}\left(\Delta \pm \sqrt{4g^2 + \Omega_T^2 + \Delta^2}\right). \tag{4}$$

When a trigger pulse is applied, the Hamiltonian and the dressed-state basis, $\{|a^0\rangle, |a^+\rangle, |a^-\rangle\}$, are changing as a function of time. Provided that all parameters change slowly, the state vector, $|\Psi\rangle$, adiabatically follows the dressed-state basis and can still be expressed as an invariant superposition of $|a\rangle$-vectors throughout the interaction.

Before the trigger pulse is applied ($\Omega_T = 0$), the atom is only coupled to the cavity mode ($2g > 0$), i.e. $\tan\Theta = 0$. Therefore, preparing the atom initially in $|u, 0\rangle$ is equivalent to a preparation of the atom-cavity system in state $|a^0\rangle$. It is obvious from (2) and (3) that any interaction with the trigger pulse leading to $\Omega_T \gg 2g$, i.e. $\tan\Theta \gg 1$, implies the evolution of $|a^0\rangle$ and, hence, the state vector, $|\Psi\rangle$, into state $|g, 1\rangle$.

Therefore, the atom is transferred to the other long-lived state, $|g\rangle$, and a photon is generated in the cavity mode at the same time. As adiabatic following must be assured, the slope of the trigger pulse must be sufficiently small to fulfill the adiabaticity constraint [15],

$$\left|\langle a^{\pm}|\frac{d}{dt}|a^0\rangle\right| \ll |\omega^0 - \omega^{\pm}| \quad \text{or} \quad |\dot{\Theta}| \ll |\omega^0 - \omega^{\pm}|. \tag{5}$$

For a Gaussian trigger pulse, $\Omega_T(t) = \Omega_0\exp(-(t/\Delta\tau)^2)$, with a duration (FWHM) of $\Delta\tau\sqrt{4\ln 2}$, and an amplitude comparable to the atom-cavity coupling, $\Omega_T(\Delta\tau) \approx 2g$, the excitation is adiabatic if

$$\Delta\tau g \gg 1/\sqrt{2}. \tag{6}$$

This constraint yields a first lower limit for the time interval required to generate one photon, because the population transfer will not work reliably with trigger pulses shorter than the inverse coupling constant, g^{-1}. A second lower limit is the cavity-decay time, $(2\kappa)^{-1}$, which is needed for the emission of the photon out of the cavity.

Up to this point, the finite lifetimes of the cavity field, κ^{-1}, and of the atom's excited state, γ^{-1}, have been omitted in the analytical treatment. To include these two decay channels, we chose $|U\rangle = |u, 0\rangle$, $|E\rangle = |e, 0\rangle$, and $|G\rangle = |g, 1\rangle$ as basis states and simulate the emission process numerically in a density matrix representation. Note that the non-interacting state $|g, 0\rangle$ is not included in this representation. The time evolution of the atom-cavity system is given by the master equation [14],

$$\frac{d}{dt}\varrho = -\frac{i}{\hbar}[H, \varrho] - \Gamma\varrho, \tag{7}$$

where the linear operator Γ describes the effect of all relaxation processes. The elements of $\Gamma\varrho$ are expressed in terms of the relaxation constants, $\gamma_E = \gamma$, $\gamma_G = 2\kappa$, $\gamma_U = 0$ (there is no loss from state $|u, 0\rangle$), and the Einstein coefficients, A_{ki}, for spontaneous transitions between the basis states:

$$[\Gamma\varrho]_{ij} = \frac{1}{2}(\gamma_i + \gamma_j)\varrho_{ij} - \delta_{ij}\sum_k \varrho_{kk}A_{ki}. \tag{8}$$

The first term on the right-hand side of (8) encompasses only losses and dampings of the ϱ_{ij}'s, whereas the second term takes into account the incoherent population flux into basis states. In the present situation, only state $|u, 0\rangle$ is populated by spontaneous emission from $|e, 0\rangle$. For simplicity we assume that this transition contributes 50% to the total decay rate of state $|e, 0\rangle$, i.e. the only non-zero Einstein coefficient is $A_{EU} = \frac{1}{2}\gamma$. The other 50% is due to the direct transition to the non-basis state $|g, 0\rangle$. This decay channel is already included in γ and, hence, taken into account by the first term. Note that the spontaneous decay process $|e, 0\rangle \longrightarrow |g, 1\rangle$ is neglected because of the typically small solid angle of the cavity mode ($\Omega/4\pi \approx 10^{-4}$). Finally, the transient photon emission rate, $2\kappa\varrho_{GG}$, is obtained from the numerical solution of (7).

Results of the simulation are shown in Fig. 2, where a trigger pulse with a Gaussian shape and realistic values for γ and κ were chosen. It is obvious that the generated photon is already emitted from the cavity before the Rabi frequency of the trigger, Ω_T, gets larger than $2g$. This early photon emission occurs if the cavity lifetime, $(2\kappa)^{-1}$, is short with respect
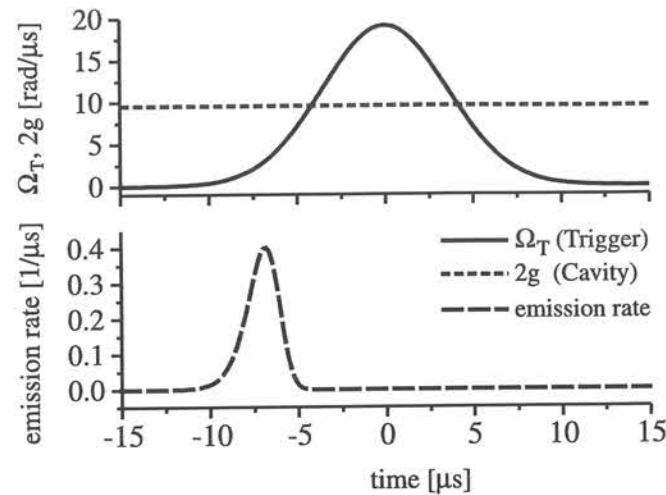
Fig. 2. Numerical simulation of a single-photon pulse. The time evolution of the trigger pulse, $\Omega_T(t)$, and the constant coupling to the cavity mode, $2g$, are shown in the upper part. Below, the corresponding photon emission rate out of the cavity is shown, assuming a cavity-decay constant of $2\kappa = 2\pi \times 1.5$ MHz and a spontaneous emission rate constant of $\gamma = 2\pi \times 6$ MHz. The integral of the emission rate yields a single-photon emission probability of 92%
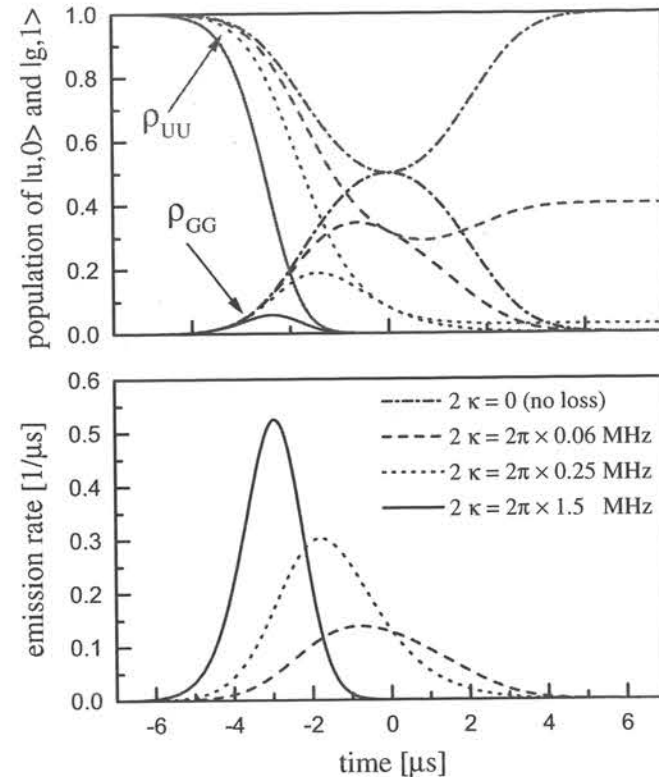

Fig. 3. Population of states $|u, 0\rangle$ and $|g, 1\rangle$ (*upper part*) and photon-emission probability (*lower part*) as a function of time for $\gamma = 2\pi \times 6$ MHz and different values of κ in response to a Gaussian trigger with $\Delta\tau = 5$ μs and a peak Rabi-frequency $\Omega_0 = 2g = 2\pi \times 9$ MHz

to the duration of the trigger pulse. Once the photon is emitted, the remaining system is in state $|g, 0\rangle$, which is decoupled from any further interaction. Therefore it is not really necessary to reach the final condition $\Omega_T \gg 2g$, and the trigger pulse could be switched off even non-adiabatically after the photon emission has taken place.

In Fig. 3, the populations of the states $|u, 0\rangle$ and $|g, 1\rangle$ are plotted together with the photon-emission rate as a function of time for different values of κ. In the loss-free case, neither a photon is emitted nor a photon remains inside the cavity mode, since the initial condition (coupling to the cavity and weak trigger pulse) is restored towards the end of the interaction. This coherent population return [16] to the initial state, $|u, 0\rangle$, occurs with the falling edge of the trigger pulse. It takes place if the cavity-decay time, $(2\kappa)^{-1}$, is longer than the trigger pulse duration. With increasing cavity-decay constant, 2κ, the emission probability not only rises, but also narrows and shifts towards earlier times. From this, one might be tempted to use a bad cavity with large loss for optimum performance. However, since the decay of the cavity field directly affects state $|g, 1\rangle$, the off-diagonal density-matrix element ϱ_{UG} is also damped and, hence, the coherence between states $|u, 0\rangle$ and $|g, 1\rangle$ gets lost. Since an incoherent superposition of these states does not project exclusively onto the dressed state $|a^0\rangle$ (see (2)), some population is transferred to the other dressed states, $|a^\pm\rangle$, which contain a contribution from $|e, 0\rangle$. Hence, the excitation can be lost by spontaneous decay. This loss is expected to be small in the case of strong coupling, $g > (\kappa, \gamma/2)$. For example for the parameters of Fig. 3, the fraction of transient population in the excited state, $|e, 0\rangle$, is less than 10^{-3} throughout the whole process. Therefore spontaneous emission loss in transverse modes other than the cavity mode is negligible and will not degrade the process significantly.

We now consider the more general case where the trigger pulse detuning, Δ_T, and the cavity detuning, Δ_C, from the appropriate atomic resonances are not necessarily equal.

Results are displayed in Fig. 4, which shows the overall photon emission probability, P_{Emission}, and the overall loss probability, P_{Loss}, as functions of Δ_T and Δ_C. Both probabilities are calculated from the time integral of the corresponding emission and loss rate, i.e. $P_{\text{Emission}} = \int 2\kappa\varrho_{GG}dt$ and $P_{\text{Loss}} = \int \frac{1}{2}\gamma\varrho_{EE}dt$, respectively. It is evident from Fig. 4a, that the emission probability as well as the losses have two maxima for $\Omega_0 \ll g$. The reason for this is the cavity-induced coupling of states $|g, 1\rangle$ and $|e, 0\rangle$, producing a new doublet of non-degenerate states. This is the well-known vacuum-Rabi splitting [17], now probed by a weak light pulse coupled to the atom [18]. The splitting survives only for weak driving, but changes drastically for larger trigger amplitudes, $\Omega_0 \geq g$, as shown in Fig. 4c. In this case, the photon emission probability is close to unity if the excitation is Raman resonant ($\Delta_T = \Delta_C$) and the losses are vanishingly small. We emphasize that this holds true even in the case of a resonant excitation ($\Delta_T = \Delta_C = 0$), i.e. an influence of the vacuum-Rabi splitting is neither visible in the emission probability nor in the spontaneous emission losses, as shown in the second row of Fig. 4. For $\Delta_T \neq \Delta_C$, these losses reach their maximum if the trigger pulse is resonant with the atomic transition ($\Delta_T = 0$), and the bandwidth of the losses power-broadens with increasing amplitude of the trigger pulse (from left to right). As mentioned above, the losses are vanishingly small only if the Raman resonance condition, $\Delta_T = \Delta_C$, is fulfilled.

The influence of the trigger amplitude and the common detuning, $\Delta = \Delta_T = \Delta_C$, on the shape of the photon emission probability is shown in the last row of Fig. 4. The duration
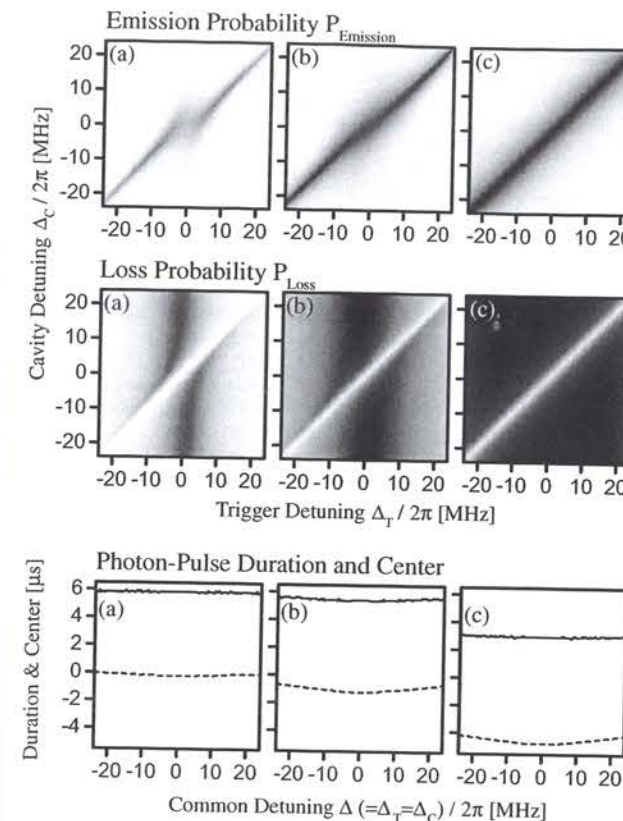
Fig. 4a–c. Photon emission probability, loss of excitation in transverse radiation modes, photon-pulse duration (FWHM) and center as functions of both cavity detuning, Δ_C, and trigger-pulse detuning, Δ_T, from the atomic resonance. The trigger pulse is $\Delta\tau = 5$ μs long. The three columns correspond to three different peak Rabi-frequencies of the trigger pulse (**a** $\Omega_0 = 2\pi \times 0.64$ MHz, **b** $\Omega_0 = 2\pi \times 1.6$ MHz, **c** $\Omega_0 = 2\pi \times 6.4$ MHz). The cavity-decay constant is $\kappa = 2\pi \times 0.75$ MHz, the spontaneous emission constant is $\gamma = 2\pi \times 6$ MHz and the atom-cavity coupling constant is $g = 2\pi \times 4.5$ MHz. The probabilities are shown in shades of gray, ranging from 0.0 (*white*) to 1.0 (*black*). The duration (*solid lines, last row*) and the center position (*dashed lines, last row*) of the emission are only shown for a Raman resonant excitation, i.e. for $\Delta_T = \Delta_C$. The center of the emission probability precedes the center of the trigger pulse in **b** and **c**

(FWHM) and center of the time-dependent emission probability vary only slightly as a function of Δ, but show a strong dependence on the trigger pulse amplitude.

Figure 5 shows the photon-emission probability, the duration and the center of the emission as functions of the trigger pulse amplitude, Ω_0, for a resonant excitation, $\Delta_T = \Delta_C = 0$. The photon-emission probability tends towards an asymptotic limit of $P_{\text{Emission}} = 95\%$ and does not reach unity with increasing trigger pulse amplitude. This limit is caused by damping of ϱ_{UG}, which was already discussed above. Note that the emission probability is already larger than 90% if the peak Rabi-frequency of the trigger, Ω_0, exceeds $g/2$.

The single-photon pulse duration varies between two limits. Figure 5 shows that it does not exceed the FWHM, $\Delta\tau\sqrt{2\ln 2}$, of the trigger-pulse *intensity*. A longer photon pulse is not possible due to the coherent population return mentioned above. Of course, the lower limit of the pulse duration is given by the cavity decay time. It can also be seen from the figure that the center of the emission shifts towards earlier times with increasing amplitude of the trigger pulse. In the case of a Gaussian trigger-pulse, a lower bound for the cen-
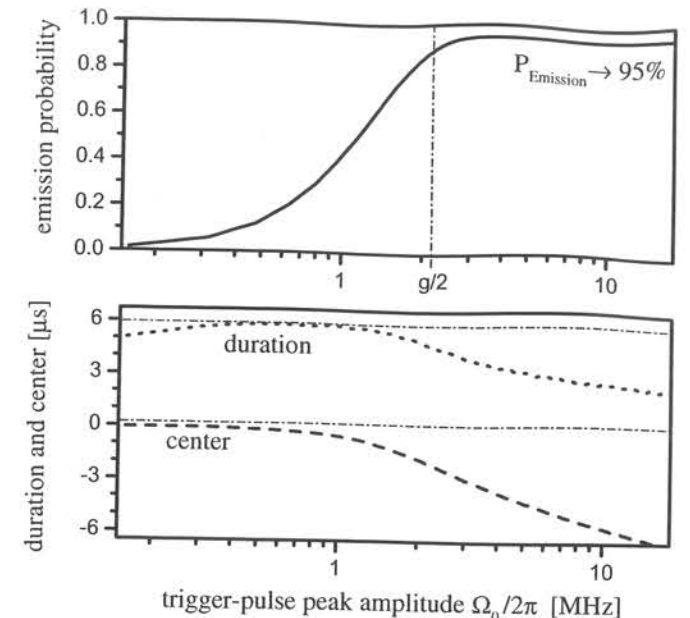
Fig. 5. The photon-emission probability (*solid line*) and its duration (FWHM, *dotted line*) and center position (*dashed line*), shown as a function of the peak Rabi-frequency Ω_0, for an atom-cavity coupling constant $g = 2\pi \times 4.5$ MHz, resonant excitation, $\Delta_T = \Delta_C = 0$, a cavity-decay constant $\kappa = 2\pi \times 0.75$ MHz and a trigger-pulse width of $\Delta\tau = 5$ μs. This corresponds to a duration (FWHM) of $\Delta\tau\sqrt{2\ln 2} = 5.9$ μs, which is also the upper limit of the photon-pulse duration. The lower limit is given by the cavity decay-time, $(2\kappa)^{-1}$. These two limits are indicated by the *horizontal dash-dotted lines*. For the parameters chosen here, the emission probability exceeds 90% if $\Omega_0 > g/2$. This regime is indicated by the *dash-dotted vertical line*

ter of the emission does not exist, since the emission occurs as soon as $\Omega_T(t)$ and g are of comparable magnitude.

We finally discuss two possible applications. First, a repetitive emission of single photons might be desirable. Hence, the emission cycle has to be completed by an independent re-pumping scheme, which brings the system back to the initial state, $|u, 0\rangle$. In Fig. 1, a possible re-pumping mechanism with a microwave π-pulse is indicated. Alternatively, one could think of a cavity-independent Raman re-pumping scheme. With the emission cycle closed, the device could produce a bit-stream of single photons as proposed in [11].

Second, an interesting aspect of the scheme is its possible use for quantum teleportation: a photon is only generated if the atom is initially prepared in state $|u\rangle$. An atom that resides already in state $|g\rangle$ cannot emit a photon. But in both cases the system reaches the same final state $|g, 0\rangle$. It follows that any initial superposition state of the form

$$|\Psi_i\rangle = \alpha|u\rangle + \beta|g\rangle$$

is transformed into

$$|\Psi_f\rangle = |g, 0\rangle \otimes (\alpha|\text{one photon}\rangle + \beta|\text{no photon}\rangle),$$

and an entanglement between the photon and the atom is not established. Instead, the information about the initial atomic state is encoded in the emitted light field. In a setup where the emitted photon is captured by a second remote atom, the initial atomic state might be reinstalled and the quantum state is teleported to the other atom.

We conclude by noting that the proposed scheme requires a single atom localized in the center of a high-finesse optical cavity. This can easily be achieved with a technique recently reported in [19,20]. With an individual atom in the cavity, the photon emission probability – and therefore the shape of the photon wavepacket – can be controlled by varying the shape and the amplitude of the trigger pulse. From our numerical simulations, we expect a photon-emission probability close to unity. It should also be possible to repeat the photon-emission process at a predefined rate using an independent re-pumping scheme to recycle the atom. Moreover, the emission process depends also on the initial state vector of the atom, so that a quantum teleportation of internal atomic states could be realized.

References

1. For a collection of more popular writings, see the special issue on quantum information: A. Zeilinger, p. 35, W. Tittel, G. Ribordy, N. Gisin, p. 41, D. Di Vicenzo, B. Terhal, p. 53: Phys. World **11** (3), (1998)
2. Q.A. Turchette, C.J. Hood, W. Lange, H. Mabuchi, H.J. Kimble: Phys. Rev. Lett. **75**, 4710 (1995)
3. C. Monroe, D.M. Meekhof, B.E. King, W.M. Itano, D.J. Wineland: Phys. Rev. Lett. **75**, 4714 (1995)
4. J.I. Cirac, P. Zoller, H.J. Kimble, H. Mabuchi: Phys. Rev. Lett. **78**, 3221 (1997)
5. W. Tittel, J. Brendel, B. Gisin, T. Herzog, H. Zbinden, N. Gisin: Phys. Rev. A **57**, 3229 (1998)
6. D. Bouwmeester, J.-W. Pan, K. Mattle, M. Eibl, H. Weinfurter, A. Zeilinger: Nature **390**, 575 (1997)
7. D. Boschi, S. Branca, F. De Martini, L. Hardy, S. Popescu: Phys. Rev. Lett. **80**, 1121 (1998)
8. A. Furusawa, J.L. Sørensen, S.L. Braunstein, C.A. Fuchs, H.J. Kimble, E.S. Polzik: Science **282**, 706 (1998)
9. J. Kim, O. Benson, H. Kan, Y. Yamamoto: Nature **397**, 500 (1999)
10. C.K. Law, J.H. Eberly: Phys. Rev. Lett. **76**, 1055 (1996)
11. C.K. Law, H.J. Kimble: J. Mod. Opt. **44**, 2067 (1997)
12. K. Bergmann, B.W. Shore in *Molecular dynamics and stimulated emission pumping*, ed. by H.L. Dai, R.W. Field (World Scientific, Singapore 1995) pp. 315–373
13. A. Kuhn, S. Steuerwald, K. Bergmann: Eur. Phys. J. D **1**, 57 (1998)
14. C. Cohen-Tannoudji, J. Dupont-Roc, G. Grynberg: *Atom-photon interactions* (Wiley New York 1992)
15. A. Messiah: *Quantum mechanics*, Vol. 2 (Wiley New York 1978) Chapt. 17
16. N.V. Vitanov: J. Phys. B **28**, L19 (1995)
17. R.J. Thompson, G. Rempe, H.J. Kimble: Phys. Rev. Lett. **68**, 1132 (1992)
18. J.J. Childs, K. An, M.S. Otteson, R.R. Dasari, M.S. Feld: Phys. Rev. Lett. **77**, 2901 (1996)
19. H. Mabuchi, Q.A. Turchette, M.S. Chapman, H.J. Kimble: Opt. Lett. **21**, 1393 (1996)
20. P. Münstermann, T. Fischer, P.W.H. Pinkse, G. Rempe: Opt. Commun. **159**, 63 (1999)

Vacuum-Stimulated Raman Scattering Based on Adiabatic Passage in a High-Finesse Optical Cavity

M. Hennrich, T. Legero, A. Kuhn, and G. Rempe

Max-Planck-Institut für Quantenoptik, Hans-Kopfermann-Strasse 1, D-85748 Garching, Germany
(Received 21 August 2000)

We report on the first observation of stimulated Raman scattering from a Λ-type three-level atom, where the stimulation is realized by the vacuum field of a high-finesse optical cavity. The scheme produces one intracavity photon by means of an adiabatic passage technique based on a counterintuitive interaction sequence between pump laser and cavity field. This photon leaves the cavity through the less-reflecting mirror. The emission rate shows a characteristic dependence on the cavity and pump detuning, and the observed spectra have a subnatural linewidth. The results are in excellent agreement with numerical simulations.

PACS numbers: 32.80.Qk, 03.67.–a, 42.50.Ct, 42.65.Dr

In the past few years, interesting proposals on the generation of nonclassical states of light in optical cavities [1,2] and on the controlled generation of single photons from such cavities [3,4] were made. All of these schemes are based on a technique known as STIRAP (stimulated Raman scattering involving adiabatic passage) [5,6] or a variant thereof, and incorporate the time dependent interaction of an atom with the field mode of an optical cavity. The operation principle is related to that of a Raman laser [7], with the difference that now a single atom interacts with an empty cavity mode. Other schemes for the preparation of Fock states are based on vacuum Rabi oscillations or, more generally, π pulses in a two-level atom. In these cases, the need for a long-lived excited atomic state restricts experiments to the microwave regime [8,9], where the photon remains stored in a high-Q cavity.

Here, we report on the experimental realization of an excitation scheme that allows one to emit a visible photon into a well-defined mode of an empty cavity. This photon then leaves the cavity in a known direction. Our method is based on the single-photon generation scheme discussed in [4]. It relies on STIRAP [5,6] but, instead of using two delayed laser pulses, we have only one exciting pump laser, combined with a strong coupling of a single atom to a single cavity mode [10,11]. This strong coupling induces the anti-Stokes transition of the Raman process.

Figure 1 depicts the excitation scheme for the ^{85}Rb-atoms used in our experiment. A Λ-type three-level scheme is realized by the two $5S_{1/2}$ hyperfine ground states $F = 3$ and $F = 2$, which we label $|u\rangle$ and $|g\rangle$, respectively. The $F = 3$ hyperfine level of the electronically excited state, $5P_{3/2}$, forms the intermediate state, $|e\rangle$. The atom interacts with a single-mode of an optical cavity, with states $|0\rangle$ and $|1\rangle$ denoting zero and one photon in the mode, respectively. The cavity resonance frequency, ω_C, is close to the atomic transition frequency between states $|e\rangle$ and $|g\rangle$, but far off resonance from the $|e\rangle$ to $|u\rangle$ transition. Hence, only the product states $|e, 0\rangle$ and $|g, 1\rangle$ are coupled by the cavity. For this transition, the vacuum

Rabi frequency,

$$2g(t) = 2g_0 \exp\left[-\left(\frac{tv}{w_C}\right)^2\right], \quad (1)$$

is time dependent since the atom moves with velocity v across the waist w_C of the Gaussian cavity mode. Its peak amplitude is given by the atom-cavity coupling coefficient at an antinode, g_0.

In addition to the interaction with the cavity mode, the atom is exposed to a pump laser beam which crosses the cavity axis at right angle. This beam is placed slightly downstream in the path of the atoms (by δ_x with respect to the cavity axis) and has a waist w_P, therefore causing a time dependent Rabi frequency

$$\Omega_P(t) = \Omega_0 \exp\left[-\left(\frac{tv - \delta_x}{w_P}\right)^2\right]. \quad (2)$$

The pump frequency is near resonant with the transition between $|u, 0\rangle$ and $|e, 0\rangle$, thereby coupling these states.

In a frame rotating with the cavity frequency and the pump laser frequency, the Hamiltonian is given by
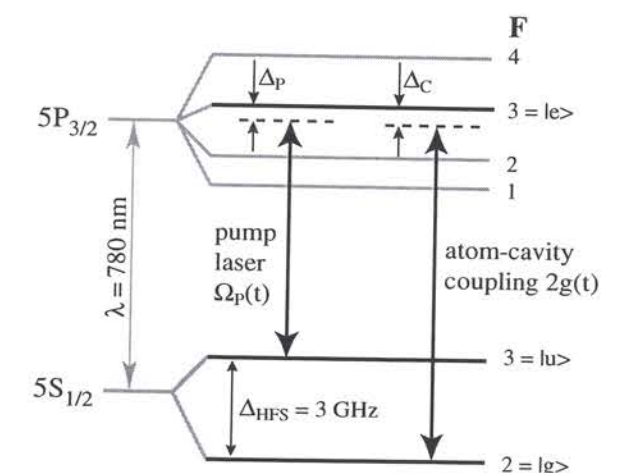

FIG. 1. Scheme of the relevant levels, transitions, and detunings of the ^{85}Rb atom coupled to the pump laser and the cavity.

$$H(t) = \hbar[\Delta_P |u\rangle\langle u| + \Delta_C |g\rangle\langle g|$$
$$+ g(t)(|e\rangle\langle g|a + a^\dagger|g\rangle\langle e|)$$
$$+ \tfrac{1}{2}\Omega_P(t)(|e\rangle\langle u| + |u\rangle\langle e|)]. \qquad (3)$$

Here, Δ_C and Δ_P denote the detunings of the cavity and the pump beam from their respective atomic resonances, and a and $a^\dagger$ are the annihilation and creation operators of the cavity field. The pump beam is treated semiclassically. On Raman resonance, i.e., for $\Delta_C = \Delta_P$, one of the eigenstates of this interaction Hamiltonian reads

$$|a^0(t)\rangle = \frac{2g(t)|u,0\rangle - \Omega_P(t)|g,1\rangle}{\sqrt{4g^2(t) + \Omega_P^2(t)}}. \qquad (4)$$

This is a dark state without any contribution from the electronically excited level $|e,0\rangle$. Therefore losses due to spontaneous emission cannot occur, provided the state vector of the system, $|\Psi\rangle$, follows $|a^0\rangle$ throughout the Raman excitation.

The atom is prepared in state $|u\rangle$ before it enters the empty cavity, i.e., atom and field start in state $|u,0\rangle$. Since the pump beam is displaced by δ_x with respect to the cavity axis, the atom is subject to a counterintuitive delayed pulse sequence, i.e., due to the initial condition $2g \gg \Omega_P$, the evolution starts with $\langle \Psi | a^0 \rangle = 1$. The subsequent interaction with the pump beam leads to $\Omega_P \gg 2g$, which implies the evolution of $|a^0\rangle$ into state $|g,1\rangle$. Provided the state vector $|\Psi\rangle$ is able to follow, the system is transferred to $|g,1\rangle$, and a photon is placed in the cavity mode. Since this photon is emitted with the cavity energy decay rate, 2κ, the empty cavity state, $|g,0\rangle$, is finally reached and the atom-cavity system decouples from any further interaction.

This simple excitation scheme relies on three conditions. First, the detunings of the cavity, Δ_C, and of the pump pulse, Δ_P, must allow a Raman transition, i.e.,

$$|\Delta_C - \Delta_P| < 2\kappa. \qquad (5)$$

Second, the condition for $|\Psi\rangle$ adiabatically following $|a^0\rangle$ must be met [4,5],

$$(2g_0 w_C/v, \Omega_0 w_P/v) \gg 1. \qquad (6)$$

Third, either the interaction time must be significantly longer than $(2\kappa)^{-1}$ to allow the emission of the photon before it is reabsorbed by the atom due to coherent population return [4,6] or, alternatively, the interaction with the pump beam must be strong when the atom leaves the cavity to avoid this reverse process.

A numerical simulation for a single atom crossing the cavity is shown in Fig. 2. To include the cavity-field decay rate, κ, and the spontaneous emission rate of the atom, Γ, we have employed the density-matrix formalism described in [4]. For the resonant situation, $\Delta_P = \Delta_C = 0$, shown here, the total emission probability, P_{emit}, is expected to reach 90%. For the considered waists and amplitudes, Fig. 2(c) shows that P_{emit} reaches its maximum for $\delta_x/v = 45$ μs. Note also that P_{emit} is vanishingly small if
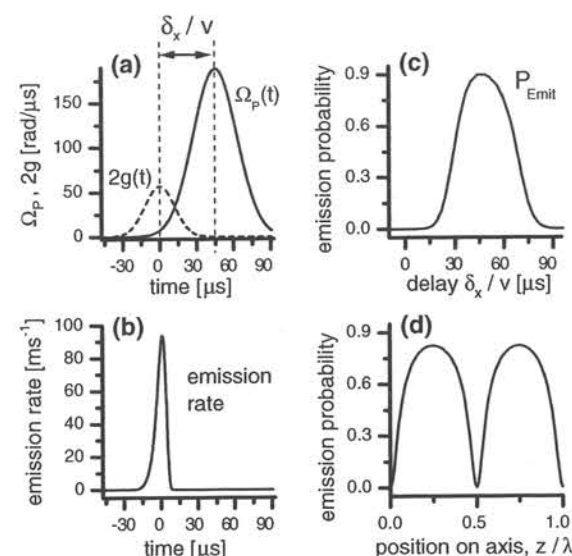
FIG. 2.   Simulation of a resonant atom-cavity interaction sequence for a cavity decay constant, $2\kappa = 2\pi \times 2.5$ MHz, an atomic decay constant of $\Gamma = 2\pi \times 6$ MHz, and atoms traveling at $v = 2$ m/s. (a) $\Omega_P(t)$ and $2g(t)$ shown for experimental amplitudes and waists, $w_C = 35$ μm and $w_P = 50$ μm. (b) Photon emission rate for a delay of $\delta_x/v = 45$ μs. The integral of the rate yields a total photon emission probability, P_{emit}, of 90%. (c) P_{emit} as a function of the delay, δ_x/v, between cavity and pump interaction. (d) P_{emit} as a function of the atomic position on the cavity axis for a delay of $\delta_x/v = 35$ μs.

the interaction with the pump beam coincides or precedes the interaction with the cavity mode. Figure 2(d) shows P_{emit} as a function of the atom's position on the cavity axis for the delay realized in the experiment. Because of the standing wave mode structure, the emission probability is zero at the nodes, and shows maxima at the antinodes. Since the dependence of P_{emit} on the position dependent coupling constant, g, is highly nonlinear and saturates for large g, the gaps around the nodes are much narrower than the plateaus surrounding the antinodes.

Figure 3 depicts the case where $\Delta_P \neq \Delta_C$. It is obvious that P_{emit} is close to unity if the excitation is Raman resonant ($\Delta_P = \Delta_C$). However, for the delay $\delta_x/v = 35$ μs chosen here, a smaller signal is expected for $\Delta_P = \Delta_C = 0$, since the waist of the pump, w_P, is larger than w_C, and resonant excitation of the atom prior to the interaction with the cavity mode cannot be neglected.

To realize the proposed scheme, we have chosen the setup sketched in Fig. 4. A cloud of ^{85}Rb atoms is prepared in the $5S_{1/2}, F = 3$ state and released from a magneto-optical trap (MOT) at a temperature of ≈ 10 μK. A small fraction (up to 100 atoms) falls through a stack of apertures and enters the mode volume of an optical cavity at a speed of 2 m/s. The cavity is composed of two mirrors with a curvature of 50 mm and a distance of 1 mm. The waist of the TEM$_{00}$ mode is $w_C = 35$ μm, and in the antinodes the coupling coefficient is $g_0 = 2\pi \times 4.5$ MHz. The finesse of 61 000 corresponds to a linewidth $2\kappa = 2\pi \times 2.5$ MHz (FWHM), which is significantly smaller than the

FIG. 3.   Photon emission probability as a function of cavity and pump detuning, calculated for a pulse delay of $\delta_x/v = 35$ μs and the parameters of Fig. 2. The chosen delay gives the best fit with the experimental data shown in Fig. 5.

natural linewidth of the ^{85}Rb atoms. While one cavity mirror is highly reflective ($1 - R = 4 \times 10^{-6}$), the transmission of the other is 25× higher to emit the photons in one direction only. A single-photon counting module (SPCM) with a quantum efficiency of 50% is used to detect them.

A reference laser is used to stabilize the cavity close to resonance with the $5S_{1/2}, F = 2 \leftrightarrow 5P_{3/2}, F = 3$ transition with a lock-in technique. However, since an empty cavity is needed for the experiment, this laser is blocked 3.7 ms before the atoms enter the cavity.

The pump beam is close to resonance with the $5S_{1/2}, F = 3 \leftrightarrow 5P_{3/2}, F = 3$ transition and crosses the cavity transverse to its axis. This laser is focused to a waist of 50 μm and has a power of 5.5 μW, which corresponds to a peak Rabi frequency $\Omega_0 = 2\pi \times 30$ MHz.

The desired counterintuitive pulse sequence for STIRAP is realized by time of flight. The atoms first enter the cavity mode and therefore experience a strong coupling on the anti-Stokes transition, whereas the interaction with the pump beam is delayed, since it crosses the cavity mode slightly downstream. This delay has been optimized to achieve a high flux of photons leaving the cavity.
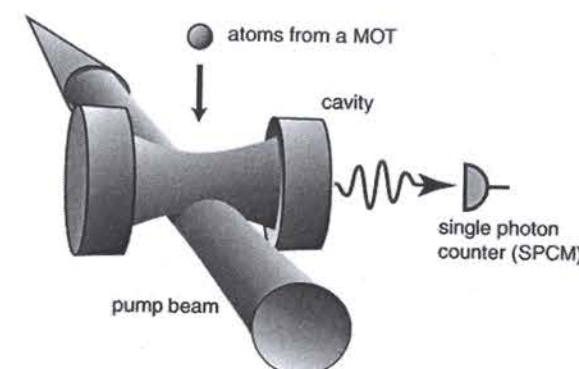
FIG. 4.   Sketch of the experimental setup. The pump beam is displaced with respect to the cavity mode.

Figure 5(a) shows the number of counted photons emerging from the cavity as a function of the pump pulse detuning, Δ_P, in case of a resonant cavity, $\Delta_C = 0$. The detunings of the cavity and the pump laser are both adjusted by means of acousto-optic modulators. To register the data, the MOT has been loaded and dropped across the cavity 50 times. The atom cloud needs 6.5 ms (FWHM) to cross the cavity mode, and, within this interval, the photons emerging from the cavity are measured by the SPCM and recorded by a transient digitizer during 2.6 ms with a time resolution of 25 MHz. Therefore, the signal is observed for a total time of 130 ms. Because of the dark count rate of 390 Hz of the SPCM, the total number of dark counts in the interval is limited to 51 ± 7.

In the resonant case, one expects a small probability for atomic excitation. This could lead to a small but cavity enhanced spontaneous emission into the cavity mode, as has been shown previously [12]. Our numerical simulation shows that an excited atom at the antinode emits into the resonant cavity mode with a probability that can be as high as 26%, indicating that even in this case most of the spontaneously emitted photons are lost in a random direction. This loss explains the smaller peak emission rate with respect to the off-resonant cases discussed below. Note that the cavity mode covers only a small solid angle of $\approx 4\pi \times 2.6 \times 10^{-5}$ sr, therefore
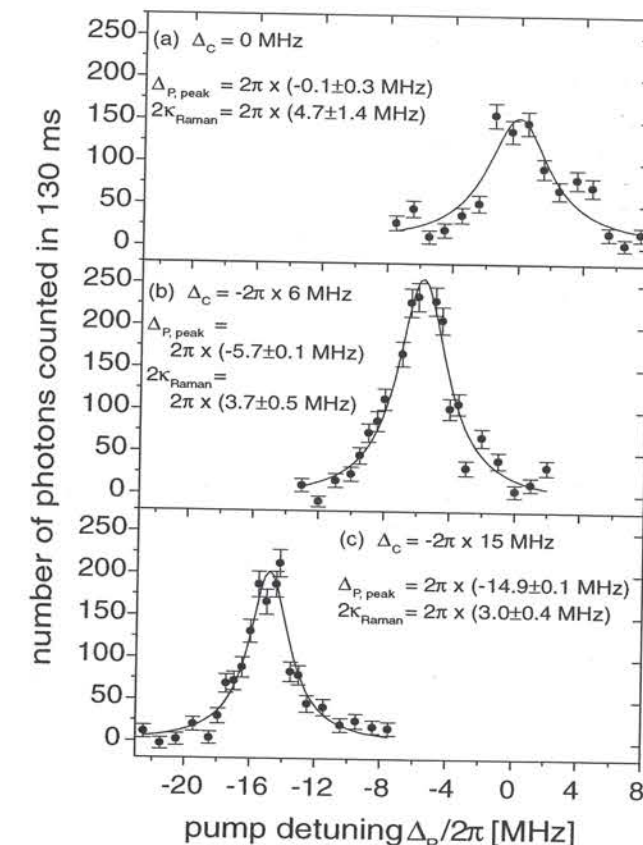
FIG. 5.   Number of photons from the cavity as a function of the pump laser detuning, Δ_P, for three different cavity detunings. The solid lines are Lorentzian fits to the data.

the calculated spontaneous emission rate into the cavity is enhanced by a factor of 10^4. However, the linewidth is subnatural, and therefore the observed signal cannot be attributed to an excitation by the pump beam followed by enhanced spontaneous emission.

This is even more evident if the cavity is detuned [Figs. 5(b) and 5(c)]. The emission peak is pulled away from the atomic resonance following the Raman resonance condition, $\Delta_P = \Delta_C$. Such a displacement proves that the light emission is not the result of a pump transition followed by enhanced spontaneous emission into the cavity. Moreover, Δ_P is too high for an electronic excitation of the atoms. Therefore, the far out-reaching wings of the pump beam no longer excite the atoms prior to their interaction with the cavity mode. The losses vanish, and the peak photon emission probability is higher than for the resonant case. Note also that the observed linewidth is much smaller than the natural linewidth, $\Gamma = 2\pi \times 6$ MHz, of the atom. For $\Delta_C = -2\pi \times 15$ MHz, the line is only 3 MHz wide and approaches the linewidth $2\kappa = 2\pi \times 2.5$ MHz of the cavity, which also limits the width of the Raman transition, since 2κ is the decay rate of the final state, $|g, 1\rangle$.

In our discussion, we have assumed that the atoms interact with the cavity one-by-one. This is justified according to the following estimation: A mechanical slit restricts the atom's maximum distance from the cavity axis to ± 50 μm. The spatial variation of g along [Fig. 2(d)] and perpendicular to the cavity axis reduces the average emission probability to 37% per atom crossing the slit and the pump beam. Because of the low quantum efficiency of the SPCM and unavoidable cavity losses, only about 40% of the generated photons are detected. Therefore the maximum measured rate of 230 events/130 ms corresponds to a generation rate of 4.4 photons/ms, and at least 12 atoms/ms are needed to explain this signal. Since the photon generation takes 12 μs [FWHM, Fig. 2(b)], the probability that a second atom interacts with the cavity simultaneously is 14%. This is small and, hence, negligible.

All observed features are in excellent agreement with our simulation, and we therefore conclude that the photon emission is caused by a vacuum-stimulated Raman transition, i.e., the coupling to the cavity, $g(t)$, and the Rabi frequency of the pump laser, $\Omega_P(t)$, are both high enough to ensure an adiabatic evolution of the system, thus forcing the state vector $|\Psi\rangle$ to follow the dark state $|a^0\rangle$ throughout the interaction. Loss due to spontaneous emission is suppressed, and the photons are emitted into a single mode of the radiation field with well-determined frequency and direction.

The scheme can be used to generate single, well-characterized photons on demand, provided the Raman excitation is performed in a controlled, triggered way. In contrast to other single-photon sources [13], these photons will have a narrow bandwidth and a directed emission. Finally, we state that the photon generation process depends on the initial state of the atom interacting with the cavity. If the atom is prepared in a superposition of states $|g, 0\rangle$ and $|u, 0\rangle$, prior to the interaction, this state will be mapped onto the emitted photon. A second atom placed in another cavity could act as a receiver, and, with the suitable pump pulse sequence applied to the emitting and the receiving atom, a quantum teleportation of the atom's internal state could be realized [14].

This work was partially supported by the focused research program, "Quantum Information Processing," of the Deutsche Forschungsgemeinschaft and the QUBITS project of the IST program of the European Union.

[1] A. S. Parkins, P. Marte, P. Zoller, and H. J. Kimble, Phys. Rev. Lett. **71**, 3095 (1993); A. S. Parkins, P. Marte, P. Zoller, O. Carnal, and H. J. Kimble, Phys. Rev. A **51**, 1578 (1995).

[2] W. Lange and H. J. Kimble, Phys. Rev. A **61**, 63817 (2000).

[3] C. K. Law and J. H. Eberly, Phys. Rev. Lett. **76**, 1055 (1996); C. K. Law and H. J. Kimble, J. Mod. Opt. **44**, 2067 (1997).

[4] A. Kuhn, M. Hennrich, T. Bondo, and G. Rempe, Appl. Phys. B **69**, 373 (1999).

[5] For a review, see K. Bergmann and B. W. Shore in *Molecular Dynamics and Stimulated Emission Pumping*, edited by H. L. Dai and R. W. Field (World Scientific, Singapore, 1995), p. 315–373.

[6] A. Kuhn, S. Steuerwald, and K. Bergmann, Eur. Phys. J. D **1**, 57 (1998).

[7] M. Becker, U. Gaubatz, K. Bergmann, and P. L. Jones, J. Chem. Phys. **87**, 5064 (1987).

[8] G. Nogues, A. Rauschenbeutel, S. Osnaghi, M. Brune, J. M. Raimond, and S. Haroche, Nature (London) **400**, 239 (1999).

[9] B. T. H. Varcoe, S. Brattke, M. Weidinger, and H. Walther, Nature (London) **403**, 743 (2000).

[10] H. Mabuchi, Q. A. Turchette, M. S. Chapman, and H. J. Kimble, Opt. Lett. **21**, 1393 (1996).

[11] P. Münstermann, T. Fischer, P. W. H. Pinkse, and G. Rempe, Opt. Commun. **159**, 63 (1999).

[12] D. J. Heinzen, J. J. Childs, J. E. Thomas, and M. S. Feld, Phys. Rev. Lett. **58**, 1320 (1987); D. J. Heinzen and M. S. Feld, Phys. Rev. Lett. **59**, 2623 (1987).

[13] J. Kim, O. Benson, H. Kan, and Y. Yamamoto, Nature (London) **397**, 500 (1999); C. Brunel, B. Lounis, P. Tamarat, and M. Orrit, Phys. Rev. Lett. **83**, 2722 (1999); C. Kurtsiefer, S. Mayer, P. Zarda, and H. Weinfurter, Phys. Rev. Lett. **85**, 290 (2000); R. Brouri, A. Beveratos, J.-P. Poizat, and P. Grangier, Opt. Lett. **25**, 1294 (2000); P. Michler, A. Imamoğlu, M. D. Mason, P. J. Carson, G. F. Strouse, and S. K. Buratto, Nature (London) **406**, 968 (2000).

[14] J. I. Cirac, P. Zoller, H. J. Kimble, and H. Mabuchi, Phys. Rev. Lett. **78**, 3221 (1997).

Deterministic Single-Photon Source for Distributed Quantum Networking

Axel Kuhn, Markus Hennrich, and Gerhard Rempe

Max-Planck-Institut für Quantenoptik, Hans-Kopfermann-Strasse 1, 85748 Garching, Germany

A sequence of single photons is emitted on demand from a single three-level atom strongly coupled to a high-finesse optical cavity. The photons are generated by an adiabatically driven stimulated Raman transition between two atomic ground states, with the vacuum field of the cavity stimulating one branch of the transition, and laser pulses deterministically driving the other branch. This process is unitary and therefore intrinsically reversible, which is essential for quantum communication and networking, and the photons should be appropriate for all-optical quantum information processing.

A future quantum network connecting remote quantum processors and memories has several advantages in processing quantum information as compared to a local quantum computer, since it combines scalability with modularity. Different kinds of networks have been proposed [1]: one is an all-optical network [2], where the nodes are linear optical components, with quantum information encoded in the number of photons flying from node to node. The nodes perform gate operations based on quantum interference effects between indistinguishable photons. In another, more general, network the nodes also serve as quantum memories storing information, e.g., in long-lived states of atoms located in an optical cavity [3]. The key requirement for such a network is its ability to interconvert stationary and flying qubits and to transmit flying qubits between specified locations [4]. The atom-cavity system, in particular, must be able to transfer quantum information between atoms and photons in a coherent manner [5,6]. It must also act as an emitter and a receiver of single-photon states. These states must therefore be generated by a reversible process. However, all deterministic single-photon emitters demonstrated so far [7–15] do not meet this essential requirement. The reason is that the emission process, namely, an electronic excitation of the system followed by spontaneous emission, cannot be described by a Hamiltonian evolution and, hence, is irreversible.

This Letter describes the realization of an intrinsically reversible single-photon source [3,16–19], which is based on a stimulated Raman process driving an adiabatic passage (STIRAP) [20] between two ground states of a single atom strongly coupled to a single mode of a high-finesse optical cavity [21,22]. A laser beam illuminating the atom excites one branch of the Raman transition, while the cavity vacuum stimulates the emission of the photon on the other branch. STIRAP is slow compared to the photon lifetime in the cavity, so that the field generated inside the cavity is instantaneously mapped to the outside world. Moreover, it employs a dark state, which has two important consequences: first, any electronic excitation is avoided, so that irreversible spontaneous processes do not occur.

Second, the scheme allows one to continuously tune the frequency of the photon within a range that is only limited by the atom-cavity coupling strength. The tuning ability has recently been demonstrated with a beam of atoms passing through the cavity [23]. This experiment produced at most one photon per passing atom, but did not operate as a single-photon source, because its continuous driving scheme simply mapped the random (Poissonian) atom statistics to the photons. The present experiment, however, uses a pulsed driving together with a pulsed recycling. This makes it possible to produce on demand a stream of several single-photon pulses from one and the same atom, triggered by the detection of a "first" photon emitted from the cavity.

Figure 1(a) shows the basic scheme of the photon-generation process. A single ^{85}Rb atom is prepared in state $|u\rangle$, which is the $F = 3$ hyperfine state of the $5S_{1/2}$ electronic ground state. The atom is located in a high-finesse optical cavity, which is near resonant with the 780 nm transition between states $|g\rangle$ and $|e\rangle$. Here, $|g\rangle$ is the $F = 2$ hyperfine state of the electronic ground state, and $|e\rangle$ is the electronically excited $5P_{3/2}(F = 3)$ state. The state of the cavity is denoted by $|n\rangle$, where n is the number of photons. When the atom is placed inside the cavity, the product states $|g, n\rangle$ and $|e, n - 1\rangle$ are coupled by the electric dipole interaction, characterized by the Rabi frequency $\Omega_n = 2g\sqrt{n}$. Here, g is the average atom-cavity coupling constant, which takes into account that neither the position of the atom in the cavity nor the magnetic quantum number of the atom is well defined in the experiment. We assume g to be constant while a pump-laser pulse with Rabi frequency $\Omega_P(t)$ is applied. This laser is close to resonance with the $|u\rangle \leftrightarrow |e\rangle$ transition, so that now the three product states $|u, n - 1\rangle$, $|e, n - 1\rangle$, and $|g, n\rangle$ of the atom-cavity system are coupled. For the one-photon manifold, $n = 1$, and a Raman-resonant excitation, where the detunings of the pump-laser, Δ_P, and the cavity, Δ_C, from the respective atomic transitions are equal, it is straightforward to find the three eigenstates of the coupled atom-cavity system, $|\phi_1^{\pm}\rangle$ and $|\phi_1^0\rangle = [2g|u, 0\rangle - \Omega_P(t)|g, 1\rangle]/\sqrt{4g^2 + \Omega_P^2(t)}$. Note that state $|\phi_1^0\rangle$ is dark, i.e., has no
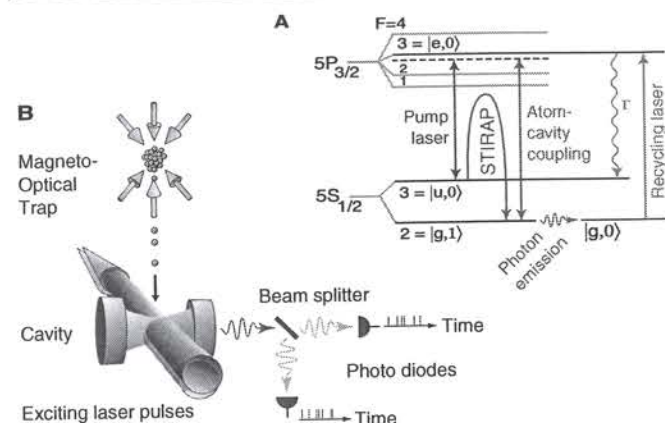
FIG. 1 (color online). Scheme of the experiment. (A) Relevant energy levels and transitions in ^{85}Rb. The atomic states labeled $|u\rangle$, $|e\rangle$, and $|g\rangle$ are involved in the Raman process, and the states $|0\rangle$ and $|1\rangle$ denote the photon number in the cavity. (B) Setup: a cloud of atoms is released from a magneto-optical trap and falls through a cavity 20 cm below in about 8 ms with a velocity of 2 m/s. The interaction time of a single atom with the TEM$_{00}$ mode of the cavity (waist $w_0 = 35$ μm) amounts to about 17.5 μs. The pump and recycling lasers are collinear and overlap with the cavity mode. Photons emitted from the cavity are detected by a pair of photodiodes with a quantum efficiency of 50%.

contribution of the excited state, $|e\rangle$, and is therefore not affected by spontaneous emission.

The dark state $|\phi_1^0\rangle$ is now used to generate a single-photon inside the cavity. This is achieved by establishing a large atom-cavity coupling constant, g, before turning on the pump pulse. In this case, the system's initial state, $|u, 0\rangle$, coincides with $|\phi_1^0\rangle$. Provided the pump pulse rises slowly, the system's state vector adiabatically follows any change of $|\phi_1^0\rangle$, and for a lossless cavity a smooth transition from $|u, 0\rangle$ to $|g, 1\rangle$ is realized as soon as $\Omega_P \gg 2g$. Hence, a single photon is generated in the relevant cavity mode. This photon leaves the cavity through that mirror which is designed as an output coupler. The emission starts as soon as the decaying state, $|g, 1\rangle$, contributes to $|\phi_1^0\rangle$, i.e., already with the rising edge of the pump pulse, because the contribution from $|g, 1\rangle$ is proportional to $\Omega_P^2(t)$. If the pump pulse rises slowly, the emission can therefore end even before $\Omega_P > 2g$. The dynamics of the simultaneous excitation and emission processes determines the duration and, hence, the linewidth of the photon. When the photon is emitted, the final state of the coupled system, $|g, 0\rangle$, is reached. This state is not coupled to the one-photon manifold, and the atom cannot be reexcited. This limits the number of photons per pump pulse and atom to one.

To emit a sequence of photons from one and the same atom, the system must be transferred back to $|u, 0\rangle$ once an emission has taken place. To do so, we apply recycling laser pulses that hit the atom between consecutive pump pulses. The recycling pulses are resonant with the $|g\rangle \leftrightarrow |e\rangle$ transition and pump the atom to state $|e\rangle$. From there, it

decays spontaneously to the initial state $|u\rangle$. Note that state $|e\rangle$ populated by the recycling laser couples to the cavity. However, spontaneous emission into the cavity is suppressed by deliberately choosing a large cavity detuning, Δ_C. The pump laser is detuned by the same amount to assure Raman resonance. If an atom that resides in the cavity is now exposed to a sequence of laser pulses, which alternate between triggering single-photon emissions and reestablishing the initial condition by optical pumping, a sequence of single-photon pulses is produced.

Figure 1(b) shows the apparatus. Atoms are released from a magneto-optical trap and pass through the TEM$_{00}$ mode of the optical cavity, where they are exposed to the sequence of laser pulses. On average, 3.4 atoms/ms enter the cavity [24], so that the probability of finding a single atom inside the cavity is 5.7%, while the probability of having more than one atom is only 0.18% which is negligible. The cavity is 1 mm long and has a finesse of 60 000. One mirror has a 25 times larger transmission coefficient than the other. Therefore, photons are preferentially emitted into one direction. These photons are counted by two avalanche photodiodes which are placed at the output ports of a beam splitter. For each experimental cycle, all photon-arrival times are recorded with transient digitizers with a time resolution of 8 ns.

In the experiment, the electric field amplitudes and, hence, the Rabi frequencies of the pump and recycling pulses have the shape of a sawtooth and increase linearly, as displayed in Fig. 2(a). This leads to a constant rate of
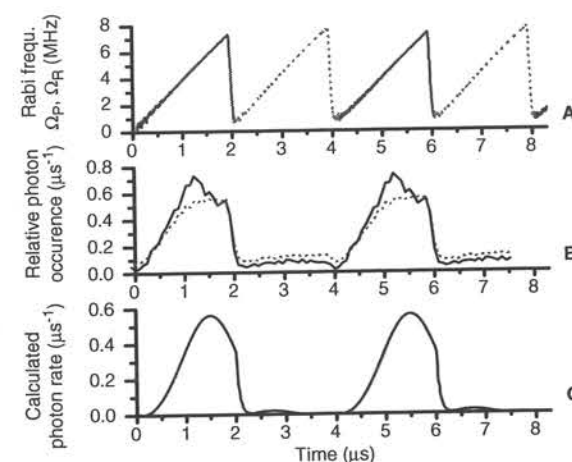
FIG. 2 (color online). Pulse shapes. (A) The atoms are periodically illuminated with 2 μs-long pulses from the pump (solid line) and the recycling laser (dotted line). (B) Measured arrival-time distribution of photons emitted from the cavity (dotted line). The solid line shows the arrival-time distribution of photons emitted from strongly coupled atoms. (C) Simulation of the process with $(g, \Omega_{P,R}^0, \Delta_{P,C}, \Gamma, \kappa) = 2\pi \times (2.5, 8.0, -20.0, 6.0, 1.25)$ MHz, where $\Omega_{P,R}^0$ are the peak Rabi frequencies of the pump and recycling pulses, and Γ and κ are the atom and cavity-field decay rates, respectively.

change of the dark state, $|\phi_1^0\rangle$, during the initial stage of the pump pulses and therefore optimal adiabaticity with minimal losses to the other eigenstates. The linear slope of the recycling pulses suppresses higher Fourier components and therefore reduces photon emission into the detuned cavity. Note that the recycling process is finished before the end of the pulse is reached, so that the final sudden drop in Rabi frequency does not influence the atom.

Also shown in Fig. 2 are two measured arrival-time distributions of the photons and a simulation of the photon-emission rate for typical experimental parameters. The simulation is based on a numerical solution of the system's master equation [22] which takes into account the decay of the relevant states. The simulation [Fig. 2(c)] reveals that the pump-pulse duration of 2 μs is slightly too short, as the emitted photon pulse is not completely finished. This is also observed in the photon arrival-time distribution [Fig. 2(b)]. Here, the measured data agree well with the simulation if only photons from strongly coupled atoms are considered (solid line). For these, we assume that several photons are detected within the atom-cavity interaction time. If solitary photons, which we attribute to weakly coupled atoms, are included in the analysis, the arrival-time distribution is given by the dotted line. Note that the envelope of the photon pulses is well explained by the expected shape of the single-photon wave packets, and therefore cannot be attributed to an uncertainty in emission time, which is not present for a unitary process. Assuming transform-limited Gaussian pulses, we infer a single-photon linewidth of $\Delta\nu = 340$ kHz (FWHM) from the 1.3 μs photon-pulse duration (FWHM). We emphasize that the pump-pulse duration was adjusted to maximize the number of photons per atom. Longer pump pulses would not truncate the photon pulses and, hence, would slightly increase the emission probability per pulse, but due to the limited atom-cavity interaction time, the total number of photons per atom would be reduced.

Figure 3 displays an example of the photon stream recorded while single atoms fall through the cavity one after the other. Obviously, the photon sequence is different for each atom. In particular, not every pump pulse leads to a detected photon, since the efficiencies of photon generation and photon detection are limited. The second-order
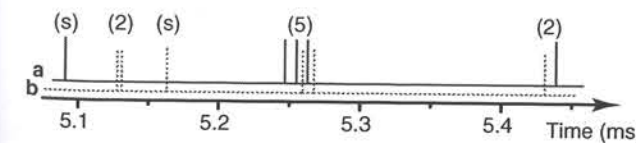
FIG. 3 (color online). Photon sequence: clip of the photon streams arriving at the photodiodes D1 and D2 (traces a and b, respectively,). Several sequences of two (2) and five (5) photon emissions are observed, with durations comparable to the atom-cavity interaction time. The solitary events (s) are either dark counts, or, more likely, photons coming from atoms that are only weakly coupled to the cavity.

intensity correlation function of the emitted photon stream is shown in Fig. 4. Displayed is the cross correlation of the photon streams registered by the two photodiodes D1 and D2. It is defined as $g^{(2)}(\Delta t) = \langle P_{D1}(t)P_{D2}(t - \Delta t)\rangle / (\langle P_{D1}(t)\rangle\langle P_{D2}(t)\rangle)$, where $P_{D1}(t)$ and $P_{D2}(t)$ are the probabilities to detect a photon at time t with photodiode D1 and D2, respectively. Note that all photon-arrival times are recorded to calculate the full correlation function, without the otherwise usual restriction of a simple start/stop measurement which would consider only neighboring events. Of course, $g^{(2)}$ includes not only correlations between photons emitted from the cavity but also those involving detector-noise counts. This last contribution has been determined from an independent measurement of the detector-noise count rate. The result is indicated by the time-independent hatched area in Fig. 4. Only the excess signal, $\tilde{g}^{(2)}(\Delta t) = g^{(2)}(\Delta t) - g^{(2)}_{noise}$, reflects the true photon statistics of the light emitted from the atom-cavity system.

The correlation function, $\tilde{g}^{(2)}(\Delta t)$, oscillates with the same periodicity as the sequence of pump pulses. This indicates that photons are emitted only during the pump pulses, and no emissions occur when recycling pulses are applied. The nearly Gaussian envelope of the comblike function is obviously a consequence of the limited atom-cavity interaction time. The most remarkable feature in Fig. 4 is the missing correlation peak at $\Delta t = 0$. In fact, photon antibunching together with $\tilde{g}^{(2)}(0) \approx 0$ is observed. This clearly demonstrates the nonclassical character of the emitted light, and proves that (a) the number of emitted photons per pump pulse is limited to one, and (b) no further emission occurs before the atom is recycled to its initial state. Note that the relatively large noise contribution is no intrinsic limitation of our system but reflects only the low atomic flux through the cavity in the present experiment.

We emphasize that the detection of a first photon signals the presence of an atom in the cavity and fixes the atom number to one. The photons emitted from this atom during subsequent pump pulses dominate the photon statistics and
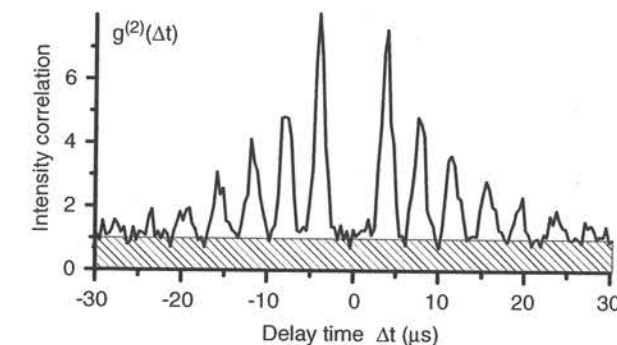
FIG. 4 (color online). Second-order intensity correlation of the emitted photon stream, averaged over 15 000 experimental cycles (loading and releasing of the atom cloud) with a total number of 184 868 photon counts. The hatched area represents correlations between photons and detector-noise counts.

give rise to antibunching. Such an antibunching would not be observed for faint laser pulses, since a random photon statistics applies to each pulse. The areas of the different peaks of the correlation function in Fig. 4 reflect the probability for the emission of further photons from one and the same atom. They are determined from a lengthy but straightforward calculation which relates the number of correlations per pulse with the total number of photons. Using the data displayed in Fig. 4, the result for the conditional emission of another photon during the (next, 3rd, 4th, 5th, 6th, 7th) pump pulse is (8.8, 5.1, 2.8, 1.4, 0.8, 0.5)%. Note that the probabilities for subsequent emissions decrease, since the photon-emission probability, P_{emit}, depends on the location of the moving atom. It is highest for an atom in an antinode and decreases if the atom moves away from this point. It is not possible to control the atom's location in the present experiment, but it is possible to calculate $P_{emit}(z)$ from the experimental data. Here, z is the atom's vertical position relative to the cavity axis, and $P_{emit}(z)$ is averaged over all possible atomic trajectories in the horizontal xy plane. Assuming a Gaussian z dependence, the deconvolution of $\tilde{g}^{(2)}(\Delta t)$ gives $P_{emit}(z) = 0.17 \exp[-(z/15.7 \; \mu m)^2]$. For $z = 0$, the average photon-emission probability of 17% is smaller than the calculated value of 67% for an atom in an antinode of the cavity. It follows that a system combining a cavity and a single atom at rest in a dipole trap [25,26], or a single ion at rest in a rf trap [27,28], should allow one to generate a continuous bit stream of single photons with a large and time-independent efficiency [21,22]. The photon repetition rate is limited by the atom-cavity coupling constant, g, which one could push into the GHz regime by using smaller cavities of wavelength-limited dimensions in, e.g., a photonic band gap material.

In conclusion, we have shown that a coupled atom-cavity system is able to emit single photons on demand. Moreover, it is possible to generate a sequence of up to seven photons on demand from one and the same atom in a time interval of about 30 μs. These photons are all generated in a well-defined radiation mode. They should have the same frequency and a Fourier-transform limited linewidth, limited from above by the decay rate of the cavity field [23]. It follows that one can expect the photons to be indistinguishable and, therefore, ideal for all-optical quantum computation schemes [2]. Moreover, the photon-generation process is unitary. This makes it possible to produce arbitrarily shaped single-photon pulses by suitably tailoring the envelope of the pump pulse. For symmetric pulses, the emission process can be reversed. This should allow one to transfer the photon's quantum state to another atom located in another cavity. Such a state mapping between atoms and photons is the key to quantum tele-

portation of atoms between distant nodes in a quantum network of optical cavities [3].

This work was supported by the research program "Quantum Information Processing" of the Deutsche Forschungsgemeinschaft and by the European Union through the IST (QUBITS) and IHP (QUEST) programming.

[1] See, e.g., C. Monroe, Nature (London) 416, 238 (2002).
[2] E. Knill, R. Laflamme, and G. J. Milburn, Nature (London) 409, 46 (2001).
[3] J. I. Cirac, P. Zoller, H. J. Kimble, and H. Mabuchi, Phys. Rev. Lett. 78, 3221 (1997).
[4] D. P. DiVincenzo, Fortschr. Phys. 48, 771 (2000).
[5] X. Maître et al., Phys. Rev. Lett. 79, 769 (1997).
[6] S. Brattke, B. T. H. Varcoe, and H. Walther, Phys. Rev. Lett. 86, 3534 (2001).
[7] J. Kim, O. Benson, H. Kan, and Y. Yamamoto, Nature (London) 397, 500 (1999).
[8] B. Lounis and W. E. Moerner, Nature (London) 407, 491 (2000).
[9] C. Kurtsiefer, S. Mayer, P. Zarda, and H. Weinfurter, Phys. Rev. Lett. 85, 290 (2000).
[10] R. Brouri, A. Beveratos, J.-P. Poizat, and P. Grangier, Opt. Lett. 25, 1294 (2000).
[11] P. Michler et al., Nature (London) 406, 968 (2000).
[12] C. Santori et al., Phys. Rev. Lett. 86, 1502 (2001).
[13] Z. Yuan et al., Science 295, 102 (2002).
[14] P. Michler et al., Science 290, 2282 (2000).
[15] E. Moreau et al., Appl. Phys. Lett. 79, 2865 (2001).
[16] S. van Enk et al., J. Mod. Opt. 44, 1727 (1997).
[17] A. S. Parkins, P. Marte, P. Zoller, and H. J. Kimble, Phys. Rev. Lett. 71, 3095 (1993).
[18] A. S. Parkins et al., Phys. Rev. A 51, 1578 (1995).
[19] T. Pellizari, S. A. Gardiner, J. I. Cirac, and P. Zoller, Phys. Rev. Lett. 75, 3788 (1995).
[20] N. V. Vitanov, M. Fleischhauer, B. W. Shore, and K. Bergmann, Adv. At. Mol. Opt. Phys. 46, 55 (2001).
[21] C. K. Law and H. J. Kimble, J. Mod. Opt. 44, 2067 (1997).
[22] A. Kuhn, M. Hennrich, T. Bondo, and G. Rempe, Appl. Phys. B 69, 373 (1999).
[23] M. Hennrich, T. Legero, A. Kuhn, and G. Rempe, Phys. Rev. Lett. 85, 4872 (2000).
[24] The flux of atoms is determined by a statistical analysis of the emitted light, with continuous pump and recycling lasers exciting the falling atoms. As the cavity acts as a detector, noninteracting atoms are ignored, so that its spatial mode structure is taken into account.
[25] N. Schlosser, G. Reymond, I. Protsenko, and P. Grangier, Nature (London) 411, 1024 (2001).
[26] S. Kuhr et al., Science 293, 278 (2001).
[27] G. R. Guthörlein et al., Nature (London) 414, 49 (2001).
[28] A. B. Mundt et al., e-print quant-ph/0202112 [Phys. Rev. Lett. (to be published)].

Comment on "Deterministic Single-Photon Source for Distributed Quantum Networking"

A recent Letter [1] describes an experiment to generate single photons within the setting of cavity QED. The authors claim that "a sequence of single photons is emitted on demand" and that their results represent "the realization of an intrinsically reversible single-photon source." Although their work is certainly an advance towards these goals, unfortunately the observational evidence reported in Ref. [1] does not support the principal claims of the demonstration of a deterministic source of single photons, nor of emission that is suitable for the coherent transfer of quantum states over a network. The underlying difficulties are that (1) photons are emitted at random and not "on demand" due to the random arrival of atoms into the interaction region, (2) the photon stream is super-Poissonian because of fluctuations in atom number, and (3) the pulse phase is random and unknown due to the stochastic character of atomic trajectories.

The data presented in Fig. 4 of Ref. [1] display the second-order intensity correlation function $g^{(2)}_{D_1,D_2}(\tau)$ for the cross-correlation of photoelectric counting events from two detectors (D_1, D_2) as a function of time separation τ. Somewhat surprisingly, $g^{(2)}_{D_1,D_2}(\tau) \gtrsim 1$, and, in particular, $g^{(2)}_{D_1,D_2}(0) \simeq 1$, so that the inferred photon statistics are *super-Poissonian* $\langle \Delta n^2 \rangle > \langle n \rangle$ [2]. This is in marked contrast to the behavior required for an on-demand single-photon source, for which $g^{(2)}(t_0) \simeq 0$ at predetermined times t_0, with *sub-Poissonian* photon statistics $\langle \Delta n^2 \rangle < \langle n \rangle$ [2]. The authors attribute this disparity to detection events other than those arising from photons emitted from the cavity. *However, $g^{(2)}_{D_1,D_2}(0)$ would remain greater than unity even if the background light were eliminated altogether, making $\tilde{g}^{(2)}$ in [1] specious.* Furthermore, neither $g^{(2)}_{D_1,D_2}$ nor $\tilde{g}^{(2)}$ incorporate nonstationarity of the underlying processes, so that conclusions about nonclassicality are not well supported.

To illustrate these points, consider the well-studied problem of resonance fluorescence from a two-state atom, with intensity correlation function $g^{(2)}_A(\tau)$ [2]. If observations are made not for a single atom but rather from a volume with a stochastic variation in atom number N, the resulting intensity correlation function $g^{(2)}_{D_1,D_2}(\tau)$ is of a markedly different form from $g^{(2)}_A(\tau)$, as illustrated in Fig. 1. *Significantly, Fig. 1 for free-space emission reproduces the essential characteristics of Fig. 4 in Ref. [1] for emission within a cavity, including that the light is super-Poissonian [4].* The commonality of these two figures arises because of fluctuations in the number of "source" atoms about which there is no *a priori* knowledge. For independent single-atom emitters, the observation of sub-Poissonian *photon statistics* requires sub-Poissonian *atom statistics*, with $g^{(2)}_{D_1,D_2}(0) < 1$ in direct correspondence to the reduction $Q_A \equiv \frac{\overline{(\Delta N)^2} - \bar{N}}{\bar{N}} < 0$ [3]. Strategies to achieve $Q_A < 0$ include conditional detection, both for Fig. 1 and for Fig. 4 in Ref. [1] [2,5].
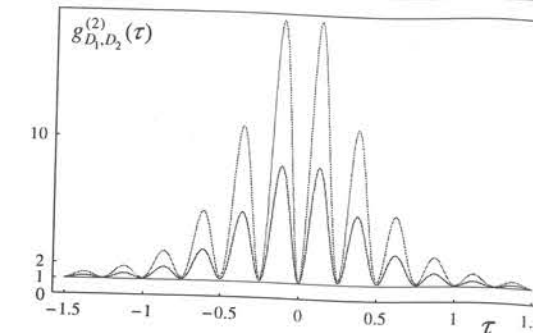
FIG. 1 (color online). $g^{(2)}_{D_1,D_2}(\tau)$ versus delay τ for the fluorescent light from a beam of atoms with average number $\bar{N} = 0.1$. The line at $g^{(2)}_{D_1,D_2}(\tau) = 1$ represents the Poisson limit for coherent light of the same mean counting rates at (D_1, D_2). τ is measured in units of the transit time t_0. The generalized Rabi frequency $\Omega' t_0 = 25$, and transverse decay rate $\beta t_0 = 0.1$. The lower trace is for background to signal ratio $= 0.5$ (appropriate to Ref. [1]), while the upper trace has no background [3].

In addition to fluctuations in arrival time and atom number, the experiment of Ref. [1] suffers from a lack of atomic localization with respect to the spatially varying coupling coefficient $g(\vec{r})$. As a result, the output pulse shapes and phases for photon emissions vary in a random fashion. A typical atom in [1] moves $\pm \frac{\lambda}{4}$ along the cavity axis during its transit, leading to an unknown phase ϕ for the emitted field, which varies from one pulse to the next. *Such randomness in ϕ makes the field unsuitable for the quantum network protocols cited in Refs. [3,16–19] of Kuhn et al. [1].* Moreover, reversible transmission to a second atom-cavity system requires knowledge of the actual time of the initial emission, as well as an "event" ready atom at the remote location. Neither of these capabilities follows from the experiment reported in Ref. [1].

H. J. Kimble
California Institute of Technology 12-33
Pasadena, California 91125, USA

[1] A. Kuhn, M. Hennrich, and G. Rempe, Phys. Rev. Lett. 89, 067901 (2002).
[2] *Optical Coherence and Quantum Optics*, edited by L. Mandel and E. Wolf (Cambridge University Press, Cambridge, 1995), Sec. 15.6.
[3] H. J. Kimble, M. Dagenais, and L. Mandel, Phys. Rev. A 18, 201 (1978), Eq. (31); see quant-ph/0210032.
[4] Quantitative differences (e.g., around $\tau = 0$) could be resolved by a three-state model with pumping and recycling.
[5] In [1] the mean number of photoelectric events per atom per pumping cycle is $\bar{n} \sim 0.04 \ll 1$. This low efficiency and the high background rate severely limit any sub-Poissonian effect via conditional detection [2].

Kuhn, Hennrich, and Rempe Reply: A recent Comment [1] addresses the question of whether a deterministic and intrinsically reversible single-photon source has been demonstrated in Ref. [2]. The author of [1] admits that [2] is an advance towards these goals, but he has four objections.

First, reversibility has not been demonstrated. This is no objection, since there is no such claim in Ref. [2]. We point out only that the Raman process used for photon generation is intrinsically reversible. This has been shown, in fact, by the author of [1] in [3].

Second, the stochastic trajectories of the atoms lead to phase fluctuations. These are neglected in [2], since the velocity of the atoms along the cavity axis is restricted to ± 5 mm/s, which leads to a phase jitter below $\pm \pi/40$ for a 2 μs long pulse. This has a negligible influence on the Raman process. Preserving a fixed phase relation between several atoms at different locations requires technical efforts which are beyond the scope of [2].

Third, it is claimed that the fluorescence from an ensemble of continuously pumped two-state atoms (Fig. 1 in [1]) reproduces the essential characteristics of our experiment. This comparison is inadequate, since $g^{(2)}(\tau) \geq 1$ is due to out-of-phase Rabi oscillations of different atoms. In [2], however, the emission probabilities of all atoms oscillate in phase because the pump laser operates periodically. This leads to a periodic modulation of $g^2(\tau)$. In Fig. 4 in [2], this contribution is hidden in the noise. To illustrate its effect, it is necessary to look at a measurement with increased atom flux [4]: Fig. 1 shows the oscillatory different-atom contribution as a hatched area, and a pedestal involving background counts as a cross-hatched area. Note that the oscillatory contribution has a time-independent amplitude. It follows that $g^{(2)}(0)$ is mainly ($> 60\%$) determined by different atoms that emit simultaneously. As the oscillatory contribution is not visible in Fig. 4 of [2], many-atom emissions can be neglected there. The fact that $g^{(2)}(0)$ does not exceed the background contribution, together with the large correlation peaks at $\tau = \pm 4$ μs, proves that a single atom emits at most a single photon per pulse. Note that for a periodically driven Poissonian emitter, $g^{(2)}(0)$ would be at least as large as all other correlation peaks.

Fourth, the author of [1] says that the measured correlation function does not support the deterministic generation of single photons. It is argued that, without *a priori* knowledge about the presence of an atom in the cavity, the Poissonian atom statistics is simply mapped to the photon statistics. This point has already been addressed in [2], where we "emphasize that the detection of a first photon signals the presence of an atom... photons emitted from this atom during subsequent pump pulses dominate the photon statistics and give rise to antibunching."
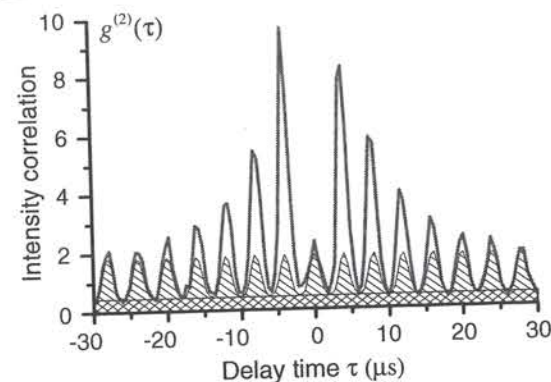
FIG. 1 (color online). Intensity correlation function, $g^{(2)}(\tau)$, for a flux of 10 atoms/ms. The hatched and cross-hatched areas indicate, respectively, the different-atom and the background-noise contributions.

However, a quantitative analysis was not presented in [2], since no established procedure exists to analyze a nonstationary nonclassical light source. In our experiment, a possible protocol is to interpret every photon detected during a pump pulse as a flag indicating the presence of an atom and then to restrict the statistical analysis to the light emitted during the adjacent pump intervals. These constitute a set of N pump intervals conditioned on the presence of atoms. The events in this set form a new data stream which is used to calculate the correlation function, $g^{(2)}(\Delta i) = \sum_{i=1}^{N} E_1(i)E_2(i + \Delta i)/(N \bar{E}_1 \bar{E}_2)$, where $E_{1,2}(i)$ are the numbers of events observed by detectors $D_{1,2}$ during the ith pulse in the new data stream. Application of this straightforward analysis to the original data of [2] yields $g^{(2)}(\Delta i = 0) = 0.25(11)$ and $g^{(2)}(\Delta i \neq 0) = 1.00(22)$. This demonstrates that the photon statistics conditioned on the presence of atoms is sub-Poissonian, as can be expected from the antibunching effect shown in [2].

Axel Kuhn, Markus Hennrich, and Gerhard Rempe
Max-Planck-Institut für Quantenoptik
Hans-Kopfermann-Strasse 1
85748 Garching, Germany

[1] H. J. Kimble, preceding Comment, Phys. Rev. Lett. **90**, 249801 (2003).
[2] A. Kuhn *et al.*, Phys. Rev. Lett. **89**, 067901 (2002).
[3] J. I. Cirac *et al.*, Phys. Rev. Lett. **78**, 3221 (1997).
[4] A. Kuhn *et al.*, in *Quantum Information Processing*, edited by G. Leuchs and T. Beth (Wiley-VCH, Weinheim, 2003), pp. 182–195.

Optical Cavity QED: Fundamentals and Application as a Single-Photon Light Source

AXEL KUHN and GERHARD REMPE

Max-Planck-Institut für Quantenoptik
Hans-Kopfermann-Str. 1
D-85748 Garching, Germany

1. – Introduction

Within the last few years, a major effort in the development of quantum cryptography, quantum communication and quantum information processing has been undertaken worldwide. Special attention has been paid to the realization of decoherence-free quantum systems for the storage of individual quantum bits (qubits) and to the conditional coupling between these qubits for the processing of quantum information. On the one hand, schemes coupling internal atomic states with external states of the atomic motion (e.g. in an ion trap) were studied, and on the other hand, the coupling of internal atomic states to quantized modes of the radiation field has been investigated. In this chapter, we concentrate on the latter. We focus our attention on an adiabatic coupling scheme between a single atom and an optical cavity, which allows one to populate either Fock states on demand, or to emit single photons into a well-defined mode of the radiation field outside the cavity. Such a deterministic single-photon source would not only enhance the security of quantum cryptography schemes [1], but would also enable optical quantum information processing with linear components [2].

The atom-cavity coupling scheme combines cavity quantum electrodynamics (CQED) with a technique known as stimulated Raman scattering by adiabatic passage (STIRAP) [3-5]. To describe the scheme, we first introduce the relevant features of CQED and the Jaynes-Cummings model [6, 7], which describes the interaction of a two-level

atom with a single lossless cavity mode. Next, we discuss the transmission properties of a dissipative cavity containing an atom and the modification of the spontaneous emission properties of the atom, like the Purcell effect [8-11]. We then describe the adiabatic passage technique. It employs a three-level atom with two dipole transitions driven by two radiation fields. One of them comes from a laser, the other is that of a cavity strongly coupled to the atom. We show how to treat the atom and the two radiation fields in a dressed-state basis [12], and how the state vector of the coupled system can be changed in such a way that exactly one photon is placed into the cavity. This photon can escape through one of the mirrors, thereby forming a single-photon pulse [13]. We evaluate the adiabaticity criterion to estimate possible losses, and compare our experimental results with a numerical simulation of the process. For comparison, we also discuss a proposal [14] where the emission of a single photon from a coupled atom-cavity system is investigated in the bad-cavity regime.

2. – A Short Review of Cavity Quantum Electrodynamics

In this section, we briefly review the interaction of a single two-level atom with a quantized mode of the radiation field in a cavity. First, the basic properties of optical cavities are introduced and a simple scheme to quantize the field is presented. We then introduce the interaction of a single two-level atom with a light field in free space, and extend this discussion to the full quantum-mechanical description of an atom coupled to a single mode of a cavity, leading to the Jaynes-Cummings picture. Finally, we describe the normal-mode splitting of a coupled atom-cavity system and the enhancement of the spontaneous emission rate of an atom coupled to a cavity.

2'1. *Optical High-Finesse Cavities.* – We first restrict our discussion to a one-dimensional Fabry-Perot cavity with mirror separation l, mirror reflectivity, $\mathcal{R}$, close to one, mirror transmission, $\mathcal{T}$, and mirror absorption loss, $\mathcal{L}$. Light of wavelength λ and intensity I_{in} impinging on one of the cavity mirrors gives rise to a circulating intensity

$$(1) \qquad I_{circ} = \frac{I_{in}\mathcal{T}_{max}/\mathcal{T}}{1 + 4(\mathcal{F}/\pi)^2 \sin^2(kl)},$$

where $k = 2\pi/\lambda$ is the wavenumber of the light, $\mathcal{T}_{max} = \mathcal{T}^2/(1-\mathcal{R})^2$ the maximum transmission and

$$(2) \qquad \mathcal{F} = \frac{\pi\sqrt{\mathcal{R}}}{1-\mathcal{R}}$$

the cavity finesse. The frequency difference between two neighbouring transmission maxima is called the free spectral range, $FSR = \pi c/l$. Since we are interested in a high mirror reflectivity, the cavity transmission in the vicinity of a resonance can be described by the Lorentzian

$$(3) \qquad \mathcal{T}_{\text{cavity}} \propto \frac{\kappa^2}{\kappa^2 + \Delta_L^2},$$

(a)   (b)
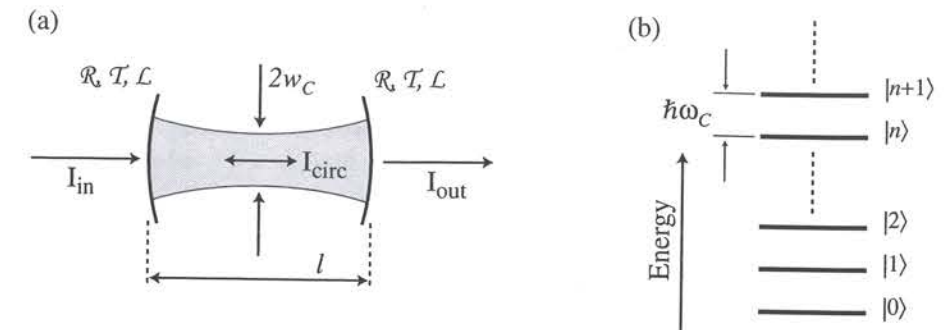
Fig. 1. – **(a)** One dimensional Fabry-Perot cavity of length l with input intensity I_{in}, circulating intensity I_{circ} and transmitted intensity I_{out}. The mirrors have the reflectivity $\mathcal{R}$, transmission $\mathcal{T}$, and absorption loss $\mathcal{L}$. The waist of the TEM_{00} mode is w_C. **(b)** Ladder of Fock states (photon number states) showing the energy stored in a single TEM_{00} mode of frequency ω_C. Like for an harmonic oscillator, the level spacing, $\hbar\omega_C$, is equidistant, and the lowest lying state $|0\rangle$ has a zero-point energy of $\hbar\omega_C/2$.

where $\Delta_L = \omega_L - \omega_C$ is the difference between the laser frequency and the frequency of the cavity resonance. The linewidth (FWHM) is $2\kappa = FSR/\mathcal{F}$. Note that the decay rate of the cavity field, κ, is only determined by the mirror reflectivity and the spacing of the mirrors.

To achieve a stable single-mode operation in a real cavity, curved mirrors are used, as shown in fig. 1(a). As long as the mirror curvature, R, is large with respect to the mirror distance, all angles within the cavity remain small and the system can be treated in the paraxial approximation. In this case, Hermite-Gaussian or Laguerre-Gaussian cavity eigenmodes are obtained. We concentrate on the Gaussian TEM_{00} mode to simplify the further discussion. The smallest ($1/e$ field strength) radius of this mode is called its waist, w_C, which is given by

$$(4) \qquad w_C^2 = \frac{\lambda}{2\pi}\sqrt{l(2R-l)}.$$

For a cavity length l shorter than the Rayleigh length, $z_R = \pi w_C^2/\lambda$, the variation of the mode diameter along the cavity axis can be neglected, and the spatial intensity distribution of the TEM_{00} mode is given by

$$(5) \qquad I_{sw}(\mathbf{r}) = 4I_{circ}|\psi(\mathbf{r})|^2 \qquad \text{with} \qquad \psi(\mathbf{r}) = \cos(kz)\exp\left(-(x^2+y^2)/w_C^2\right),$$

where the modefunction $\psi(\mathbf{r})$ reflects the standing wave in the cavity. It is normalized to one at the antinodes. The mode volume is defined by

$$(6) \qquad V \equiv \int |\psi(\mathbf{r})|^2 d\mathbf{r} = \frac{\pi}{4}w_C^2 l.$$

2˙2. Field Quantization. – In this section, we briefly discuss the quantization of the electromagnetic field in the cavity. Without loss of generality, we restrict ourselves to a single mode of the cavity with resonance frequency ω_C, as in the previous section. For each photon added to this mode, the energy stored in the cavity increases by $\hbar\omega_C$, and for n photons in the mode the total energy is $\hbar\omega_C(n + \frac{1}{2})$, where the zero-point energy of $\hbar\omega_C/2$ has been associated with the vacuum field. The equidistant energy spacing imposes an analogue treatment of the cavity's photon-number states, the so-called Fock states, $|n\rangle$, to the energy levels of an harmonic oscillator, as shown in fig. 1(b). Consequently, creation and annihilation operators for a photon in the cavity mode, $a^\dagger$ and a, respectively, can be used to express the Hamiltonian of the cavity field,

$$(7) \qquad H_C = \hbar\omega_C\left(a^\dagger a + \frac{1}{2}\right).$$

Note that this Hamiltonian does not include losses. In a real cavity, all photon number states decay until the vacuum state, i.e. the state with no photon in the cavity, is reached.

2˙3. Two-Level Atom coupled to a Laser. – Prior to the analysis of a two level atom interacting with the quantized electromagnetic field in a cavity, we restrict our discussion to an atom being exposed to a monochromatic laser beam of frequency ω_L, which is treated classically. The atom is assumed to have two eigenstates, a ground state, $|g\rangle$, and an electronically excited state, $|e\rangle$, with energies $\hbar\omega_g$ and $\hbar\omega_e$, respectively. A dipole transition between these levels therefore occurs at the frequency $\omega_{eg} = \omega_e - \omega_g$. The Hamiltonian of the undisturbed atom reads

$$(8) \qquad H_A = \hbar\omega_g|g\rangle\langle g| + \hbar\omega_e|e\rangle\langle e|.$$

The atom is exposed to an oscillating electric field $E(t) = (E_0/2)(e^{-i\omega_L t} + c.c.)$, where E_0 is assumed to vary slowly in time. This is expressed by the interaction Hamiltonian

$$(9) \qquad H_{int}(t) = -\frac{\hbar}{2}\left(\frac{\mu_{eg}2E(t)}{\hbar}\right)[|e\rangle\langle g| + |g\rangle\langle e|],$$

where μ_{eg} is the transition dipole moment between states $|g\rangle$ and $|e\rangle$. In a frame rotating with frequency ω_L, and in the rotating-wave approximation (RWA), the Hamiltonian of the coupled system, $H = H_A + H_{int}$, is given by

$$(10) \qquad H = \frac{\hbar}{2}(2\Delta|e\rangle\langle e| - \Omega|e\rangle\langle g| - \Omega|g\rangle\langle e|),$$

where $\Delta = \omega_{eg} - \omega_L$ is the detuning of the laser from the atom's transition, and $\Omega = \mu_{eg}E_0/\hbar$ is the Rabi-frequency of the driving field, assumed to be real by, e.g., an appropriate choice of the phases of the atomic wavefunctions. This system shows two non-degenerate eigenfrequencies,

$$(11) \qquad \omega^\pm = \frac{1}{2}\left(\Delta \pm \sqrt{\Omega^2 + \Delta^2}\right),$$
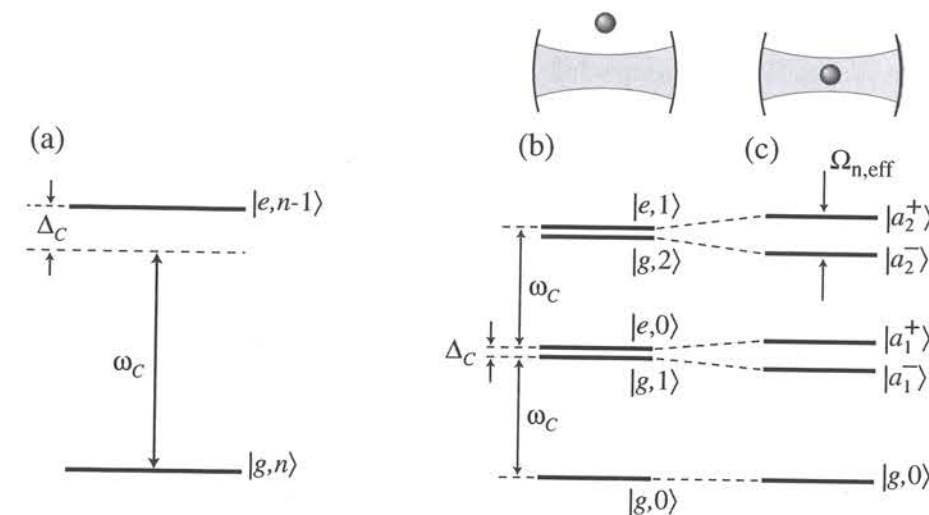
Fig. 2. – **(a)** A two-level atom with ground state $|g\rangle$ and excited state $|e\rangle$ coupled to a cavity containing n photons, yielding a Rabi frequency of $2g_0\sqrt{n}$. The detuning of the cavity from the atomic resonance is $\Delta_C = \omega_{eg} - \omega_C$. **(b)** Dressed-level scheme of the combined atom-cavity system while the atom is outside the cavity, i.e. for a vanishing coupling between atom and cavity. Note that the degeneracy of the state doublets is only lifted by the detuning Δ_C between atom and cavity. **(c)** The same as (b), but for an atom interacting with the cavity. The doublets are now split by the effective Rabi frequency, $\Omega_{n,\text{eff}} = \sqrt{\Omega^2 + \Delta_C^2} \equiv \sqrt{4ng_0^2 + \Delta_C^2}$. This scheme is named after Jaynes and Cummings, and the state doublets are the so-called Jaynes-Cummings doublets.

with the respective eigenstates

$$(12) \qquad |a^+\rangle = \cos\phi|g\rangle - \sin\phi|e\rangle \quad \text{and} \quad |a^-\rangle = \sin\phi|g\rangle + \cos\phi|e\rangle,$$

where the mixing angle ϕ is given by

$$(13) \qquad \tan\phi = \frac{\Omega}{\sqrt{\Omega^2 + \Delta^2} - \Delta} = \frac{\sqrt{\Omega^2 + \Delta^2} + \Delta}{\Omega}.$$

The level splitting between the two eigenstates, $\Omega_{\text{eff}} = \sqrt{\Omega^2 + \Delta^2}$, is called the effective Rabi frequency. It is the rate at which the relative phase of the two eigenstates develops in time, according to $\Omega_{\text{eff}} \times t$. If we now start from the assumption that both eigenstates are populated and ask for the probability to find the atom in either one of its bare states, interference terms oscillating at the frequency Ω_{eff} arise, i.e. part of the atomic population oscillates between states $|g\rangle$ and $|e\rangle$ at the effective Rabi frequency.

2˙4. Two-Level Atom coupled to a Cavity. – Now we assume that the two-level atom interacts with n photons in the relevant field mode of the cavity. In this case, the resonant

Rabi frequency is

$$(14) \qquad \Omega_C = 2g(\mathbf{r}) = 2g_0\sqrt{n}\,\psi(\mathbf{r}), \qquad \text{with} \qquad g_0 = \sqrt{\frac{\mu_{eg}^2 \omega_C}{2\hbar\epsilon_0 V}}.$$

The description of an atom interacting with a quantized field is similar to the description of an atom interacting with a classical field of a given amplitude, with one important difference, namely conservation of energy in the absorption and emission processes. It is evident that any change of the atom's internal state must be reflected by an according change of the cavity's photon number. It follows that the interaction Hamiltonian of the atom-cavity system now encompasses also the creation and annihilation operators, $a^\dagger$ and a, for the photons in the cavity. On the cavity axis, and in an antinode of the relevant mode, this Hamiltonian is given by

$$(15) \qquad H_{int} = -\frac{\hbar}{2}(2g_0)\left[|e\rangle\langle g|a + a^\dagger|g\rangle\langle e|\right].$$

For any arbitrary excitation number, n, only the pair of product states $|g,n\rangle$ and $|e,n-1\rangle$ is coupled. Therefore, the situation corresponds to a set of independent two-level systems, one for each excitation number n. Note that between the pair of states characterized by n and the neighbouring one with quantum number $n+1$ or $n-1$, an energy difference of $\hbar\omega_C$ results from the cavity Hamiltonian H_C.

Apart from this energy difference between neighbouring pairs of states, the analogy with single two-level systems can be used to write down the eigenfrequencies of the complete system Hamiltonian, $H = H_C + H_A + H_{int}$. In the rotating wave approximation, they read

$$(16) \qquad \omega_n^\pm = \omega_C\left(n + \frac{1}{2}\right) + \frac{1}{2}\left(\Delta_C \pm \sqrt{4ng_0^2 + \Delta_C^2}\right),$$

where $\Delta_C = \omega_{eg} - \omega_C$ is the detuning between the atom and the cavity. The eigenstates of each coupled pair of states correspond to the ones given in (12), provided the replacements $|g\rangle \to |g,n\rangle$ and $|e\rangle \to |e,n-1\rangle$ are made. Therefore, the atom-cavity interaction splits the photon number states into a doublet of two non-degenerate dressed states. These doublets are named after Jaynes and Cummings, who pioneered this way of describing a coupled atom-cavity system [6,7].

It must be emphasized that there is one exception to the rule. Without excitation, both, the atom and the cavity are in their ground states, $|g\rangle$ and $|0\rangle$, respectively. The only possible product state, $|g,0\rangle$, is not coupled to any other state. Therefore, its eigenfrequency, $\omega_0 = \omega_C/2$, is not altered, and no splitting occurs.

Like in the case of a two-level atom coupled to a classical field, Rabi oscillations also occur in a cavity. For an atom initially in the ground state and n photons in the cavity, the probability to find the system in either one of the bare states, $|g,n\rangle$ or $|e,n-1\rangle$, oscillates with the effective Rabi frequency $\Omega_{n,\text{eff}} = \sqrt{4ng_0^2 + \Delta_C^2}$. This means that the

cavity field stimulates the emission of an excited atom into the cavity, thus deexciting the atom and increasing the photon number by one. Subsequently, the atom is reexcited by absorbing a photon from the cavity field, and so forth. Since a single excited atom and a cavity containing initially only a vacuum field, i.e. no photon at all, are sufficient to start the oscillation between $|e,0\rangle$ and $|g,1\rangle$ at frequency $\sqrt{4g_0^2 + \Delta_C^2}$, this oscillatory energy exchange is called vacuum-Rabi oscillation. For a resonant interaction, the oscillation frequency is $2g_0$, which is therefore called the vacuum-Rabi frequency.

2˙5. *Normal-Mode Splitting.* – For suitable parameters, the atom-cavity interaction leads to a splitting of the cavity transmission into two peaks, one below and the other above the unperturbed resonance frequency, ω_C, as shown in fig. 3. This effect is called normal-mode splitting. A detailed analysis goes beyond the simple Jaynes-Cummings model because the decay rates of the excited atomic level, 2γ, and the cavity field, κ, must be included, as well as the external field driving the atom-cavity system. We start our discussion by considering the relaxation rates first. These rates lead to a non-Hermitian Hamiltonian, which reads

$$(17) \qquad H' = H_C + H_A - \hbar g_0\left(|e\rangle\langle g|a + a^\dagger|g\rangle\langle e|\right) - i\hbar\gamma|e\rangle\langle e| - i\hbar\kappa a^\dagger a.$$

For a cavity which is in resonance with the atom, and with n denoting the number of excitations, the eigenfrequencies of this damped system,

$$\omega_n^\pm = \omega_C\left(n + \frac{1}{2}\right) + \tilde{\omega}_n^\pm, \qquad \text{with}$$

$$(18) \qquad \tilde{\omega}_n^\pm = \pm\frac{1}{2}\sqrt{4ng_0^2 - (\gamma - \kappa)^2} - \frac{i}{2}(\gamma + \kappa(2n-1)) \qquad \text{for} \quad n \geq 1,$$

are now given by complex numbers. The imaginary parts of the eigenfrequencies cause a decay of the eigenstates, $|a_n^\pm\rangle$, while the real part of $\tilde{\omega}_n^\pm$ describes the splitting. Obviously, a necessary condition for a level splitting to occur is

$$(19) \qquad 4ng_0^2 > (\gamma - \kappa)^2.$$

Otherwise, $\tilde{\omega}_n^\pm$ would be purely imaginary, describing an overdamped system. But note that condition (19) is not sufficient to resolve the level splitting. This is only possible if the real part of $\tilde{\omega}_n^\pm$ is larger than its imaginary part, which is given by the averaged damping rate $(\gamma + \kappa(2n-1))/2$.

In case of weak excitation of the atom-cavity system, only the two states with $n = 1$ are relevant for the transmission properties of the cavity. The difference between the two corresponding eigenfrequencies amounts to

$$(20) \qquad \Omega_{\text{split}} = \sqrt{4g_0^2 - (\gamma - \kappa)^2}.$$

This splitting can be resolved for sufficiently small decay rates, $(\kappa, \gamma) \ll g_0$. This condition characterizes the strong-coupling regime of cavity QED. Note that the presence of
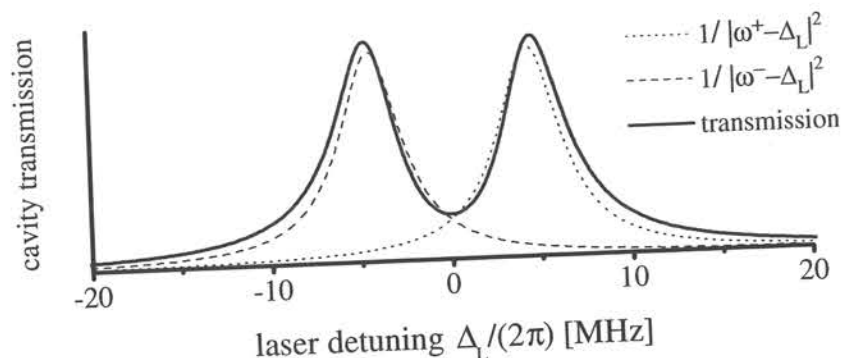
Fig. 3. – The frequency-dependent transmission of a cavity resonant with a single atom placed in its mode volume displays two peaks, indicating a normal-mode splitting. The atom-cavity parameters are $(g_0, \gamma, \kappa) = 2\pi \times (4.5, 3, 1.25)\,\text{MHz}$. The cavity transmission is shown as a function of the laser-cavity detuning, $\Delta_L = \omega_C - \omega_L$.

the decay channels can lead to a significant reduction of the splitting with respect to a lossless atom-cavity system.

To calculate the cavity transmission quantitatively, we follow [15] and consider a weak laser beam impinging on one cavity mirror. The corresponding pump Hamiltonian

$$(21) \qquad H_P = -i\hbar\eta(a - a^\dagger)$$

describes a coherent pumping of the cavity field with a rate η. As shown below, this leads to, on average, η^2/κ^2 photons in the resonant cavity containing no atom. With an atom present, and for sufficiently weak pumping, characterized by $\eta \ll g_0$ and $\eta < (\kappa + \gamma)/2$, the system is mainly in its ground state, $|g, 0\rangle$, and only the small fraction placed in the first excited doublet is of interest. In this case, the relevant state vector of the coupled atom-cavity system can be written as

$$(22) \qquad |\Psi(t)\rangle = c_e(t)|e, 0\rangle + c_g(t)|g, 1\rangle + c_0|g, 0\rangle.$$

With $c_0 \approx 1$, the pump Hamiltonian (21) describes a population flow into state $|g, 1\rangle$. As above, the atom and the cavity are assumed to be in resonance, whereas the laser can be detuned by an amount $\Delta_L = \omega_C - \omega_L$. In the rotating-wave approximation and in a frame rotating with the laser frequency, ω_L, the relevant terms of the Schrödinger equation now read

$$(23) \qquad \begin{aligned} i\dot{c}_e &= -g_0 c_g + (\Delta_L - i\gamma)c_e \quad \text{and} \\ i\dot{c}_g &= -g_0 c_e + (\Delta_L - i\kappa)c_g + i\eta. \end{aligned}$$

The transmission of the cavity, $\mathcal{T}_{\text{cavity}}$, can be calculated from the average photon number, $\langle n \rangle$, which is given by the population of state $|g, 1\rangle$. Using the steady-state solution of (23) with $\dot{c}_g = \dot{c}_e = 0$, we get

$$(24) \qquad \mathcal{T}_{\text{cavity}}(\Delta_L) \propto \langle n \rangle = c_g c_g^* = \left(\frac{\eta}{\kappa}\right)^2 \left| \frac{\kappa(\gamma - i\Delta_L)}{(\Delta_L - \tilde{\omega}_1^+)(\Delta_L - \tilde{\omega}_1^-)} \right|^2.$$

The cavity transmission is shown in fig. 3. To guide the eye, two Lorentzians centred around $\Re(\tilde{\omega}_1^\pm) = \pm\frac{1}{2}\sqrt{4g_0^2 - (\gamma - \kappa)^2}$ with a width of $-\Im(\tilde{\omega}_1^\pm) = \frac{1}{2}(\gamma + \kappa)$ (HWHM) are also shown. Note that the cavity transmission cannot be decomposed into a sum of two Lorentzians.

We emphasize that the single-atom induced normal-mode spectrum as described here has not been observed yet. All experiments performed so far have either been carried out with several atoms randomly distributed over the cavity mode in such a way that their combined effect resembles that of a single atom at an antinode [16-18], or with a single atom exhibiting a complicated motional behaviour depending on the frequency of the probe laser [19].

2'6. *Enhanced Spontaneous Emission.* – It has been proposed by Purcell [8] and demonstrated by Heinzen et al. [9] and Morin et al. [11] that the spontaneous emission properties of an atom coupled to a cavity are significantly different from those in free space. For an analysis of the atom's behaviour, it suffices to look at the $n = 1$ doublet. Like in the previous section, we include the decay rates γ and κ and make use of the Hamiltonian (17). There is no light coupled into the cavity, i.e. $\eta = 0$, and therefore the Schrödinger equation for the coefficients $c_{g,e}$ reads

$$(25) \qquad i\dot{c}_e = -g_0 c_g - i\gamma c_e \quad \text{and} \quad i\dot{c}_g = -g_0 c_e - i\kappa c_g.$$

Figure 4(a) shows the time evolution of the atom-cavity system when $\kappa \gg g_0$. The strong damping of the cavity's one-photon state inhibits any vacuum-Rabi oscillation, since the photon is emitted from the cavity before it can be reabsorbed by the atom. Therefore the transient population in state $|g, 1\rangle$ is negligible if the atom is initially (at $t = 0$) in its excited state $|e\rangle$. In this case, the adiabatic approximation $\dot{c}_g \approx 0$ can be applied, which gives

$$(26) \qquad \frac{d}{dt}c_e = -\gamma c_e - \frac{g_0^2}{\kappa}c_e, \quad i.e. \quad c_e(t) = \exp\left(-\left[\gamma + \frac{g_0^2}{\kappa}\right]t\right).$$

It is obvious that the ratio of the emission into the cavity to the spontaneous emission probability into free space reads $g_0^2/(\kappa\gamma)$. This equals twice the one-atom cooperativity parameter, originally introduced in the context of optical bistability [20]. Note that the atom radiates mainly into the cavity if $g_0^2/\kappa \gg \gamma$. Together with $\kappa \gg g_0$, this condition constitutes the bad-cavity regime.
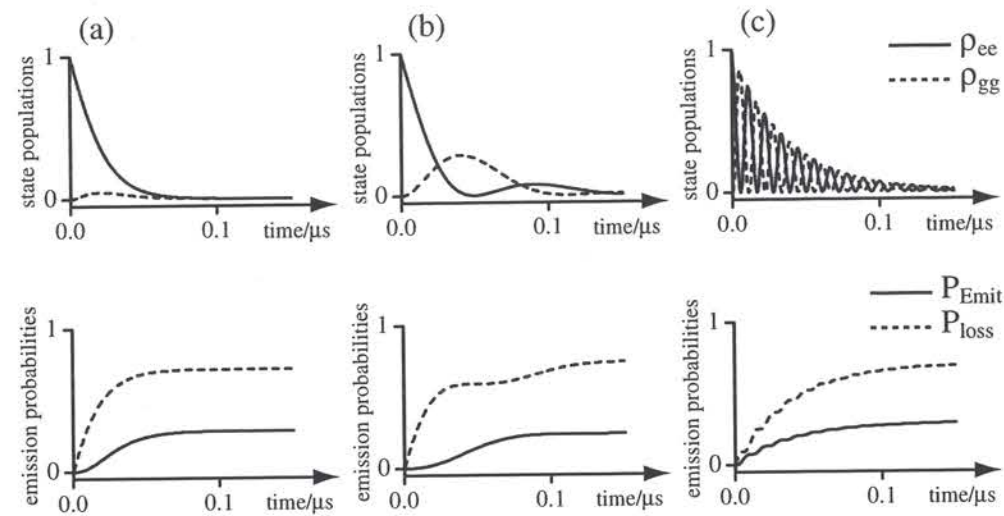
Fig. 4. – Time evolution of an excited two-level atom placed in a resonant optical cavity at $t = 0$. The initial photon number is zero. The upper row of diagrams shows the populations, ρ_{ee} and ρ_{gg}, of the product states, $|e, 0\rangle$ and $|g, 1\rangle$, respectively. The lower row of diagrams shows the corresponding integrated emission rate, i.e. the emission probabilities as a function of time, with P_{loss} denoting the probability for spontaneous emission not leading to a photon emission from the cavity, and P_{Emit} denoting the probability to emit a photon through one of the cavity mirrors. All traces in this figure result from a numerical evaluation of the master equation describing the coupled system. The three columns belong to three different coupling strengths and loss rates: **(a)** $(g_0, \gamma, \kappa) = 2\pi \times (4.5, 3, 12.5)$ MHz. **(b)** $(g_0, \gamma, \kappa) = 2\pi \times (4.5, 3, 1.25)$ MHz. **(c)** $(g_0, \gamma, \kappa) = 2\pi \times (45, 3, 1.25)$ MHz.

In the strong-coupling regime, $g_0 \gg (\kappa, \gamma)$, however, the atom-cavity system is subject to a vacuum-Rabi oscillation between states $|e, 0\rangle$ and $|g, 1\rangle$, both decaying at the respective rates γ and κ. Figure 4(c) shows a situation where the atom-cavity coupling, g_0, saturates the $|e, 0\rangle \leftrightarrow |g, 1\rangle$ transition. On average, the probabilities to find the system in either one of these two states are equal, and the average ratio of the photon-emission probability out of the cavity, P_{Emit}, to the spontaneous photon-emission probability, P_{loss}, is given by κ/γ. The fast Rabi oscillation leads only to a small ripple on the photon emission and loss probabilities in the beginning of the interaction.

In the intermediate regime, the enhancement of the atom's spontaneous emission into the cavity cannot be written in terms of simple analytic expressions. As the bad-cavity regime and the strong-coupling regime display a dramatically different dynamical behaviour, not even an interpolation is allowed. To illustrate this statement, we assume, e.g., atom-cavity parameters $(g_0, \gamma, \kappa) = 2\pi \times (4.5, 3, 1.25)$ MHz, which lead to the time evolution shown in fig. 4(b). It is obvious that here the decay is neither exponential, as would be the case in the bad-cavity regime, nor displays ripples indicating the fast Rabi oscillation in the strong-coupling regime. Hence, if g_0 is too small to strongly saturate

the atomic transition, a simulation is mandatory to determine the system's dynamics. It reveals (see fig. 4(b)) a Rabi oscillation starting so slowly from state $|e, 0\rangle$, that the initial spontaneous emission loss from $|e, 0\rangle$ dominates the photon emission probability from the cavity.

3. – Three-Level Atoms

Now, we consider an atom with a Λ-type three-level scheme, providing transition frequencies $\omega_{eu} = \omega_e - \omega_u$ and $\omega_{eg} = \omega_e - \omega_g$, as depicted in fig. 5. This atom is either interacting with two classical light fields of frequencies ω_P and ω_S, or, alternatively, with one classical field and a cavity mode, respectively. Assuming a Raman-resonant interaction, i.e. setting $\omega_{eu} - \omega_P = \omega_{eg} - \omega_S \equiv \Delta$, the behaviour of the atom is described in a rotating frame by the Hamiltonian

$$(27) \qquad H = \frac{\hbar}{2}[2\Delta|e\rangle\langle e| - \Omega_S(|e\rangle\langle g| + |g\rangle\langle e|) - \Omega_P(|e\rangle\langle u| + |u\rangle\langle e|)],$$

where Ω_P and Ω_S are the Rabi frequencies of the two fields, respectively. Note that we have used an extended version of the rotating-wave approximation to obtain this Hamiltonian – not only contributions rotating at twice the optical frequency were eliminated, but also all other off-resonant terms of the order of $\omega_g - \omega_u$ have been neglected, i.e. we assume that the pump laser (frequency ω_P) only couples to the $|u\rangle \leftrightarrow |e\rangle$ transition, and the Stokes laser (frequency ω_S) only to the $|g\rangle \leftrightarrow |e\rangle$ transition. This is justified whenever the condition $\max(\Omega_P, \Omega_S, |\Delta|) \ll |\omega_g - \omega_u|$ is met.

It is convenient to express the state vector of the atom coupled to the two radiation fields in the basis of the Hamiltonian's eigenstates, which read

$$(28) \qquad \begin{aligned} |a^0\rangle &= \cos\Theta|u\rangle - \sin\Theta|g\rangle, \\ |a^+\rangle &= \cos\Phi\sin\Theta|u\rangle - \sin\Phi|e\rangle + \cos\Phi\cos\Theta|g\rangle, \\ |a^-\rangle &= \sin\Phi\sin\Theta|u\rangle + \cos\Phi|e\rangle + \sin\Phi\cos\Theta|g\rangle, \end{aligned}$$

where the mixing angles Θ and Φ are given by

$$(29) \qquad \tan\Theta = \frac{\Omega_P}{\Omega_S} \quad \text{and} \quad \tan\Phi = \frac{\sqrt{\Omega_S^2 + \Omega_P^2}}{\sqrt{\Omega_S^2 + \Omega_P^2 + \Delta^2} - \Delta},$$

with Ω_P and Ω_S assumed to be real. The corresponding eigenfrequencies are

$$(30) \qquad \omega^0 = 0 \quad \text{and} \quad \omega^\pm = \frac{1}{2}\left(\Delta \pm \sqrt{\Omega_S^2 + \Omega_P^2 + \Delta^2}\right).$$

We note that the interaction with the light lifts the degeneracy of the three eigenstates as soon as the Rabi-frequencies are non-zero. Furthermore, it must be emphasized that one of these states, namely $|a^0\rangle$, is neither subject to an energy shift, nor does the
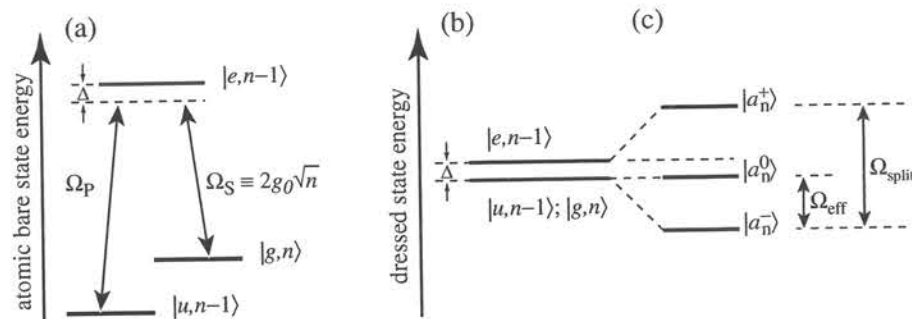
Fig. 5. – **(a)** A Λ-type three-level atom with two long-lived ground states $|u\rangle$ and $|g\rangle$ and excited state $|e\rangle$. The transition $|u\rangle \leftrightarrow |e\rangle$ is driven by a classical laser field with Rabi frequency Ω_P, and the $|g\rangle \leftrightarrow |e\rangle$ transition is either driven by a second classical laser field of Rabi frequency Ω_S, or coupled to a cavity containing n photons, with Rabi frequency $2g_0\sqrt{n}$. The common detuning of the cavity and the classical field(s) from their respective resonances is $\Delta = \omega_{eu} - \omega_P = \omega_{eg} - \omega_C$. **(b)** Dressed-level scheme of the combined system for vanishing coupling strengths between atom, fields and cavity. Note that the degeneracy of the state triplet is only partially lifted by the detuning Δ. **(c)** Same as (b), but for an atom interacting with laser field(s) and/or cavity. The state triplet is now split by $\Omega_{\text{split}} = \sqrt{\Omega_P^2 + \Omega_S^2 + \Delta^2} \equiv \sqrt{\Omega_P^2 + 4g_0^2 n + \Delta^2}$. Note that for a detuning Δ which is large compared to all Rabi frequencies, the Raman transition $|u\rangle \leftrightarrow |g\rangle$ is driven at the effective Rabi frequency $\Omega_{\text{eff}} = \frac{1}{2}(\Omega_{\text{split}} - |\Delta|) \approx (\Omega_P^2 + \Omega_S^2)/|4\Delta|$. This is not the usual Raman Rabi-frequency, $\Omega_{\text{Raman}} = \Omega_P\Omega_S/2\Delta$, in an "effective" two-level atom, because the differential light shift, $\Delta_{\text{light}} = (\Omega_P^2 - \Omega_S^2)/4\Delta$, is taken into account. Our expression corresponds to $\Omega_{\text{eff}} = \sqrt{\Omega_{\text{Raman}}^2 + \Delta_{\text{light}}^2}$. We emphasize that the Jaynes-Cummings doublets for a two-level atom-cavity system are now replaced by triplets. The dark state $|a_n^0\rangle$, which belongs to the triplet, is not shifted in energy.

excited atomic state contribute to it. In the literature, $|a^0\rangle$ is therefore called a "dark state", since its population cannot be lost by spontaneous emission from the excited state $|e\rangle$, and because an atomic system prepared in $|a^0\rangle$ remains dark even when being exposed to pump and Stokes light of Rabi frequencies Ω_P and Ω_S, respectively. The lack of spontaneous emission from atoms in $|a^0\rangle$ manifests itself as a "dark resonance" in Raman spectra, when the two-photon Raman-resonance condition, $\Delta_P = \Delta_S$, is met.

The previously discussed three-level atom is now placed in the mode volume of a cavity, with the Stokes transition driven by the atom-cavity interaction in place of an externally applied field. Analogous to the case of a two-level atom discussed above, the Rabi frequency and the detuning of the Stokes transition need to be replaced by

$$(31) \qquad \Omega_S \longrightarrow 2g\sqrt{n}$$
$$(32) \qquad \Delta_S \longrightarrow \Delta_C.$$

In addition, the photon creation and annihilation operators, $a^\dagger$ and a, respectively, must be introduced in the interaction Hamiltonian. In a rotating frame, the interaction Hamil-

tonian now reads

$$(33) \qquad H_{\text{int}} = \hbar\left[\Delta_P|u\rangle\langle u| + \Delta_C|g\rangle\langle g| - g(|e\rangle\langle g|a + a^\dagger|g\rangle\langle e|) - \frac{1}{2}\Omega_P(|e\rangle\langle u| + |u\rangle\langle e|)\right].$$

Note that the cavity-induced Stokes Rabi frequency is proportional to $\sqrt{n}$, since $\langle n|a^\dagger|n-1\rangle = \sqrt{n} = \langle n-1|a|n\rangle$. Given an arbitrary excitation number n, this Hamiltonian couples only the three states $|u, n-1\rangle$, $|e, n-1\rangle$, $|g, n\rangle$. For this state triplet and a Raman-resonant interaction with $\Delta_P = \Delta_C \equiv \Delta$, the eigenfrequencies of the coupled system read

$$(34) \qquad \omega_n^0 = \omega_C\left(n + \frac{1}{2}\right) \quad \text{and}$$
$$\omega_n^\pm = \omega_C\left(n + \frac{1}{2}\right) + \frac{1}{2}\left(\Delta \pm \sqrt{4ng^2 + \Omega_P^2 + \Delta^2}\right),$$

with eigenvectors according to (28). Of course, the replacement $|u\rangle \to |u, n-1\rangle$, $|e\rangle \to |e, n-1\rangle$ and $|g\rangle \to |g, n\rangle$ has to be made. As a consequence, the former Jaynes-Cummings doublet is now replaced by the state triplet $\{|a_n^0\rangle, |a_n^+\rangle, |a_n^-\rangle\}$ with the above mentioned eigenfrequencies. In the limit of vanishing Ω_P, the states $|a_n^\pm\rangle$ correspond exactly to the Jaynes-Cummings doublet which has been discussed in the previous section, and the third eigenstate, $|a_n^0\rangle$, coincides with $|u, n-1\rangle$. Note that ω_n^0 is not affected by Ω_P or g. Therefore transitions between dark states of different n, $|a_n^0\rangle$, are always in resonance with the cavity frequency ω_C. This holds, in particular, for the transition from $|a_1^0\rangle$ to $|g, 0\rangle$, since the $n = 0$ state does not split (the corresponding states $|u, -1\rangle$ and $|e, -1\rangle$ do not exist).

4. – Adiabatic Passage

Adiabatic passage techniques have been used for coherent population transfer in atoms or molecules for many years now. In two-level systems, usually a frequency chirp across the relevant resonance line is applied to a single driving field. In three-level systems, either a variation of the amplitudes of the two driving fields is used, or a frequency chirp across the relevant two-photon (Raman) resonance drives the passage. First realizations were in the rf-regime, with the aim to flip nuclear spins in NMR [21]. In the optical domain, frequency-chirped interactions have been realized for atomic or molecular samples, using either a Stark shift or the dynamical Stark effect to chirp the resonance across the fixed laser frequency [22-24]. This kind of frequency chirp has been extended to three-level systems. For example, it has been shown that population transfer can be achieved by a Stark-chirped rapid adiabatic passage (SCRAP) across the Raman resonance [25]. Moreover, driving the Raman transition with frequency-chirped laser pulses allowed a velocity-selective excitation and Raman cooling of atoms [26, 27]. Without frequency chirp, but with the Raman transition driven by two distinct pulses of variable amplitudes, effects like electromagnetically induced transparency (EIT) [28, 29], slow light [30-33], and

stimulated Raman scattering by adiabatic passage (STIRAP) [3-5] can be observed. We emphasize that these effects have all been demonstrated with classical light fields.

The common feature of these techniques is that the time evolution of the system's state vector,

$$(35) \qquad |\Psi(t)\rangle = \sum_i \alpha_i \exp\left(-i \int_0^t \omega_i(t')dt'\right)|a_i(t)\rangle,$$

is only determined by the behaviour of the eigenstates, $|a_i(t)\rangle$, of the interaction Hamiltonian, and their respective eigenfrequencies, $\omega_i(t)$. The eigenstates as well as the eigenfrequencies may change in time, whereas the linear coefficients, α_i, are assumed to be non-varying in time throughout the whole interaction. In this context, the non-decaying dark state, $|a^0\rangle$, introduced above, is of enormous significance to the adiabatic passage phenomenon.

In principle, any three-level quantum system initially prepared in $|a^0\rangle$ stays in this state forever, thus allowing to control the relative population of the contributing atomic states, $|u\rangle$ and $|g\rangle$, by adjusting the values of the pump and Stokes Rabi frequencies, Ω_P and Ω_S, respectively. To show this, let us start with a system initially prepared in the state $|u\rangle$. As can be easily seen from (28), this state coincides with the dark state $|a^0\rangle$ if the condition $\Omega_S \gg \Omega_P$ is met in the beginning of the interaction:

$$(36) \qquad |\langle u|a^0\rangle|^2 = \frac{\Omega_S^2}{\Omega_P^2 + \Omega_S^2} \xrightarrow{\Omega_S \gg \Omega_P} 1.$$

Similarly, for an atom interacting with a cavity in place of the stimulating Stokes field, the initial condition for the dark state preparation reads $2\sqrt{n}g \gg \Omega_P$. Once the system has been successfully prepared in the dark state, and if the state vector $|\Psi\rangle$ follows $|a^0\rangle$ during the interaction, the ratio between the populations of the contributing states always reads

$$(37) \qquad \frac{|\langle u|\Psi\rangle|^2}{|\langle g|\Psi\rangle|^2} = \frac{\Omega_S^2}{\Omega_P^2} \equiv \frac{4ng^2}{\Omega_P^2} = \frac{|\langle u, n-1|\Psi\rangle|^2}{|\langle g, n|\Psi\rangle|^2}.$$

Therefore the final state of the system is determined by the relative amplitudes of the two fields when the interaction ends. In principle, this allows to establish arbitrary state superpositions of $|u\rangle$ and $|g\rangle$, or $|u, n-1\rangle$ and $|g, n\rangle$ if the atom is coupled to a cavity. In the latter case, the photon number in the cavity is affected in the same manner as the atomic states.

Up to this point, we have argued that the state vector of the system, $|\Psi\rangle$ is not only expressed in the basis of the eigenstates, but also that it *adiabatically follows* any change in the eigenstates with respect to the atom's and the cavity's bare state basis. Such a behaviour is not evident, and it holds only when the eigenstates are changing slowly. In order to analyse the criteria that must be met for "adiabatic following" in detail, we follow Messiah [34], and consider the state vector expressed by a superposition of the

triplet of eigenstates,

$$(38) \qquad |\Psi\rangle = \alpha^0|\tilde{a}^0\rangle + \alpha^+|\tilde{a}^+\rangle + \alpha^-|\tilde{a}^-\rangle,$$

with the phase evolution included in the base vectors, $|\tilde{a}^0\rangle \equiv \exp(-i \int_{t_0}^t \omega^0(t')dt')|a^0(t)\rangle$ and $|\tilde{a}^\pm\rangle \equiv \exp(-i \int_{t_0}^t \omega^\pm(t')dt')|a^\pm(t)\rangle$. For a system prepared in the dark state $|\tilde{a}^0\rangle$ at time t_0, the probability to find it in either one of the other two eigenstates at a later time t_1 is

$$(39) \qquad P_\pm(t_1) = |\langle \tilde{a}^\pm(t_1)|\Psi(t_1)\rangle|^2 = |\alpha^\pm(t_1)|^2.$$

An adiabatic evolution of the interaction requires $P_\pm$ to be close to zero at all times. Using the Schrödinger equation, $\langle \tilde{a}^\pm|\frac{d}{dt}|\Psi\rangle = \langle \tilde{a}^\pm| -\frac{i}{\hbar}H|\Psi\rangle$, we get

$$(40) \qquad \langle \tilde{a}^\pm| \sum_{j=0,\pm} \left[(\dot{\alpha}^j - i\omega^j\alpha^j)|\tilde{a}^j\rangle + \alpha^j \exp\left(-i \int_{t_0}^t \omega^j dt'\right)\frac{d}{dt}|a^j\rangle\right] = -i\omega^\pm\alpha^\pm.$$

As long as the non-adiabatic losses cause only a small perturbation, the approximations $\alpha^0 \approx 1$ and $\alpha^\mp\langle a^\pm|\frac{d}{dt}|a^\mp\rangle \approx 0$ are justified, and the transition probability to the non-dark eigenstates reads

$$(41) \qquad P_\pm(t_1) = \left| \int_{t_0}^{t_1} \left[\exp\left(-i \int_{t_0}^t (\omega^\pm - \omega^0)dt'\right)\langle a^\pm|\frac{d}{dt}|a^0\rangle\right] dt \right|^2.$$

The integrand on the right-hand side is the product of $\langle a^\pm|\frac{d}{dt}|a^0\rangle$ and an exponential oscillating at frequency $\omega^\pm - \omega^0$. In a sufficiently short time interval $[t_0 \ldots t_1]$, we consider these two expressions to be time-independent. Hence (41) is easily integrated to give

$$(42) \qquad P_\pm(t_1) = \left| \frac{\langle a^\pm|\frac{d}{dt}|a^0\rangle}{\omega^\pm - \omega^0} \right|^2 2 \left(1 - \cos[(\omega^\pm - \omega^0)(t_1 - t_0)]\right).$$

Now we allow $\langle a^\pm|\frac{d}{dt}|a^0\rangle$ and the difference frequency $\omega^\pm - \omega^0$ to vary smoothly in time. Therefore the probability, $P_\pm$, to loose population from the dark state will be limited by the maximum value attained by (42),

$$(43) \qquad P_\pm \leq \max \left| \frac{\langle a^\pm|\frac{d}{dt}|a^0\rangle}{\omega^\pm - \omega^0} \right|^2 \times 4.$$

From (43) we see that the condition for adiabatic following, $P_\pm \ll 1$, is satisfied if

$$(44) \qquad |\omega^\pm - \omega^0| \gg |\langle a^\pm|\frac{d}{dt}|a^0\rangle|$$
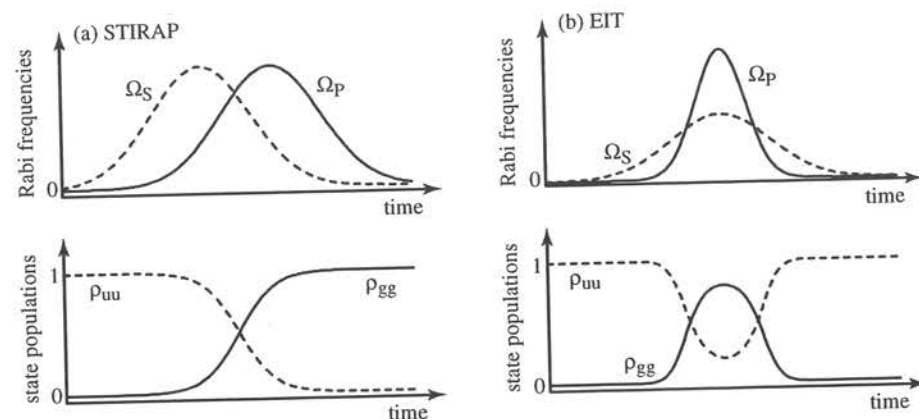
Fig. 6. – **(a)** Counter-intuitive interaction sequence for STIRAP realized by either two de-layed Gaussian laser pulses, or by an atom travelling across two shifted Gaussian beam waists. If adiabatic following is assured, the $|u\rangle$-state population, ρ_{uu}, and the $|g\rangle$-state population, ρ_{gg}, behave as shown in the lower half of the diagram. The population is inverted, and both state populations are equal when Ω_P equals Ω_S. **(b)** The pump laser pulse is embedded in the stimulating Stokes laser pulse, which corresponds to the EIT (electromagnetically induced transparency) configuration. In case of adiabatic following, no net absorption and/or emission takes place, since the initial condition is reestablished in the end. However, the evolution of the state populations, shown in the lower half, reveals that a transient population inversion occurs whenever $\Omega_P > \Omega_S$.

is met throughout the interaction. We emphasize that it is usually sufficient to fulfil this condition for the "most critical" moment in time, i.e. when the maximum of (43) is reached.

4˙1. Population Transfer and Fock-State Preparation. – In Λ-type three-level systems, adiabatic passage has been successfully used for coherent population transfer between two long-lived ground states, $|u\rangle$ and $|g\rangle$, of atoms and molecules. The excitation is performed by means of a stimulated Raman transition and is known as STIRAP, first pioneered by Bergmann et al. [3,4]. In this scheme, the atom first experiences a strong field coupling states $|g\rangle$ and $|e\rangle$, i.e. $\Omega_S \gg \Omega_P$. Therefore the initially populated state $|u\rangle$ coincides with the dark state $|a^0\rangle$. Provided adiabatic following is assured, any final condition leading to $\Omega_P \gg \Omega_S$ causes a complete population transfer to state $|g\rangle$, since $|a^0\rangle$ coincides with $|g\rangle$ in the end. This means that the interaction with the stimulating field has to start first, whereas the interaction with the pump field must be delayed. Such a sequence is often called to be counter-intuitive. It can be realized by two Gaussian laser pulses of duration τ which are delayed by δ_t with respect to each other, with $\Omega_{P,S}(t) = \Omega_{P,S}^0 \exp(-(t \pm \delta_t/2)^2/\tau^2)$. Adiabaticity is best fulfilled when they are delayed by a time interval $\delta_t = -\tau$. If the two peak Rabi frequencies, Ω_P^0 and Ω_S^0, are nearly

equal, the condition for adiabatic following reads

$$(45) \qquad\qquad \Omega_P^0 \approx \Omega_S^0 \gg 1/\tau.$$

As proposed in [12], we now assume that the stimulating field, Ω_S, is replaced by the interaction of the atom with a cavity mode, populated with $n-1$ photons. If the atom is travelling through the cavity at velocity v, it experiences a Gaussian "stimulating pulse" on the $|g\rangle \leftrightarrow |e\rangle$ transition of duration $\tau = w_C/v$, where, again, w_C is the waist of the cavity mode. When the pump-laser beam, coupling the $|u\rangle \leftrightarrow |e\rangle$ transition, is shifted slightly downstream, the atom is exposed to a counter-intuitive interaction sequence and is therefore subject to a STIRAP-like population transfer. However, we have to take the change of the cavity's photon number into account: The coupled system evolves from $|u, n-1\rangle$ to $|g, n\rangle$, and therefore the photon number in the field mode increases by one for each atom travelling across the cavity. Once the photon is added, the atom leaves the cavity while it is still exposed to a strong pump field, with $\Omega_P \gg 2g\sqrt{n}$, and therefore the atom cannot reabsorb the photon again. If we furthermore neglect a possible decay of the photons from the cavity, i.e. for $\kappa = 0$, this method would allow one to prepare arbitrary Fock states [35]. Starting from an empty cavity, $|0\rangle$, and repeating the sequence with N atoms moving through the cavity one after the other, the Fock state $|N\rangle$ can be prepared.

It should be mentioned that adiabatic population transfer in a three-level atom is also possible via $|a^+\rangle$ or $|a^-\rangle$, provided the common detuning $\Delta = (\Delta_P + \Delta_S)/2$ is either positive or negative, respectively. In such a case, the contribution of $|e\rangle$ to $|a^+\rangle$ (or $|a^-\rangle$) becomes negligible, and the corresponding eigenstate is a pseudo-dark state. The adiabatic passage can be driven by a chirp of the Raman detuning, $\Delta_P - \Delta_S$, across zero. This method has been used for velocity-selective excitation of atoms and sideband cooling of neutral atoms [26, 27].

4˙2. Electromagnetically Induced Transparency. – Closely related to the technique of adiabatic population transfer is the effect of electromagnetically induced transparency (EIT) [28, 29]. In this case, the pump-laser pulse is shorter than the stimulating Stokes-laser pulse, and it is "embedded" in the Stokes pulse in a way that both the initial and the final conditions read $\Omega_S \gg \Omega_P$. Therefore the population is transferred from state $|u\rangle$ to the dark state $|a^0\rangle$ with the rising edge of the Stokes-laser pulse, and back to the initial state $|u\rangle$ with the trailing edge of the pulse. Despite a possible transient energy exchange between atom and fields during the interaction, no net energy is exchanged in the end, i.e. the photon numbers in the two laser pulses remain unchanged, and the system is subject to a coherent population return.

In this configuration, the stimulating Stokes laser pulse could also be replaced by the interaction of the atom with a field mode of a cavity. Provided the same timing is realized, i.e. the atom experiences a strong coupling to the cavity mode before and after it interacts with the pump beam, no change in the cavity's photon number takes place. It must be emphasized that a transient photon is placed in the cavity mode while the

atom sees a strong pump laser pulse. Only if this photon is not emitted through one of the cavity mirrors, it is reabsorbed by the atom when the atom leaves the pump beam.

4`3. *Emission of Photons.* – We now consider the special case where the cavity is empty in the beginning of the interaction with the atom, i.e. the initial state of the relevant field mode is $|0\rangle$. As we have seen, both the STIRAP and the EIT techniques are able to increase the photon number by one. It follows that a single photon is placed into the cavity, where it is either stored in case of STIRAP, or from where it is reabsorbed by the atom in the EIT configuration. However, a real optical cavity is always subject to photon losses because the cavity mirrors have a non-negligible transmission. Therefore a single photon will be emitted through one of the mirrors if the cavity-field decay time, κ^{-1}, is much shorter than the so-called "critical time", t_c, which is either the time needed to place a second photon into the cavity (for STIRAP), or the time to loose the photon by another mechanism, e.g. by photon reabsorption in the EIT configuration or by photon absorption in the mirror coatings.

5. – Single-Photon Sources

In paragraph 4`3, we have already pointed out that a coupled atom-cavity system could be employed as a single photon source. The availability of such a source, which emits single photons into a well-defined mode of the radiation field, is the basis for many attempts to realize elementary quantum-logic gates, as well as feasible schemes for quantum cryptography and quantum teleportation. Moreover, all-optical quantum information processing based only on linear optics seems possible, provided highly efficient single-photon sources and single-photon detectors are available [2].

5`1. *State-of-the-Art.* – So far, most schemes used for photon generation rely on spontaneous emission or parametric down-conversion and produce photons at more or less random times. Only during the last few years, different photon generation schemes have been demonstrated, like a single-photon turnstile device based on the Coulomb blockade mechanism in a quantum dot [36], the fluorescence of a single molecule [37, 38], or a single colour centre (Nitrogen vacancy) in diamond [39, 40], or the photon emission of a single quantum dot [41]. All these new schemes emit photons upon an external trigger event. However, the photons are spontaneously emitted into many modes of the radiation field and usually show a broad energy distribution. Only recently, cavity-enhanced spontaneous emission techniques for single-photon generation from a quantum dot have been proposed [42] and demonstrated [43, 44].

5`2. *Cavity Enhanced Spontaneous Emission.* – Before we describe a single-photon source based on the adiabatic passage scheme introduced in section 4, we discuss a situation where a three-level atom is excited by a pump pulse, thereby emitting a photon into a cavity by enhanced spontaneous emission. This situation has been analysed in

detail by Law et al. [45, 14]. They consider the bad-cavity regime,

$$(46) \qquad \kappa \gg g^2/\kappa \gg \gamma,$$

where the loss of excitation into unwanted modes of the radiation field is small. In this regime, the cavity-field decay rate κ sets the fastest time scale, while the spontaneous emission rate into the cavity, g^2/κ, dominates the usual incoherent decay rate, 2γ, of the population from the excited atomic level. It is assumed that any decay leads to a loss from the three-level system. Therefore the evolution of the wave vector is governed by the non-Hermitian Hamiltonian

$$(47) \qquad H' = H - i\hbar\kappa a^\dagger a - i\hbar\gamma|e\rangle\langle e|,$$

with H given in (33). To simplify the analysis, we consider only the vacuum state, $|0\rangle$, and the one-photon state, $|1\rangle$, of the cavity. Hence the state vector can be written as

$$(48) \qquad |\Psi(t)\rangle = c_u(t)|u,0\rangle + c_e(t)|e,0\rangle + c_g(t)|g,1\rangle,$$

where c_u, c_e and c_g are complex amplitudes. The time evolution of the amplitudes is given by the Schrödinger equation, $i\hbar\frac{d}{dt}|\Psi\rangle = H'|\Psi\rangle$), which yields

$$(49) \qquad \begin{aligned} i\dot{c}_u &= \frac{\Omega_P(t)}{2}c_e \\ i\dot{c}_e &= \frac{\Omega_P(t)}{2}c_u + gc_g - i\gamma c_e \\ i\dot{c}_g &= gc_e - i\kappa c_g, \end{aligned}$$

with the initial condition $c_u(0) = 1$, $c_e(0) = c_g(0) = 0$ and $\Omega_P(0) = 0$. A so-called "adiabatic solution" of (49) can be derived if the exciting pump pulse satisfies $\Omega_P(t) \ll g^2/\kappa$. Under these conditions, the decay is so fast that c_e and c_g are nearly time independent. This allows one to make the approximations $\dot{c}_e = 0$ and $\dot{c}_g = 0$, with the result

$$(50) \qquad \begin{aligned} c_u(t) &\approx \exp\left(-\frac{\alpha}{4}\int_0^t \Omega_P^2(t')dt'\right) \\ c_e(t) &\approx -i\frac{\alpha}{2}\Omega_P(t)c_u(t) \\ c_g(t) &\approx -i\frac{g}{\kappa}c_e(t), \end{aligned}$$

where $\alpha = 2/(2\gamma + 2g^2/\kappa)$. Since photons are emitted out of the cavity from state $|g,1\rangle$ only, the photon emission rate is $R_E(t) = 2\kappa|c_g(t)|^2$, and the photon emission probability reads

$$(51) \quad P_E(\tau) = 2\kappa\int_0^\tau |c_g(t)|^2 dt = \frac{g^2\alpha}{\kappa}\left[1 - \exp\left(-\frac{\alpha}{2}\int_0^\tau \Omega_P^2(t)dt\right)\right] \xrightarrow{\Omega_P\tau\to\infty} \frac{g^2\alpha}{\kappa}.$$
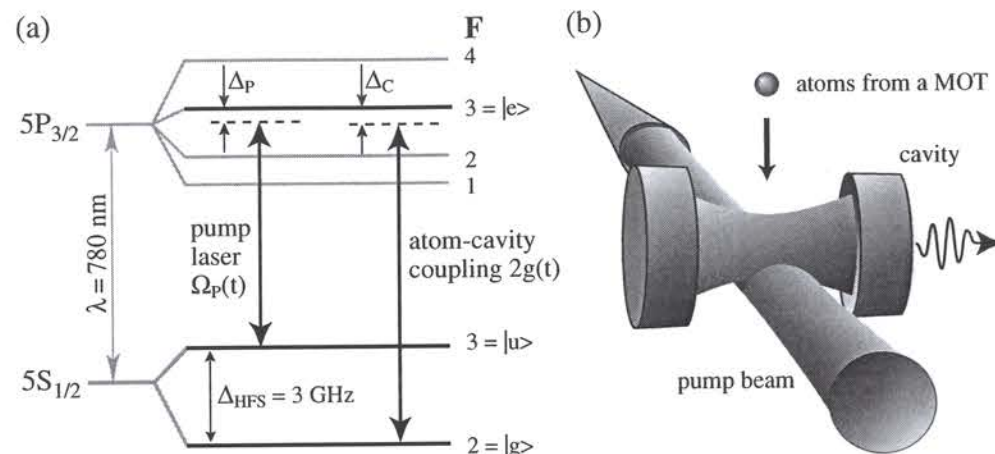
Fig. 7. – (a) Scheme of the relevant energy levels, transitions, and detunings of a ^{85}Rb atom coupled to a pump laser and a cavity. Δ_P and Δ_C denote the pump and cavity detunings from the respective atomic transitions. (b) Sketch of the experimental setup. The pump beam is displaced with respect to the cavity mode.

Note that the exponential in (51) vanishes in case of a sufficiently large area, $\int_0^\tau \Omega_P(t)dt$, of the exciting pump pulse. In this limit, the photon emission probability does not depend on the shape and amplitude of the pump pulse. As the other parameters, g, α, and κ, are in principle under the control of the experimentalist, arbitrary high photon emission probabilities could be reached. In [14], a realistic scheme using a Cs atom was proposed with $(g, \kappa, \gamma)/2\pi = (45, 45, 2.25)$ MHz. For an excitation of this system with a $3\gamma^{-1}$ long sine-squared pump pulse of peak Rabi-frequency $\Omega_P^0 = 2\pi \times 45$ MHz, a photon emission probability of 96.7 % is found numerically.

5˙3. Vacuum-Stimulated Raman Scattering. – We now report on an experimental scheme [12,13] which employs a mixture of the STIRAP and EIT techniques discussed in section **4**, and where the strong coupling of a single atom to a single cavity mode induces the Stokes transition of the Raman process.

Figure 7(a) depicts the excitation scheme for the ^{85}Rb atoms used in the experiment. A Λ-type three-level scheme is realized by the two $5S_{1/2}$ hyperfine ground states $F = 3$ and $F = 2$, which we label $|u\rangle$ and $|g\rangle$, respectively. The $F = 3$ hyperfine level of the electronically excited state $5P_{3/2}$ forms the intermediate state, $|e\rangle$. The atom interacts with a single-mode of an optical cavity, whose frequency ω_C is close to the atomic transition frequency between states $|e\rangle$ and $|g\rangle$, but far-off resonance from the $|e\rangle$ to $|u\rangle$ transition. Hence, only the product states $|e, 0\rangle$ and $|g, 1\rangle$ are coupled by the

cavity. For this transition, the vacuum Rabi frequency,

$$(52) \qquad 2g(t) = 2g_0 \exp\left(-\left(\frac{t\,v}{w_C}\right)^2\right),$$

is time dependent since the atom moves with velocity v across the waist, w_C, of the Gaussian cavity mode, as indicated in fig. 7(b).

The pump laser beam crosses the cavity axis at right angle. This beam is placed slightly downstream in the path of the atoms (by an amount $-\delta_X$ with respect to the cavity axis) and has a waist w_P, therefore causing a time-dependent Rabi frequency

$$(53) \qquad \Omega_P(t) = \Omega_P^0 \exp\left(-\left(\frac{t\,v + \delta_X}{w_P}\right)^2\right).$$

The pump frequency is near resonant with the transition between $|u, 0\rangle$ and $|e, 0\rangle$, thereby coupling these states.

Due to the pump-beam displacement, the atom experiences the desired counter-intuitive interaction sequence while travelling through the cavity. Since the cavity photon number is initially zero, and the atom is initially in state $|u\rangle$, the system's state vector $|\Psi\rangle$ should follow the dark state

$$(54) \qquad |a^0(t)\rangle = \frac{2g(t)|u, 0\rangle - \Omega_P(t)|g, 1\rangle}{\sqrt{4g^2(t) + \Omega_P^2(t)}},$$

of the $n = 1$ triplet, provided the condition for adiabatic following,

$$(55) \qquad \min(2g_0 w_C/v,\ \Omega_P^0 w_P/v) \gg 1$$

is met. Furthermore, the detunings of the cavity, Δ_C, and of the pump pulse, Δ_P, from the corresponding atomic transition frequencies must be equal or, more precisely, the condition

$$(56) \qquad |\Delta_C - \Delta_P| < 2\kappa$$

must be fulfilled. Note that the cavity decay rate determines the linewidth of the Raman transition.

As stated in section **4**, adiabaticity does not assure photon emission. Hence, either the interaction time must be significantly longer than $(2\kappa)^{-1}$ to allow the emission, or the interaction with the pump beam must be strong when the atom leaves the cavity to avoid photon reabsorption. Once the photon is emitted, the empty cavity state, $|g, 0\rangle$, is reached and no further excitation is possible.

5˙4. *Loss Mechanisms.* – For each atom falling through the cavity, there are four possible scenarios, which either lead to no excitation at all, a loss of the excitation by spontaneous emission, or the desired emission of the photon from the cavity:

1. The atom is not excited and leaves the cavity in its initial state. Therefore no photon is emitted from the cavity. In such a case, the system either stays in state $|u, 0\rangle$, or this state is repopulated by spontaneous emission from $|e, 0\rangle$, or is reestablished by coherent population return in the EIT configuration.

2. The atom is excited to state $|e, 0\rangle$ and emits a photon into free space outside the cavity. In this case the excitation is lost. If the atom reaches $|g, 0\rangle$, it decouples from any further interaction and leaves the cavity. Note that the atom can be "recycled" if it decays back to state $|u, 0\rangle$.

3. The atom is excited to $|e, 0\rangle$, and cavity-enhanced spontaneous decay leads to the emission of a photon into the cavity. Subsequently, the desired photon emission from the cavity takes place. In this way, the system reaches $|g, 0\rangle$ and decouples from any further interaction.

4. The population of state $|e, 0\rangle$ is always zero, and $|g, 1\rangle$ is reached by adiabatic passage via the dark state. The photon is emitted from the cavity as desired, and the system reaches $|g, 0\rangle$, thereby decoupling from any further interaction.

In the following section, some possible loss mechanisms are discussed in detail.

5˙4.1. *Non-Adiabatic Evolution.* A partially non-adiabatic evolution of the system's state vector, $|\Psi\rangle$, to the non-dark eigenstates $|a^\pm\rangle$ is a possible loss channel for the photon generation process. An upper bound for these losses is given in (43), which can be evaluated further if some basic assumptions are made: First, the timing can be adjusted in such a way that the photon is most probably generated at $t = 0$, i.e. when the atom is on the axis of the cavity. Hence, we can assume $\dot{g}(0) = 0$ and $g(0) = g_0$. Second, when $\Delta \gg \max(g_0, \Omega_P^0)$, we have

$$(57) \qquad |a^+\rangle \approx -|e, 0\rangle \qquad \text{and} \qquad |a^-\rangle \approx \sin\Theta|u, 0\rangle + \cos\Theta|g, 1\rangle.$$

It can be seen from (28), (29) and (34) that the denominator of (43) is given by

$$(58) \qquad |\langle a^- | \frac{d}{dt} | a^0 \rangle|^2 = |\dot{\Theta}|^2 \approx \left| \frac{2g_0 \dot{\Omega}_P(0)}{\Omega_P^2(0) + 4g_0^2} \right|^2,$$

where $\Omega_P(0)$ is the pump-laser Rabi frequency on the cavity axis. From (53), we obtain for a nearly optimal situation with $2g_0 = \Omega_P^0$ and $\delta_X = -w_P$:

$$(59) \qquad \Omega_P(0) = 2g_0/e \quad \text{and} \quad \dot{\Omega}_P(0) = -\frac{4v}{ew_P} g_0,$$

where, again, w_P is the waist of the pump beam. Under these conditions, the denominator of (43) is

$$(60) \qquad |\langle a^- | \frac{d}{dt} | a^0 \rangle|^2 = \left| \frac{2v}{w_P e} \right|^2 \left(1 + \frac{1}{e^2}\right)^{-2},$$

whereas the nominator is

$$(61) \qquad |\omega^\pm - \omega^0|^2 \approx \left| \frac{g_0^2}{\Delta} \right|^2 \left(1 + \frac{1}{e^2}\right)^2.$$

Therefore, in case of a detuning Δ much larger than g_0, the non-adiabatic population losses to the non-dark eigenstates are limited by

$$(62) \qquad P_\pm \leq 4 \times \left| \frac{2v\Delta}{ew_P g_0^2} \right|^2 \left(1 + \frac{1}{e^2}\right)^{-4} \approx 1.2 \times (v/w_P)^2 (\Delta/g_0^2)^2.$$

If the detuning Δ is zero, an analogous estimation yields

$$(63) \qquad P_\pm \leq 4 \times \left| \frac{2v}{ew_P g_0} \right|^2 \left(1 + \frac{1}{e^2}\right)^{-3} \approx 1.2 \times (v/w_P)^2 (1/g_0^2).$$

For our experimental parameters, $v = 2\,\text{m/s}$, $w_P \approx w_C = 35\,\mu\text{m}$, and $g_0 = 2\pi \times 4.5\,\text{MHz}$, non-adiabatic losses according to (63) are below 2×10^{-5} and, hence, negligible. A similarly small result holds for a detuning of $\Delta \approx 2\pi \times 10\,\text{MHz}$. It follows that the Raman transition could be driven much faster than assumed here. For example, the atom could be excited by a pump pulse which matches the photon decay rate of the cavity, 2κ. In this case, one has to substitute v/w_P by 2κ in (63). For $2\kappa = 2\pi \times 2.5\,\text{MHz}$, one finds that the resulting losses, $P_\pm \approx 1.2 \times (2\kappa/g_0)^2$, may reach 50 % in this case.

5˙4.2. *Spontaneous Emission.* Even when the state vector of the system, $|\Psi\rangle$, follows $|a^0\rangle$ adiabatically, the excitation can possibly be lost by spontaneous emission if the excited state, $|e, 0\rangle$, makes a small contribution to state $|a^0\rangle$. In such a case, the otherwise dark state turns grey, and the time-dependent contributions of states $|e, 0\rangle$ and $|g, 1\rangle$ to state $|a^0\rangle$ determine the lost fraction. The ratio of the loss rate from the excited state to the total emission rate of the system gives the maximum spontaneous emission loss,

$$(64) \qquad P_{\text{loss}} \leq \max\left(\frac{2\gamma\rho_{ee}}{2\gamma\rho_{ee} + 2\kappa\rho_{gg}} \right),$$

where the populations of $|e, 0\rangle$ and $|g, 1\rangle$ are denoted by ρ_{ee} and ρ_{gg}, respectively. They are determined exclusively by the decomposition of $|a^0\rangle$ in case of an adiabatic evolution, since the other eigenstates do not contribute.

It is evident that $|a^0\rangle$ turns grey if the Raman-resonance condition, $\Delta_P = \Delta_C$, is not fulfilled. Moreover, it can bee seen from (47) that the cavity-field decay rate, κ,
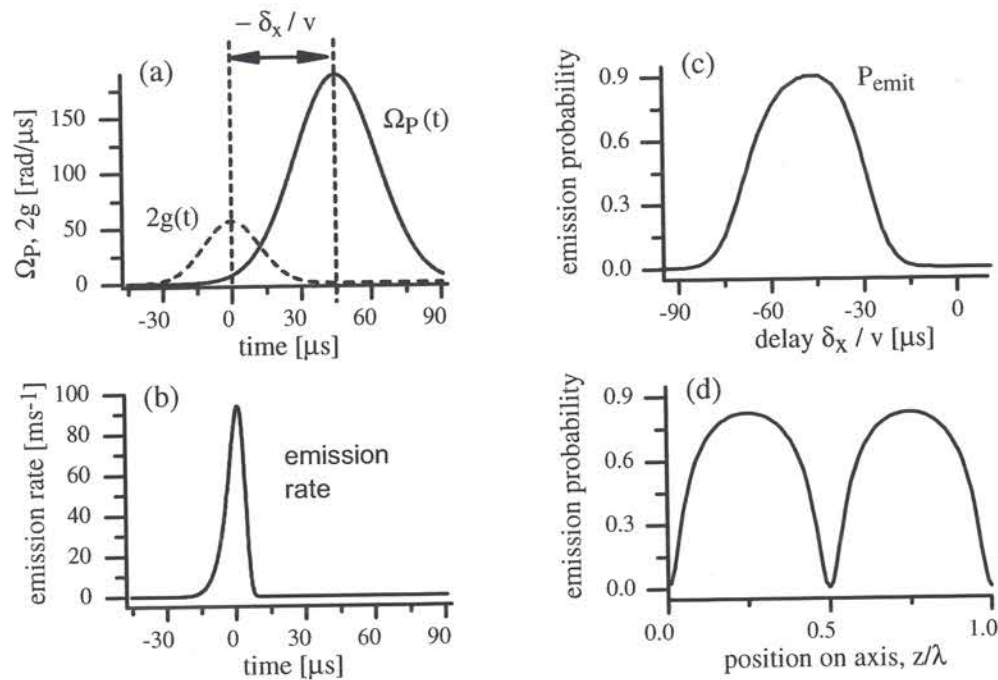
Fig. 8. – Simulation of a resonant atom-cavity interaction sequence for a cavity decay constant, $2\kappa = 2\pi \times 2.5$ MHz, an atomic population decay rate of $2\gamma = 2\pi \times 6$ MHz, and atoms travelling at $v = 2$ m/s. (a) $\Omega_P(t)$ and $2g(t)$ shown for experimental amplitudes and waists, $w_C = 35\,\mu$m and $w_P = 50\,\mu$m. (b) photon emission rate for a delay of $\delta_X/v = -45\,\mu$s. The integral of the rate yields a total photon emission probability, P_{Emit}, of 90%. (c) P_{Emit} as a function of the delay, δ_X/v, between cavity and pump interaction. (d) P_{Emit} as a function of the atomic position on the cavity axis for a delay of $\delta_X/v = -35\mu$s.

is equivalent to an imaginary "detuning" of the cavity from resonance, $\Delta_C \equiv i\kappa$. This complex pseudo-detuning cannot be compensated by an appropriate complex pump de-tuning, since the latter should not have an imaginary part to avoid decay of the atom from the initial state $|u, 0\rangle$. A consequence of the imaginary detuning is that the excited state, $|e, 0\rangle$, contributes to state $|a^0\rangle$, even in case of a Raman-resonant excitation. It follows that part of the excitation is lost by spontaneous emission.

An analytical treatment of this effect is far beyond the scope of this chapter. However, the size of the effect can be estimated from a numerical simulation like the one shown in fig. 8(a) and 8(b). In this case, we estimate that the photon emission from the cavity occurs around $t = 0$. At this moment, the atom is exposed to the Rabi frequencies $2g \approx 2g_0$ from the cavity, and $\Omega_P \approx g_0/2$ from the pump laser. In case of a resonant excitation with $\Delta_P = \Delta_C = 0$, and for the relevant set of parameters at the moment of the photon emission, $(\Omega_P, g, \gamma, \kappa) = 2\pi \times (2.25, 4.5, 3, 1.25)$ MHz, the eigenstates of

the non-Hermitian Hamiltonian (47) can be calculated numerically. The eigenstate $|a^0\rangle$, which is a dark state in the absence of dissipation, now reads

$$(65) \qquad |a^0\rangle = 0.976|u, 0\rangle + i\,0.055|e, 0\rangle - 0.208|g, 1\rangle,$$

and the relevant populations are $\rho_{ee} = |c_e|^2 = 0.003$ and $\rho_{gg} = |c_g|^2 = 0.043$. According to (64), the spontaneous emission losses are $P_{loss} \leq 14\%$. Since we have neglected that the atom may also decay back to its initial state from where it can be recycled, the actual losses do never reach such a high value. This is evident from the numerical simulation which is discussed in the next section. It shows that only 10% of the excitation is really lost by spontaneous emission from state $|e, 0\rangle$ to state $|g, 0\rangle$, from where recycling is not possible.

5`5. *Numerical Simulation.* – A numerical simulation for a single atom crossing the cavity is shown in Fig. 8. To include the cavity-field decay rate, κ, and the spontaneous emission rate of the atom, 2γ, we have employed the density-matrix formalism described in [12]. For the resonant situation, $\Delta_P = \Delta_C = 0$ shown here, the total emission probability, P_{Emit}, is expected to reach 90%. For the considered waists and amplitudes, Fig. 8(c) shows that P_{Emit} reaches its maximum for $\delta_X/v = -45\,\mu$s. Note also that P_{Emit} is vanishingly small if the interaction with the pump beam coincides or precedes the interaction with the cavity mode. Fig. 8(d) shows P_{Emit} as a function of the atom's position on the cavity axis for the delay realized in the experiment. Due to the standing wave mode structure, the emission probability is zero at the nodes, and shows maxima at the antinodes. Since the dependence of P_{Emit} on the position-dependent coupling constant, g, is highly nonlinear and saturates for large g, the gaps around the nodes are much narrower than the plateaus surrounding the antinodes.

5`6. *Experimental Realization.* – To realize the proposed scheme, we have chosen the setup sketched in Fig. 7(b). A cloud of ^{85}Rb atoms is prepared in the $5S_{1/2}, F = 3$ state and released from a magneto-optical trap (MOT) at a temperature of $\approx 10\,\mu$K. A small fraction (up to 100 atoms) falls through a stack of apertures and enters the mode volume of an optical cavity at a speed of 2 m/s. The cavity is composed of two mirrors with a radius of curvature of 50 mm and a distance of 1 mm. The waist of the TEM_{00} mode is $w_C = 35\,\mu$m, and in the antinodes the coupling coefficient is $g_0 = 2\pi \times 4.5$ MHz. The finesse of $61\,000$ corresponds to a linewidth $2\kappa = 2\pi \times 2.5$ MHz (FWHM), which is significantly smaller than the natural linewidth of the ^{85}Rb atoms, $2\gamma = 2\pi \times 6$ MHz. While one cavity mirror is highly reflective $(1 - R = 4 \times 10^{-6})$, the transmission of the other is 25-times higher, so that photons are emitted preferably in one direction. An avalanche photodiode (APD) with a quantum efficiency of 50% is used to detect them.

A reference laser is used to stabilize the cavity close to resonance with the $5S_{1/2}, F = 2 \longleftrightarrow 5P_{3/2}, F = 3$ transition with a lock-in technique. However, since an empty cavity is needed for the experiment, this laser is blocked 3.7 ms before the atoms enter the cavity. The pump beam is close to resonance with the $5S_{1/2}, F = 3 \longleftrightarrow 5P_{3/2}, F = 3$ transition
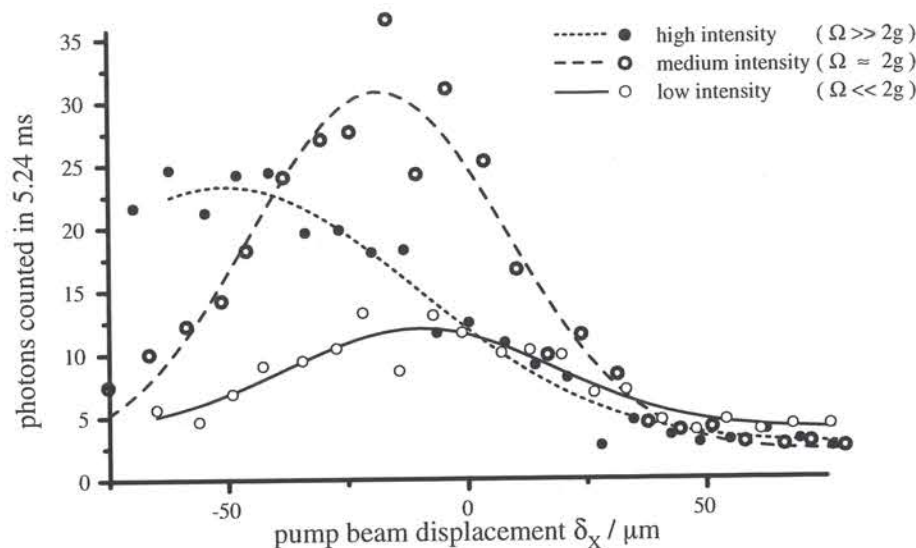
Fig. 9. – Number of photons emitted from the cavity in 5.24 ms as a function of the displacement δ_X of the pump beam (shift along the atom's trajectories) for three different intensities. A counter-intuitive interaction sequence for STIRAP is realized for negative δ_X.

and crosses the cavity transverse to its axis. This laser is focussed to a waist of 50 μm and has a power of 5.5 μW, which corresponds to a peak Rabi frequency $\Omega_P^0 = 2\pi \times 30$ MHz.

To adjust the delay between the atom-cavity and the atom-pump coupling, we displace the pump beam along the vertical direction. Figure 9 shows the number of photons emitted from the cavity for a single cloud of Rb atoms released from the MOT as a function of the pump-beam displacement, δ_X, for three different values of the pump amplitude. It is obvious that a negative δ_X, i.e. a counter-intuitive pulse sequence, is needed to reach a maximum photon emission probability. Moreover, the position of the peak of the emission shifts to more negative values when the peak Rabi frequency, Ω_P^0, is increased. This is because the pulse amplitude needed to generate a photon is reached earlier, which is also the best condition for adiabatic following.

The left hand side of fig. 10 depicts the case for arbitrary Δ_P and Δ_C. From this numerical simulation, it is evident that P_{Emit} is largest if the excitation is Raman resonant ($\Delta_P = \Delta_C$). However, for the delay $\delta_X/v = -35\,\mu$s chosen in the experiment, a slight reduction is expected for $\Delta_P = \Delta_C = 0$, since the waist of the pump, w_P, is larger than the waist of the cavity, w_C, and resonant excitation of the atom prior to the interaction with the cavity mode cannot be neglected. The right hand side of fig. 10 shows the corresponding experimental results. The detunings of the cavity and the pump laser are both adjusted by means of acousto-optic modulators. To register the data, the MOT has been loaded and dropped across the cavity 50 times. The atom cloud needs 6.5 ms

(FWHM) to cross the cavity mode, and within this interval, the photons emerging from the cavity are measured by the APD and recorded by a transient digitizer during 2.6 ms with a time resolution of 25 MHz. Therefore, the signal is observed for a total time of 130 ms. Due to the dark-count rate of 390 Hz of the APD, the total number of dark counts in the interval is limited to 51 ± 7.

Figure 10(a) shows the number of counted photons emerging from the cavity resonant with the atomic transition, $\Delta_C = 0$, as a function of the pump pulse detuning, Δ_P. In this case, a small probability for atomic excitation is expected, which could lead to a small but cavity-enhanced spontaneous emission into the cavity mode, as has been shown previously [9-11]. The numerical simulation shows that an excited atom, suddenly placed at an antinode, would emit into the resonant cavity with a probability of 26% (see section 2'6), which indicates that most of the spontaneously emitted photons are lost in a random direction. This loss explains the smaller peak emission rate with respect to the off-resonant cases discussed below. Note that the cavity mode covers only a small solid angle of $\approx 4\pi \times 2.6 \times 10^{-5}$ srad, which means that the calculated spontaneous emission rate into the cavity is enhanced by a factor 10^4. However, as can be seen in fig. 10(a), the measured linewidth is sub-natural, and therefore the observed signal cannot be attributed to an excitation by the pump beam followed by enhanced spontaneous emission.

This is even more evident if the cavity is detuned (Fig. 10(b,c)). The emission peak is pulled away from the atomic resonance, following the Raman resonance condition, $\Delta_P = \Delta_C$. Such a displacement proofs that the light emission is not the result of a pump transition followed by enhanced spontaneous emission into the cavity. Moreover, Δ_P is too large for an electronic excitation of the atoms. Therefore, the exponentially decreasing wing of the pump beam cannot excite the atoms prior to their interaction with the cavity mode as in fig. 10(a). Hence, the losses vanish, and the peak photon emission probability is higher than for the resonant case. Note also that the observed linewidth is much smaller than the natural linewidth, $2\gamma = 2\pi \times 6$ MHz, of the atom. For $\Delta_C = -2\pi \times 15$ MHz, the line is only 3 MHz wide and its width approaches the cavity linewidth $2\kappa = 2\pi \times 2.5$ MHz, which limits the width of the Raman transition, since 2κ is the decay rate of the final state, $|g, 1\rangle$.

In our discussion, we have assumed that the atoms interact with the cavity one-by-one. This is justified according to the following estimation: A mechanical slit restricts the atom's maximum distance from the cavity axis to ±50 μm. The spatial variation of g along (Fig. 8(d)) and perpendicular to the cavity axis reduces the average emission probability to 37% per atom crossing the slit and the pump beam. Due to the low quantum efficiency of the APD and unavoidable cavity losses, only about 40% of the generated photons are detected. Therefore the maximum measured rate of 230 events/130 ms corresponds to a generation rate of 4.4 photons/ms, and 12 atoms/ms are needed to explain this signal. Since the photon generation takes 12 μs (FWHM, Fig. 8(b)), the probability that two atoms interact with the cavity is at most 14%. This is small and, hence, negligible.

All observed features are in excellent agreement with our simulation, and we therefore conclude that the photon emission is caused by a vacuum-stimulated Raman transition,
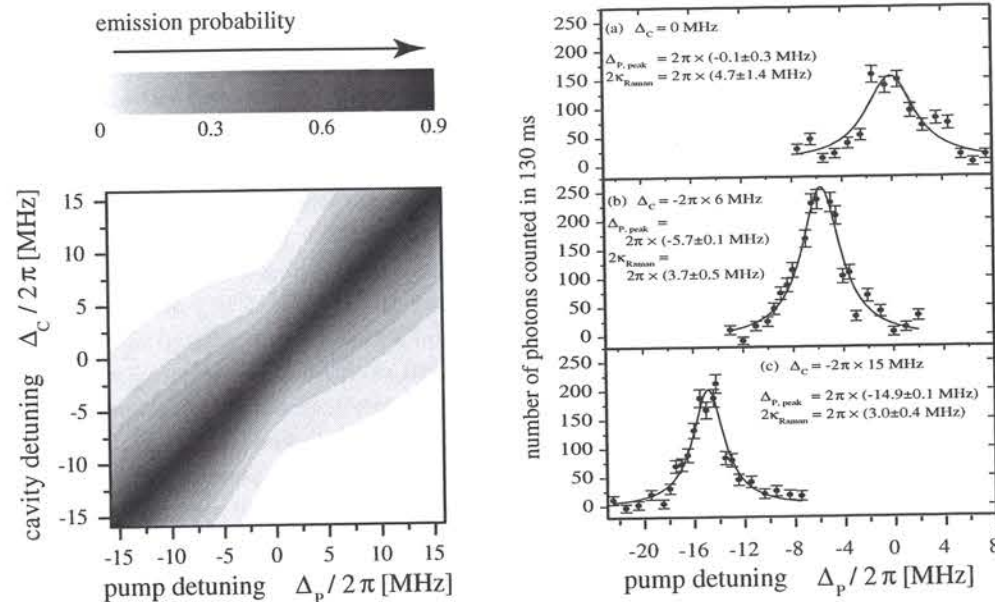
Fig. 10. – **left:** Photon emission probability as a function of cavity and pump detuning, calculated for a pulse delay of $\delta_X/v = -35\,\mu s$ and the parameters of Fig. 8. The chosen delay gives the best fit with the experimental data shown on the **right:** Observed number of photons emitted from the cavity as a function of the pump laser detuning, Δ_P, for three different cavity detunings. The solid lines are Lorentzian fits to the data. The magneto-optical trap was loaded and dropped through the cavity 50 times to record the data shown here. A small background level was subtracted from the data displayed in the figure.

i.e. the coupling to the cavity, $g(t)$, and the Rabi frequency of the pump laser, $\Omega_P(t)$, are both high enough to assure an adiabatic evolution of the system, thus forcing the state vector $|\Psi\rangle$ to follow the dark state $|a^0\rangle$ throughout the interaction. Loss due to spontaneous emission is suppressed, and the photons are emitted into a single mode of the radiation field with well determined frequency and direction.

6. – Summary and Outlook

Vacuum-stimulated Raman scattering driven by an adiabatic passage can be used to generate single, well characterized photons on demand, provided the Raman excitation is performed in a controlled, triggered way. In contrast to most other single-photon sources [36-41], these photons will have a narrow bandwidth and a directed emission. With a single atom trapped inside the cavity, a suitable repumping mechanism should allow to re-establish the initial condition after each photon emission. Repeated adiabatic passage and repumping cycles should therefore lead to a bit-stream of single photons. Finally, we state that the photon generation process depends on the initial state of the

atom interacting with the cavity. If the atom is prepared in a superposition of states $|g,0\rangle$ and $|u,0\rangle$ prior to the interaction, this state will be mapped onto the emitted photon. A second atom placed in another cavity could act as a receiver, and with the suitable pump pulse sequence applied to the emitting and the receiving atom, a quantum teleportation of the atom's internal state could be realized [46].

$$* \quad * \quad *$$

REFERENCES

[1] W. Tittel, G. Ribordy, and N. Gisin. Quantum Cryptography. *Phys. World*, page 41, March 1998.

[2] E. Knill, R. Laflamme, and G. J. Milburn. A scheme for efficient quantum computing with linear optics. *Nature*, 409:46–52, 2001.

[3] K. Bergmann and B. W. Shore. Coherent Population Transfer. In H. L. Dai and R. W. Field, editors, *Molecular dynamics and stimulated emission pumping*, pages 315–373. World Scientific, Singapore, 1995.

[4] K. Bergmann, H. Theuer, and B. W. Shore. Coherent Population Transfer Among Quantum States of Atoms and Molecules. *Rev. Mod. Phys.*, 70:1003–1026, 1998.

[5] A. Kuhn, S. Steuerwald, and K. Bergmann. Coherent Population Transfer in NO with Pulsed Lasers: The Consequences of Hyperfine Structure, Doppler Broadening and Electromagnetically Induced Absorption. *Eur. Phys. J. D*, 1:57–70, 1998.

[6] E. T. Jaynes and F. W. Cummings. Comparison of Quantum and Semiclassical Radiation Theories with Application to the Beam Maser. *Proc. IEEE*, 51:89–109, 1963.

[7] B. W. Shore and P. L. Knight. The Jaynes-Cummings Model. *J. Mod. Opt.*, 40:1195, 1993.

[8] E. M. Purcell. Spontaneous Emission Probabilities at Radio Frequencies. *Phys. Rev.*, 69:681, 1946.

[9] D. J. Heinzen, J. J. Childs, J. E. Thomas, and M. S. Feld. Enhanced and inhibited spontaneous emission by atoms in a confocal resonator. *Phys. Rev. Lett.*, 58:1320–1323, 1987.

[10] D. J. Heinzen and M. S. Feld. Vacuum radiative level shift and spontaneous-emission linewidth of an atom in an optical resonator. *Phys. Rev. Lett.*, 59:2623–2626, 1987.

[11] S. E. Morin, C. C. Yu, and T. W. Mossberg. Strong atom-cavity coupling over large volumes and the observation of subnatural intracavity atomic linewidths. *Phys. Rev. Lett.*, 73:1489–1492, 1994.

[12] A. Kuhn, M. Hennrich, T. Bondo, and G. Rempe. Controlled Generation of Single Photons from a Strongly Coupled Atom-Cavity System. *Appl. Phys. B*, 69:373–377, 1999.

[13] M. Hennrich, T. Legero, A. Kuhn, and G. Rempe. Vacuum-Stimulated Raman Scattering Based on Adiabatic Passage in a High-Finesse Optical Cavity. *Phys. Rev. Lett.*, 85:4872–4875, 2000.

[14] C. K. Law and H. J. Kimble. Deterministic Generation of a Bit-Stream of Single-Photon Pulses. *J. Mod. Opt.*, 44:2067–2074, 1997.

[15] G. Hechenblaikner, M. Gangl, P. Horak, and H. Ritsch. Cooling an Atom in a Weakly Driven High-Q Cavity. *Phys. Rev. A*, 58:3030–3042, 1998.

[16] R. J. Thompson, G. Rempe, and H. J. Kimble. Observation of Normal-Mode Splitting for an Atom in an Optical Cavity. *Phys. Rev. Lett.*, 68:1132–1135, 1992.

[17] J. J. Childs, K. An, M. S. Otteson, R. R. Dasari, and M. S. Feld. Normal Mode Line Shapes for Atoms in Standing-Wave Optical Resonators. *Phys. Rev. Lett.*, 77:2901–2904, 1996.

[18] P. Münstermann, T. Fischer, P. Maunz, P. W. H. Pinkse, and G. Rempe. Observation of cavity-mediated long-range light forces between strongly coupled atoms . *Phys. Rev. Lett.*, 84:4068–4071, 2000.

[19] C. J. Hood, M. S. Chapman, T. W. Lynn, and H. J. Kimble. Real-time cavity QED with single atoms. *Phys. Rev. Lett.*, 80:4157, 1998.

[20] L. A. Lugiato. Theory of optical bistability. volume XXI, pages 71–216, B. V., 1984. Elsevier Science Publishers.

[21] A. Abragam. *The Principles of Nulcear Magnetism*. Oxford University Press, Oxford, 1961.

[22] M. M. T. Loy. Self-induced rapid adiabatic passage. *Phys. Rev. Lett.*, 32:814–817, 1974.

[23] M. M. T. Loy. Observation of two-photon optical nutation and free-induction decay. *Phys. Rev. Lett.*, 36:1454–1457, 1976.

[24] M. M. T. Loy. Two-photon adiabatic inversion. *Phys. Rev. Lett.*, 41:473–475, 1978.

[25] L. P. Yatsenko, B. W. Shore, T. Halfmann, and K. Bergmann. Source of metastable H(2s) atoms using the Stark chirped rapid-adiabatic-passage technique. *Phys. Rev. A*, 60:R4237–R4240, 1999.

[26] A. Kuhn, H. Perrin, W. Hänsel, and C. Salomon. Three Dimensional Raman Cooling using Velocity Selective Rapid Adiabatic Passage. In K. Burnett, editor, *OSA TOPS on Ultracold Atoms and BEC*, volume 7, pages 58–65. OSA, 1996.

[27] H. Perrin, A. Kuhn, I. Bouchoule, and C. Salomon. Sideband cooling of neutral atoms in a far-detuned optical lattice. *Europhys. Lett.*, 42:395–400, 1998.

[28] S. E. Harris. Electromagnetically Induced Transparency with Matched Pulses. *Phys. Rev. Lett.*, 70:552–555, 1993.

[29] S. E. Harris. Electromagnetically Induced Transparency. *Phys. Today*, 50(7):36, 1997.

[30] L. V. Hau, S. E. Harris, Z. Dutton, and C. H. Behroozi. Light speed reduction to 17 metres per second in an ultracold atomic gas. *Nature*, 397:594–598, 1999.

[31] M. D. Lukin, S. F. Yelin, and M. Fleischhauer. Entanglement of Atomic Ensembles by Trapping Coherent Photon States. *Phys. Rev. Lett.*, 84:4235–4238, 2000.

[32] M. Fleischhauer and M. D. Lukin. Dark-State Polaritons in Electromagnetically Induced Transparency. *Phys. Rev. Lett.*, 84:5094–5097, 2000.

[33] D. F. Phillips, A. Fleischhauer, A. Mair, R. L. Walsworth, and M. D. Lukin. Storage of Light in Atomic Vapor. *Phys. Rev. Lett.*, 86:783–786, 2001.

[34] A. Messiah. *Quantum Mechanics*, volume 2, chapter 17. J. Wiley & Sons, NY, 1958.

[35] A. S. Parkins, P. Marte, P. Zoller, and H. J. Kimble. Synthesis of Arbitrary Quantum States Via Adiabatic Transfer of Zeeman Coherence. *Phys. Rev. Lett.*, 71:3095, 1993.

[36] J. Kim, O. Benson, H. Kan, and Y. Yamamoto. A Single Photon Turnstile Device. *Nature*, 397:500–503, 1999.

[37] C. Brunel, B. Lounis, P. Tamarat, and M. Orrit. Triggered Source of Single Photons Based on Controlled Single Molecule Fluorescence. *Phys. Rev. Lett.*, 83:2722–2725, 1999.

[38] B. Lounis and W. E. Moerner. Single Photons on Demand from a Single Molecule at Room Temperature. *Nature*, 407:491–493, 2000.

[39] C. Kurtsiefer, S. Mayer, P. Zarda, and H. Weinfurter. Stable Solid-State Source of Single Photons. *Phys. Rev. Lett.*, 85:290–293, 2000.

[40] R. Brouri, A. Beveratos, J.-P. Poizat, and P. Grangier. Photon Antibunching in the Fluorescence of Individual Color Centers in Diamond. *Opt. Lett.*, 25:1294–1296, 2000.

[41] P. Michler, A. Imamoglu, M. D. Mason, P. J. Carson, G. F. Strouse, and S. K. Buratto. Quantum Correlation Among Photons from a Single Quantum Dot at Room Temperature. *Nature*, 406:968–970, 2000.

[42] O. Benson, C. Santori, M. Pelton, and Y. Yamamoto. Regulated and entangled photons from a single quantum dot. *Phys. Rev. Lett.*, 84:2513–2516, 2000.

[43] C. Santori, M. Pelton, G. Solomon, Y. Dale, and Y. Yamamoto. Triggered Single Photons from a Quantum Dot. *Phys. Rev. Lett.*, 86:1502–1505, 2001.

[44] P. Michler, A. Kiraz, C. Becher, W. V. Schoenfeld, P. M. Petroff, L. Zhang, E. Hu, and A. Imamoglu. A Quantum Dot Single Photon Turnstile Device. *Science*, 290:2282–2285, 2000.

[45] C. K. Law and J. H. Eberly. Arbitrary Control of a Quantum Electromagnetic Field. *Phys. Rev. Lett.*, 76:1055, 1996.

[46] J. I. Cirac, P. Zoller, H. J. Kimble, and H. Mabuchi. Quantum State Transfer and Entanglement Distribution Among Distant Nodes in a Quantum Network. *Phys. Rev. Lett.*, 78:3221–3224, 1997.

15 Strongly Coupled Atom-Cavity Systems

Axel Kuhn, Markus Hennrich, and Gerhard Rempe

Max-Planck-Institut für Quantenoptik
Hans-Kopfermann-Str. 1
85748 Garching
Germany

15.1 Introduction

Worldwide, major efforts are made to realize decoherence-free systems for the storage of individual quantum bits (qubits) and to conditionally couple different qubits for the processing of quantum information. Ultra-cold trapped neutral atoms or ions are ideal to store quantum information in long-lived internal states. Photons are ideal to transmit quantum information between quantum memories. In this chapter, the coupling of internal atomic states to a quantized mode of the radiation field is discussed. We introduce an adiabatic coupling scheme between a single atom and an optical cavity, which is based on a unitary evolution of the coupled atom-cavity system and therefore is intrinsically reversible. It allows one to populate either Fock states on demand, or to emit single optical photons into a well-defined mode of the radiation field outside the cavity. Such a deterministic single-photon source is essential for optical quantum information processing with linear components [KLM01], and it makes possible quantum networking between different cavities, where the key requirement is the ability to interconvert stationary and flying qubits [CZKM97, DiV00]. These features distinguish the present scheme from other methods of Fock-state preparation in the microwave regime [MHN+97, BVW01], where the photons remain trapped inside the cavity.

15.2 Atoms, Cavities and Light

The atom-cavity coupling scheme combines cavity quantum electrodynamics (CQED) with stimulated Raman scattering by adiabatic passage (STIRAP) [VFSB01]. To describe the scheme, we first introduce the relevant features of CQED and the Jaynes-Cummings model [JC63, SK93], then we focus on three-level atoms with two dipole transitions driven by two radiation fields. One of them comes from a laser, the other is that of a cavity strongly coupled to the atom. We show how to control the state vector of the system so that exactly one photon is emitted through one of the cavity mirrors, thereby forming a single-photon pulse [HLKR00, KHR02].

15.2.1 Field Quantization in a Fabry-Perot Cavity

A Fabry-Perot cavity with mirror separation l and reflectivity $\mathcal{R}$ has a free spectral range $FSR = \pi c/l$, and its finesse is defined as $\mathcal{F} = \pi \sqrt{\mathcal{R}}/(1 - \mathcal{R})$. In the vicinity of a resonance, the transmission is a Lorentzian with a linewidth (FWHM) of $2\kappa = FSR/\mathcal{F}$, which is twice the decay rate of the cavity field, κ. Stable single-mode operation is achieved using curved mirrors, so that Hermite-Gaussian or Laguerre-Gaussian cavity eigenmodes are obtained. Within this chapter, we consider a single TEM_{00} mode with mode function $\psi(\mathbf{r})$ and resonance frequency ω_C. The electromagnetic field of the mode is quantized, so that its state vector is, in general, a superposition of photon-number states, the so-called Fock states, $|n\rangle$. Each contributing photon carries an energy of $\hbar\omega_C$, and for n photons in the mode the total energy is $\hbar\omega_C(n + \frac{1}{2})$, where $\hbar\omega_C/2$ is the zero-point energy. The equidistant energy spacing imposes an analogue treatment of the cavity to an harmonic oscillator. Consequently, creation and annihilation operators for a photon, $a^\dagger$ and a, respectively, are used to express the Hamiltonian of the cavity,

$$H_C = \hbar\omega_C \left(a^\dagger a + \frac{1}{2} \right). \tag{15.1}$$

Note that this Hamiltonian does not include losses. In a real cavity, all photon number states decay until thermal equilibrium with the environment is reached. In the optical domain, this corresponds to the vacuum state, $|0\rangle$, with no photon in the cavity.

15.2.2 Two-Level Atom

We now analyze how the quantized field interacts with a two-level atom with ground state, $|g\rangle$, and excited state, $|e\rangle$, with energies $\hbar\omega_g$ and $\hbar\omega_e$, respectively, and transition dipole moment μ_{eg}. The Hamiltonian of the atom reads

$$H_A = \hbar\omega_g |g\rangle\langle g| + \hbar\omega_e |e\rangle\langle e|. \tag{15.2}$$

The coupling to the field mode of the cavity is expressed by the atom-cavity coupling constant,

$$g(\mathbf{r}) = g_0 \, \psi(\mathbf{r}), \qquad \text{with} \qquad g_0 = \sqrt{(\mu_{eg}^2 \omega_C)/(2\hbar\epsilon_0 V)}, \tag{15.3}$$

where V is the mode volume of the cavity. In a closed system, any change of the atom's internal state must be reflected by an according change of the cavity's photon number, n. It follows that the interaction Hamiltonian of the atom-cavity system,

$$H_{int} = -\hbar g \left[|e\rangle\langle g| a + a^\dagger |g\rangle\langle e| \right], \tag{15.4}$$

includes the creation and annihilation operators, $a^\dagger$ and a. For a given excitation number, n, only the pair of product states $|g, n\rangle$ and $|e, n - 1\rangle$ is coupled, and for a cavity resonant with the atomic transition, the population oscillates with the Rabi frequency $\Omega_C = 2g\sqrt{n}$ between these states.
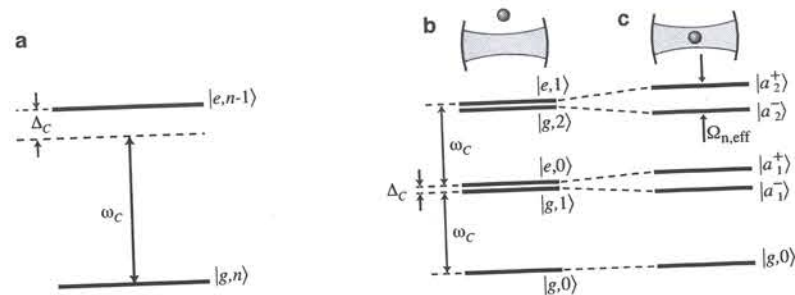
Figure 15.1: (a) A two-level atom with ground state $|g\rangle$ and excited state $|e\rangle$ coupled to a cavity containing n photons. In the dressed-level scheme of the combined atom-cavity system with the atom outside (b) or inside (c) the cavity, the state doublets are either split by Δ_C or by the effective Rabi frequency, $\Omega_{n,\text{eff}}$, respectively.

The eigenfrequencies of the total Hamiltonian, $H = H_C + H_A + H_{int}$, can be found easily. In the rotating wave approximation, they read

$$\omega_n^\pm = \omega_C \left(n + \frac{1}{2} \right) + \frac{1}{2} \left(\Delta_C \pm \sqrt{4ng^2 + \Delta_C^2} \right), \tag{15.5}$$

where $\Delta_C = \omega_e - \omega_g - \omega_C$ is the detuning between the atom and the cavity. The level splitting between the two corresponding eigenstates, $\Omega_{n,\text{eff}} = \sqrt{4ng^2 + \Delta^2}$, is the effective Rabi frequency of the population oscillation between states $|g,n\rangle$ and $|e,n-1\rangle$. This means that the frequency of the population oscillation between states $|g,n\rangle$ and $|e,n-1\rangle$. This means that the cavity field stimulates the emission of an excited atom into the cavity, thus deexciting the atom and increasing the photon number by one. Subsequently, the atom is reexcited by absorbing a photon from the cavity field, and so forth. Since an excited atom and a cavity containing no photon initially are sufficient to start the oscillation between $|e,0\rangle$ and $|g,1\rangle$ at frequency $\sqrt{4g^2 + \Delta_C^2}$, this phenomenon is called vacuum-Rabi oscillation. For a resonant interaction, the oscillation frequency is $2g$, which is therefore called the vacuum-Rabi frequency.

So far, we have shown that the atom-cavity interaction splits the photon number states into doublets of non-degenerate dressed states, which are named after Jaynes and Cummings [JC63, SK93]. However, there is one exception to the rule: Without excitation, the atom and the cavity are in their ground states, $|g\rangle$ and $|0\rangle$, respectively. The only possible product state, $|g,0\rangle$, is not coupled to any other state and therefore no splitting occurs.

15.2.3   Three-Level Atom

Now we consider an atom with a Λ-type three-level scheme providing transition frequencies $\omega_{eu} = \omega_e - \omega_u$ and $\omega_{eg} = \omega_e - \omega_g$ as depicted in fig. 15.2. The $|u\rangle \leftrightarrow |e\rangle$ transition is driven by a classical light field of frequency ω_P with Rabi frequency Ω_P, the so-called pump field, and a cavity mode with frequency ω_C couples to the $|g\rangle \leftrightarrow |e\rangle$ transition. If we define the respective detunings as $\Delta_P = \omega_{eu} - \omega_P$ and $\Delta_C = \omega_{eg} - \omega_C$, and assume that the pump laser and the cavity only couple to their respective transitions, the behaviour of the atom-cavity
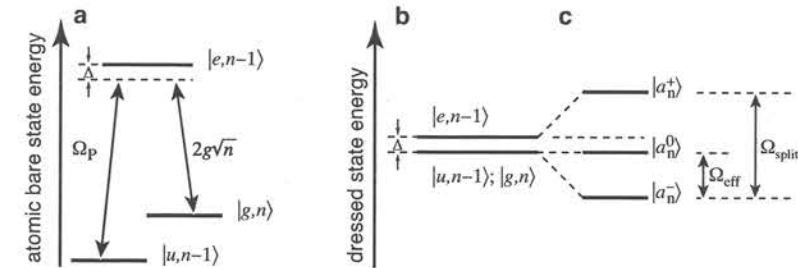
Figure 15.2: (a) A three-level atom driven by a classical laser field of Rabi frequency Ω_P, coupled to a cavity containing n photons. (b) Dressed-level scheme of the combined system for vanishing coupling strengths and for an atom interacting with laser and cavity (c). The triplet is split by $\Omega_{\text{split}} = \sqrt{4ng^2 + \Omega_P^2 + \Delta^2}$. Note that for a detuning Δ which is large compared to all Rabi frequencies, the Raman transition $|u,n-1\rangle \leftrightarrow |g,n\rangle$ is driven at the effective Rabi frequency $\Omega_{\text{eff}} = \frac{1}{2} \left(\Omega_{\text{split}} - |\Delta| \right) \approx (4ng^2 + \Omega_P^2)/|4\Delta|$.

system is described by the interaction Hamiltonian

$$H_{\text{int}} = \hbar \left[\Delta_P |u\rangle\langle u| + \Delta_C |g\rangle\langle g| - g(|e\rangle\langle g|a + a^\dagger|g\rangle\langle e|) - \frac{1}{2}\Omega_P(|e\rangle\langle u| + |u\rangle\langle e|) \right]. \tag{15.6}$$

Given an arbitrary excitation number n, this Hamiltonian couples only the three states $|u,n-1\rangle, |e,n-1\rangle, |g,n\rangle$. For these triplets and a Raman-resonant interaction with $\Delta_P = \Delta_C \equiv \Delta$, the eigenfrequencies of the coupled system read

$$\omega_n^0 = \omega_C \left(n + \frac{1}{2} \right) \quad \text{and} \quad \omega_n^\pm = \omega_C \left(n + \frac{1}{2} \right) + \frac{1}{2} \left(\Delta \pm \sqrt{4ng^2 + \Omega_P^2 + \Delta^2} \right). \tag{15.7}$$

Note that the Jaynes-Cummings state doublets of the two-level atom are now replaced by state triplets, with eigenstates

$$\begin{aligned}
|\phi_n^0\rangle &= \cos\Theta |u,n-1\rangle - \sin\Theta |g,n\rangle, \\
|\phi_n^+\rangle &= \cos\Phi \sin\Theta |u,n-1\rangle - \sin\Phi |e,n-1\rangle + \cos\Phi \cos\Theta |g,n\rangle, \\
|\phi_n^-\rangle &= \sin\Phi \sin\Theta |u,n-1\rangle + \cos\Phi |e,n-1\rangle + \sin\Phi \cos\Theta |g,n\rangle,
\end{aligned} \tag{15.8}$$

where the mixing angles Θ and Φ are given by

$$\tan\Theta = \frac{\Omega_P}{2g\sqrt{n}} \quad \text{and} \quad \tan\Phi = \frac{\sqrt{4ng^2 + \Omega_P^2}}{\sqrt{4ng^2 + \Omega_P^2 + \Delta^2} - \Delta}, \tag{15.9}$$

with Ω_P and g assumed to be real. We note that the interaction with the light lifts the degeneracy of the three eigenstates as soon as the Rabi-frequencies are non-zero. Furthermore, it must be emphasized that one of these states, namely $|\phi_n^0\rangle$, is neither subject to an energy shift,

nor does the excited atomic state contribute to it. In the literature, $|\phi_n^0\rangle$ is therefore called a "dark state" since its population cannot be lost by spontaneous emission.

In the limit of vanishing Ω_P, the states $|\phi_n^\pm\rangle$ correspond to the Jaynes-Cummings doublet and the third eigenstate, $|\phi_n^0\rangle$, coincides with $|u, n-1\rangle$. Note that ω_n^0 is not affected by Ω_P or g. Therefore transitions between the dark states $|\phi_{n+1}^0\rangle$ and $|\phi_n^0\rangle$ are always in resonance with the cavity. This holds, in particular, for the transition from $|\phi_1^0\rangle$ to $|\phi_0^0\rangle \equiv |g, 0\rangle$ since the $n = 0$ state does not split (the corresponding states $|u, -1\rangle$ and $|e, -1\rangle$ do not exist).

15.2.4 Adiabatic Passage

Adiabatic passage in the optical domain is used for coherent population transfer in atoms or molecules for many years now. In two-level systems, it can be driven by a frequency chirp of a light field across the relevant resonance [Loy74, Loy78]. This technique has been successfully extended to three-level systems [YSHB99], and it is also used for velocity-selective excitation and Raman cooling of atoms [KPHS96, PKBS98]. Without chirp, but with a Raman transition driven by two distinct pulses of variable amplitudes, effects like electromagnetically induced transparency (EIT) [Har93, Har97], slow light [HHDB99, PFM$^+$01], and stimulated Raman scattering by adiabatic passage (STIRAP) [VFSB01] are observed. All these effects have been demonstrated with classical light fields.
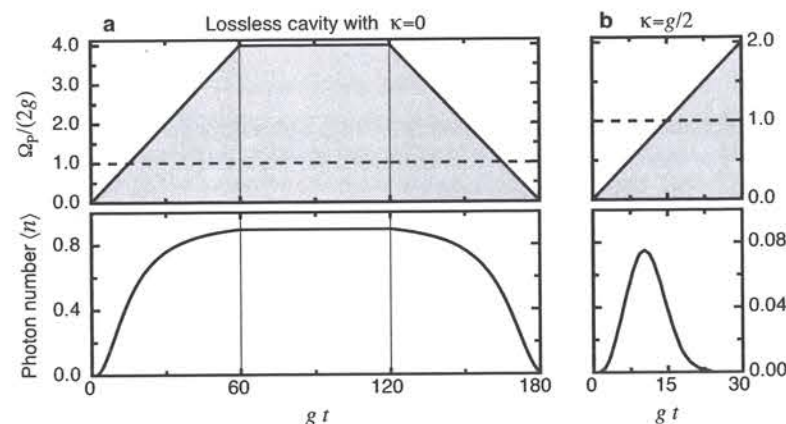
Figure 15.3: Relative Rabi frequency, $\Omega_P/(2g)$, and corresponding mean photon number, $\langle n \rangle$, as a function of the dimensionless time, gt, and an atom-cavity system initially prepared in state $|u, 0\rangle$. **(a)** For a lossless cavity, the mean photon number $\langle n \rangle$ is given by the population of state $|g, 1\rangle$, which obeys Eq. (15.10). When the pump pulse is turned off adiabatically, the photon is reabsorbed and the system returns to the initial state. **(b)** In case of a lossy cavity, the photon escapes during the rising edge of the pump pulse. For the chosen parameters, the area of the $\langle n \rangle$-pulse indicates a probability of 74 % for a single-photon emission.

These techniques have in common that the system's state vector, $|\Psi\rangle$, always coincides with a single eigenstate, e.g. $|\phi_n^0\rangle$, of the time-dependent interaction Hamiltonian. In principle, the time evolution of the system is completely controlled by the variation of this eigen-

state. However, a more detailed analysis [Mes58, KR02] reveals that the eigenstates must change slowly with respect to the eigenfrequency differences. Adiabaticity is assured if the condition $|\omega_n^\pm - \omega_n^0| \gg |\langle \phi_n^\pm| \frac{d}{dt} |\phi_n^0\rangle|$ is met throughout the interaction, and as long as the system does not decay via some other channel. In this context, the non-decaying dark state, $|\phi_n^0\rangle$, is of enormous significance.

It follows that an atom-cavity system, once prepared in $|\phi_n^0\rangle$, should stay there, thus allowing one to control the relative population of the contributing product states, $|u, n-1\rangle$ and $|g, n\rangle$, simply by adjusting the pump Rabi frequency, Ω_P. To show this, let us start with a system initially prepared in state $|u, n-1\rangle$. As can be seen from (15.8), this state coincides with $|\phi_n^0\rangle$ if the condition $2g\sqrt{n} \gg \Omega_P$ is met in the beginning of the interaction. Once the system has been successfully prepared in the dark state, the ratio between the populations of the contributing states reads

$$\frac{|\langle u, n-1|\Psi\rangle|^2}{|\langle g, n|\Psi\rangle|^2} = \frac{4ng^2}{\Omega_P^2}. \tag{15.10}$$

As proposed in [KHBR99], we now assume that an atom in state $|u\rangle$ is placed in a cavity mode populated with $n-1$ photons driving the $|g, n\rangle \leftrightarrow |e, n-1\rangle$ transition with the effective Rabi frequency $2g\sqrt{n}$, so that the initial state coincides with $|\phi_n^0\rangle$. The atom is then exposed to a pump laser pulse coupling the $|u\rangle \leftrightarrow |e\rangle$ transition with a slowly rising amplitude that finally leads to $\Omega_P \gg 2g\sqrt{n}$. The system evolves from $|u, n-1\rangle$ to $|g, n\rangle$, and therefore the photon number increases by one. If decay is neglected, the successive application of this method would allow one to prepare arbitrary photon-number states [PMZK93]. To do so, the pump pulse must be turned off suddenly. Otherwise the system would adiabatically return to its initial state, as shown in Fig. 15.3(a).

The situation changes if the cavity-field decay time, κ^{-1}, is finite and comparable or shorter than the exciting laser pulse. Starting from the atom-cavity system prepared in state $|u, 0\rangle$, a single photon is generated and emitted from the cavity during the excitation process (see Fig. 15.3(b)). Once the photon escapes, the system reaches state $|g, 0\rangle$ and stays there, since it decouples from the cavity and the pump field.

15.3 Single-Photon Sources

So far, one of the most popular schemes used for the generation of single photons relies on parametric down-conversion. This scheme produces photons at more or less random times and, hence, requires post selection. Only during the last few years, different photon generation schemes have been demonstrated, like a single-photon turnstile device based on the Coulomb blockade mechanism in a quantum dot [KBKY99], the fluorescence of a single molecule [BLTO99, LM00], or a single colour centre (Nitrogen vacancy) in diamond [KMZW00, BBPG00], or the photon emission of a single quantum dot [MIM$^+$00, YKS$^+$02]. All these new schemes emit photons upon an external trigger event. However, the photons are spontaneously emitted into many modes of the radiation field and usually show a broad energy distribution. Only recently, cavity-enhanced spontaneous emission techniques for single-photon generation from a quantum dot have been proposed [BSPY00] and demonstrated [SPS$^+$01, MKB$^+$00, MRG$^+$01]. However, all these single-photon emitters cannot transfer

quantum information between atoms and photons in a coherent manner and, therefore, do not meet the essential requirement for quantum networking. The reason is that the emission process, namely an electronic excitation of the system followed by spontaneous emission, cannot be described by a Hamiltonian evolution and, hence, is irreversible.

15.3.1 Vacuum-Stimulated Raman Scattering

We now report on an experimental scheme [KHBR99, HLKR00] which employs the adiabatic passage technique discussed in section 15.2.4, and where the strong coupling of a single atom to a single cavity mode stimulates one branch of a Raman transition.
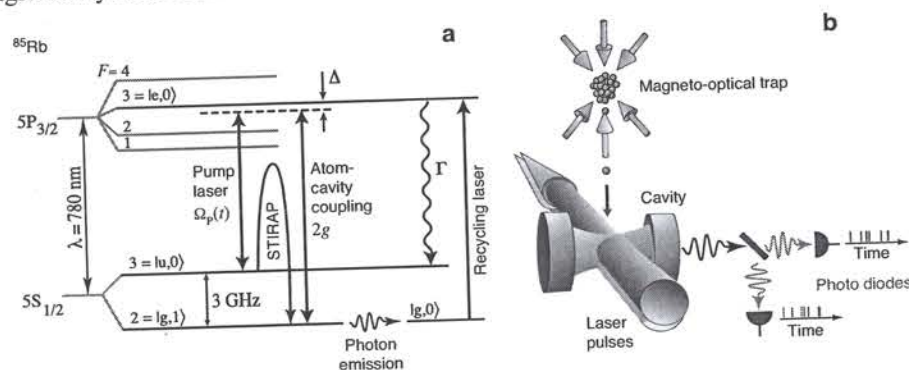
Figure 15.4: Scheme of the experiment. **(a)** Relevant energy levels and transitions in ^{85}Rb. The atomic states labeled $|u\rangle$, $|e\rangle$ and $|g\rangle$ are involved in the Raman process, and the states $|0\rangle$ and $|1\rangle$ denote the photon number in the cavity. **(b)** Setup: A cloud of atoms is released from a magneto-optical trap and falls through a cavity 20 cm below in about 8 ms with a velocity of 2 m/s. The interaction time of a single atom with the TEM$_{00}$ mode of the cavity (waist $w_0 = 35\,\mu m$) amounts to about 17.5 μs. The pump and recycling lasers are collinear and overlap with the cavity mode. Photons emitted from the cavity are detected by a pair of photodiodes with a quantum efficiency of 50%.

Figure 15.4(a) shows the basic scheme of the process. A ^{85}Rb-atom is prepared in state $|u\rangle$ which is the $F = 3$ hyperfine state of the $5S_{1/2}$ electronic ground state. The atom is located in a high-finesse optical cavity which is near resonant with the transition between the $F = 2$ hyperfine state of the electronic ground state and the electronically excited $5P_{3/2}(F = 3)$ state, $|g\rangle$ and $|e\rangle$, respectively. Here, the average atom-cavity coupling constant, g, takes into account that neither the position of the atom in the cavity nor the magnetic quantum number of the atom is well defined in the experiment. We assume g to be constant while pump-laser pulses close to resonance with the $|u\rangle \leftrightarrow |e\rangle$ transition and with Rabi frequency $\Omega_P(t)$ are applied. As described in the preceding section, each pulse generates a single photon which leaves the cavity through that mirror which is designed as an output coupler. The pump pulse rises slowly so that the emission ends before $\Omega_P > 2g$ is reached. The dynamics of the simultaneous excitation and emission process determines the duration and, hence, the

linewidth of the photon. When the photon is emitted, the final state of the coupled system, $|g, 0\rangle$, is reached. This state is not coupled to the one-photon manifold and the atom cannot be reexcited. This limits the number of photons per pump pulse and atom to one.

To emit a sequence of photons from one-and-the-same atom, the system must be transferred back to $|u, 0\rangle$ once an emission has taken place. To do so, we apply recycling laser pulses that hit the atom between consecutive pump pulses. The recycling pulses are resonant with the $|g\rangle \leftrightarrow |e\rangle$ transition and pump the atom to state $|e\rangle$. From there, it decays spontaneously to the initial state, $|u\rangle$. If an atom that resides in the cavity is exposed to a sequence of laser pulses, which alternate between triggering single-photon emissions and re-establishing the initial condition by optical pumping, a sequence of single-photon pulses is produced.

Figure 15.4(b) shows the apparatus. Atoms are released from a magneto-optical trap and pass through the TEM$_{00}$ mode of the optical cavity. The flux of atoms[1] is freely adjusted between 0 and 1000 atoms/ms. In the cavity, they are exposed to the sequence of laser pulses. The cavity is 1 mm long and has a finesse of 60 000. One mirror has a larger transmission coefficient than the other so that photons leave the cavity through this output coupler with a probability of 90%. For each experimental cycle, all photon arrival times are recorded using two avalanche photodiodes which are placed at the output ports of a beam splitter.

15.3.2 Deterministic single-photon sequences

Figure 15.5(a) displays an example of the photon stream recorded while single atoms fall through the cavity one after the other. Obviously, the photon sequence is different for each atom. In particular, not every pump pulse leads to a detected photon, since the efficiencies of photon generation and photon detection are limited.

In the experiment, the applied Rabi frequencies of the pump and recycling pulses have the shape of a saw-tooth and increase linearly, as displayed in Fig. 15.5(b). This leads to a constant rate of change of the dark state, $|\phi_1^0\rangle$, during the initial stage of the pump pulses and therefore optimal adiabaticity with minimal losses to the other eigenstates. The linear slope of the recycling pulses suppresses higher Fourier components and therefore reduces photon emission into the detuned cavity. Note that the recycling process is finished before the end of the pulse is reached, so that the final sudden drop in Rabi frequency has no effect.

Also shown in Fig. 15.5(c) are two measured arrival-time distributions of the photons. It is obvious that the pump-pulse duration of 2 μs is slightly too short, as the emitted photon pulse is not completely finished. The measured data agree well with the simulation (see Fig. 15.3(b)) if only photons from strongly coupled atoms are considered (solid line). For these we assume that several photons are detected within the atom-cavity interaction time. If solitary photons which we attribute to weakly coupled atoms are included in the analysis, the arrival-time distribution is given by the dotted line. Note that the envelope of the photon pulses is well explained by the expected shape of the single-photon wavepackets, and therefore cannot be attributed to an uncertainty in emission time which is not present for a unitary process. We emphasize that the pump-pulse duration was adjusted to maximize the number of photons per atom. Longer pump pulses would not truncate the photon pulses and, hence, would slightly

---

[1]The flux is determined by a statistical analysis of the emitted light, with continuous pump- and recycling lasers exciting the atoms. As the cavity acts as an atom detector, atoms not interacting with the cavity mode are ignored, so that its spatial mode structure is automatically taken into account.
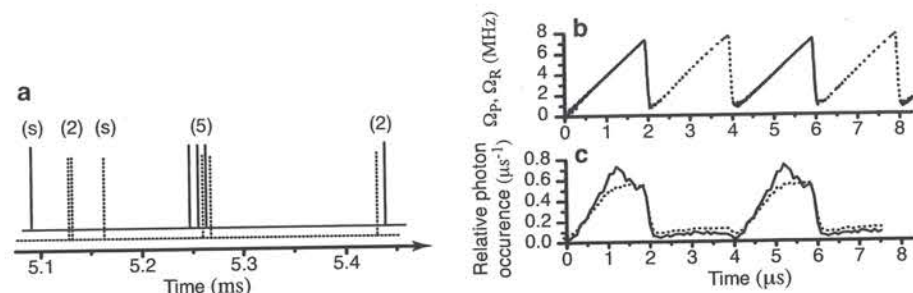
Figure 15.5: Photon emission. **(a)** Clip of the photon streams arriving at the photodiodes. Several sequences of two (2) and five (5) photon emissions are observed, with durations comparable to the atom-cavity interaction time. The solitary events (s) are either dark counts, or, more likely, photons coming from atoms that are only weakly coupled to the cavity. **(b)** Laser pulse shape: The atoms are periodically illuminated with $2\,\mu$s-long pulses from the pump (solid line) and the recycling laser (dotted line). **(c)** Arrival-time distribution of all photons emitted from the cavity (dotted line). The solid line shows the arrival-time distribution of photons emitted from strongly coupled atoms (see text), with $(g,\ \Omega^0_{P,R},\ \Delta,\ \Gamma,\ \kappa) = 2\pi \times (2.5,\ 8.0,\ -20.0,\ 6.0,\ 1.25)$ MHz, where $\Omega^0_{P,R}$ are the peak Rabi frequencies of the pump- and recycling pulses, and Γ and κ are the atom and cavity-field decay rates, respectively.

increase the emission probability per pulse, but due to the limited atom-cavity interaction time the total number of photons per atom would be reduced.

The second-order intensity correlation of the photon stream is shown in Fig. 15.6. Displayed is the cross-correlation of the photon streams registered by the two photodiodes. It is defined as $g^{(2)}(\Delta t) = \langle P_{D1}(t)P_{D2}(t - \Delta t)\rangle / (\langle P_{D1}(t)\rangle \langle P_{D2}(t)\rangle)$, where $P_{D1}(t)$ and $P_{D2}(t)$ are the probabilities to detect a photon at time t with photodiode $D1$ and $D2$, respectively. Note that all photon-arrival times are recorded to calculate the full correlation function, without the otherwise usual restriction of a simple start/stop measurement which would consider only neighbouring events.

All measured correlation functions oscillate with the same periodicity as the sequence of pump pulses, which indicates that photons are only emitted during the pump pulses, and no emissions occur when recycling pulses are applied. The nearly Gaussian envelope of the comb-like function is obviously a consequence of the limited atom-cavity interaction time. The most remarkable feature, however, is the (nearly) missing correlation peak at $\Delta t = 0$. To discuss this, note that for an atomic flux of 10 atoms/ms the probability to meet an atom in the cavity is 15 %, while the probability to have more than one atom is 1.4 %, which is not negligible. It is therefore clear that additional atoms also coupled to the cavity give rise to excess photons. In this case, the central correlation peak does not vanish completely (Fig. 15.6a). For a smaller atomic flux of 3.4 atoms/ms, the probability to find a single atom inside the cavity is 5.7 %, while the probability of having more than one atom is only 0.18 %. This is negligible, and indeed, the correlation peak at $\Delta t = 0$ vanishes (Fig. 15.6b). Even in case of a high atom flux, a straightforward approach allows one to isolate the single-atom contribution to the
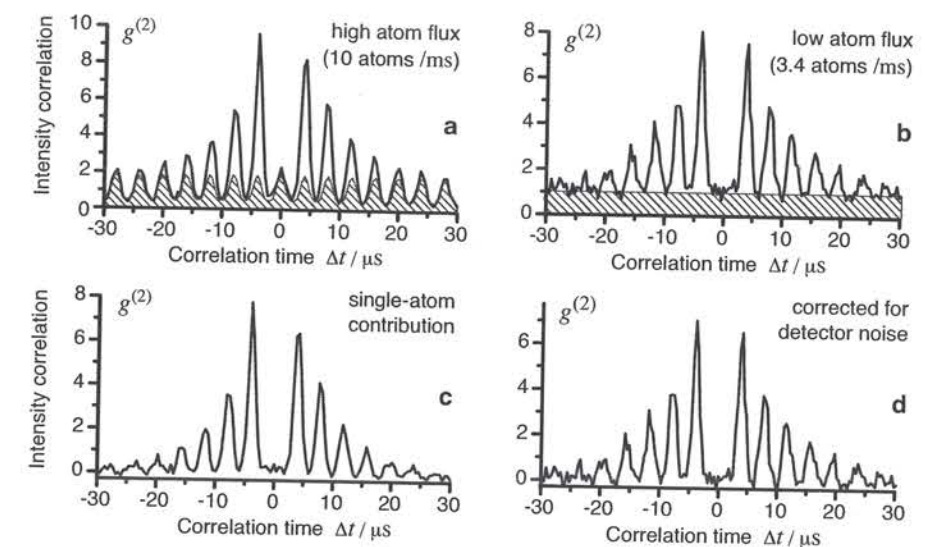
Figure 15.6: Second-order intensity correlation of the emitted photon stream. **(a)** High atom flux, averaged over 4997 experimental cycles (loading and releasing of the atom cloud) with a total number of 151089 photon counts. The hatched area represents correlations mainly caused by excess photons emitted from different atoms. For correlation times larger than the atom-cavity interaction time, only this different-atoms contribution persists. **(b)** Low atom flux, averaged over 15000 experimental cycles with a total number of 184868 photon counts. The probability to have more than one atom inside the cavity can be neglected here. The hatched area represents mainly correlations between photons and detector-noise counts. **(c,d)** Single-atom contribution to the correlation function, obtained after subtraction of the different-atom contribution from (a) or the detector-noise contribution from (b), respectively.

signal. Photons coming from different atoms give rise to a periodic contribution to the correlation function, which extends well beyond the atom-cavity interaction time and continues to oscillate with constant amplitude. In the regime $|\Delta t| \rightarrow \infty$, a periodic function is fitted to the correlation function and then continued into the relevant time regime around $\Delta t \approx 0$. This fit function, which is shown as a hatched area in Fig. 15.6a, is then subtracted from the measured correlation function. It follows that only the correlations between photons emitted from one-and-the-same atom remain (Fig. 15.6c). In fact, the central correlation peak disappears. Note also that in case of the smaller atom flux (Fig. 15.6b), the minimum of $g^{(2)}(\Delta t)$ does not reach zero, but equals one, a value solely caused by correlations between photons and detector noise counts. Subtraction of this noise contribution, shown as a hatched area in Fig. 15.6b, from the correlation function leads again to the single-atom contribution to $g^{(2)}(\Delta t)$ (Fig. 15.6d). The two data sets displayed in Fig. 15.6(c and d) demonstrate the nonclassical character of the emitted light. Strong antibunching together with a vanishing correlation around $\Delta t = 0$ is observed. This proves that the number of photons per pump pulse and atom is limited to one,

and no second emission occurs before the atom is recycled to its initial state.

We emphasize that the detection of a first photon signals the presence of an atom in the cavity and fixes the atom number to one. The photons emitted from this atom during subsequent pump pulses dominate the photon statistics and give rise to antibunching. Such an antibunching would not be observed for faint laser pulses, since a random photon statistics applies to each pulse.

The areas of the different peaks of the correlation function in Fig. 15.6 reflect the probability for the emission of further photons from one-and-the-same atom. They are determined from a lengthy but straightforward calculation, which relates the number of correlations per pulse with the total number of photons. Using the data displayed in Fig. 15.6(c and d), the result for the conditional emission of another photon during the (next, 3rd, 4th, 5th, 6th, 7th) pump pulse is (8.8, 5.1, 2.8, 1.4, 0.8, 0.5) %. Note that the probabilities for subsequent emissions decrease, since the photon emission probability, P_{emit}, depends on the location of the moving atom. It is highest for an atom in an antinode, and decreases if the atom moves away from this point. It is not possible to control the atom's location in the present experiment, but it is possible to calculate $P_{emit}(z)$ from the experimental data. Here, z is the atom's vertical position relative to the cavity axis, and $P_{emit}(z)$ is averaged over all possible atomic trajectories in the horizontal xy-plane. Assuming a Gaussian z-dependence, the deconvolution of $g^{(2)}(\Delta t)$ gives $P_{emit}(z) = 0.17 \exp\left[-(z/15.7\,\mu m)^2\right]$. For $z = 0$, the average photon-emission probability of 17% is smaller than the calculated value of 67% for an atom in an antinode of the cavity. It follows that a system combining a cavity and a single atom at rest in a dipole trap [SRPG01, KAS$^+$01], or a single ion at rest in a rf-trap [GKH$^+$01, MKB$^+$], should allow one to generate a continuous bit-stream of single photons with a large and time-independent efficiency [LK97, KHBR99]. The photon repetition rate is limited by the atom-cavity coupling constant, g, which one could push into the GHz regime by using smaller cavities of wavelength-limited dimensions in, e.g., a photonic bandgap material.

15.4   Summary and Outlook

Vacuum-stimulated Raman scattering driven by an adiabatic passage in a strongly coupled atom-cavity system can be used to generate single photons on demand. It is possible to generate a sequence of several photons on demand from one-and-the-same atom while it interacts with the cavity. These photons are generated in a well-defined radiation mode. They should have the same frequency, defined by the Raman-resonance condition, and a Fourier-transform limited linewidth. It follows that one can expect the photons to be indistinguishable and, therefore, ideal for all-optical quantum computation schemes [KLM01]. Finally, we state that the photon generation process depends on the initial state of the atom interacting with the cavity. If the atom is prepared in a superposition of states $|g, 0\rangle$ and $|u, 0\rangle$ prior to the interaction, this state will be mapped onto the emitted photon. The photon-generation process is unitary, so that it can be reversed in time and a second atom, placed in another cavity, could act as a photon receiver. This should allow one to transfer quantum states between different atoms, which is the key to quantum communication in a distributed network of optical cavities [CZKM97].

This work was partially supported by the focused research program "Quantum Information

Bibliography

[BBPG00]   R. Brouri, A. Beveratos, J.-P. Poizat, and P. Grangier. Photon Antibunching in the Fluorescence of Individual Color Centers in Diamond. *Opt. Lett.*, 25:1294–1296, 2000.

[BLTO99]   C. Brunel, B. Lounis, P. Tamarat, and M. Orrit. Triggered Source of Single Photons Based on Controlled Single Molecule Fluorescence. *Phys. Rev. Lett.*, 83:2722–2725, 1999.

[BSPY00]   O. Benson, C. Santori, M. Pelton, and Y. Yamamoto. Regulated and entangled photons from a single quantum dot. *Phys. Rev. Lett.*, 84:2513–2516, 2000.

[BVW01]   S. Brattke, B. T. H. Varcoe, and H. Walther. Generation of Photon Number States on Demand via Cavity Quantum Electrodynamics. *Phys. Rev. Lett.*, 86:3534–3537, 2001.

[CZKM97]   J. I. Cirac, P. Zoller, H. J. Kimble, and H. Mabuchi. Quantum State Transfer and Entanglement Distribution Among Distant Nodes in a Quantum Network. *Phys. Rev. Lett.*, 78:3221–3224, 1997.

[DiV00]   D. P. DiVincenzo. The physical implementation of quantum computation. *Fortschr. Phys.*, 48:771, 2000.

[GKH$^+$01]   G. R. Guthörlein, M. Keller, K. Hayasaka, W. Lange, and H. Walther. A single ion as a nanoscopic probe of an optical field. *Nature*, 414:49–51, 2001.

[Har93]   S. E. Harris. Electromagnetically Induced Transparency with Matched Pulses. *Phys. Rev. Lett.*, 70:552–555, 1993.

[Har97]   S. E. Harris. Electromagnetically Induced Transparency. *Phys. Today*, 50(7):36, 1997.

[HHDB99]   L. V. Hau, S. E. Harris, Z. Dutton, and C. H. Behroozi. Light speed reduction to 17 metres per second in an ultracold atomic gas. *Nature*, 397:594–598, 1999.

[HLKR00]   M. Hennrich, T. Legero, A. Kuhn, and G. Rempe. Vacuum-Stimulated Raman Scattering Based on Adiabatic Passage in a High-Finesse Optical Cavity. *Phys. Rev. Lett.*, 85:4872–4875, 2000.

[JC63]   E. T. Jaynes and F. W. Cummings. Comparison of Quantum and Semiclassical Radiation Theories with Application to the Beam Maser. *Proc. IEEE*, 51:89–109, 1963.

[KAS$^+$01]   S. Kuhr, W. Alt, D. Schrader, M. Müller, V. Gomer, and D. Meschede. Deterministic Delivery of a Single Atom. *Science*, 293:278–280, 2001.

[KBKY99]   J. Kim, O. Benson, H. Kan, and Y. Yamamoto. A Single Photon Turnstile Device. *Nature*, 397:500–503, 1999.

[KHBR99]   A. Kuhn, M. Hennrich, T. Bondo, and G. Rempe. Controlled Generation of Single Photons from a Strongly Coupled Atom-Cavity System. *Appl. Phys. B*, 69:373–377, 1999.

[KHR02]   A. Kuhn, M. Hennrich, and G. Rempe. Deterministc single-photon source for distributed quantum networking. *Phys. Rev. Lett.*, 89:067901, 2002.

[KLM01]   E. Knill, R. Laflamme, and G. J. Milburn. A scheme for efficient quantum computing with linear optics. *Nature*, 409:46–52, 2001.

[KMZW00]   C. Kurtsiefer, S. Mayer, P. Zarda, and H. Weinfurter. Stable Solid-State Source of Single Photons. *Phys. Rev. Lett.*, 85:290–293, 2000.

[KPHS96]   A. Kuhn, H. Perrin, W. Hänsel, and C. Salomon. Three Dimensional Raman Cooling using Velocity Selective Rapid Adiabatic Passage. In K. Burnett, editor, *OSA TOPS on Ultracold Atoms and BEC*, volume 7, pages 58–65. OSA, 1996.

[KR02]   A. Kuhn and G. Rempe. Optical cavity qed: Fundamentals and application as a single-photon light source. In *Varenna Lecture Notes 2001*, in print. Int. School of Physics Enrico Fermi, IOS, 2002.

[LK97]   C. K. Law and H. J. Kimble. Deterministic Generation of a Bit-Stream of Single-Photon Pulses. *J. Mod. Opt.*, 44:2067–2074, 1997.

[LM00]   B. Lounis and W. E. Moerner. Single Photons on Demand from a Single Molecule at Room Temperature. *Nature*, 407:491–493, 2000.

[Loy74]   M. M. T. Loy. Self-induced rapid adiabatic passage. *Phys. Rev. Lett.*, 32:814–817, 1974.

[Loy78]   M. M. T. Loy. Two-photon adiabatic inversion. *Phys. Rev. Lett.*, 41:473–475, 1978.

[Mes58]   A. Messiah. *Quantum Mechanics*, volume 2, chapter 17. J. Wiley & Sons, NY, 1958.

[MHN+97]   X. Maître, E. Hagley, G. Nogues, C. Wunderlich, P. Goy, M. Brune, J.-M. Raimond, and S. Haroche. Quantum Memory with a Single Photon in a Cavity. *Phys. Rev. Lett.*, 79:769–772, 1997.

[MIM+00]   P. Michler, A. Imamoglu, M. D. Mason, P. J. Carson, G. F. Strouse, and S. K. Buratto. Quantum Correlation Among Photons from a Single Quantum Dot at Room Temperature. *Nature*, 406:968–970, 2000.

[MKB+]   A. B. Mundt, A. Kreuter, C. Becher, D. Leibfried, J. Eschner, F. Schmidt-Kaler, and R. Blatt. Coupling a single atomic quantum bit to a high finesse optical cavity. e-print quant-ph/0202112. *Phys. Rev. Lett.*(to be published)

[MKB+00]   P. Michler, A. Kiraz, C. Becher, W. V. Schoenfeld, P. M. Petroff, L. Zhang, E. Hu, and A. Imamoglu. A Quantum Dot Single Photon Turnstile Device. *Science*, 290:2282–2285, 2000.

[MRG+01]   E. Moreau, I. Robert, J. M. Gérard, I. Abram, L. Maniv, and V. Thierry-Mieg. Single-mode solid-state single photon source based on isolated quantum dots in pillar microcavities. *Appl. Phys. Lett.*, 79:2865–2867, 2001.

[PFM+01]   D. F. Phillips, A. Fleischhauer, A. Mair, R. L. Walsworth, and M. D. Lukin. Storage of Light in Atomic Vapor. *Phys. Rev. Lett.*, 86:783–786, 2001.

[PKBS98]   H. Perrin, A. Kuhn, I. Bouchoule, and C. Salomon. Sideband cooling of neutral atoms in a far-detuned optical lattice. *Europhys. Lett.*, 42:395–400, 1998.

[PMZK93]   A. S. Parkins, P. Marte, P. Zoller, and H. J. Kimble. Synthesis of Arbitrary Quantum States Via Adiabatic Transfer of Zeeman Coherence. *Phys. Rev. Lett.*, 71:3095, 1993.

[SK93]   B. W. Shore and P. L. Knight. The Jaynes-Cummings Model. *J. Mod. Opt.*, 40:1195, 1993.

[SPS+01]   C. Santori, M. Pelton, G. Solomon, Y. Dale, and Y. Yamamoto. Triggered Single Photons from a Quantum Dot. *Phys. Rev. Lett.*, 86:1502–1505, 2001.

[SRPG01]   N. Schlosser, G. Reymond, I. Protsenko, and P. Grangier. Sub-poissonian loading of single atoms in a microscopic dipole trap. *Nature*, 411:1024–1027, 2001.

[VFSB01]   N. V. Vitanov, M. Fleischhauer, B. W. Shore, and K. Bergmann. Coherent manipulation of atoms and molecules by sequential laser pulses. *Adv. At. Mol. Opt. Phys.*, 46:55–190, 2001.

[YKS+02]   Z. Yuan, B. E. Kardynal, R. M. Stevenson, A. J. Shields, C. J. Lobo, K. Cooper, N. S. Beattie, D. A. Ritchie, and M. Pepper. Electrically Driven Single-Photon Source. *Science*, 295:102–105, 2002.

[YSHB99]   L. P. Yatsenko, B. W. Shore, T. Halfmann, and K. Bergmann. Source of metastable H(2s) atoms using the Stark chirped rapid-adiabatic-passage technique. *Phys. Rev. A*, 60:R4237–R4240, 1999.

Taylor & Francis
Taylor & Francis Group

MARKUS HENNRICH, THOMAS LEGERO, AXEL KUHN
and GERHARD REMPE

Max-Planck-Institut für Quantenoptik, Hans-Kopfermann-Str.1,
85748 Garching, Germany; e-mail: gerhard.rempe@mpq.mpg.de

Vacuum-stimulated Raman scattering in strongly coupled atom–cavity systems allows one to generate free-running single photon pulses on demand. Most properties of the emitted photons are well defined, provided spontaneous emission processes do not contribute. Therefore, electronic excitation of the atom must not occur, which is assured for a system adiabatically following a dark state during the photon-generation process. We experimentally investigate the conditions that must be met for adiabatic following in a time-of-flight driven system, with atoms passing through a cavity and a pump beam oriented transverse to the cavity axis. From our results, we infer the optimal intensity and relative pump-beam position with respect to the cavity axis.

During the last years, many different types of single-photon sources have been proposed and successfully demonstrated [1–15]. These activities were motivated by current quantum-cryptography schemes [16], which rely on the transmission of single photons between two parties to be secure, and by recent proposals [17] on all-optical quantum information processing [18] and distributed quantum networking [19]. For quantum networking, indistinguishable photons must be generated by a unitary, reversible process in order to transport single quantum bits from node to node. This last requirement is not met by most of the single-photon sources available so far. Only photon-generation schemes that are based on a deterministic and unitary energy exchange between a single emitter, e.g. an atom, and a single mode of the quantized radiation field [19–23] might, in principle, meet the above requirements. Such a deterministic energy exchange has been successfully demonstrated in the microwave regime [24, 25], but these experiments do not provide free-running photons.

In this paper, we concentrate on a strongly coupled atom–cavity system in the optical domain, where the photons are transmitted through one of the cavity mirrors. The photons are generated by a vacuum-stimulated Raman transition [12–15] which is adiabatically driven by a pump laser beam, interacting with the atoms while they are coupled to the cavity mode. The excitation scheme implements stimulated Raman scattering by adiabatic passage [26] (STIRAP), with the vacuum field of the cavity instead of a stimulating laser. Figure 1 illustrates this scheme: a cloud of rubidium atoms in state $|u\rangle$, i.e. the $5S_{1/2}(F = 3)$ hyperfine state of the electronic ground state, is released from a magneto-optical trap (MOT). The atoms fall through a 1 mm long cavity of finesse $F = 60\,000$ which is placed 20 cm
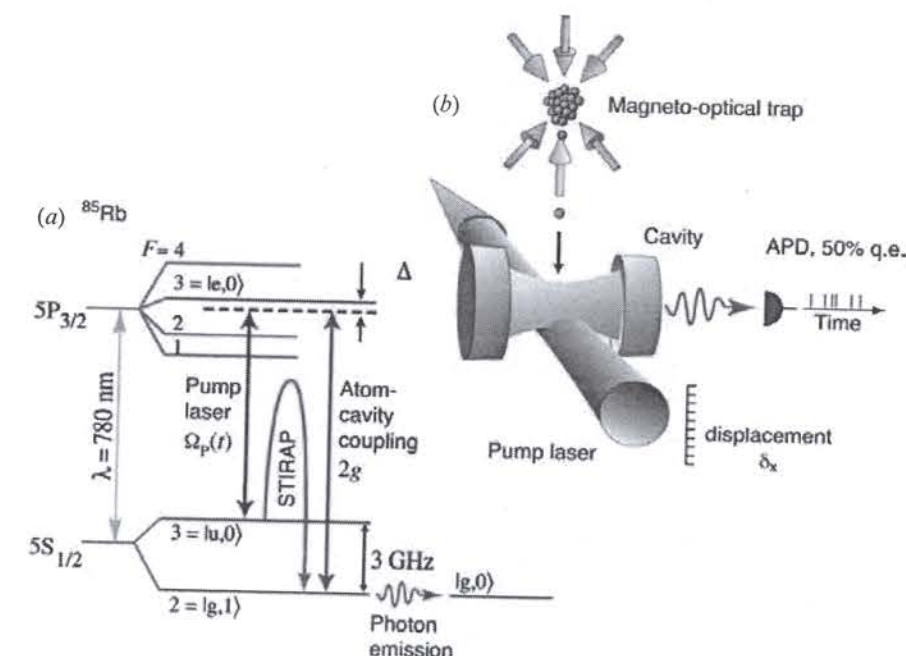
Figure 1. Experimental scheme. (a) Energy levels and transitions in ^{85}Rb. The states labelled $|u\rangle$, $|e\rangle$ and $|g\rangle$ are involved in the process, and states $|0\rangle$ and $|1\rangle$ denote the photon number in the cavity. (b) Set-up: a cloud of atoms is released from a magneto-optical trap and falls through a cavity 20 cm below in about 8 ms with a velocity of 2 m s^{-1}. The interaction time of a single atom with the TEM$_{00}$ mode of the cavity (waist $w_C = 35\,\mu$m) amounts to about 17.5 μs. The pump laser partially overlaps with the cavity mode. Photons emitted from the cavity are detected by an avalanche photodiode with a quantum efficiency of 50%.

below the MOT, so that the atoms passing through the cavity have acquired a transverse (vertical) velocity of $v = 2$ m s^{-1}. One TEM$_{00}$ mode of the cavity with waist $w_C = 35\,\mu$m stimulates the Raman process, since it is resonant with the $|e\rangle \leftrightarrow |g\rangle$ transition of the atom, with $|e\rangle$ being an electronically excited state and $|g\rangle$ being the other hyperfine ground state, $5S_{1/2}(F = 2)$. The transition is pumped by a continuous laser beam of waist $w_P \approx w_C$, resonant with the $|u\rangle \leftrightarrow |e\rangle$ transition, which perpendicularly crosses the cavity axis and the trajectory of the falling atoms. With δ_X being the distance between the crossing points of the cavity and the beam axis, respectively, with the atomic trajectory, the Rabi frequency of the pump beam driving the $|u\rangle \leftrightarrow |e\rangle$ transition, Ω_P, and the vacuum-Rabi frequency induced by the cavity coupling the $|e\rangle \leftrightarrow |g\rangle$ transition, Ω_C, become time dependent and delayed due to the motion of the atoms, according to

$$\Omega_P(t) = \Omega_0 \exp\left[-\left(\frac{vt + \delta_X}{w_P}\right)^2\right],$$

$$\Omega_C(t) = 2g(t) = 2g_0 \exp\left[-\left(\frac{vt}{w_C}\right)^2\right], \tag{1}$$

where Ω_0 is the peak Rabi frequency of the pump beam and g_0 is the peak atom–cavity coupling constant. In case of positive δ_X, the atoms are first exposed to the pump beam, while the interaction with the cavity mode is delayed by δ_X/v. The opposite situation is met in the case of negative δ_X. If we consider a Raman-resonant excitation with the detunings, Δ, of the cavity and the pump beam from their respective transitions being equal, the interaction Hamiltonian of the coupled laser–atom–cavity system reads (in a rotating frame)

$$H_{\text{int}} = \frac{\hbar}{2}[2\Delta\sigma_{ee} - 2g(\sigma_{eg}a + a^\dagger\sigma_{ge}) - \Omega_P(\sigma_{eu} + \sigma_{ue})]. \tag{2}$$

Without coupling and for zero detuning, the three product states forming the one-photon manifold $\{|u,0\rangle, |e,0\rangle, |g,1\rangle\}$ are degenerate ($|0\rangle$ and $|1\rangle$ denote the photon number states of the cavity). In the case of a coupled system, the degeneracy is lifted and the eigenfrequencies read

$$\omega^0 = 0 \quad \text{and} \quad \omega^\pm = \tfrac{1}{2}(\Delta \pm (4g^2 + \Omega_P^2 + \Delta^2)^{1/2}). \tag{3}$$

The corresponding eigenstates are

$$|\phi^0\rangle = \cos\Theta|u,0\rangle - \sin\Theta|g,1\rangle,$$
$$|\phi^+\rangle = \cos\Phi\sin\Theta|u,0\rangle - \sin\Phi|e,0\rangle + \cos\Phi\cos\Theta|g,1\rangle,$$
$$|\phi^-\rangle = \sin\Phi\sin\Theta|u,0\rangle + \cos\Phi|e,0\rangle + \sin\Phi\cos\Theta|g,1\rangle, \tag{4}$$

where the mixing angles Θ and Φ are given by

$$\tan\Theta = \frac{\Omega_P}{2g} \quad \text{and} \quad \tan\Phi = \frac{(4g^2 + \Omega_P^2)^{1/2}}{(4g^2 + \Omega_P^2 + \Delta^2)^{1/2} - \Delta}. \tag{5}$$

Recently, we have proposed [12] and demonstrated [13–15] that the dark state $|\phi^0\rangle$ can be used to generate photons in the cavity in a deterministic way. To do so, the interaction of a single atom with the cavity must be strong when the interaction starts, so that

$$|\langle u,0|\phi^0\rangle| = 1 \quad \text{for} \quad 2g \gg \Omega_P. \tag{6}$$

Provided the system's state vector, $|\Psi\rangle$, adiabatically follows the dark state, $|\phi^0\rangle$, throughout the interaction, the contribution of $|g,1\rangle$ increases with rising pump Rabi frequency Ω_P, so that the transient photon-emission rate from the cavity reads

$$R_{\text{emit}} = 2\kappa|\langle g,1|\phi^0\rangle|^2\,\text{tr}(\rho) = 2\kappa\frac{\Omega_P^2}{4g^2 + \Omega_P^2}\,\text{tr}(\rho), \tag{7}$$

where κ is the field decay rate of the cavity and $\rho = |\Psi\rangle\langle\Psi|$ the density matrix of the considered three-level system, which is not closed. Hence, $\text{tr}(\rho)$ is not one, but denotes the population remaining in the coupled system at any given moment. With the other eigenstates, $|\phi^\pm\rangle$, not being populated, transverse spontaneous emission losses from the excited state $|e\rangle$ do not occur, and the overall photon emission probability is

$$P_{\text{emit}} = \int_0^\tau dt\, R_{\text{emit}} \to 1 \quad \text{for} \quad 2\kappa\tau\left\langle\frac{\Omega_P^2}{4g^2 + \Omega_P^2}\right\rangle \gg 1, \tag{8}$$
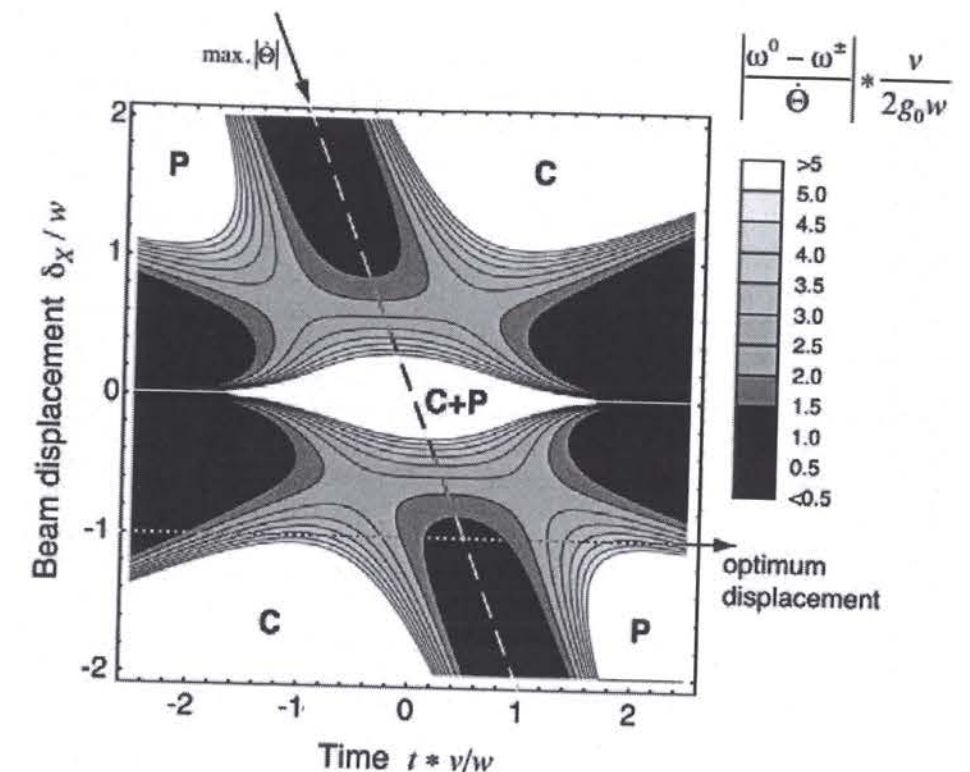
Figure 2. Regimes of high and low adiabaticity: the grey map shows $|(\omega^0 - \omega^\pm)/\dot{\Theta}|$ as a function of time and beam displacement for $\Delta = 0$, $w_C = w_P \equiv w$ and $\Omega_0 = 2g_0$. In the areas marked with C and/or P, the atom is interacting with the cavity and/or the pump laser beam, respectively. In the dark regions, adiabaticity is not assured. The dashed line indicates the position of the maxima of $|\dot{\Theta}|$, where the probability for non-adiabatic losses is highest. All atom trajectories, regardless of δ_X, cross this line. The dotted horizontal line indicates the optimal atom trajectory which leads to the maximal photon emission probability in our experiment.

where $\langle\ldots\rangle$ denotes the average of its argument in the relevant time interval, $[0\ldots\tau]$. Obviously, the process can reach a photon-generation efficiency close to unity, provided adiabatic following is assured. Therefore, the set of parameters [27] $\{\Omega_0, g_0, w_C, w_P, \Delta, \delta_X\}$ must be chosen in such a way that the adiabaticity criterion [27]

$$|\omega^0 - \omega^\pm| \gg \left|\left\langle\phi^\pm\left|\frac{d}{dt}\right|\phi^0\right\rangle\right| = |\dot{\Theta}| \tag{9}$$

is met throughout the whole process. This requires a careful adjustment of the displacement, δ_X, between pump laser beam and cavity axis.

Figure 2 shows $|(\omega^0 - \omega^\pm)/\dot{\Theta}|$ as a function of t and δ_X. The smaller this ratio, the higher the probability to have a non-adiabatic evolution. Obviously, for any choice of δ_X, such situations are encountered. The evolution is always non-adiabatic long before and long after the atom interacts with the laser beam and/or the cavity. However, since the coupling constant and the Rabi frequency are both weak in these regimes and Θ changes only slowly, the population in the

atomic bare states is not affected. A very crucial situation is met when $|\dot{\Theta}|$ reaches its maximum, i.e. when the atom crosses the dashed line in figure 2, which lies between the cavity axis and the pump beam. For $|\delta_X| > \max(w_C, w_P)$, the level splitting $|(\omega^0 - \omega^{\pm})|$ is too small to assure adiabaticity and losses to other eigenstates occur. Only in the intermediate regime, where the pump beam partially overlaps the cavity mode, i.e. for $|\delta_X/2| \leqslant \min(w_C, w_P)$, adiabaticity is assured even for large $|\dot{\Theta}|$, and the behaviour of the system is predetermined by the projection of the initial state $|u, 0\rangle$ onto the eigenstates as soon as the adiabatic regime is entered. In this case, three major scenarios must be distinguished: (a) $\delta_X > 0$. The atom first interacts with the pump beam, the initial state projects onto $|\phi^{\pm}\rangle$, and the photon is lost by transverse spontaneous emission. (b) $\delta_X \approx 0$. The dark state $|\phi^0\rangle$ is partially populated, so that the probability of a photon emission from the cavity might reach 50%. (c) $\delta_X < 0$. The atom first interacts with the cavity, the initial state $|u, 0\rangle$ projects onto the dark state $|\phi^0\rangle$, so that no losses occur except the desired photon emission from the cavity with a probability approaching 100%.

Figure 3 shows the number of photons emitted from the cavity as a function of pump beam displacement δ_X for five different pump intensities. The photons are counted during 5.24 ms while a single cloud of atoms passes through the cavity. Pump beam and cavity are Raman resonant, with a common detuning of $\Delta = 10$ MHz from the direct atomic transitions. The pump beam displacement is adjusted using a piezoelectric mirror assembly, and beam position and waist are monitored by a CCD (charge-coupled device) camera. The trace which belongs to the smallest pump intensity is used to calibrate the δ_X-origin, assuming that the
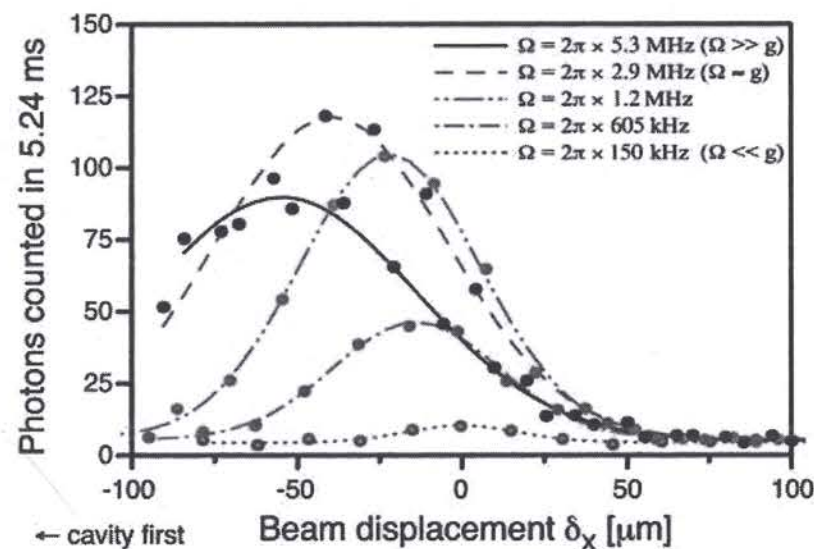
Figure 3. Number of photons emitted from the cavity in 5.24 ms as a function of the displacement δ_X of the pump beam from the cavity axis (along the atom's trajectories) for different pump intensities. A counter-intuitive interaction sequence (cavity first, pump later) is realized for negative δ_X. Note that the indicated Rabi frequencies result from the measured beam intensities and an assumed pump-beam waist of $w_P = 44 \, \mu$m, which gives the best agreement with numerical simulations (see figure 4).

small Rabi frequency gives rise to an adiabatic evolution only for $\delta_X = 0$, so that the peak photon number is found there. From this position, the peak emission shifts towards negative δ_X with increasing Rabi frequency, since the level splitting $|\omega^0 - \omega^{\pm}|$ and therefore the adiabatic regime both increase with Ω_0. This allows one to pull the pump beam and the cavity further apart without losing adiabaticity, so that the fraction of the initial state which projects onto the dark state $|\phi^0\rangle$ when the adiabatic regime is entered increases as well. The data also reveal that a significant overlap between pump beam and cavity mode is mandatory, otherwise adiabaticity is not assured when the atom reaches the point of maximum $|\dot{\Theta}|$, which is located between the cavity mode and the pump beam axis, so that the number of emitted photons decreases again for $\delta_X \longrightarrow -\infty$. In our experiment, the optimum is found for $\Omega_P \approx g_0$ and $\delta_X \approx -(w_C + w_P)/2$.

A comparison of the experimental results with a numerical simulation of the process must take into account that the atomic trajectories are not controlled. Therefore the effective atom–cavity coupling depends on the random 'point of impact', $r = (y, z)$, of every single atom with respect to the cavity's mode function, so that

$$g_0(y, z) \approx g_0^{\max} \cos(2\pi z/\lambda) \exp\left(-(y/w_C)^2\right). \quad (10)$$

The variation of w_C along z is neglected here, since the Rayleigh length of the cavity mode exceeds the cavity length. The dependence of the photon emission probability P_{emit} on g_0 is highly nonlinear, so that g_0 cannot be replaced by its mean value prior to a numerical calculation of P_{emit}. Instead, we have to average P_{emit} over all possible points of impact, according to

$$\bar{P}_{\text{emit}} = \int_0^{\lambda} dz \int_{-S_y/2}^{S_y/2} dy \, \frac{P_{\text{emit}}(g_0(y, z))}{\lambda \, S_y}. \quad (11)$$

Note that $S_y = 100 \, \mu$m is the width of a slit aperture which is installed above the cavity. This aperture constrains the atomic trajectories perpendicular to the cavity axis to the interval $[-S_y/2 \ldots + S_y/2]$. To calculate $P_{\text{emit}}(g_0(y, z))$, we numerically solve the master equation of the coupled system [12] and integrate (11). This calculation takes the cavity–field decay rate, κ, and the decay rate of the excited atomic level, γ, into account.

Figure 4 shows a simulation of the average $\bar{P}_{\text{emit}}$ as a function of δ_X for the range of pump intensities investigated in the experiment (see figure 3). For the smallest Rabi frequency the maximum photon emission probability is found at $\delta_X = 0$, which justifies our δ_X calibration. Moreover, the simulation shows the same trend which is observed in the experiment, with the peak emission probability shifting towards negative δ_X with increasing Rabi frequency. However, simulation and experiment do not agree perfectly, and also the experimentally observed photon-number reduction at high pump intensities is not reproduced. These discrepancies lead to the conclusion that either the pump beam deviates from an ideal Gaussian beam in its wings, or that weak stray light of the pump beam (e.g. from the vacuum viewports) also hits the atoms. Both effects give rise to an electronic excitation of the atoms if the pump beam is very intense, which results in an early loss of photons by spontaneous emission into transverse modes.

From the theoretical considerations, the experimental results and the numerical calculations, we draw the conclusion that vacuum-stimulated Raman transi-
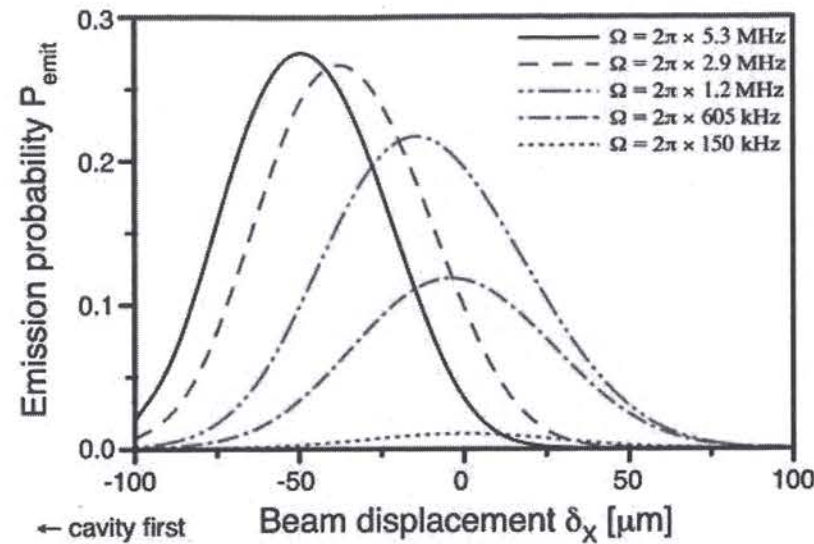
Figure 4. Simulation of the photon emission probability averaged over all possible points of impact as a function of the displacement δ_X of the pump beam from the cavity axis for different pump intensities, with $\{g_0^{max}, \Delta, \kappa, \gamma\} = 2\pi \{2.5, 10, 1.25, 6\}$ MHz, cavity waist $w_C = 35\,\mu m$ and pump waist $w_P = 44\,\mu m$.

tions are most effectively driven by an adiabatic passage which results from a counter-intuitive interaction sequence, where the atoms are first coupled to the vacuum field of an empty cavity, stimulating the transition, and then exposed to a pump laser beam. To assure adiabaticity and to avoid losses to other states, a significant overlap of cavity mode and pump beam is required. Optimum conditions are found experimentally for a pump Rabi frequency which equals the maximum atom–cavity coupling constant, g_0^{max}, and for a beam displacement which equals the average waist of the cavity and the pump beam.

[1] LAW, C. K., and EBERLY, J. H., 1996, *Phys. Rev. Lett.*, 1055.
[2] LAW, C. K., and KIMBLE, H. J., 1997, *J. mod. Optics*, 2067.
[3] KIM, J., BENSON, O., KAN, H., and YAMAMOTO, Y., 1999, *Nature*, 500.
[4] LOUNIS, B., and MOERNER, W. E., 2000, *Nature*, 491.
[5] KURTSIEFER, C., MAYER, S., ZARDA, P., and WEINFURTER, H., 2000, *Phys. Rev. Lett.*, 290.
[6] BROURI, R., BEVERATOS, A., POIZAT, J.-P., and GRANGIER, P., 2000, *Optics Lett.*,
[7] MICHLER, P., IMAMOGLU, A., MASON, M. D., CARSON, P. J., STROUSE, G. F., and BURATTO, S. K., 2000, *Nature*, 968.

[8] SANTORI, C., PELTON, M., SOLOMON, G., DALE, Y., and YAMAMOTO, Y., 2001, *Phys. Rev. Lett.*, 1502.
[9] YUAN, Z., KARDYNAL, B. E., STEVENSON, R. M., SHIELDS, A. J., LOBO, C. J., COOPER, K., BEATTIE, N. S., RITCHIE, D. A., and PEPPER, M., 2002, *Science*, 102.
[10] MICHLER, P., KIRAZ, A., BECHER, C., SCHOENFELD, W. V., PETROFF, P. M., ZHANG, L., HU, E., and IMAMOGLU, A., 2000, *Science*, 2282.
[11] MOREAU, E., ROBERT, I., GÉRARD, J. M., ABRAM, I., MANIV, L., and THIERRY-MIEG, V., 2001, *Appl. Phys. Lett.*, 2865.
[12] KUHN, A., HENNRICH, M., BONDO, T., and REMPE, G., 1999, *Appl. Phys. B*, 373.
[13] HENNRICH, M., LEGERO, T., KUHN, A., and REMPE, G., 2000, *Phys. Rev. Lett.*, 4872.
[14] KUHN, A., and REMPE, G., *Proceedings of the Varenna School on 'Experimental Quantum Information'* 2001 (in print).
[15] KUHN, A., HENNRICH, M., and REMPE, G., 2002, *Phys. Rev. Lett.*, 067901.
[16] TITTEL, W., RIBORDY, G., and GISIN, N., 1998, *Phys. World*, 41.
[17] MONROE, C., 2002, *Nature*, 238.
[18] KNILL, E., LAFLAMME, R., and MILBURN, G. J., 2001, *Nature*, 46.
[19] CIRAC, J. I., ZOLLER, P., KIMBLE, H. J., and MABUCHI, H., 1997, *Phys. Rev. Lett.*, 3221.
[20] VAN ENK, S., CIRAC, J. I., ZOLLER, P., KIMBLE, H. J., and MABUCHI, H., 1997, *J. mod. Optics*, 1727.
[21] PARKINS, A. S., MARTE, P., ZOLLER, P., and KIMBLE, H. J., 1993, *Phys. Rev. Lett.*, 3095.
[22] PARKINS, A. S., MARTE, P., ZOLLER, P., CARNAL, O., and KIMBLE, H. J., *Phys. Rev. A*, 1578.
[23] PELLIZARI, T., GARDINER, S. A., CIRAC, J. I., and ZOLLER, P., 1995, *Phys. Rev. Lett.*, 3788.
[24] RAUSCHENBEUTEL, A., NOGUES, G. OSNAGHI, S., BERTET, P., BRUNE, M., RAIMOND, J.-M., and HAROCHE, S., 1999, *Phys. Rev. Lett.*, 5166.
[25] BRATTKE, S., VARCOE, B. T. H., and WALTHER, H., 2001, *Phys. Rev. Lett.*, 3534.
[26] VITANOV, N. V., FLEISCHHAUER, M., SHORE, B. W., and BERGMANN, K., 2001, *Adv. at. molec. opt. Phys.*, 55.
[27] MESSIAH, A., 1958, *Quantum Mechanics*, Vol. 2 (New York: J. Wiley & Sons), chapter 17.

T. LEGERO
T. WILK ✉
A. KUHN ✉
G. REMPE

Time-resolved two-photon quantum interference

Max-Planck-Institut für Quantenoptik, Hans-Kopfermann-Str. 1, 85748 Garching, Germany

ABSTRACT The interference of two independent single-photon pulses impinging on a beam splitter is analysed in a generalised time-resolved manner. Different aspects of the phenomenon are elaborated using different representations of the single-photon wave packets, like the decomposition into single-frequency field modes or spatio-temporal modes matching the photonic wave packets. Both representations lead to equivalent results, and a photon-by-photon analysis reveals that the quantum-mechanical two-photon interference can be interpreted as a classical one-photon interference once a first photon is detected. A novel time-dependent quantum-beat effect is predicted if the interfering photons have different frequencies. The calculation also reveals that full two-photon fringe visibility can be achieved under almost any circumstances by applying a temporal filter to the signal.

PACS 42.50.Dv; 42.50.Ct

1   Introduction

Single-photon light pulses are a central ingredient of quantum-teleportation and quantum-communication protocols, as well as of quantum computation with linear optics [1–4]. Many of these schemes are based on the quantum interference of two indistinguishable photons that impinge simultaneously on different entrance ports of a $50:50$ beam splitter. In this case, both photons leave the beam splitter at the same output port. This quantum interference effect was first observed by Hong, Ou, and Mandel with photons from a parametric down-conversion source [5–7]. When the two photons had different frequencies, a spatial quantum-beat phenomenon was observed [8]. The two-photon quantum interference effect has also been observed with photons from independent down-conversion sources [9, 10], and the phenomenon has been used by Santori et al. [11] to demonstrate the indistinguishability of photons emitted from a quantum dot embedded in a microcavity. Theoretical descriptions that apply to the interference of independent single photons have been worked out by Zukowski et al. [12] and Bylander et al. [13].

✉ Fax: +49-89/32905-311, E-mail: axel.kuhn@mpq.mpg.de

So far, all these experiments use photons that are short compared with the time resolution of the employed photodetectors, and temporal effects are therefore neglected. However, we have recently developed a novel type of single-photon emitter that employs a strongly coupled atom–cavity system [14–16] to emit single-photon wave packets of $2\,\mu s$ duration. This duration exceeds the typical response time of solid-state photodetectors by more than three orders of magnitude and allows two-photon quantum interference effects to be studied in a time-resolved manner. This paper therefore presents a detailed analytical treatment of the two-photon interference process. It takes into account the time evolution of the amplitudes and phases of the interfering single-photon wave packets. The analysis is valid for independent photons, and therefore extends the model for frequency-entangled photon pairs of Steinberg et al. [17].

While preparing this paper, we realised that there is apparently no commonly adopted approach to deal with free-running single-photon wave packets [18]. One possibility is to express the quantum state of a single-photon wave packet as a superposition state of an infinite number of single-frequency modes, and another is to use a superposition state of spatio-temporal modes. To demonstrate that these approaches lead to the same result, we now analyse the two-photon interference effect along both routes.

2   Two-photon interference

As a starting point for the following discussion, we first review the two-photon interference phenomenon in the Fock-state picture; i.e. we consider two single photons that impinge on the entrance ports labelled '1' and '2' of the beam splitter shown in Fig. 1. This initial situation corresponds to the quantum state $|1_1 1_2\rangle = a_1^\dagger a_2^\dagger |0\rangle$, which is obtained by applying the appropriate photon-creation operators $a_i^\dagger$ on the vacuum state $|0\rangle$. The effect of the $50:50$ beam splitter on the field is usually described by the unitary transformations

$$a_1^\dagger = (a_3^\dagger + a_4^\dagger)/\sqrt{2} \quad \text{and} \quad a_3^\dagger = (a_1^\dagger + a_2^\dagger)/\sqrt{2}\,.$$
$$a_2^\dagger = (a_3^\dagger - a_4^\dagger)/\sqrt{2} \qquad\qquad a_4^\dagger = (a_1^\dagger - a_2^\dagger)/\sqrt{2} \tag{1}$$

If we use these relations to express the initial state in terms of photons created in the two output ports labelled '3' and '4', we immediately see that this leads to an entangled state with

FIGURE 1 Two single-photon wave packets impinge with a relative delay of $\delta\tau$ on ports '1' and '2' of a beam splitter. The pulse duration is longer than the time resolution of the detectors monitoring ports '3' and '4' of the beam splitter. Therefore, the time difference, τ, between two photon detections must be taken into account in the analysis of the photon statistics

either both photons in one or the other output port:

$$|1_1 1_2\rangle = a_1^\dagger a_2^\dagger |0\rangle = \frac{1}{2}(a_3^\dagger + a_4^\dagger)(a_3^\dagger - a_4^\dagger)|0\rangle$$
$$= \frac{1}{2}([a_3^\dagger]^2 - [a_4^\dagger]^2)|0\rangle$$
$$= (|2_3 0_4\rangle - |0_3 2_4\rangle)/\sqrt{2}\,. \tag{2}$$

This simple picture qualitatively explains the observed interference phenomena, but since the photonic modes that belong to the creation operators are neither specified in space, frequency, nor time (albeit they are assumed to be identical for both photons), quantitative results for photon wave packets cannot be obtained from this approach.

2.1   Space–time domain

To obtain more insight, we now consider a description of the arriving single-photon wave packets in the space–time domain. The free-running photons are not subject to boundary conditions that restrict the photon creation and annihilation operators, $a_k^\dagger$ and a_k, to specific frequency modes. Therefore we are free to define these operators in such a way that they create or annihilate photons in arbitrarily chosen modes (labelled by the index k) in space and time, which we define by the one-dimensional spatio-temporal mode functions

$$\zeta_k(z, t) = \varepsilon_k(t - z/c)\, e^{-i\phi_k(t - z/c)}\,. \tag{3}$$

Beside an arbitrary phase evolution, $\phi_k(t)$, the mode functions incorporate amplitude envelopes, $\varepsilon_k(t)$, which are assumed to be normalised so that $\int dt |\varepsilon_k(t)|^2 = 1$. By placing the beam splitter at $z = 0$, we can omit the spatial coordinate, z, in the following. Now we can assume that the whole Hilbert space is spanned by an orthonormal set of spatio-temporal modes, $\zeta_k(t)$, so that the electric field operators read

$$\hat{E}^+(t) = \sum_k \zeta_k(t) a_k \quad \text{and} \quad \hat{E}^-(t) = \sum_k \zeta_k^*(t) a_k^\dagger\,. \tag{4}$$

Provided that a photon is present in mode i, the probability of measuring it at a given time t is then

$$P_i(t) = \langle 1_i| \hat{E}^-(t) \hat{E}^+(t) |1_i\rangle = \zeta_i^*(t)\zeta_i(t) = |\varepsilon_i(t)|^2\,, \tag{5}$$

which is solely defined by the amplitude envelope of the photon, $\varepsilon_i(t)$. To analyse the effect of the beam splitter, we now attribute field operators, $\hat{E}^\pm_{1,2,3,4}$, to each of the four input/output ports. For the two input ports we only consider the occupied modes that are described by the mode functions $\zeta_1(t)$ and $\zeta_2(t)$, respectively. This restricts the Hilbert subspaces of the input ports to single modes. Therefore the field operators that belong to the two input ports can be written as $\hat{E}^+_1 = \zeta_1(t)a_1$ and $\hat{E}^+_2 = \zeta_2(t)a_2$, respectively. Using these operators, the effect of the beam splitter is now described as a transformation between input and output modes:

$$\hat{E}^+_3(t) = [\hat{E}^+_1(t) + \hat{E}^+_2(t)]/\sqrt{2}$$
$$= [\zeta_1(t)a_1 + \zeta_2(t)a_2]/\sqrt{2}\,,$$
$$\hat{E}^+_4(t) = [\hat{E}^+_1(t) - \hat{E}^+_2(t)]/\sqrt{2}$$
$$= [\zeta_1(t)a_1 - \zeta_2(t)a_2]/\sqrt{2}\,. \tag{6}$$

Note that this is a more general form than the simple operator relation (1), which is equivalent to (6) if all mode functions, ζ_i, are equal.

2.1.1 Joint photon-detection probability:
To obtain the probability for photon detections in the output ports '3' and '4' at times t_0 and $t_0 + \tau$, respectively, we have to apply the field operators $\hat{E}^\pm_3(t_0)$ and $\hat{E}^\pm_4(t_0 + \tau)$. With two photons impinging on the two input ports in modes $\zeta_1(t)$ and $\zeta_2(t)$, the incoming state is $|\Psi_{in}\rangle = a_1^\dagger a_2^\dagger |0\rangle$, and the joint probability for photon detections reads

$$P_{\text{joint}}(t_0, \tau) = g_{34}(t_0, t_0 + \tau) =$$
$$\langle 0| a_1 a_2 \hat{E}^-_3(t_0) \hat{E}^-_4(t_0 + \tau) \hat{E}^+_4(t_0 + \tau) \hat{E}^+_3(t_0) a_1^\dagger a_2^\dagger |0\rangle\,. \tag{7}$$

With the field-operator relations defined in (6) and the restriction to single-photon states, i.e. using $\langle 1|a^\dagger a^\dagger = a\,a|1\rangle = 0$, one easily verifies that (7) leads to

$$P_{\text{joint}}(t_0, \tau) = \frac{1}{4}|\zeta_1(t_0 + \tau)\zeta_2(t_0) - \zeta_2(t_0 + \tau)\zeta_1(t_0)|^2\,. \tag{8}$$

The most striking feature of this joint probability function is that it vanishes for $\tau = 0$, no matter how different the mode functions of the two incoming photons are. Moreover, if the phase relation between ζ_1 and ζ_2 is lost for $\tau \gg \tau_c$, where τ_c is the mutual coherence time of the incoming photons, the interference term in (8), averaged over an ensemble of different photon pairs, is zero, and P_{joint} reduces to

$$\overline{P_{\text{joint}}}(t_0, \tau) \xrightarrow{\tau \gg \tau_c} \frac{1}{4}(P_1(t_0)P_2(t_0 + \tau) + P_2(t_0)P_1(t_0 + \tau))\,. \tag{9}$$

2.1.2 Photon-by-photon analysis.
Despite the fact that the full interference phenomenon is described by (8), it is hard to acquire an intuitive understanding of the interference process from the two-photon approach. This is not the case if one analyses the effect step-by-step. We therefore use the same spatio-temporal mode functions as before and ask now for the probability of detecting a photon in output port '4' at time $t_0 +$

τ conditioned on a photon detection in output port '3' at time t_0. The probability of finding a photon in port '3' reads

$$P_3(t_0) = \langle\Psi_{in}|\hat{E}_3^-(t_0)\,\hat{E}_3^+(t_0)|\Psi_{in}\rangle =$$
$$\langle 1_1 1_2|\left(\hat{E}_1^-(t_0)+\hat{E}_2^-(t_0)\right)\frac{1}{2}\left(\hat{E}_1^+(t_0)+\hat{E}_2^+(t_0)\right)|1_1 1_2\rangle =$$
$$\frac{1}{2}\left(|\varepsilon_1(t_0)|^2+|\varepsilon_2(t_0)|^2\right). \qquad (10)$$

Note that this expression includes no interference term, since the initial product state is composed of single-photon Fock states that have no relative phase. The state $|\Psi_{cond}\rangle$, conditioned on the detection of a photon in port '3' at time t_0, is obtained by applying the field operator $\hat{E}_3^+(t_0)$ to the incoming state, $|1_1 1_2\rangle$. After re-normalisation, this leads to

$$\hat{E}_3^+(t_0)|1_1 1_2\rangle \xrightarrow{norm} \frac{\zeta_2(t_0)|1_1 0_2\rangle+\zeta_1(t_0)|0_1 1_2\rangle}{\sqrt{|\varepsilon_1(t_0)|^2+|\varepsilon_2(t_0)|^2}} = |\Psi_{cond}\rangle. \qquad (11)$$

The conditioned state, $|\Psi_{cond}\rangle$, describes a single photon that either impinges on port '1' or port '2' of the beam splitter, with the amplitude and phase relations between these two modes given by $\zeta_2(t_0)$ and $\zeta_1(t_0)$. This photon now gives rise to classical interference fringes that start in phase at time t_0; i.e. the second photon is found in the same port as the first photon if it is detected at the same instant. However, the phase evolves in time according to $\zeta_1(t)$ and $\zeta_2(t)$. Therefore the probabilities of detecting the second photon in output ports '3' or '4' at time $t_0+\tau$ read

$$P_{3,4}(t_0+\tau) = \langle\Psi_{cond}|\hat{E}_{3,4}^-(t_0+\tau)\,\hat{E}_{3,4}^+(t_0+\tau)|\Psi_{cond}\rangle$$
$$= \frac{|\zeta_1(t_0+\tau)\,\zeta_2(t_0)\pm\zeta_2(t_0+\tau)\,\zeta_1(t_0)|^2}{2(|\varepsilon_1(t_0)|^2+|\varepsilon_2(t_0)|^2)}. \qquad (12)$$

Together with (10), the joint photon-detection probability for a first detection in output port '3' at time t_0 and a subsequent photon detection in output port '4' at time $t_0+\tau$ is

$$P_{joint}(t_0,\tau) = P_3(t_0)\,P_4(t_0+\tau)$$
$$= \frac{1}{4}|\zeta_1(t_0+\tau)\,\zeta_2(t_0)-\zeta_2(t_0+\tau)\,\zeta_1(t_0)|^2. \qquad (13)$$

Result (13) is identical to (8). However, the step-by-step analysis reveals the equivalence of classical one-photon interference and two-photon interference conditioned on the detection of a first photon. Note that the field operators at the output ports commute, i.e. $[\hat{E}_3^+(t_0),\hat{E}_4^+(t_0+\tau)]=0$. Therefore the sequence of operators is irrelevant, and for a negative detection-time delay, τ, which corresponds to a reverse order of photon detections, the same results are obtained.

2.2   Single-frequency field modes

A standard way to attack the problem of two interfering photons is based on the decomposition of single-photon wave packets into an infinite number of single-frequency field modes. To do so, a single photon in one of the two spatio-temporal input modes ($i = 1, 2$) is expressed as one quantum of excitation occupying a superposition of all possible frequency modes,

$$|1_i\rangle = \int d\omega\,\Phi_i(\omega)a_i^\dagger(\omega)|0\rangle, \qquad (14)$$

where the spectral amplitude of the single-photon pulse, $\Phi_i(\omega)$, is assumed to be normalised so that $\int d\omega\,\Phi_i^*(\omega)\Phi_i(\omega) = 1$. The continuum of spectral fields allows one to express the time-dependent electric field operators as

$$\hat{E}_i^+(t) = \frac{1}{\sqrt{2\pi}}\int d\omega\,e^{-i\omega t}a_i(\omega) \quad \text{and}$$
$$\hat{E}_i^-(t) = \frac{1}{\sqrt{2\pi}}\int d\omega\,e^{i\omega t}a_i^\dagger(\omega). \qquad (15)$$

To evaluate the effect of the field operator, $\hat{E}_i^+(t)$, acting on the single-photon state $|1_i\rangle$ defined in (14), we make use of the fact that the Fourier transformation of the spectrum, $\Phi_i(\omega)$, equals the spatio-temporal mode-function,

$$\zeta_i(t) = \frac{1}{\sqrt{2\pi}}\int d\omega\,\Phi_i(\omega)\,e^{-i\omega t}, \qquad (16)$$

which leads to

$$\hat{E}_i^+(t)|1_i\rangle = \frac{1}{\sqrt{2\pi}}\int\int d\omega d\tilde{\omega}\,e^{-i\omega t}a_i(\omega)\Phi_i(\tilde{\omega})a_i^\dagger(\tilde{\omega})|0\rangle$$
$$= \frac{1}{\sqrt{2\pi}}\int d\omega\,\Phi_i(\omega)\,e^{-i\omega t}|0\rangle \equiv \zeta_i(t)|0\rangle. \qquad (17)$$

Therefore, one easily verifies that the probability of finding the photon at time t reads

$$P_i(t) = \langle 1_i|\hat{E}_i^-(t)\hat{E}_i^+(t)|1_i\rangle$$
$$= \langle 0|\zeta_i^*(t)\zeta_i(t)|0\rangle = \zeta_i^*(t)\zeta_i(t), \qquad (18)$$

which is equivalent to (5), since the two approaches were mapped onto one another (see (16)).

In the field-mode picture, the effect of the beam splitter is described by the transformation relations in (1), and the quantum state of the two incoming photons, $|1_1 1_2\rangle$, is expressed as a product state of field-mode superposition states, as defined in (14). Therefore we make use of the relations in (1) and replace $a_1^\dagger(\omega_1)$ and $a_2^\dagger(\omega_2)$ by the respective sums and differences of $a_3^\dagger(\omega)$ and $a_4^\dagger(\omega)$, which leads to

$$|1_1 1_2\rangle = \int\int d\omega_1 d\omega_2\Phi_1(\omega_1)\,\Phi_2(\omega_2)\,a_1^\dagger(\omega_1)\,a_2^\dagger(\omega_2)|0\rangle$$
$$= \int\int d\omega_1 d\omega_2\Phi_1(\omega_1)\,\Phi_2(\omega_2)$$
$$\times \frac{1}{2}\left[a_3^\dagger(\omega_1)+a_4^\dagger(\omega_1)\right]\left[a_3^\dagger(\omega_2)-a_4^\dagger(\omega_2)\right]|0\rangle. \qquad (19)$$

We now use (7) to calculate the joint detection probability,

$$P_{joint}(t_0,\tau) =$$
$$\langle 1_1 1_2|\hat{E}_3^-(t_0)\,\hat{E}_4^-(t_0+\tau)\,\hat{E}_4^+(t_0+\tau)\,\hat{E}_3^+(t_0)|1_1 1_2\rangle, \qquad (20)$$

for two photons detected in output ports '3' and '4' at times t_0 and $t_0+\tau$, respectively. We use (19) to express the state $|1_1 1_2\rangle$ in terms of the creation operators $a_3^\dagger$ and $a_4^\dagger$ to obtain the right-hand side of the operator-bracket in (20),

$$\hat{E}_4^+(t_0+\tau)\,\hat{E}_3^+(t_0)|1_1 1_2\rangle =$$
$$\frac{1}{4\pi}\int d\omega_{1...4}\Phi_1(\omega_1)\,\Phi_2(\omega_2)\,e^{-i\omega_3 t}\,e^{-i\omega_4(t+\tau)}$$
$$\times [\delta(\omega_3-\omega_2)\,\delta(\omega_4-\omega_1)-\delta(\omega_3-\omega_1)\,\delta(\omega_4-\omega_2)]|0\rangle. \qquad (21)$$

We now make use of the Fourier-transformation relation between $\Phi_i(\omega)$ and $\zeta_i(t)$ from (16) to evaluate the above integral, which leads to

$$\hat{E}_4^+(t_0+\tau)\,\hat{E}_3^+(t_0)|1_1 1_2\rangle =$$
$$\frac{1}{2}[\zeta_1(t_0+\tau)\zeta_2(t_0)-\zeta_1(t_0)\zeta_2(t_0+\tau)]|0\rangle, \qquad (22)$$

so that the joint photon-detection probability finally reads

$$P_{joint}(t_0,\tau) = \frac{1}{4}|\zeta_1(t_0+\tau)\,\zeta_2(t_0)-\zeta_1(t_0)\,\zeta_2(t_0+\tau)|^2, \qquad (23)$$

which is again equivalent to (8). Therefore we conclude that the different approaches for modelling single-photon wave packets all lead to the same expression for the joint two-photon detection probability, $P_{joint}(t_0,\tau)$. But note that the standard way of using single-frequency field modes is not well adapted to the problem and requires a lengthy and cumbersome calculation. This is not the case in the space–time domain, where the joint detection probability can be calculated in a fast and elegant way (Sect. 2.1.1). However, physical insight is only obtained from the photon-by-photon analysis (Sect. 2.1.2), which reveals that the two-photon quantum interference is in fact equivalent to a classical interference phenomenon once a first photon detection has taken place. In the collapsed state, the relative phases and amplitudes of the two interfering modes are fixed. Therefore an oscillating quantum-beat signal is expected if the two spatio-temporal mode functions, $\zeta_1(t)$ and $\zeta_2(t)$, evolve at different rates.

3   Quantum beat

To illustrate the quantum-beat signal in the interference of two photons with slightly different frequencies, we now consider the case of two equally long Fourier-limited Gaussian single-photon pulses that impinge on a 50 : 50 beam splitter with a relative delay time of $\delta\tau$ and a carrier-frequency difference of $\Delta = \omega_2 - \omega_1$. These pulses are described by the two spatio-temporal mode functions

$$\zeta_1(t) = \sqrt[4]{2/\pi}\exp\left(-(t-\delta\tau/2)^2-i(\omega-\Delta/2)t\right)$$

and

$$\zeta_2(t) = \sqrt[4]{2/\pi}\exp\left(-(t+\delta\tau/2)^2-i(\omega+\Delta/2)t\right), \qquad (24)$$

with $\omega = (\omega_1 + \omega_2)/2$. For the sake of simplicity, the time, t, the photon delay, $\delta\tau$, and the detection-time delay, τ, are expressed in units of the pulse duration, δt (half width at $1/e$ maximum), while the frequencies, ω and Δ, are expressed in units of $1/\delta t$.

With the spatio-temporal modes defined in (24), a straightforward evaluation of (8) leads to the joint photon-detection
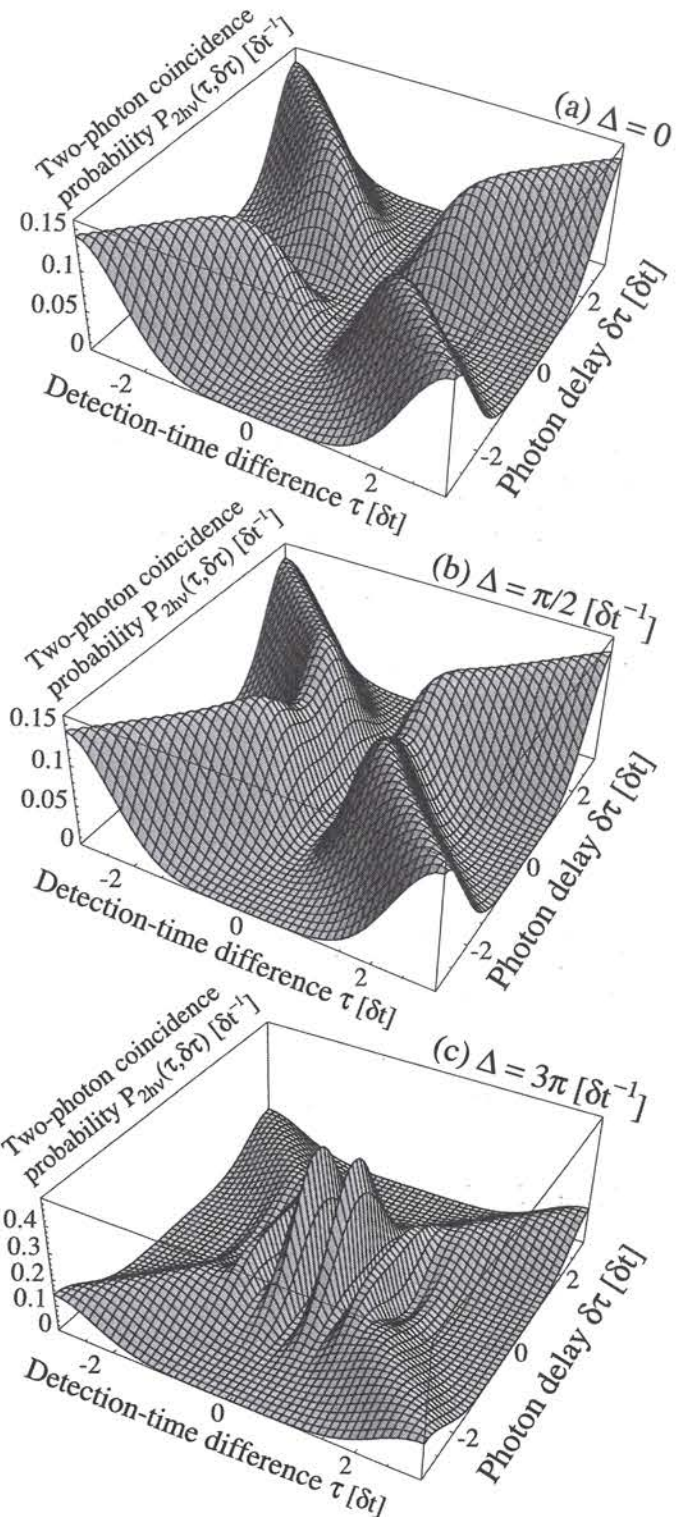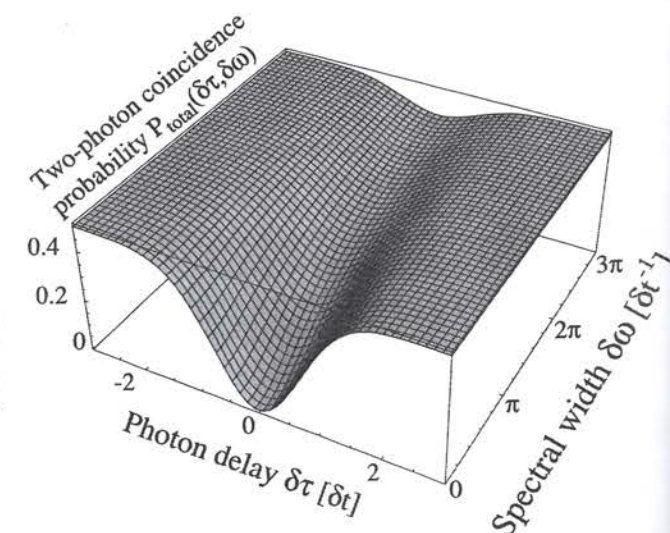

FIGURE 2   Joint probability, $P_{2h\nu}$, for the detection of photon pairs as a function of the relative delay between the two impinging photon wave packets, $\delta\tau$, and the delay between photon detections, τ, for the three frequency differences $\Delta = 0; \pi/2; 3\pi$. All times and frequencies are normalised by the photon-pulse duration, δt, and, hence, are dimensionless

probability

$$P_{\text{joint}}(t_0, \tau, \delta\tau, \Delta) = \frac{\cosh(2\tau\delta\tau) - \cos(\tau\Delta)}{\pi}$$
$$\times \exp(-4t_0(t_0 + \tau) - \delta\tau^2 - 2\tau^2), \quad (25)$$

which depends on the photon detection times, t_0 and $t_0 + \tau$. To obtain the probability of detecting two photons in the ports '3' and '4' with a time difference of τ, we integrate over all possible values of t_0, which leads to

$$P_{2h\nu}(\tau, \delta\tau, \Delta) = g_{3,4}^{(2)}(\tau)|_{\delta\tau, \Delta} = \int dt_0\, P_{\text{joint}}(t_0, \tau, \delta\tau, \Delta)$$
$$= \frac{\cosh(2\tau\delta\tau) - \cos(\tau\Delta)}{2\sqrt{\pi}} \times \exp(-\delta\tau^2 - \tau^2). \quad (26)$$

This joint two-photon detection probability is displayed in Fig. 2 as a function of the photon-delay, $\delta\tau$, and the detection-time delay, τ, for three different values of the frequency difference, Δ.

The case with $\Delta = 0$ is depicted in Fig. 2a. As expected, no coincidences are found if the photons arrive simultaneously, i.e. for $\delta\tau = 0$. This situation is well explained by the Fock-state model of two interfering indistinguishable photons. Moreover, even if the two photons are delayed with respect to each other, we see that simultaneous photon detections (with $\tau = 0$) never occur. This is well-explained by (8), which yields $P_{\text{joint}}(t_0, \tau = 0) \equiv 0$, no matter how different the mode functions are. In particular, the second photon leaves the beam splitter through the same port as the first one, provided no dephasing takes place, i.e. for $|\zeta_1(t_0 + \tau)\zeta_2(t_0) - \zeta_1(t_0)\zeta_2(t_0 + \tau)| \ll 1$.

Figure 2b and c show situations in which the two impinging photon wave packets have a frequency difference of $\Delta = \pi/2$ or $\Delta = 3\pi$, respectively. Most remarkable is that simultaneous detections (with $\tau = 0$) still do not occur, although the two photons are now distinguishable. Moreover, for simultaneously arriving photon wave packets (with $\delta\tau = 0$), the coincidence probability now oscillates as a function of τ with the frequency difference Δ. We emphasise that this beat note always starts at zero for $\tau = 0$, due to the in-phase starting condition imposed by the detection of the first photon.

It follows that the coincidence probability remains zero even in the case of an inhomogeneous broadening of the frequency differences, Δ. To illustrate this, we assume a Gaussian frequency distribution,

$$f_{\delta\omega}(\Delta) = \frac{1}{\delta\omega\sqrt{\pi}} \exp(-(\Delta/\delta\omega)^2), \quad (27)$$

where $\delta\omega$ defines the bandwidth of the spectrum (half width at $1/e$ maximum). The integral of this frequency distribution is normalised to one, so that we can use it to calculate the photon detection probability for simultaneously arriving photon wave packets (with $\delta\tau = 0$) by evaluating

$$P_{\text{inh}}(\tau, \delta\omega) = \int d\Delta\, f_{\delta\omega}(\Delta) P_{2h\nu}(\tau, \delta\tau = 0, \Delta)$$
$$= \frac{\exp(-\tau^2)}{2\sqrt{\pi}} \left(1 - \exp\left(-\left(\frac{\tau}{2/\delta\omega}\right)^2\right)\right). \quad (28)$$

Figure 3 shows that the inhomogeneous broadening of the photonic spectrum leads to a dip in the two-photon detection probability with width $2/\delta\omega$ (half width at $1/e$ dip depth). We emphasise that this dip in P_{inh} reaches zero. Therefore it is possible to achieve perfect two-photon coalescence if a temporal filter is applied that restricts the detection-time difference to $|\tau| \ll 2/\delta\omega$.

To connect our results to previous experiments with ultrashort photons, we now calculate the total two-photon coincidence probability by integrating over the detection-time delay, τ. In the case of inhomogeneous broadening, as discussed above, this leads to

$$P_{\text{total}}(\delta\tau, \delta\omega) = \int\int d\tau\, d\Delta\, f_{\delta\omega}(\Delta) P_{2h\nu}(\tau, \delta\tau, \Delta)$$
$$= \frac{1}{2} - \frac{\exp(-\delta\tau^2)}{\sqrt{4 + \delta\omega^2}}. \quad (29)$$
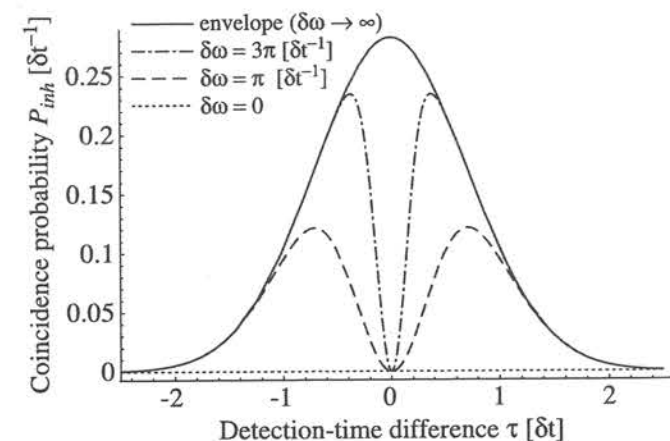
FIGURE 3 Time-resolved two-photon detection probability, P_{inh}, as a function of the detection-time difference, τ, in the case of simultaneously arriving equally long single-photon wave packets ($\delta\tau = 0$) for different inhomogeneous spectral widths, $\delta\omega$. The *solid line* represents non-interfering photons and therefore reflects the amplitude envelope of the photonic wave packets

FIGURE 4 Total probability of detecting photon pairs as a function of the relative delay between the two impinging photon wave packets, $\delta\tau$, and the inhomogeneous spectral width, $\delta\omega$, of the interfering photons

The total two-photon coincidence probability is shown in Fig. 4 as a function of the arrival-time delay, $\delta\tau$, and the inhomogeneous spectral width, $\delta\omega$. In this case, it is evident that the two-photon coincidence dip reaches zero only if $\delta\omega = 0$, i.e. only if the two photons are mutually coherent. Increasing the bandwidth has no effect on the width of the dip, but only decreases its depth. Therefore spectral filtering is mandatory if the time resolution does not allow photon-detection times to be filtered.

4 Conclusion

A rich substructure is expected in two-photon interference experiments if the photons can be detected with good time resolution. For example, distinguishable photons of different frequencies are expected to give rise to a pronounced oscillation of the joint photon-detection probability behind the beam splitter. The ability to generate long single-photon pulses by means of a strongly coupled atom–cavity system opens up the possibility to 'zoom' into the quantum state of a single-photon pulse by measuring two-photon quantum interference fringes as a function of time.

REFERENCES

1 D. Bouwmeester, J.-W. Pan, K. Mattle, M. Eibl, H. Weinfurter, A. Zeilinger: Nature **390**, 575 (1997)
2 D. Boschi, S. Branca, F. de Martini, L. Hardy, S. Popescu: Phys. Rev. Lett. **80**, 1121 (1998)
3 E. Knill, R. Laflamme, G.J. Milburn: Nature **409**, 46 (2001)
4 For a review, see, e.g., D. Bouwmeester, A. Ekert, A. Zeilinger (Eds.): *The Physics of Quantum Information* (Springer, Berlin 2000)
5 C.K. Hong, Z.Y. Ou, L. Mandel: Phys. Rev. Lett. **59**, 2044 (1987)
6 For a detailed theoretical description, see, e.g., Z.Y. Ou: Phys. Rev. A **37**, 1607 (1988); H. Fearn, R. Loudon: J. Opt. Soc. Am. B **6**, 917 (1989)
7 For an overview, see, e.g., L. Mandel: Rev. Mod. Phys. **71**, 274 (1999), and references therein
8 Z.Y. Ou, L. Mandel: Phys. Rev. Lett. **61**, 54 (1988)
9 H. de Riedmatten, I. Marcikic, W. Tittel, H. Zbinden, N. Gisin: Phys. Rev. A **67**, 022301 (2003)
10 T.B. Pittman, J.D. Franson: Phys. Rev. Lett. **90**, 240401 (2003)
11 C. Santori, D. Fattal, J. Vučković, G.S. Solomon, Y. Yamamoto: Nature **419**, 594 (2002)
12 M. Zukowski, A. Zeilinger, H. Weinfurter: Ann. N.Y. Acad. Sci. **755**, 91 (1995)
13 J. Bylander, I. Robert-Philip, I. Abram: Eur. Phys. J. D **22**, 295 (2003)
14 A. Kuhn, M. Hennrich, G. Rempe: Phys. Rev. Lett. **89**, 067901 (2002)
15 A. Kuhn, G. Rempe: In: *Experimental Quantum Computation and Information, Vol. 148*, ed. by F. DeMartini, C. Monroe (IOS-Press, Amsterdam 2002) p. 37
16 A. Kuhn, M. Hennrich, G. Rempe: In: *Quantum Information Processing*, ed. by T. Beth, G. Leuchs (Wiley-VCH, Berlin 2003) p. 182
17 A.M. Steinberg, P.G. Kwiat, R.Y. Chiao: Phys. Rev. A **45**, 6659 (1992)
18 L. Mandel, E. Wolf: *Optical Coherence and Quantum Optics* (Cambridge University Press, Cambridge 1995)

New Journal of Physics

Photon statistics of a non-stationary periodically driven single-photon source

M Hennrich, T Legero, A Kuhn and G Rempe

Max-Planck-Institut für Quantenoptik, Hans-Kopfermann-Str. 1,
85748 Garching, Germany
E-mail: axel.kuhn@mpq.mpg.de

Abstract. We investigate the photon statistics of a single-photon source that operates under non-stationary conditions. The photons are emitted by shining a periodic sequence of laser pulses on single atoms falling randomly through a high-finesse optical cavity. Strong antibunching is found in the intensity correlation of the emitted light, demonstrating that a single atom emits photons one at a time. However, the number of atoms interacting with the cavity follows a Poissonian statistics so that, on average, no sub-Poissonian photon statistics is obtained, unless the measurement is conditioned on the presence of single atoms.

Contents

1. Introduction

Worldwide, major efforts have been made to realize systems for the storage of individual quantum bits (qubits) and to conditionally couple different qubits for the processing of quantum information [1]. Ultra-cold trapped neutral atoms or ions are ideal quantum memories that store qubits in long-lived states, while single photons may act as flying qubits that allow for linear optical quantum computing [2]. On the route to a scalable quantum-computing network, interconverting these stationary and flying qubits is essential [3]. One way to accomplish such an interface is by an adiabatic coupling between a single atom and a single photon in an optical cavity [4, 5].

The present work focuses on the properties of a coupled atom–cavity system which is operated as a single-photon emitter [6]–[9]. In contrast with other methods of Fock-state preparation in the microwave regime [10, 11], where the photons remain trapped inside the cavity, our scheme allows one to emit single optical photons on demand into a well-defined mode of the radiation field outside the cavity [12, 13]. However, in contrast with many other single-photon sources, like solid-state systems [14]–[16], our source operates under non-stationary conditions, because atoms enter and leave the cavity randomly. Only during the presence of a single atom, the atom–cavity system is acting as a single-photon emitter. No photons are generated without atoms, and if more than one atom is present, the number of simultaneously emitted photons might exceed one. These circumstances have a significant impact on the photon statistics of the emitted light [17, 18], which is analysed here in detail.

2. Single photons from a cavity-QED system

Figure 1 illustrates the basic scheme of the process. A dilute cloud of ^{85}Rb atoms, prepared in state $|u\rangle \equiv |5S_{1/2}(F = 3)\rangle$, is released from a magneto-optical trap (MOT) and falls with a velocity of $2\,\mathrm{m\,s^{-1}}$ through a 1-mm-long optical cavity of finesse $F = 60\,000$. The density of the cloud, and therefore the average number of atoms simultaneously interacting with the TEM$_{00}$ mode of the cavity, is freely adjustable. The cavity is near-resonant with the transition between the $|5S_{1/2}(F = 2)\rangle$ hyperfine state of the electronic ground state and the electronically excited $|5P_{3/2}(F = 3)\rangle$ state, labelled $|g\rangle$ and $|e\rangle$, respectively. Initially, the cavity is empty, so that the state of the coupled atom–cavity system can only move within the Hilbert space spanned by the product states $|u, 0\rangle$, $|e, 0\rangle$, $|g, 1\rangle$ and $|g, 0\rangle$, with $|0\rangle$ and $|1\rangle$ denoting the relevant photon number states of the cavity. The dynamics of this system is determined by $(g_{max}, \kappa, \gamma_\perp, \Delta)/2\pi = (2.5, 1.25, 3.0, -20.0)\,\mathrm{MHz}$, where g_{max} is the cavity-induced coupling between states $|e, 0\rangle$ and $|g, 1\rangle$ for an atom optimally coupled to the cavity, and κ and $\gamma_\perp$ are the field and polarization decay rates of the cavity and the atom, respectively, and Δ is the detuning of the cavity from the atomic transition. One mirror has a larger transmission coefficient than the other so that photons leave the cavity through this output coupler with a probability of 90%. While an atom interacts with the cavity, it experiences a sequence of laser pulses that alternate between triggering single-photon emissions and recycling the atom to state $|u\rangle$: the 2-μs-long pump pulses are detuned by Δ from the $|u\rangle \leftrightarrow |e\rangle$ transition, so that they adiabatically drive a stimulated Raman transition (STIRAP) [8, 19] from $|u, 0\rangle$ to $|g, 1\rangle$ with a Rabi frequency that increases linearly from 0 to $\Omega_{max}/2\pi = 8.0\,\mathrm{MHz}$. This Raman transition goes hand-in-hand with a photon emission. Once the photon is emitted, the system reaches $|g, 0\rangle$, which is not coupled to the single-excitation manifold, $\{|u, 0\rangle, |e, 0\rangle, |g, 1\rangle\}$, and therefore cannot be re-excited. This limits the number of photons per pump pulse and atom to one.

To emit a sequence of photons from one-and-the-same atom, the system is transferred back to $|u, 0\rangle$ after each emission. To do so, we apply 2-μs-long recycling laser pulses that hit the
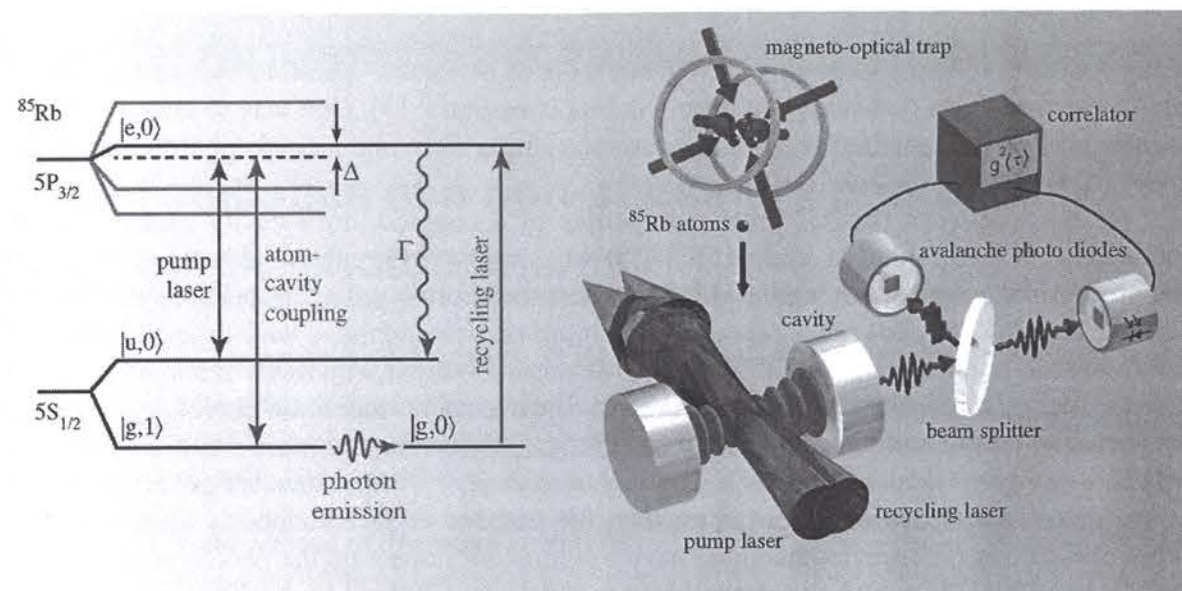
Figure 1. Scheme of the experiment. Left: relevant levels and transitions in ^{85}Rb. The atomic states labelled $|u\rangle$, $|e\rangle$ and $|g\rangle$ are involved in the Raman process, and the states $|0\rangle$ and $|1\rangle$ denote the photon number in the cavity. Right: the experimental setup. A cloud of atoms is released from a magneto-optical trap and falls through a cavity 20 cm below in about 8 ms with a velocity of $2\,\mathrm{m\,s^{-1}}$. The interaction time of each atom in the cloud with the TEM$_{00}$ mode of the cavity amounts to about $20\,\mu$s. The pump and recycling lasers are collinear and overlap with the cavity mode. The light emitted from the cavity is registered by a pair of photodiodes in Hanbury-Brown and Twiss configuration in order to analyse the photon statistics. (See the animation.)

atom between consecutive pump pulses. The recycling pulses are resonant with the $|g\rangle \leftrightarrow |e\rangle$ transition and excite the atom to state $|e\rangle$. From there, it decays spontaneously to the initial state $|u\rangle$. This way, an atom that resides in the cavity can emit a sequence of single-photon pulses. For each experimental cycle, these photons are recorded using two avalanche photodiodes with 50% quantum efficiency, which are placed at the output ports of a beam splitter.

3. Photon statistics

The two photodiodes constitute a Hanbury-Brown and Twiss setup [20] used to measure the normalized intensity correlation of the photon stream emitted from the cavity,

$$g^{(2)}(\tau) = \frac{\langle I_1(t) I_2(t+\tau)\rangle}{\langle I_1(t)\rangle\langle I_2(t)\rangle}, \tag{1}$$

where $I_n(t)$ is the count rate recorded by detector $n = 1, 2$. If $\bar{I}$ denotes the mean count rate recorded by each detector and $\bar{I}_N$ is the mean noise-count rate, the mean rate of photon counts

reads $\bar{I}_P = \bar{I} - \bar{I}_N$. This allows us to estimate two of the following three contributions to the correlation function:

(a) Correlations between a noise count and either a real photon or another noise count are randomly distributed and occur with a probability proportional to $\bar{I}_N^2 + \bar{I}_P\bar{I}_N + \bar{I}_N\bar{I}_P = \bar{I}^2 - \bar{I}_P^2$. Therefore these correlations lead to a constant background contribution,

$$g_N^{(2)} = \frac{\bar{I}^2 - \bar{I}_P^2}{\bar{I}^2} = 1 - \frac{\bar{I}_P^2}{\bar{I}^2}, \tag{2}$$

to the normalized correlation function.

(b) Correlations between photons that stem from different atoms lead to a modulation of $g^{(2)}(\tau)$, since the periodicity of the pump laser leads to a modulation of the photon emission probability. The pump intervals have the same duration as the recycling intervals, and the probability for photon emissions during recycling is close to zero. This increases the average rate of photons emitted during pumping to $2\bar{I}_P$, so that photon–photon correlations between pump pulses are found with a probability proportional to $(2\bar{I}_P)^2$, while the probability to get photon correlations between pump and recycling intervals is vanishingly small. The average normalized contribution of photon–photon correlations to $g^{(2)}$ therefore oscillates between

$$g_{P,min}^{(2)} = 0 \quad \text{and} \quad g_{P,max}^{(2)} = \frac{1}{2}\frac{(2\bar{I}_P)^2}{\bar{I}^2} = 2\frac{\bar{I}_P^2}{\bar{I}^2}. \tag{3}$$

In order to obtain this simple estimation, we use the factor $\frac{1}{2}$ in $g_{P,max}^{(2)}$ to take into account that photons are emitted only during pump pulses, which are active half of the time, and we neglect any time dependence of I_P within the pump pulses. In the experiment, however, I_P varies with time, which causes small deviations from the estimated values, as further discussed below.

(c) Correlations between photons emitted from one-and-the-same atom are, of course, most interesting. They cannot be estimated from the average count rates, $\bar{I}$ and $\bar{I}_N$. However, due to the limited atom–cavity interaction time, τ_{int}, it is clear that they only contribute to $g^{(2)}(\tau)$ in the time interval $[-\tau_{int}, \tau_{int}]$, and therefore this contribution can be distinguished from (a) and (b) as explained below.

Figure 2, obtained for a different flux of atoms, shows that the three contributions above are easily identified in the measured correlation function. Due to the limited atom–cavity interaction time, all correlations with $|\tau| \gg \tau_{int}$ belong either to category (a) or (b). The oscillatory behaviour of $g^{(2)}(\tau)$ in this regime stems from photons emitted by different atoms, whereas the time-independent pedestal is mainly caused by correlations involving noise counts. These two contributions are indicated as hatched and cross-hatched areas, respectively. They were obtained from the autocorrelation of the pulse-averaged count rate, $\tilde{I}(t) = (1/N)\sum_{n=1}^N I(t + n\tau_{period})$, where N is the total number of recorded pump and recycle intervals of duration $\tau_{period} = 4\,\mu$s. This gives an oscillation of the intensity correlation function between $g_{C,min}^{(2)}$ and $g_{C,max}^{(2)}$.

These two values of $g^{(2)}$ can also be estimated from the mean count rates, $\bar{I}$ and $\bar{I}_N$. This estimation predicts an oscillation of $g^{(2)}$ with the periodicity of the applied sequence between
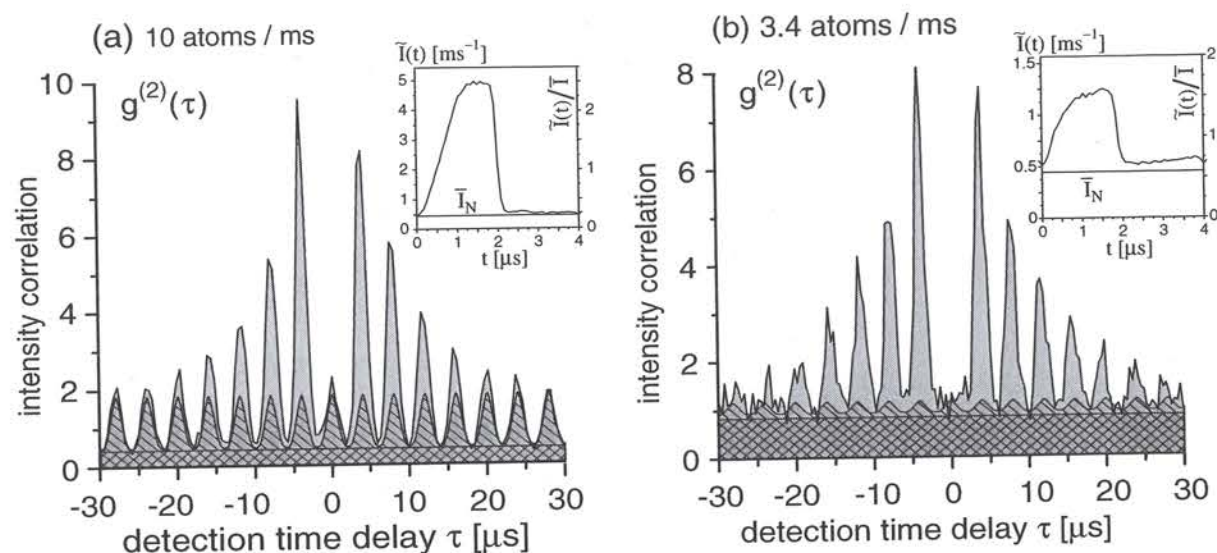
Figure 2. Unconditional photon statistics of the emitted light: intensity correlation, $g^{(2)}(\tau)$, with different-atom (hatched) and noise (cross-hatched) contributions. For correlation times larger than the atom–cavity interaction time, only these contributions persist. They are obtained from the autocorrelation of the respective pulse-averaged count rates, $\bar{I}(t)$, which are shown in the two insets. (a) High atom flux, averaged over 4997 experimental cycles (loading and releasing of the atom cloud) with a total number of 151 089 photon counts. (b) Low atom flux, averaged over 15 000 experimental cycles with a total number of 184 868 photon counts.

the two extrema $g^{(2)}_{E,min} = 1 - \bar{I}^2_P/\bar{I}^2$ and $g^{(2)}_{E,max} = 1 + \bar{I}^2_P/\bar{I}^2$. For the data underlying figure 2, we obtain the following result:

	High atom flux (figure 2(a))	Low atom flux (figure 2(b))
$\bar{I}$	$1976\,\text{s}^{-1}$	$783\,\text{s}^{-1}$
$\bar{I}_N$	$446\,\text{s}^{-1}$	$446\,\text{s}^{-1}$
$\bar{I}_P = \bar{I} - \bar{I}_N$	$1530\,\text{s}^{-1}$	$337\,\text{s}^{-1}$
$g^{(2)}_{E,min}, g^{(2)}_{E,max}$	0.40, 1.60	0.81, 1.19
$g^{(2)}_{C,min}, g^{(2)}_{C,max}$	0.46, 1.82	0.91, 1.13

As mentioned above, the estimated values deviate slightly from the values obtained from the autocorrelation of the pulse-averaged count rate. This was expected since our estimation is based on the simplified model. Note that contributions (a) and (b) persist also in the regime $|\tau| < \tau_{int}$, since the atoms have a Poissonian distribution. Obviously, the excess signal observed here belongs to category (c), i.e. it reflects the single-atom contribution to the correlation signal. Most remarkably, no excess signal is found around $\tau = 0$, i.e. all correlations registered during one-and-the-same pump pulse either involve noise counts or photons from different atoms. Correlations between photons that stem from one-and-the-same atom (c) are only found between different
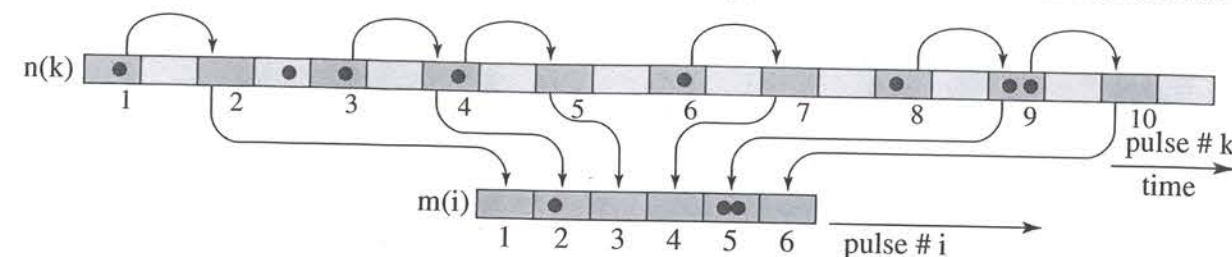
Figure 3. Conditioning on the presence of atoms (schematic): all events (red bullets) are first recorded as a function of time. If photons are detected in a time interval where the pump laser is active (blue intervals), we assume that an atom is present and take the following pump-laser interval into account. Events recorded during recycling (green intervals) are ignored. The pump-laser intervals selected this way form a new set of data, which is then used to calculate the intensity correlation function.

pump pulses. Moreover, antibunching with $g^{(2)}(0) < g^{(2)}(\tau = n\tau_{period})$, $n = \pm 1, \pm 2, \ldots$, is observed. This effect cannot be observed for a classical light source, where the Cauchy–Schwartz inequality predicts that $g^{(2)}(0) \geqslant g^{(2)}(\tau)$ [21]. Therefore the observation of antibunching indicates that a single atom emits photons one at a time.

For a stationary single-photon source, the non-classicality of the emitted radiation would lead to a sub-Poissonian photon statistics with $g^{(2)}(0) < 1$. In the present case, however, atoms arrive randomly in the cavity, and the Poissonian atom statistics leads to $g^{(2)}(0) > 1$. An *a priori* knowledge of the presence of an atom is therefore needed to operate the apparatus as a single-photon emitter. Indeed, if the statistical analysis of the emitted photon stream is restricted to time intervals where the presence of an atom in the cavity is assured with very high probability, a sub-Poissonian photon statistics is found. Figure 3 illustrates the conditioning scheme. To detect an atom, we depend on the fact that photons are only emitted while an atom resides in the cavity. Thus a photon that is detected during a pump pulse signals the presence of an atom with probability $p_{atom} = \bar{n}_P/(\bar{n}_P + \bar{n}_N)$, where $\bar{n}_N = 2\bar{I}_N\tau_P$ is the mean number of noise counts per pump pulse counted by both detectors and $\bar{n}_P = 2\int_0^{\tau_P}(\bar{I}(t) - \bar{I}_N)dt$ is the mean number of detected photons per pulse, with $\tau_P = 2\,\mu$s being the pulse duration. For the data underlying figure 2, we obtain $(\bar{n}_P, \bar{n}_N, p_{atom}) = (11.6 \times 10^{-3}, 1.8 \times 10^{-3}, 87\%)$ and $(2.3 \times 10^{-3}, 1.8 \times 10^{-3}, 56\%)$ for high and low atom flux, respectively. The small value of $\bar{n}_P$ is due to the fact that the cavity contains no atom most of the time. But once an atom is detected, it moves only $\frac{1}{5}$ of the cavity waist until the next pump pulse arrives. We can therefore safely assume that the atom still resides in the cavity at that moment. In the statistical analysis of the light emitted from the system, we now include only the time interval corresponding to this next pump pulse. This is accomplished by first denoting the numbers, $k_1, \ldots, k_M$, of the M pump intervals with $n(k_i) > 0$, where $n(k_i)$ denotes the number of photons detected in the k_ith interval. The time intervals of the adjacent pump pulses then form the new stream of selected data, where the number of photons counted with the detector 1 and 2, respectively, is given by $m_{1,2}(i) = n_{1,2}(k_i + 1)$. From this, the conditioned correlation function

$$g^{(2)}(\Delta i) = \frac{1}{M}\sum_{i=1}^{M}\frac{m_1(i)m_2(i + \Delta i)}{\bar{m}_1\bar{m}_2}, \qquad (4)$$
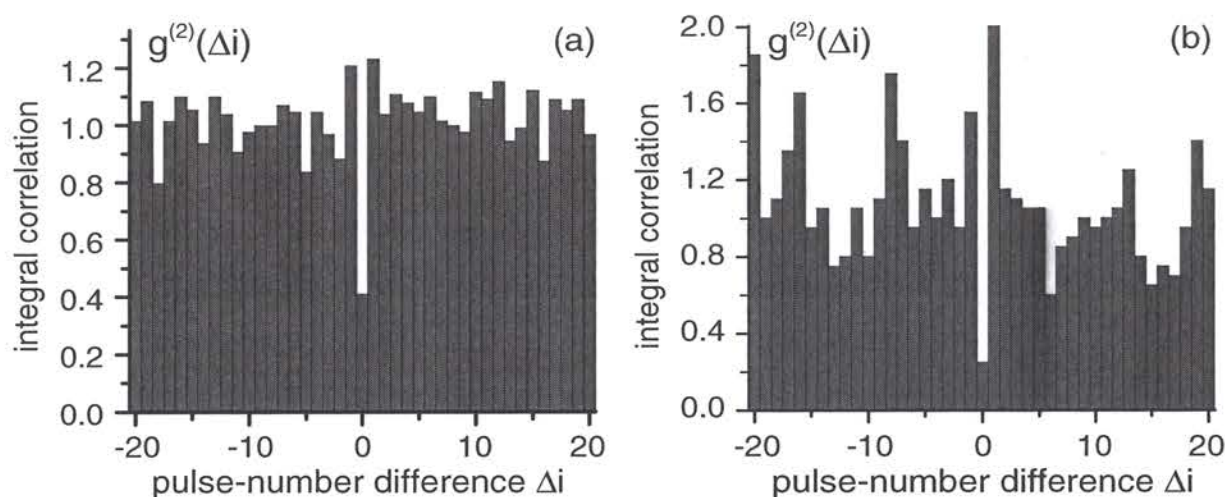
Figure 4. Conditional photon statistics: a sub-Poissonian photon statistics is found in the pulse-to-pulse photon correlation, $g^{(2)}(\Delta i)$, conditioned on the presence of atoms in the cavity. Data are shown for high atom flux (a) and low atom flux (b) as shown in figure 2.

shown in figure 4, is calculated. For a small average atom number, see figure 4(b), conditioning yields $g^{(2)}(\Delta i = 0) = 0.25(11)$, which is well below unity. If the atom flux is increased (figure 4(a)), one obtains $g^{(2)}(\Delta i = 0) = 0.41(6)$. Obviously, the larger value is due to the fact that the probability of having more than one atom interacting with the cavity is not negligible. Nevertheless, the photon statistics conditioned on the presence of atoms is sub-Poissonian in both cases, which is demonstrating a noise reduction below the shot-noise level. Note that the errors in $g^{(2)}(\Delta i)$ are derived from the standard deviations, $\sigma_{\Delta i} = \sqrt{n_e(\Delta i)}$, where $n_e(\Delta i)$ denotes the number of events that constitute $g^{(2)}(\Delta i)$ prior to normalization. We count $n_e(\Delta i = 0) = 5 \pm 2.2$ and 53 ± 7.3 events, whereas for $\Delta i \neq 0$, we count, on average, $\bar{n}_e = 21$ and 130 events with $\sigma_{\Delta i \neq 0} = 4.6$ and 11.4, which yields $\bar{g}^{(2)}(\Delta i \neq 0) = 1.00(20)$ and $1.00(9)$, for low and high atom flux, respectively. The fluctuations of $g^{(2)}(\Delta i \neq 0)$ in figure 4 are well explained by this shot noise.

From the recorded stream of events, we can also characterize the efficiency of the photon source by evaluating the probability for the conditional emission of photons during the pump pulses that follow the detection of an atom by a first photodetection (figure 5). The evaluation must encompass a correction for detector effects like noise counts and reduced quantum efficiencies. Hence, we take into account that a single photodetection actually signals the presence of an atom only with probability p_{atom}, and we also consider that the following photons are detected with an overall quantum efficiency of $\eta = 0.36$ (photodiodes and spatial filtering). We then use the M pump intervals with $n(k_i) > 0$ as starting points to calculate the average photo-emission probabilities during the neighbouring pulses,

$$\bar{p}(\Delta k) = \frac{1}{\eta p_{atom}} \frac{1}{M} \sum_{i=1}^{M} [n(k_i + \Delta k) - \bar{n}_N - \bar{n}_P - \delta_{\Delta k,0}]. \tag{5}$$

Here, $n(k) = n_1(k) + n_2(k)$ is the total number of events counted by both detectors during the kth pump pulse. The mean number of noise counts per pulse, $\bar{n}_N$, and the mean number of photons per
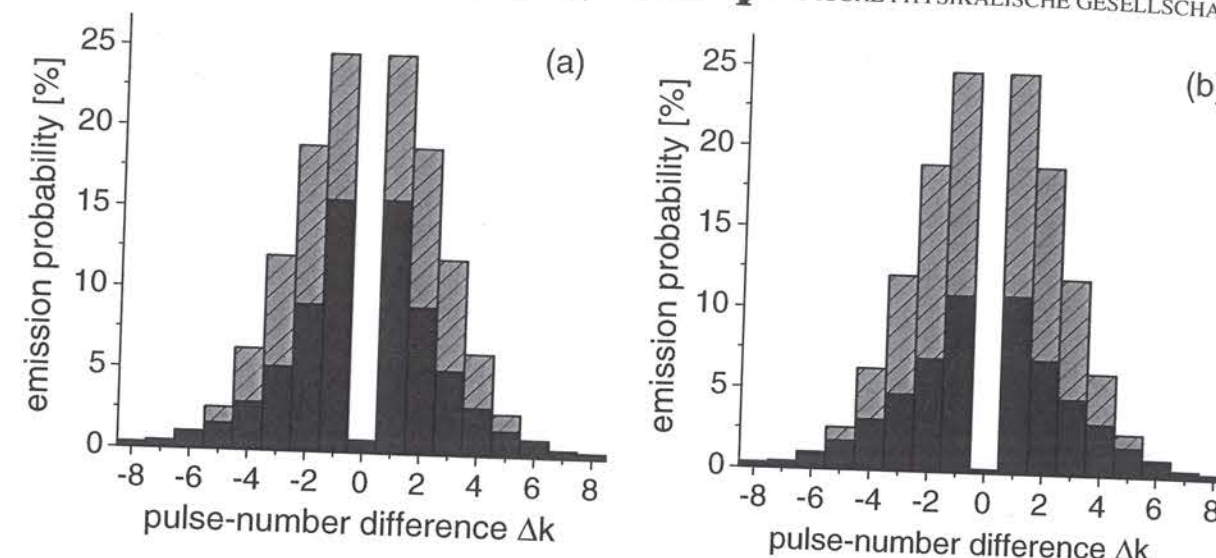
Figure 5. Photon emission probability, conditioned on a photon detection at $\Delta k = 0$. The theoretical expectation values are represented by the green dashed bars, while the experimentally found probabilities are indicated by the solid blue bars. Data are shown for high (a) and low (b) atom flux as shown in figure 2. The decrease of the experimentally observed probabilities in (b) compared with (a) is attributed to a small misalignment of the setup for low atom flux.

pulse, $\bar{n}_P$, are subtracted from each count number to ensure that only photons emitted from one-and-the same atom are considered. We also correct for false triggers, i.e. noise counts signalling atoms which are not present, and the quantum efficiency of the photodetection. Note that the M conditioning photodetections are not counted twice, since we subtract $\delta_{\Delta k,0}$ from the calculated probabilities, with $\delta_{i,j} = 1$ for $i = j$ and $\delta_{i,j} = 0$ otherwise. Obviously, the probabilities for subsequent photon emissions decrease from pulse-to-pulse, since the efficiency of the photon generation depends on the location of the moving atom. It is highest in an antinode on the cavity axis and decreases if the atom moves away from this point. A simulation of the process, based on a numerical solution of the master equation, allows the calculation of the expected photon-emission probabilities averaged over the random trajectories of the atoms travelling through the cavity. This leads to the same qualitative results, but the experimentally determined emission probabilities are smaller than the expected ones. We attribute this discrepancy to the random distribution of the atom among its magnetic sublevels after recycling, which reduces the overall efficiency of photon generation. In our numerical simulation, this has been neglected. A more rigorous analysis is beyond the scope of this paper. Another significant feature of the numerical analysis is the prediction of a single-photon generation efficiency of 61.6% for an atom which is optimally coupled to the cavity. Therefore we expect that the present scheme is able to produce single photons in a highly efficient way provided the atom is held at rest by, e.g., a dipole-force trap [22]–[24].

4. Summary

We have statistically analysed the photon stream emitted from a strongly coupled atom–cavity system in response to laser pulses that adiabatically drive Raman transitions between two atomic

9

states. The laser pulses excite one branch of the transition, while the vacuum field of the cavity stimulates the other branch. The system operates as a non-stationary single-photon source, since the atoms enter and leave the mode volume randomly, with a maximum number of about seven successive photon emissions per atom. Without any *a priori* knowledge of the state of the system, antibunching is observed, which indicates that a single atom emits photons one at a time. Furthermore, a preselection has been applied to restrict the analysis to time intervals where the presence of an atom is assured. This gives a sub-Poissonian photon statistics with $g^{(2)}(0) < 1$. Our setup therefore operates as a deterministic single-photon emitter, although the atom statistics is Poissonian.

Acknowledgments

References

[1] Bouwmeester D, Ekert A and Zeilinger A ed 2000 *The Physics of Quantum Information* (Berlin: Springer)
[2] Knill E, Laflamme R and Milburn G J 2001 *Nature* **409** 46
[3] DiVincenzo D P 2000 *Fortschr. Phys.* **48** 771
[4] van Enk S, Cirac J I, Zoller P, Kimble H J and Mabuchi H 1997 *J. Mod. Opt.* **44** 1727
[5] Cirac J I, Zoller P, Kimble H J and Mabuchi H 1997 *Phys. Rev. Lett.* **78** 3221
[6] Kuhn A, Hennrich M, Bondo T and Rempe G 1999 *Appl. Phys. B* **69** 373
[7] Kuhn A and Rempe G 2002 *Experimental Quantum Computation and Information* vol 148, ed F De Martini and C Monroe (Amsterdam: IOS Press) p 37
[8] Hennrich M, Kuhn A and Rempe G 2003 *J. Mod. Opt.* **50** 936
[9] Kuhn A, Hennrich M and Rempe G 2003 *Quantum Information Processing* ed T Beth and G Leuchs (Berlin: Wiley-VCH) p 182
[10] Maître X, Hagley E, Nogues G, Wunderlich C, Goy P, Brune M, Raimond J-M and Haroche S 1997 *Phys. Rev. Lett.* **79** 769
[11] Brattke S, Varcoe B T H and Walther H 2001 *Phys. Rev. Lett.* **86** 3534
[12] Hennrich M, Legero T, Kuhn A and Rempe G 2000 *Phys. Rev. Lett.* **85** 4872
[13] Kuhn A, Hennrich M and Rempe G 2002 *Phys. Rev. Lett.* **89** 067901
[14] Kurtsiefer C, Mayer S, Zarda P and Weinfurter H 2000 *Phys. Rev. Lett.* **85** 290
[15] Beveratos A, Brouri R, Gacoin T, Poizat J-P and Grangier P 2001 *Phys. Rev. A* **64** 061802
[16] Santori C, Fattal D, Vučković J, Solomon G S and Yamamoto Y 2002 *Nature* **419** 594
[17] Kimble H J 2003 *Phys. Rev. Lett.* **90** 249801
[18] Kuhn A, Hennrich M and Rempe G 2003 *Phys. Rev. Lett.* **90** 249802
[19] Vitanov N V, Fleischhauer M, Shore B W and Bergmann K 2001 *Adv. At. Mol. Opt. Phys.* **46** 55
[20] Hanbury-Brown R and Twiss R Q 1956 *Nature* **178** 1046
[21] Walls D F and Milburn G J 1994 *Quantum Optics* (Berlin: Springer)
[22] Kuhr S, Alt W, Schrader D, Müller M, Gomer V and Meschede D 2001 *Science* **293** 278
[23] Sauer J A, Fortier K M, Chang M S, Hamley C D and Chapman M S 2003 *Preprint* quant-ph/0309052
[24] McKeever J, Boca A, Boozer A D, Buck J R and Kimble H J 2003 *Nature* **425** 268

Quantum Beat of Two Single Photons

Thomas Legero, Tatjana Wilk, Markus Hennrich, Gerhard Rempe, and Axel Kuhn

Max-Planck-Institut für Quantenoptik, Hans-Kopfermann-Strasse 1, D-85748 Garching, Germany
(Received 15 March 2004; published 13 August 2004)

The interference of two single photons impinging on a beam splitter is measured in a time-resolved manner. Using long photons of different frequencies emitted from an atom-cavity system, a quantum beat with a visibility close to 100% is observed in the correlation between the photodetections at the output ports of the beam splitter. The time dependence of the beat amplitude reflects the coherence properties of the photons. Most remarkably, simultaneous photodetections are never observed, so that a temporal filter allows one to obtain perfect two-photon coalescence even for nonperfect photons.

The quantum nature of light impressively manifests itself in the fourth-order interference of two identical and mutually coherent single photons that impinge simultaneously on a beam splitter (BS). The photons coalesce and both leave the beam splitter in the same direction. Hong *et al.* first demonstrated this phenomenon with photon pairs from parametric down-conversion [1], and Santori *et al.* used the same effect to show the indistinguishability of independently generated photons that are successively emitted from a quantum dot embedded in a microcavity [2]. In all experiments performed so far, the photons were short compared to the time resolution of the employed detectors, so that interference phenomena were observed only as a function of the spatial delay between the interfering photons [3].

To investigate the temporal dynamics behind this interference phenomenon, we now use an adiabatically driven, strongly coupled atom-cavity system as a single-photon emitter [4–7]. Photons are generated by a unitary process, so that their temporal and spectral properties can be arbitrarily adjusted. In fact, the duration of the photons used in our experiment exceeds the time resolution of the employed single-photon counters by 3 orders of magnitude. This allows for the first time an experimental investigation of fourth-order interference phenomena in a time-resolved manner with photons arriving simultaneously at the beam splitter [8]. We find perfect interference even if the frequency difference between the two photons exceeds their bandwidths. This surprising result is very robust against all kinds of fluctuation and opens up new possibilities in all-optical quantum information processing [9].

The principal scheme of the experiment is sketched in Fig. 1. We consider an initial situation where two single photons in modes A and B impinge simultaneously on a BS. In front of the BS, we distinguish states $|1_{A,B}\rangle$ and $|0_{A,B}\rangle$, where a photon is either present or has been annihilated by transmission through the BS and subsequent detection by detector C or D. Mode A is an extended spatiotemporal photonic field mode, traveling along an optical fiber, which initially carries a photon. The photon

in mode B emerges from a strongly coupled atom-cavity system, which is driven in a way that the photon is deterministically generated by a vacuum-stimulated Raman transition between two long-lived atomic states [4,5]. In particular, the photon emitted from B matches the photon from A. The initial state of the total system, A and B, is given by the product state $|\Psi_i\rangle = |1_A 1_B\rangle$. The effect of a first photodetection in the output mode C or D at time t_0 is evaluated by applying the respective photon annihilation operator $\hat{a}_C$ or $\hat{a}_D$ to $|\Psi_i\rangle$. The two operators behind the BS are linked to the two operators before the BS by the unitary relation

$$\hat{a}_{C,D} = (\hat{a}_B \pm \hat{a}_A)/\sqrt{2}, \qquad (1)$$

where $\hat{a}_A$ and $\hat{a}_B$ are operators that remove one photon from A and B, respectively. As the detection reveals no which-way information, the system is projected into one of the two superposition states,

$$|\Psi_\pm(t_0)\rangle = \hat{a}_{C,D}|1_A 1_B\rangle = (|1_A, 0_B\rangle \pm |0_A, 1_B\rangle)/\sqrt{2}, \quad (2)$$
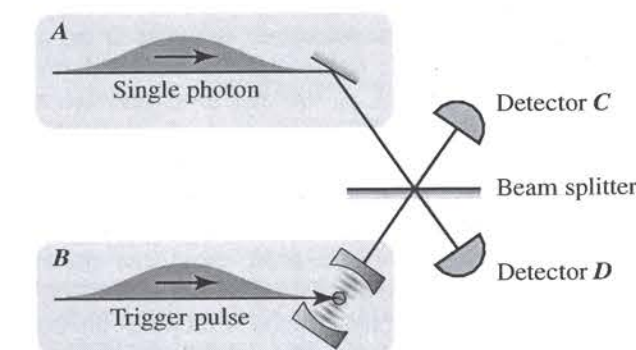
depending on which detector clicks.

FIG. 1 (color online). Fourth-order interference. Single photons emerge from A and B and impinge simultaneously on a beam splitter. The photons are so long that they give rise to distinct photodetections. The first detection projects the system into a superposition, which then determines the probability of detecting the second photon with either one or the other detector.

    0031-9007/04/93(7)/070503(4)$22.50

The initial purity of the superposition, i.e., the balance between its two parts and their phase coherence, and, hence, also the mutual coherence time of the interfering photons, can now be measured by monitoring the time evolution of $|\Psi_\pm\rangle$. Moreover, the superposition can be systematically varied by controlling the relative phase between its two parts. The latter is achieved by introducing a small frequency difference between the photons from A and B. Assume that the photon in the fiber has a frequency difference Δ with respect to the photon from the cavity. In this case, the two components of $|\Psi_\pm\rangle$ evolve with different frequencies, so that after a time τ, the two states have acquired a phase difference $\Delta\tau$. The new state then reads

$$|\Psi_\pm(t_0+\tau)\rangle = (|1_A, 0_B\rangle \pm e^{i\Delta\tau}|0_A, 1_B\rangle)/\sqrt{2}. \quad (3)$$

This state can be monitored by photodetections. The probability to count a second photon with either detector C or D, as a function of the relative phase $\Delta\tau$, reads

$$\langle\Psi_\pm|\hat{a}_C^\dagger \hat{a}_C|\Psi_\pm\rangle = \tfrac{1}{2}(1 \pm \cos\Delta\tau)$$
$$\text{and} \quad \langle\Psi_\pm|\hat{a}_D^\dagger \hat{a}_D|\Psi_\pm\rangle = \tfrac{1}{2}(1 \mp \cos\Delta\tau). \quad (4)$$

In a photon correlation experiment, a frequency difference between the interfering photons therefore results in a quantum-beat signal in the correlation function that oscillates with frequency Δ. Moreover, Eq. (4) implies that the first and second photon hit the same detector for $\Delta = 0$. This corresponds to the well-known behavior of two indistinguishable photons that impinge simultaneously on a BS [1,2]. However, in the present case, the two photodetections can have a time delay that can be as large as the duration of the interfering photons. Nevertheless, perfect two-photon coalescence is expected. Another remarkable consequence from Eq. (3) is that the initial phase difference between its two parts, induced by the first photodetection, is either 0 or π. Therefore, the beat starts to oscillate at zero with the detection of a first photon, so that the cross-correlation function between the two BS output ports shows fringes with a visibility of 100%. This distinguishes the present situation dramatically from the situation of two interfering coherent fields with frequency difference Δ that are superposed on a BS. In the latter case, the cross-correlation function would oscillate with a fringe visibility not exceeding 50%, since photodetections do not influence the relative phase of the coherent fields. The present scheme is also different from other experiments, where quantum state reduction has been observed in optical cavity QED [10,11]. In these experiments, the detection of a photon changes the state of a single system, whereas in the present case, the relative phase of two distinct modes, A and B, is determined.

We emphasize that the above way of calculating joint photodetection probabilities is strongly simplified. A

more detailed analysis that comes to the same conclusions can be found in Ref. [8].

The experimental setup is sketched in Fig. 2(a). ^{85}Rb atoms released from a magneto-optical trap fall with 2 m/s through a cavity of finesse $F = 60,000$ with $(g_{max}, \kappa, \gamma)/2\pi = (3.1, 1.25, 3.0)$ MHz, where g_{max} is the optimal atom-cavity coupling constant, and κ and γ are the field decay rates of cavity and atom, respectively. The atoms enter one at a time with a probability that is 66 times higher than the probability of having more atoms. Each atom is prepared in $|e\rangle \equiv |5S_{1/2}, F=3\rangle$, while the cavity is resonant with the transition between $|g\rangle \equiv |5S_{1/2}, F=2\rangle$ and $|x\rangle \equiv |5P_{3/2}, F=3\rangle$. The atom experiences a sequence of laser pulses that alternate between triggering single-photon emissions and repumping the atom to state $|e\rangle$: The 2 μs long trigger pulses are resonant with the $|e\rangle \leftrightarrow |x\rangle$ transition and their Rabi
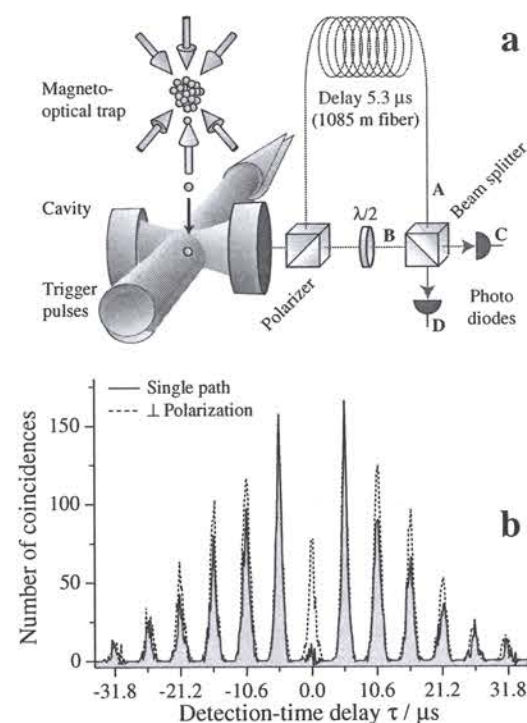

FIG. 2 (color online). Atoms and photons. (a) Triggered by laser pulses, an atom-cavity system emits unpolarized single photons. They are randomly directed by a polarizing beam splitter along two paths towards a nonpolarizing beam splitter (BS). A photon traveling along path A gets delayed so that it impinges on the BS simultaneously with a subsequent photon that travels along path B. (b) Number of coinciding photodetections in the two output ports as a function of the time difference between the detections: If only a single path is open, a Hanbury-Brown–Twiss measurement of the intensity correlation is performed, showing antibunching (solid line). If both paths are open but have perpendicular polarization, no interference takes place and the BS randomly directs the photons to C and D. This leads to coincidences at $\tau \approx 0$ (dashed line). All traces result from a convolution with a 48 ns wide square time-bin function.

frequency increases linearly to $\Omega_{max}/2\pi = 17.8$ MHz. In connection with the vacuum field of the cavity stimulating the $|x\rangle \leftrightarrow |g\rangle$ transition, these pulses adiabatically drive a stimulated Raman transition to $|g\rangle$. This transition goes hand in hand with a photon emission. Between two emissions, another laser pumps the atom from $|g\rangle$ to $|x\rangle$, from where it decays back to $|e\rangle$. This is complemented by a π-polarized laser driving the transition $|5S_{1/2}, F=3\rangle \leftrightarrow |5P_{3/2}, F=2\rangle$ to produce a high degree of spin polarization in $m_F = \pm 3$, with a large coupling to the cavity. To discard the photons emerging during this process, the detectors are electronically gated. This leads to a modulation of the dark-count rate and, hence, to a triangular modulation of the background contribution to all correlation functions measured with detectors C and D, with maxima showing an average number of 3.2 correlations/48 ns. All data shown here have been corrected for this periodic background.

We now consider the case where the atom-cavity system emits two photons, one after the other, with a time separation of 5.3 μs, deliberately introduced by the periodicity of our trigger pulse sequence. We suppose that the first photon travels along an optical fiber (mode A) and hits a 50:50 BS at the fiber output at the same time as the second photon, provided the latter comes directly from the cavity (mode B). To characterize the system, we first close the fiber, so that photons impinge only in mode B. For this situation, Fig. 2(b) shows the intensity correlation function, measured with detectors C and D, as a function of the time difference τ between photodetections as a solid line. The central peak is missing; i.e., the light shows strong antibunching and photons are emitted one by one [4]. Next, both paths to the BS are opened, so that photons can impinge simultaneously on the BS. Interference is suppressed by adjusting the $\lambda/2$ retardation plate at input port B so that the two light fields are polarized perpendicular to each other (dashed line). In this case, each photon is randomly directed onto one of the detectors, C or D. This leads to a nonvanishing correlation signal at $\tau \approx 0$, which is a factor of 2 smaller than the neighboring peaks at $\tau = \pm 5.3$ μs. The central peak has a duration of 640 ns (half width at $1/e$ maximum), which comes from the convolution of two 450 ns long single photons (half width at $1/e$ maximum of the intensity). In the following, the signal obtained for perpendicularly polarized photons is used as a reference, since any interference leads to a significant deviation. Note that all the experimental traces presented here are not sensitive to photon losses, since only measured coincidences contribute. Moreover, they can be compared without normalization, since data was always recorded until 980 coincidences were obtained in the correlation peaks at $\tau = \pm 5.3$ μs. This required loading and releasing atoms from the magneto-optical trap about 10^5 times.

Experimental results obtained for parallel polarization are displayed in Fig. 3(a). The photons interfere and the

first photodetection reveals no which-way information. Therefore, the system is projected into the superposition state $|\Psi_\pm\rangle$. In contrast to the expectations from the above discussion, the correlation signal does not vanish completely, in particular, for nonzero detection-time delay $\tau = 0$. Instead, a pronounced minimum is observed around $\tau = 0$. We interpret the depth of this minimum as a measure of the initial purity of the superposition state, and we attribute its limited width to the average mutual dephasing of the interfering photons (see below). Moreover, as shown in Fig. 3(b), we resolve a pronounced oscillation of the correlation function, starting with a minimum at $\tau = 0$, when a frequency difference of $\Delta/2\pi = 3$ MHz is introduced between the interfering photons. The first maxima of the oscillation are found at $|\tau| \approx \pi/\Delta$, where the two parts of $|\Psi_\pm\rangle$ have acquired a phase difference of $\pm\pi$. If the photons are detected with this time difference, they are registered by different detectors and give rise to a coincidence count. Therefore, the
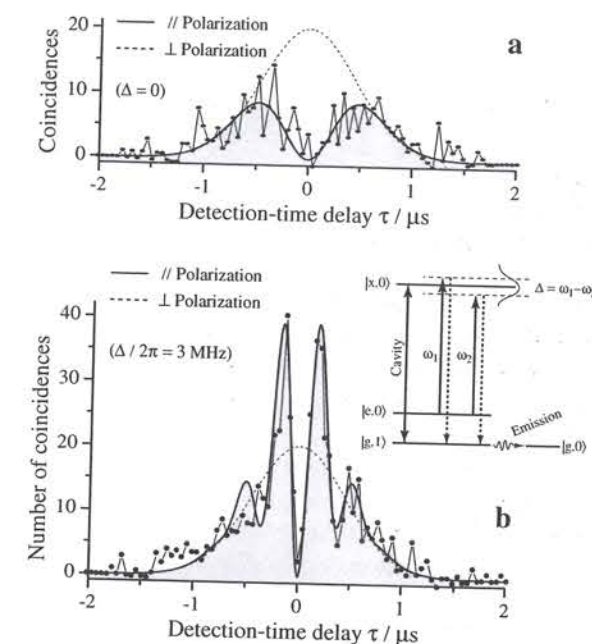

FIG. 3. Quantum beat. Number of coinciding photodetections as a function of the time difference τ between the detections [only the central peak is shown; see Fig. 2(b)]. Both paths are open and have parallel polarization (circles). The solid lines represent a numerical fit to the data [8]. A Gaussian fit to the reference signal (perpendicular polarization, dashed line) is also shown. (a) Photons of identical frequencies lead to a 460 ns wide central minimum. This lack of coincidences is caused by coalescing photons that leave the BS through the same port. Depth and width of the minimum indicate the initial purity of the superposition and the mutual coherence time of the photons, respectively. (b) The atom-cavity system is driven by a sequence of laser pulses with a frequency difference $\Delta = |\omega_1 - \omega_2| = 2\pi \times 3$ MHz between consecutive pulses (see level scheme). This gives rise to a frequency difference between consecutive photon emissions, which leads to a quantum beat in the correlation function starting at $\tau = 0$.

number of coincidences in these maxima exceeds the reference level, measured with perpendicular polarization, by a factor of 2. This underpins the phase coherence of the whole process and shows that it is possible to arbitrarily adjust the relative phase between the two parts of $|\Psi_\pm\rangle$. The initial purity of the superposition and the balance between its two parts is characterized by the visibility of the beat signal at $\tau = 0$. This visibility exceeds 90%, indicating that the superposition is nearly perfect.

The mutual coherence time of the interfering photons is obtained from the damping of the quantum beat or, alternatively, from the width of the two-photon interference dip. In both cases, a coherence time of 460 ns (half width at $1/e$ dip depth) is observed, which exceeds the 64 ns decay time of the cavity, as well as the 27 ns lifetime of the atom's excited state. Hence, the intrinsic lifetimes do not limit the coherence. However, for perfectly transform limited photons, one would expect to see no decrease of the quantum-beat visibility for $\Delta \neq 0$, and no correlation at all for $\Delta = 0$. This is obviously not the case—a numerical fit to the measured data based on an analytical model [8] (solid lines in Fig. 3) shows that the observed coherence time can be explained by an inhomogeneous broadening of $\delta\omega/2\pi = 690$ kHz, which exceeds the 350 kHz bandwidth of transform limited photons. No specific broadening mechanism could be identified, and therefore we attribute this to several technical reasons: static and fluctuating magnetic fields affect the energies of the magnetic substates and spread the photon frequencies over a range of 160 kHz, and the trigger laser has a linewidth of 50 kHz, which is mapped to the photons. Moreover, diabatically generated photons lead to an additional broadening.

To summarize, we have observed the fourth-order interference of two individual photons impinging on a beam splitter in a time-resolved manner. With photons of different frequencies, a quantum beat is found in the correlation between the photodetections at the output ports of the beam splitter. This beat oscillates with the frequency difference of the interfering photons. The interference fringes are visible only for photons that are detected within their mutual coherence time. Moreover, our measurements reveal that identical photons coalesce; i.e., they leave the beam splitter as a pair, provided they do not dephase with respect to each other. Any deviation from perfect coalescence, observed for nonzero detection-time delay, can be attributed to a random dephasing due to an inhomogeneous broadening of the photon spectrum. We therefore conclude that a temporal filter, which accepts only time intervals between photodetections shorter than the mutual coherence time, is a way to obtain nearly perfect two-photon interference, even if the coherence properties of the photons are not ideal. This makes linear optical quantum computing [9] much more feasible with today's technology.

Moreover, we point out that the present experiment is formally equivalent to a setup composed of two independent atom-cavity systems, since the photon traveling along the optical fiber could as well be released directly from an independent (second) atom-cavity system. Provided the time the photons need to travel from the cavities to the detectors is much shorter than their mutual coherence time (as is in fact the case for mode B in our experiment), the first photodetection would establish an entanglement between the distant atom-cavity systems [12–15], since the states $|1_{A,B}\rangle$ and $|0_{A,B}\rangle$ refer in this case to these systems. This entanglement would live until it is destructively probed by a second photodetection. Our results therefore pave the way towards distributed quantum computing and teleportation of atomic quantum states [16,17].

[1] C. K. Hong, Z. Y. Ou, and L. Mandel, Phys. Rev. Lett. **59**, 2044 (1987).

[2] C. Santori, D. Fattal, J. Vučković, G. S. Solomon, and Y. Yamamoto, Nature (London) **419**, 594 (2000).

[3] Z. Y. Ou and L. Mandel, Phys. Rev. Lett. **61**, 54 (1988).

[4] A. Kuhn, M. Hennrich, and G. Rempe, Phys. Rev. Lett. **89**, 067901 (2002).

[5] M. Hennrich, T. Legero, A. Kuhn, and G. Rempe, Phys. Rev. Lett. **85**, 4872 (2000).

[6] A. Kuhn and G. Rempe, in *Experimental Quantum Computation and Information*, edited by F. D. Martini and C. Monroe (IOS Press, Amsterdam, 2002), Vol. 148, pp. 37–66.

[7] A. Kuhn, M. Hennrich, and G. Rempe, in *Quantum Information Processing*, edited by T. Beth and G. Leuchs (Wiley-VCH, Berlin, 2003), pp. 182–195.

[8] T. Legero, T. Wilk, A. Kuhn, and G. Rempe, Appl. Phys. B **77**, 797 (2003).

[9] E. Knill, R. Laflamme, and G. J. Milburn, Nature (London) **409**, 46 (2001).

[10] G. Rempe, R. J. Thompson, R. J. Brecha, W. D. Lee, and H. J. Kimble, Phys. Rev. Lett. **67**, 1727 (1991).

[11] G. T. Foster, L. A. Orozco, H. M. Castro-Beltran, and H. J. Carmichael, Phys. Rev. Lett. **85**, 3149 (2000).

[12] C. Cabrillo, J. I. Cirac, P. García-Fernández, and P. Zoller, Phys. Rev. A **59**, 1025 (1999).

[13] J. Hong and H.-W. Lee, Phys. Rev. Lett. **89**, 237901 (2002).

[14] X.-L. Feng, Z.-M. Zhang, X.-D. Li, S.-Q. Gong, and Z.-Z. Xu, Phys. Rev. Lett. **90**, 217902 (2003).

[15] D. E. Browne, M. B. Plenio, and S. F. Huelga, Phys. Rev. Lett. **91**, 067901 (2003).

[16] S. Bose, P. L. Knight, M. B. Plenio, and V. Vedral, Phys. Rev. Lett. **83**, 5158 (1999).

[17] S. Lloyd, M. S. Shahriar, J. H. Shapiro, and P. R. Hemmer, Phys. Rev. Lett. **87**, 167903 (2001).

Transition from Antibunching to Bunching in Cavity QED

Markus Hennrich,* Axel Kuhn, and Gerhard Rempe

Max-Planck-Institut für Quantenoptik, Hans-Kopfermann-Strasse 1, D-85748 Garching, Germany
(Received 4 June 2004; published 10 February 2005)

The photon statistics of the light emitted from an atomic ensemble into a single field mode of an optical cavity is investigated as a function of the number of atoms. The light is produced in a Raman transition driven by a pump laser and the cavity vacuum, and a recycling laser is employed to repeat this process continuously. For weak driving, a smooth transition from antibunching to bunching is found for about one intracavity atom. Remarkably, the bunching peak develops within the antibunching dip. The observed behavior is well explained by a model describing an ensemble of independent emitters.

The photon statistics of light reveals whether it originates from a classical or a quantum source like a single atom. These sources can be distinguished by their intensity correlation function, $g^{(2)}(\tau)$ [1]. Classical light fulfills the Cauchy-Schwarz inequality, $g^{(2)}(0) \geq g^{(2)}(\tau)$, whereas light that violates this inequality must be described by the laws of quantum physics. In this case, a local minimum at $\tau = 0$ is found, i.e. $g^{(2)}(0) < g^{(2)}(\tau)$, which is defined as antibunching [2]. First experiments demonstrating antibunching were performed with a weak beam of atoms [3]. Limitations imposed by number fluctuations [4] were later eliminated by using a single emitter [5–11]. The deterministic control of the nonclassical light radiated by a single emitter [12–18] has interesting applications, e.g., in quantum information processing. Classical bunching, $g^{(2)}(0) > g^{(2)}(\tau)$, has been observed in the fluorescence of a large number of independently radiating atoms as early as 1956 [19], and has regained new interest in the context of cold-atom physics [20,21].

A smooth transition between antibunching and bunching is expected if the number of atoms gradually increases. Such a transition has not been observed so far, since a good photon-collection efficiency, and thus a large solid angle, is essential to obtain a photon count rate large enough to discriminate the antibunching signal from background noise, while spatial coherence of the detected light is required to observe bunching. For a distributed ensemble of atoms, this calls for a small solid angle. Obviously, these two requirements contradict each other, making the experiment difficult in the interesting regime of just a few radiating particles.

In the work presented here, all emitters are coupled to a single mode in a high-finesse optical cavity. Only the light in this mode is investigated, so that spatial coherence is granted. At the same time, the enhanced spontaneous emission into the cavity mode gives a good photon-collection efficiency. The experiment is performed in a regime where an emitted photon leaves the cavity before being reabsorbed and before affecting other atoms. Vacuum-Rabi oscillations and collective effects are there-

fore largely suppressed. Moreover, the laser beams exciting the atoms are running perpendicular to the cavity axis, so that the photon statistics of the light emitted from the cavity is not the result of a driving field interfering with the atomic emission, as for an axially excited cavity [22–24]. It follows that all requirements to observe the transition between antibunching and bunching for independently fluorescing atoms with one-and-the-same experimental setup are fulfilled. In fact, we find that, with an increasing number of atoms, a strong bunching peak (demonstrating the wave character of the light) develops inside the antibunching minimum at $\tau = 0$ (characterizing the particle nature of the light).

Figure 1 illustrates the setup. A cloud of ^{85}Rb atoms released from a magneto-optical trap (MOT) falls through a 1 mm long optical cavity of finesse $F = 60\,000$. The average number of atoms simultaneously interacting with the cavity, $\bar{N}$, is freely adjustable by the loading time of the trap between $\bar{N} = 0$ and $\bar{N} \approx 140$. In the cavity, the atoms are exposed to two laser beams. The pump laser continu-
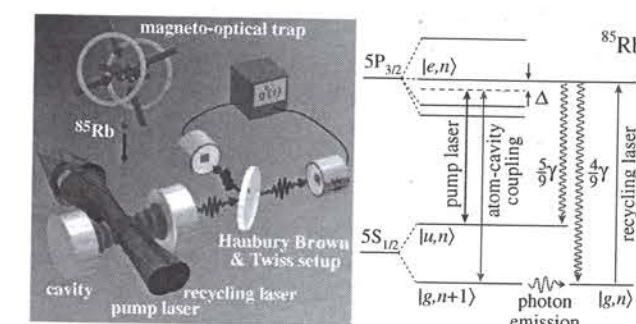

FIG. 1 (color online). Scheme of the experiment. Left: The setup shows that atoms are released from a magneto-optical trap and fall through a cavity 20 cm below with a velocity of 2 m/s. Each atom interacts with the TEM$_{00}$ mode of the cavity for about 20 μs and is exposed to pump and recycling laser beams. The light emitted from the cavity is registered by a pair of photodiodes. Right: Relevant levels and transitions in ^{85}Rb. The atomic states $|u\rangle$, $|e\rangle$, and $|g\rangle$ are involved in the Raman process, and the states $|n\rangle$ and $|n + 1\rangle$ denote the cavity's photon number.

ously drives the transition between the state $|u\rangle \equiv |5S_{1/2}(F=3)\rangle$ and the excited state $|e\rangle \equiv |5P_{3/2}(F=3)\rangle$ with Rabi frequency Ω_P, while the cavity couples $|e\rangle$ to the other hyperfine ground state, $|g\rangle \equiv |5S_{1/2}(F=2)\rangle$. Both fields are detuned by an amount Δ from the respective atomic transition so that they resonantly drive a Raman transition between $|u\rangle$ and $|g\rangle$ which also changes the intracavity photon number by one. At the same time, a recycling laser of Rabi frequency Ω_R resonantly drives the transition from $|g\rangle$ to $|e\rangle$, from where the atoms decay back to state $|u\rangle$. This closes the excitation loop and enables each atom to emit several photons on its way through the cavity. Because of the continuous driving, the Raman transitions are stochastic in contrast to the adiabatically driven Raman transition process reported in [15,25–27]. The dynamics of the system is determined by $(g_{max}, \kappa, \gamma, \Omega_P, \Omega_R, \Delta) = 2\pi \times (2.5, 1.25, 3.0, 7.6, 3.3, -20)$ MHz, where g_{max} is the cavity-induced coupling between states $|e, 0\rangle$ and $|g, 1\rangle$ for an atom optimally

FIG. 2 (color online). Intensity correlation, $g^{(2)}(\tau)$, as a function of the detection time delay, τ, for different values of the average atom number, $\bar{N}$. A transition from antibunching to bunching is observed for $\bar{N} \approx 1$. To adjust $\bar{N}$, we load the trap between 20 ms and 2.5 s. For each trace, we load and release atoms from the MOT 500 times and register photons during $\delta t = 8$ ms while the atom cloud traverses the cavity.

coupled to the cavity, and κ and γ are the field and polarization decay rates of the cavity and the atom, respectively. The maximum recycling rate is achieved when the transition between $|g\rangle$ and $|e\rangle$ is strongly saturated. In this case, both levels are equally populated leading to a recycling rate of $R_{max} = \frac{5}{9}\gamma = 2\pi \times 1.7$ MHz, where $\frac{5}{9}$ is the average branching ratio for a decay from $|e\rangle$ to $|u\rangle$. Therefore the recycling is always slower than the decay of the cavity excitation, 2κ. For the above value of Ω_R, the recycling is about 4 times slower than the cavity decay, so that the cavity returns to the vacuum state before the next photon is placed into its mode from the same atom. Therefore nonclassical antibunching can be observed. The maximum effective Rabi frequency of the Raman process, $\Omega_{eff} = g_{max}\Omega_P/\Delta = 2\pi \times 0.95$ MHz, is also smaller than the cavity decay rate. Therefore the system is overdamped and shows no Rabi oscillations; i.e., both the reabsorption of emitted photons and the cavity-mediated interaction between different atoms are negligible. The cavity decay is mainly caused by the 100 ppm transmittance of one of the mirrors. Photons leave the cavity through this output coupler with a probability of 90%, and are detected by two photodiodes with 50% quantum efficiency that are placed at the output ports of a beam splitter. They form a Hanbury Brown and Twiss setup to measure the $g^{(2)}(\tau)$ intensity correlation function of the light. To avoid a limitation to a waiting-time distribution between successive photons, all photodetection times are registered and taken into account in the evaluation.

Figure 2 shows $g^{(2)}(\tau)$ for different settings of the atom flux. For an average atom number below one, $\bar{N} = 0.15$, it shows nonclassical antibunching, i.e., a local minimum at $\tau = 0$ in Fig. 2(a). Note that sub-Poissonian light with $g^{(2)}(0) < 1$ is not observed because the Poissonian statistics of the atomic cloud is mapped to the photon statistics. When the atom flux is increased to $\bar{N} > 1$, a transition to bunching, i.e., a local maximum at $\tau = 0$, is observed; see Figs. 2(b) and 2(c).

This transition from nonclassical light for $\bar{N} < 1$ to classical light for $\bar{N} > 1$ can be explained with a model [4] that describes an ensemble of independent emitters where the electric field of all atoms,

$$E(t) = \sum_{i=1}^{N(t)} E_i(t), \qquad (1)$$

is the sum of the fields radiated by the individual atoms, $E_i(t)$. Obviously, the individual fields interfere with the fields radiated by the other atoms. For independent emitters, correlations between the fields of different atoms can be neglected. Following [4] and provided the atom distribution is Poissonian with an average atom number $\bar{N}$ [28], the intensity correlation function reads

$$g^{(2)}(\tau) = 1 + |f(\tau)g_A^{(1)}(\tau)|^2 + f(\tau)g_A^{(2)}(\tau)/\bar{N}. \qquad (2)$$

It consists of three different contributions: (i) The constant term 1 stems from photons that are independently emitted by different atoms, i.e., it reflects the atom statistics which is directly mapped to the light. (ii) The bunching term, $|f(\tau)g_A^{(1)}(\tau)|^2$, with $g_A^{(1)}(\tau)$ the autocorrelation function of the electric field emitted by one atom and $f(\tau)$ given below [29], results from the beating of the light emitted by different atoms. Constructive or destructive interference leads to a fluctuating intensity [1]. If a photon is detected, constructive interference is likely and the probability for a second photodetection is increased. The opposite holds for destructive interference. The interference and the correlated behavior vanish if the two photodetections are separated by more than the coherence time. Therefore the bunching contribution decreases with the square of $g_A^{(1)}(\tau)$, whose $\frac{1}{e}$ decay defines the coherence time, τ_c. Note that this contribution does not depend on the number of atoms and therefore persists for very high atom flux. (iii) The antibunching term, $f(\tau)g_A^{(2)}(\tau)/\bar{N}$, with $g_A^{(2)}(\tau)$ the single-atom intensity correlation function, is attributed to the photons emitted from an individual atom. After a photon emission, the atom must be recycled to state $|u\rangle$ before it can emit another photon. This leads to antibunching. Because of the statistical nature of the recycling, photons are uncorrelated for large $|\tau|$, and $g_A^{(2)}(\tau \to \pm\infty)$ reaches 1. However, only photons emitted from one-and-the-same atom during its limited interaction time with the cavity contribute. The envelope function, $f(\tau)$, with $f(\tau \to \pm\infty) = 0$, takes this into account. Note that the antibunching term scales with the inverse average atom number, $1/\bar{N}$, and therefore vanishes for large $\bar{N}$.

The three contributions explain the observed transition from antibunching to bunching shown in Fig. 2(c): the antibunching contribution for $\bar{N} < 1$ vanishes with increasing atom number while the bunching contribution does not change. For a detailed comparison of this model with the experiment, we write the correlation function as

$$g^{(2)}(\tau, 1/\bar{N}) = A(\tau) + B(\tau)/\bar{N}, \text{ with}$$

$$|g_A^{(1)}(\tau)|^2 = \frac{A(\tau) - 1}{f^2(\tau)}, \qquad g_A^{(2)}(\tau) = \frac{B(\tau)}{f(\tau)}. \qquad (3)$$

For every value of τ, we can now obtain $A(\tau)$ and $B(\tau)$ from a linear fit to the experimentally observed $g^{(2)}(\tau, 1/\bar{N})$ as a function of $1/\bar{N}$ [30]. For the two examples $\tau = 0$ and $\tau = 1$ μs, Fig. 3(a) shows that this procedure is indeed justified, as the experimental data show a linear dependence on $1/\bar{N}$. The same result holds for other values of τ. The offset $A(\tau) = \lim_{\bar{N}\to\infty} g^{(2)}(\tau, 1/\bar{N})$ represents the two $\bar{N}$-independent contributions, (i) and (ii), from above, whereas the slope $B(\tau) = d(g^{(2)}(\tau, 1/\bar{N}))/d(1/\bar{N})$ determines the size of the antibunching contribution. A decomposition of $g^{(2)}(\tau, 1/\bar{N})$ into these contributions is shown in Fig. 3(b). $A(\tau)$ consists of the constant term 1 plus the bunching peak, whereas $B(\tau)$ shows an antibunching dip and decays with an envelope function $f(\tau)$ that is imposed by the atom transit.

Figure 4 shows the single-atom correlation functions deduced from $A(\tau)$ and $B(\tau)$ using the relations (3). These functions reveal the relevant experimental time scales. The minimum delay between two successive photons from one-and-the-same atom corresponds to the $1/e$ half width of the antibunching dip, $\tau_A = 430 \pm 10$ ns. This is much larger than the photon lifetime in the cavity, $\kappa^{-1}/2 = 64$ ns, so that successive photons from a single atom hardly overlap. From the decay of the field correlation function, $|g_A^{(1)}(\tau)|^2$, we calculate a coherence time of the emitted light of $\tau_c = 170 \pm 2$ ns (half $1/e^2$ width), larger than the decay time of the cavity field, $\kappa^{-1} = 128$ ns. This seemingly unexpected result is not surprising as the coherence properties are controlled by the photon-
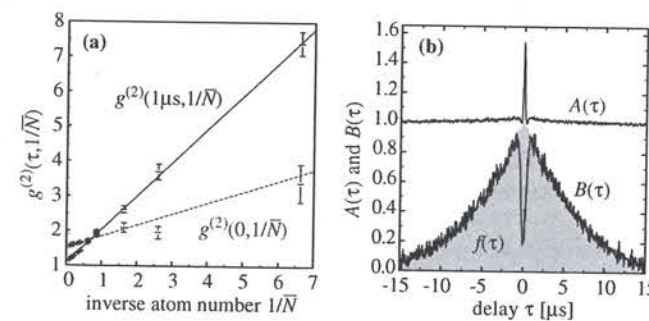

FIG. 3 (color online). (a) Decomposition of $g^{(2)}(\tau, 1/\bar{N})$: Linear-regression fit as a function of $1/\bar{N}$ for $\tau = 0$ and $\tau = 1$ μs. For each τ, the offset $A(\tau)$ and the slope $B(\tau)$ are obtained from such fits. (b) Bunching and antibunching contributions, $A(\tau)$ and $B(\tau)$, respectively. Modeling $B(\tau)$ for $|\tau| > 1.0$ μs yields the empirical envelope, $f(\tau) = \exp(-|\tau/6.5 \ \mu s|^{1.22})$ (shaded).
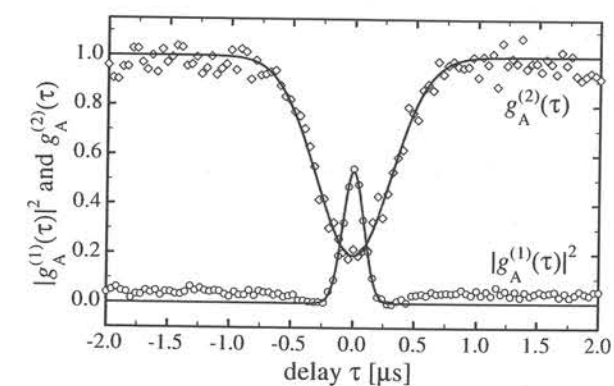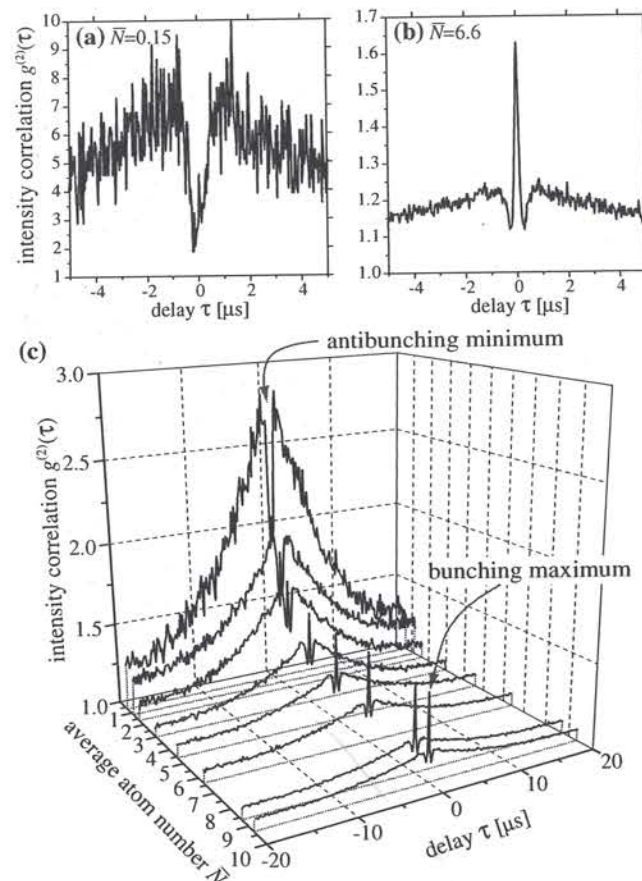

FIG. 4 (color online). Single-atom correlations, $|g_A^{(1)}(\tau)|^2$ and $g_A^{(2)}(\tau)$, deduced from $A(\tau)$, $B(\tau)$, and $f(\tau)$ using Eq. (3). The two contributions weighted according to Eq. (2) determine the observed photon statistics, $g^{(2)}(\tau)$, as shown in Fig. 2. Because of a small cross talk between $g_A^{(2)}(\tau)$ and $|g_A^{(1)}(\tau)|^2$, the latter stays larger than zero for values of τ smaller than the atom-cavity interaction time.

ously drives the transition between the state $|u\rangle \equiv |5S_{1/2}(F=3)\rangle$ and the excited state $|e\rangle \equiv |5P_{3/2}(F=3)\rangle$ with Rabi frequency Ω_P, while the cavity couples $|e\rangle$ to the other hyperfine ground state, $|g\rangle \equiv |5S_{1/2}(F=2)\rangle$. Both fields are detuned by an amount Δ from the respective atomic transition so that they resonantly drive a Raman transition between $|u\rangle$ and $|g\rangle$ which also changes the intracavity photon number by one. At the same time, a recycling laser of Rabi frequency Ω_R resonantly drives the transition from $|g\rangle$ to $|e\rangle$, from where the atoms decay back to state $|u\rangle$. This closes the excitation loop and enables each atom to emit several photons on its way through the cavity. Because of the continuous driving, the Raman transitions are stochastic in contrast to the adiabatically driven Raman transition process reported in [15,25–27]. The dynamics of the system is determined by $(g_{max}, \kappa, \gamma, \Omega_P, \Omega_R, \Delta) = 2\pi \times (2.5, 1.25, 3.0, 7.6, 3.3, -20)$ MHz, where g_{max} is the cavity-induced coupling between states $|e,0\rangle$ and $|g,1\rangle$ for an atom optimally

coupled to the cavity, and κ and γ are the field and polarization decay rates of the cavity and the atom, respectively. The maximum recycling rate is achieved when the transition between $|g\rangle$ and $|e\rangle$ is strongly saturated. In this case, both levels are equally populated leading to a recycling rate of $R_{max} = \frac{5}{9}\gamma = 2\pi \times 1.7$ MHz, where $\frac{5}{9}$ is the average branching ratio for a decay from $|e\rangle$ to $|u\rangle$. Therefore the recycling is always slower than the decay of the cavity excitation, 2κ. For the above value of Ω_R, the recycling is about 4 times slower than the cavity decay, so that the cavity returns to the vacuum state before the next photon is placed into its mode from the same atom. Therefore nonclassical antibunching can be observed. The maximum effective Rabi frequency of the Raman process, $\Omega_{eff} = g_{max}\Omega_P/\Delta = 2\pi \times 0.95$ MHz, is also smaller than the cavity decay rate. Therefore the system is overdamped and shows no Rabi oscillations; i.e., both the reabsorption of emitted photons and the cavity-mediated interaction between different atoms are negligible. The cavity decay is mainly caused by the 100 ppm transmittance of one of the mirrors. Photons leave the cavity through this output coupler with a probability of 90%, and are detected by two photodiodes with 50% quantum efficiency that are placed at the output ports of a beam splitter. They form a Hanbury Brown and Twiss setup to measure the $g^{(2)}(\tau)$ intensity correlation function of the light. To avoid a limitation to a waiting-time distribution between successive photons, all photodetection times are registered and taken into account in the evaluation.

Figure 2 shows $g^{(2)}(\tau)$ for different settings of the atom flux. For an average atom number below one, $\bar{N} = 0.15$, it shows nonclassical antibunching, i.e., a local minimum at $\tau = 0$ in Fig. 2(a). Note that sub-Poissonian light with $g^{(2)}(0) < 1$ is not observed because the Poissonian statistics of the atomic cloud is mapped to the photon statistics. When the atom flux is increased to $\bar{N} > 1$, a transition to bunching, i.e., a local maximum at $\tau = 0$, is observed; see Figs. 2(b) and 2(c).

This transition from nonclassical light for $\bar{N} < 1$ to classical light for $\bar{N} > 1$ can be explained with a model [4] that describes an ensemble of independent emitters where the electric field of all atoms,

$$E(t) = \sum_{i=1}^{N(t)} E_i(t), \qquad (1)$$

is the sum of the fields radiated by the individual atoms, $E_i(t)$. Obviously, the individual fields interfere with the fields radiated by the other atoms. For independent emitters, correlations between the fields of different atoms can be neglected. Following [4] and provided the atom distribution is Poissonian with an average atom number $\bar{N}$ [28], the intensity correlation function reads

$$g^{(2)}(\tau) = 1 + |f(\tau)g_A^{(1)}(\tau)|^2 + f(\tau)g_A^{(2)}(\tau)/\bar{N}. \qquad (2)$$

FIG. 2 (color online). Intensity correlation, $g^{(2)}(\tau)$, as a function of the detection time delay, τ, for different values of the average atom number, $\bar{N}$. A transition from antibunching to bunching is observed for $\bar{N} \approx 1$. To adjust $\bar{N}$, we load the trap between 20 ms and 2.5 s. For each trace, we load and release atoms from the MOT 500 times and register photons during $\delta t = 8$ ms while the atom cloud traverses the cavity.

It consists of three different contributions: (i) The constant term 1 stems from photons that are independently emitted by different atoms, i.e., it reflects the atom statistics which is directly mapped to the light. (ii) The bunching term, $|f(\tau)g_A^{(1)}(\tau)|^2$, with $g_A^{(1)}(\tau)$ the autocorrelation function of the electric field emitted by one atom and $f(\tau)$ given below [29], results from the beating of the light emitted by different atoms. Constructive or destructive interference leads to a fluctuating intensity [1]. If a photon is detected, constructive interference is likely and the probability for a second photodetection is increased. The opposite holds for destructive interference. The interference and the correlated behavior vanish if the two photodetections are separated by more than the coherence time. Therefore the bunching contribution decreases with the square of $g_A^{(1)}(\tau)$, whose $\frac{1}{e}$ decay defines the coherence time, τ_c. Note that this contribution does not depend on the number of atoms and therefore persists for very high atom flux. (iii) The antibunching term, $f(\tau)g_A^{(2)}(\tau)/\bar{N}$, with $g_A^{(2)}(\tau)$ the single-atom intensity correlation function, is attributed to the photons emitted from an individual atom. After a photon emission, the atom must be recycled to state $|u\rangle$ before it can emit another photon. This leads to antibunching. Because of the statistical nature of the recycling, photons are uncorrelated for large $|\tau|$, and $g_A^{(2)}(\tau \to \pm\infty)$ reaches 1. However, only photons emitted from one-and-the-same atom during its limited interaction time with the cavity contribute. The envelope function, $f(\tau)$, with $f(\tau \to \pm\infty) = 0$, takes this into account. Note that the antibunching term scales with the inverse average atom number, $1/\bar{N}$, and therefore vanishes for large $\bar{N}$.

The three contributions explain the observed transition from antibunching to bunching shown in Fig. 2(c): the antibunching contribution for $\bar{N} < 1$ vanishes with increasing atom number while the bunching contribution does not change. For a detailed comparison of this model with the experiment, we write the correlation function as
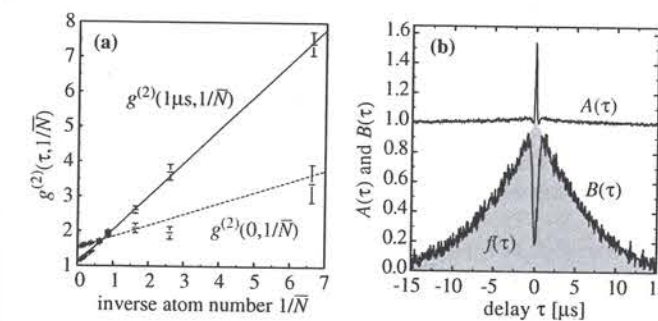

FIG. 3 (color online). (a) Decomposition of $g^{(2)}(\tau, 1/\bar{N})$: Linear-regression fit as a function of $1/\bar{N}$ for $\tau = 0$ and $\tau = 1$ μs. For each τ, the offset $A(\tau)$ and the slope $B(\tau)$ are obtained from such fits. (b) Bunching and antibunching contributions, $A(\tau)$ and $B(\tau)$, respectively. Modeling $B(\tau)$ for $|\tau| > 1.0$ μs yields the empirical envelope, $f(\tau) = \exp(-|\tau/6.5\ \mu s|^{1.22})$ (shaded).

$$g^{(2)}(\tau, 1/\bar{N}) = A(\tau) + B(\tau)/\bar{N}, \text{ with}$$

$$|g_A^{(1)}(\tau)|^2 = \frac{A(\tau)-1}{f^2(\tau)}, \qquad g_A^{(2)}(\tau) = \frac{B(\tau)}{f(\tau)}. \qquad (3)$$

For every value of τ, we can now obtain $A(\tau)$ and $B(\tau)$ from a linear fit to the experimentally observed $g^{(2)}(\tau, 1/\bar{N})$ as a function of $1/\bar{N}$ [30]. For the two examples $\tau = 0$ and $\tau = 1$ μs, Fig. 3(a) shows that this procedure is indeed justified, as the experimental data show a linear dependence on $1/\bar{N}$. The same result holds for other values of τ. The offset $A(\tau) = \lim_{\bar{N} \to \infty} g^{(2)}(\tau, 1/\bar{N})$ represents the two $\bar{N}$-independent contributions, (i) and (ii), from above, whereas the slope $B(\tau) = d(g^{(2)}(\tau, 1/\bar{N}))/d(1/\bar{N})$ determines the size of the antibunching contribution. A decomposition of $g^{(2)}(\tau, 1/\bar{N})$ into these contributions is shown in Fig. 3(b). $A(\tau)$ consists of the constant term 1 plus the bunching peak, whereas $B(\tau)$ shows an antibunching dip and decays with an envelope function $f(\tau)$ that is imposed by the atom transit.

Figure 4 shows the single-atom correlation functions deduced from $A(\tau)$ and $B(\tau)$ using the relations (3). These functions reveal the relevant experimental time scales. The minimum delay between two successive photons from one-and-the-same atom corresponds to the $1/e$ half width of the antibunching dip, $\tau_A = 430 \pm 10$ ns. This is much larger than the photon lifetime in the cavity, $\kappa^{-1}/2 = 64$ ns, so that successive photons from a single atom hardly overlap. From the decay of the field correlation function, $|g_A^{(1)}(\tau)|^2$, we calculate a coherence time of the emitted light of $\tau_c = 170 \pm 2$ ns (half $1/e^2$ width), larger than the decay time of the cavity field, $\kappa^{-1} = 128$ ns. This seemingly unexpected result is not surprising as the coherence properties are controlled by the photon-
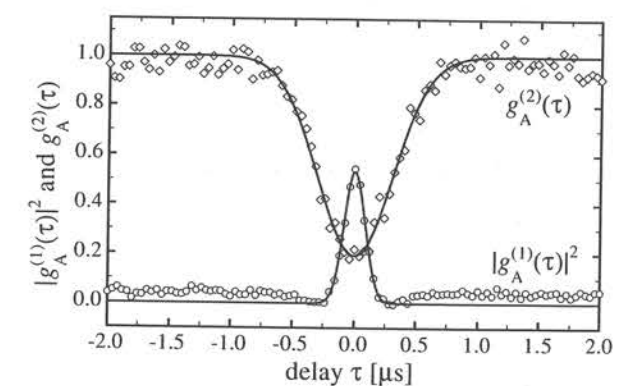

FIG. 4 (color online). Single-atom correlations, $|g_A^{(1)}(\tau)|^2$ and $g_A^{(2)}(\tau)$, deduced from $A(\tau)$, $B(\tau)$, and $f(\tau)$ using Eq. (3). The two contributions weighted according to Eq. (2) determine the observed photon statistics, $g^{(2)}(\tau)$, as shown in Fig. 2. Because of a small cross talk between $g_A^{(2)}(\tau)$ and $|g_A^{(1)}(\tau)|^2$, the latter stays larger than zero for values of τ smaller than the atom-cavity interaction time.

generating Raman process, which takes longer than the cavity decay time [31]. We also note that the peak amplitude of the field correlation function, $|g_A^{(1)}(0)|^2 = 0.53 \pm 0.01$, is very close to the expectation value for independently emitting atoms, which is $|g_A^{(1)}(0)|^2 = 0.5$ for unpolarized light [32].

The only small discrepancy from our expectations is that $g_A^{(2)}(\tau = 0)$ does not vanish completely as one would expect for the resonance fluorescence of single atoms [33]. Instead, we obtain $g_A^{(2)}(0) = 0.19 \pm 0.02$. This slight departure from perfect antibunching indicates that some atoms emit a second photon before the first photon has left the cavity. To assure that such collective effects do not dominate, we have verified that the photon number increases linearly with the average atom number in our parameter regime. Only with at least 100 atoms and drive Rabi frequencies raised by a factor of 3, does the average photon number show a slightly nonlinear increase with $\bar{N}$; i.e., a moderate amplification is found. However, no kink in the photon number is observed that would signal a lasing threshold. In fact, laser operation relies on a recycling rate much larger than the cavity decay rate, so that the photons remain long enough in the cavity to stimulate further emissions.

In conclusion, we have observed the transition from antibunching to bunching in the fluorescence light emitted from a high-finesse cavity with an increasing average number of atoms in the cavity. The cavity decay determines the fastest time scale, so that the atoms act as independent emitters. The agreement of our data with the predicted scaling behavior of the photon statistics is excellent, so that the single-atom correlation functions for antibunching and bunching, $g_A^{(2)}(\tau)$ and $g_A^{(1)}(\tau)$, respectively, can be extracted. It would be interesting to apply a similar analysis to a lasing atom-cavity system [7], where cooperative effects are expected to dominate the photon statistics.

---

*Present address: ICFO–Institut de Ciències Fotòniques, Jordi Girona 29, Nexus II, 08034 Barcelona, Spain.

[1] M.O. Scully and M. Zubairy, *Quantum Optics* (Cambridge University Press, Cambridge, U.K., 1997).

[2] L. Mandel and E. Wolf, *Optical Coherence and Quantum Optics* (Cambridge University Press, Cambridge, U.K., 1995), Chap. 14.7.3.

[3] H. J. Kimble, M. Dagenais, and L. Mandel, Phys. Rev. Lett. **39**, 691 (1977).

[4] H. J. Carmichael, P. Drummond, P. Meystre, and D. F. Walls, J. Phys. A **11**, L121 (1978).

[5] F. Diedrich and H. Walther, Phys. Rev. Lett. **58**, 203 (1987).

[6] V. Gomer, F. Strauch, B. Ueberholz, S. Knappe, and D. Meschede, Phys. Rev. A **58**, R1657 (1998).

[7] J. McKeever, A. Boca, A. D. Boozer, J. R. Buck, and H. J. Kimble, Nature (London) **425**, 268 (2003).

[8] F. De Martini, G. Di Giuseppe, and M. Marrocco, Phys. Rev. Lett. **76**, 900 (1996).

[9] P. Michler *et al.*, Nature (London) **406**, 968 (2000).

[10] C. Kurtsiefer, S. Mayer, P. Zarda, and H. Weinfurter, Phys. Rev. Lett. **85**, 290 (2000).

[11] A. Beveratos, R. Brouri, T. Gacoin, J.-P. Poizat, and P. Grangier, Phys. Rev. A **64**, 061802 (2001).

[12] B. Lounis and W. E. Moerner, Nature (London) **407**, 491 (2000).

[13] P. Michler *et al.*, Science **290**, 2282 (2000).

[14] C. Santori, D. Fattal, J. Vučković, G. S. Solomon, and Y. Yamamoto, Nature (London) **419**, 594 (2002).

[15] A. Kuhn, M. Hennrich, and G. Rempe, Phys. Rev. Lett. **89**, 067901 (2002).

[16] A. Beveratos *et al.*, Phys. Rev. Lett. **89**, 187901 (2002).

[17] J. McKeever *et al.*, Science **303**, 1992 (2004).

[18] M. Keller, B. Lange, K. Hayasaka, W. Lange, and H. Walther, Nature (London) **431**, 1075 (2004).

[19] R. Hanbury Brown and R. Q. Twiss, Nature (London) **178**, 1046 (1956).

[20] C. Jurczak *et al.*, Phys. Rev. Lett. **77**, 1727 (1996).

[21] S. Bali, D. Hoffmann, J. Simán, and T. Walker, Phys. Rev. A **53**, 3469 (1996).

[22] J. Carmichael, R. J. Brecha, and P. R. Rice, Opt. Commun. **82**, 73 (1991).

[23] G. Rempe, R. J. Thompson, R. J. Brecha, W. D. Lee, and H. J. Kimble, Phys. Rev. Lett. **67**, 1727 (1991).

[24] S. L. Mielke, G. T. Foster, and L. A. Orozco, Phys. Rev. Lett. **80**, 3948 (1998).

[25] M. Hennrich, T. Legero, A. Kuhn, and G. Rempe, Phys. Rev. Lett. **85**, 4872 (2000).

[26] A. Kuhn and G. Rempe, in *Experimental Quantum Computation and Information*, edited by F. De Martini and C. Monroe (IOS Press, Amsterdam, 2002), Vol. 148, pp. 37–66.

[27] M. Hennrich, A. Kuhn, and G. Rempe, J. Mod. Opt. **50**, 935 (2003).

[28] For $\tau \geq 1\ \mu s$, we assume that $g_A^{(2)} = 1$ and $g_A^{(1)} \approx 0$. With $f(1\ \mu s) \approx 1$, this leads to $g^{(2)}(1\ \mu s, \bar{N} = 1) \approx 2$. This value is used to calibrate the atom flux leading to $\bar{N} = 1$. Relative to this calibration, $\bar{N}$ is then adjusted by laser-induced fluorescence.

[29] H. J. Kimble, M. Dagenais, and L. Mandel, Phys. Rev. A **18**, 201 (1978).

[30] Variations of the atom density lead to a small modulation of $g^{(2)}(\tau)$ in the millisecond regime. This contribution was subtracted to prevent a falsification of the fit.

[31] T. Legero, T. Wilk, M. Hennrich, G. Rempe, and A. Kuhn, Phys. Rev. Lett. **93**, 070503 (2004).

[32] With $|g_A^{(1)}(0)|^2 = 1$ for each polarization mode, and uncorrelated orthogonal modes (in both ways), the average of these four contributions leads to $|g_A^{(1)}(0)|^2 = 0.5$.

[33] H. J. Carmichael and D. F. Walls, J. Phys. B **9**, 1199 (1976).

Time-Resolved and State-Selective Detection of Individual Free Atoms

T. Bondo, M. Hennrich, T. Legero, A. Kuhn, and G. Rempe

Max-Planck-Institut für Quantenoptik, Hans-Kopfermann-Str. 1, 85748 Garching, Germany

E-mail: axel.kuhn@mpq.mpg.de

Abstract. We report on the detection of single, slowly moving Rb atoms using laser-induced fluorescence. The atoms move at 3 m/s while they are detected with a time resolution of 60 μs. The detection scheme employs a near-resonant laser beam, which excites a closed transition of the atoms, and a highly efficient mirror setup to focus a large fraction of the fluorescence to a photo-multiplier tube. On average, 20 photons per atom are counted.

1. Introduction

A tremendous number of experiments in atomic physics employ state-selective atom detection methods. An overview of the various detection techniques can be found in [1]. In many cases, these schemes are based on the interaction of atoms with laser light, which excites an atomic resonance [2]. The atoms manifest themselves by absorption, emission and dispersion of radiation, and all of these effects can be observed. However, for moving atoms, the number of scattered photons is usually too small to discriminate the presence of individual entities. The situation is different for trapped ions or atoms, where a closed transition between two energy levels can be excited. In this case, the atom cycles between these levels and spontaneously emits photons at a high rate. This allows one to detect individual particles, provided the interaction time with the exciting laser is long enough. Such schemes have been demonstrated successfully in several experiments, where either a single or a small number of atoms was observed in a dipole trap or a magneto-optical trap [3–5], or a single ion in a Paul-trap [6]. Even single molecules in solvents and solids have been detected in this way, since their relaxation rate to the ground state is so fast that they can emit more than one photon while they are observed [7, 8]. Only recently, it has been shown that a single atom's dispersion is sufficient to switch the transmission of a high-finesse Fabry-Perot type optical cavity [9, 10]. However, the

latter method is experimentally very challenging and far too complicated for simple single-atom detection.

Other methods for the detection of metastable particles are based on a release of their large internal energy. Such a process is destructive and does rarely allow to determine the inner state of the particle, but its extension to a multi-step detection method, like resonance enhanced multi-photon ionization [11, 12], is state selective and also allows for the detection of individual particles. However, the ionization process is not very efficient, and only a small fraction of the formerly neutral atoms gives rise to a signal.

In this article, we focus on laser-induced fluorescence which allows to monitor individual, freely moving atoms in a time-resolved and state-selective manner. The atoms are released from a magneto-optical trap (MOT) and arrive at the detector in **free** fall with a velocity of $v = 3\,\mathrm{m/s}$. The motion of the atoms limits the interaction time with the exciting laser beam to about $60\,\mu s$. Within this time interval, a significant number of photons is recorded from every atom, so that it's presence can be discriminated from the background noise. This is achieved with a highly efficient collection system for the emitted photons.

2. Collecting Photons

As spontaneous emission is not directed, an efficient detector must cover a large solid angle to collect a significant amount of fluorescence photons. Our collection optics resembles the one that has been developed for the spectroscopic detection of fast molecules [13–15]. Figure 1 shows our setup, which is a combination of an ellipsoidal and a spherical coated aluminium mirror. It covers a solid angle close to 4π, provided the atoms fluoresce in the left focal point of the ellipsoid. Photons going to the left hit the ellipsoidal mirror and are focused to the right focal point of the ellipsoid. Photons going to the right hit the spherical mirror, are reflected back to their origin, and leave this point to the left towards the ellipsoidal mirror. Finally, they are also focused to the right focal point of the ellipsoid. However, the atoms are not well localised but move through the probe laser beam that excites them in a fluorescing volume of about $1\,\mathrm{mm}^3$ around the first focal point. In addition, holes in the mirrors are necessary to allow the probe beam and the atoms to enter the detector, and to finally extract the fluorescence photons. These geometrical restrictions limit the collection efficiency to about 80 %. We also note that the surface of the hollow mirrors is far from being perfect. The coated aluminium surface shows a reflectivity of only 80 %, therefore the total collection efficiency of the mirror setup is limited to 64 %.

Furthermore, the design of our apparatus did not allow placing the cathode of a photo-multiplier tube (PMT) directly in the second focal point. A telescope consisting of an aspheric condenser lens ($f = 35\,\mathrm{mm}$), a planoconvex lens ($f = 100\,\mathrm{mm}$), and a biconvex lens ($f = 70\,\mathrm{mm}$) is used to image the photons onto the PMT, which is located outside the vacuum chamber. To reduce the background of visible radiation to
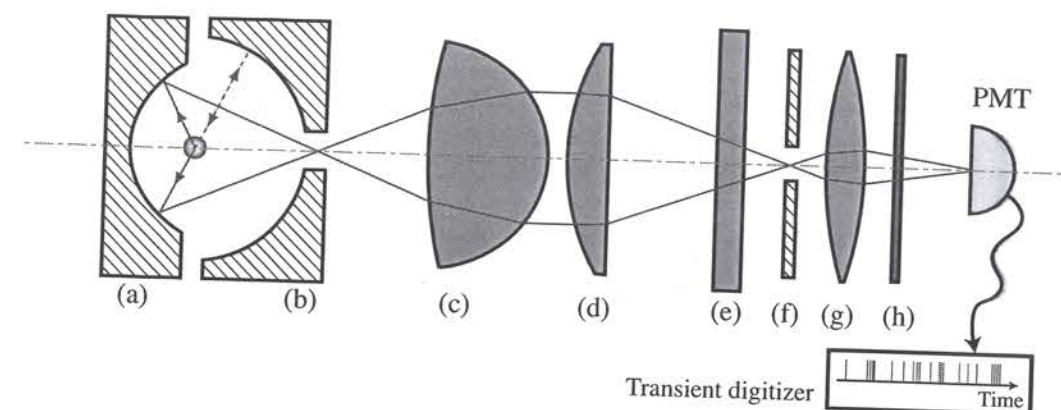
Figure 1. Fluorescence collection and imaging system (not to scale): An ellipsoidal mirror (**a**) and a spherical mirror (**b**) collect the photons which are emitted from one focal point of the ellipsoid. The photons are imaged to the second focal point of the ellipsoid. From there, a telescope consisting of lenses (**c**) and (**d**) focuses them through the window of the vacuum chamber (**e**) onto an aperture (**f**), which acts as a spatial filter. Finally, they are imaged by the biconvex lens (**g**) through a bandpass filter (**h**) onto the cathode of a photomultiplier tube (**PMT**). The events from the PMT are recorded by a transient digitizer.

an acceptable level, a 10 nm wide band-pass filter is used. Moreover, a spatial filter in the image plane of the telescope between the second and third lens is used to reduce light scattered from the edges of the hollow mirrors.

All the elements of the imaging system lead to a further attenuation of the light. The telescope lenses and the window of the vacuum chamber have a transmission of 99 % each, the band-pass filter transmits 70 %, and the uncoated double-window of the PMT's cooling chamber 85 %. We must also take into account that the rather large observation volume is not focused perfectly onto the PMT, since it is not completely covered by the acceptance angle of the condenser lens. We estimate that as much as 1/3 of the photons are lost by these geometric effects. Hence, the collection efficiency of the whole setup (mirrors, lenses, windows and filters) amounts to about 25 %. The remaining photons are imaged onto the photocathode of a Hamamatsu R943-02 photomultiplier tube, with a quantum efficiency of 12 %. Therefore the overall detection efficiency is estimated to be 3 %.

3. Fluorescence Signal

Many atomic species provide a closed two-level system, i.e. a non-decaying stable energy level and an electronically excited level, which decays exclusively to the stable one. In a dilute gas, collisional losses can be neglected, and if the transition between the two levels is driven by a probe laser, the atom cycles between these levels, and a photon is emitted spontaneously whenever a decay from the excited level occurs. In our experiment, the probe laser with a wavelength of $\lambda = 780\,\mathrm{nm}$ excites the $5S_{1/2}(F = 3) \longleftrightarrow 5P_{3/2}(F' = 4)$ transition of $^{85}\mathrm{Rb}$ (see fig. 2). In the limit of strong saturation and resonant excitation,
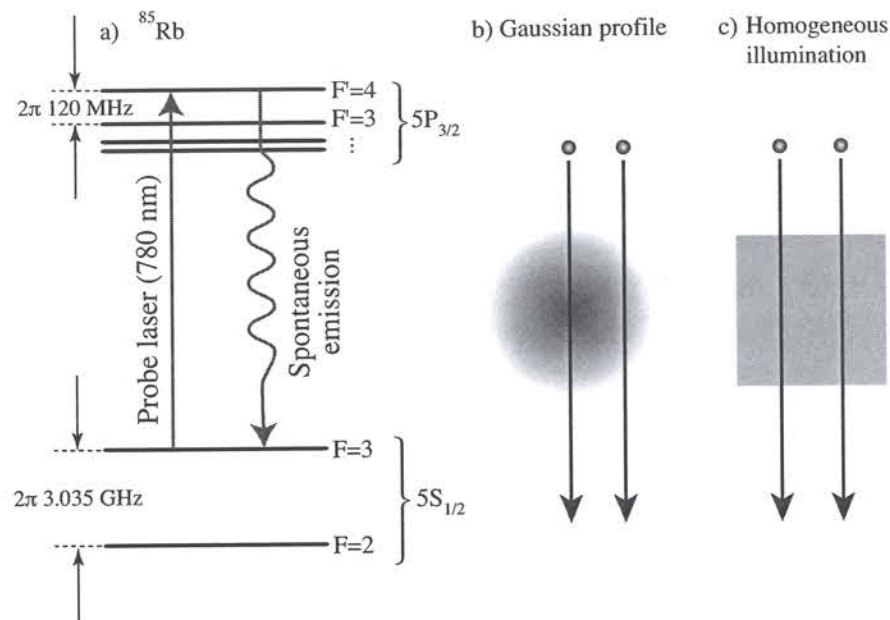
Figure 2. Detection of ^{85}Rb atoms by laser-induced fluorescence: (a) The $5S_{1/2}(F = 3) \longleftrightarrow 5P_{3/2}(F' = 4)$ transition provides a (nearly) closed two-level system and is used to probe the atoms. (b) Atoms traveling through a Gaussian probe beam are exposed to different peak intensities depending on their individual trajectories. This gives rise to an ambiguous fluorescence signal, since the duration of the photon burst and the number of photons per atom depend on the atom's trajectory with respect to the beam axis. (c) A clear signal is obtained from atoms interacting with a rectangular, homogeneously illuminated area, since all atoms experience identical conditions. The number of emitted photons does not depend on the atom's trajectory, and the interaction time is well-defined. To achieve these conditions, we illuminate a small rectangular aperture with a large laser beam and image the aperture onto the atoms.

the spontaneous photon-emission rate, Γ, approaches $\gamma/2$ per atom, where γ is the spontaneous decay rate of the excited level. However, the probe laser intensity, I, is finite, the probe laser can be detuned from the atomic resonance by an amount Δ, and any velocity of the atom with respect to the probe beam, $v_\parallel$, gives rise to a Doppler shift. Therefore the photon emission rate reads

$$\Gamma(I, \Delta, v_\parallel(t)) = \frac{\gamma}{2} \frac{I}{I + I_{sat}\left(1 + \left(\frac{\Delta - k v_\parallel(t)}{\gamma/2}\right)^2\right)}, \quad (1)$$

where $k = 2\pi/\lambda$ and the saturation intensity, averaged over all magnetic sublevels of the considered transition, is $I_{sat} = 3.9\,\text{mW/cm}^2$. We assume that I and Δ do not change during the interaction of the atoms with the probe beam, but we take into account that the atoms are accelerated because of light pressure. For each spontaneously emitted photon (with an average momentum transfer of zero), a probe photon is absorbed and the atom's velocity changes by the recoil velocity, $v_{rec} = \hbar k/m$, in the direction of the

---

laser beam. This acceleration continues according to

$$\frac{d}{dt}v_\parallel = v_{rec}\Gamma(I, \Delta, v_\parallel(t)), \quad (2)$$

until the atom is Doppler shifted out of resonance and stops fluorescing. Figure 3(a) shows the average fluorescence duration of ^{85}Rb atoms as a function of the probe-beam height, Δz. The interaction time of the atoms with the beam is given by $\Delta\tau = \Delta z/v$. For $\Delta\tau \leq 60\,\mu s$, the dependence is almost linear and the fluorescence duration equals
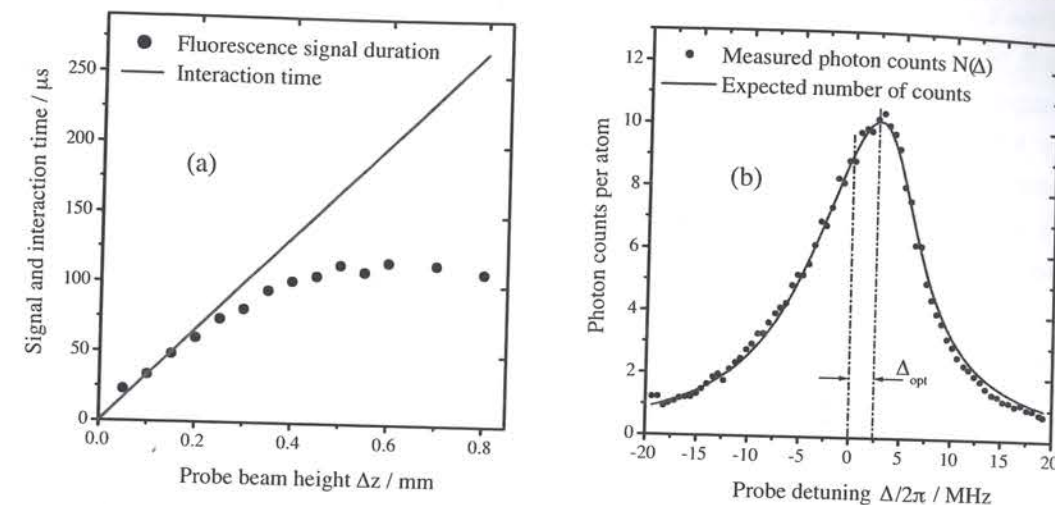
Figure 3. Fluorescence duration and spectrum for a three-fold saturated probe transition:

(a): Duration of the observed fluorescence from individual atoms, which are crossing the probe beam with a perpendicular velocity $v_\perp = 3\,\text{m/s}$, as a function of the probe-beam height, Δz, for $\Delta = +\gamma$. The solid line shows the transit time of the atoms through the rectangular beam.

(b): Average number of photon counts, $N(\Delta)$, per atom in $\Delta\tau = 50\,\mu s$ as a function of the probe detuning, Δ. The solid line shows the expected photon number, $N_{phot}(\Delta)$, which is obtained by numerically solving Eq. (3). Its amplitude is scaled down by a factor 58 to meet the experimental data, which is reduced due to the limited detection efficiency of the system.

$\Delta\tau$. For longer interaction times, the fluorescence duration is limited to $120\,\mu s$, due to the acceleration of the atoms and also possible losses to the $5S_{1/2}(F = 2)$ level, as will be discussed later. Hence, we must integrate Eqs. (1,2) in order to obtain the total number of fluorescence photons per atom,

$$N_{phot} = \int_0^{\Delta\tau} \Gamma(I, \Delta, v_\parallel(t))dt. \quad (3)$$

Figure 3(b) shows that the acceleration has a significant influence on the number of emitted photons, even for $\Delta\tau$ as small as $50\,\mu s$. The maximum number of photons is counted when the probe beam is blue detuned from the atomic resonance by $\Delta_{opt} = 2\pi \times 2.4\,\text{MHz}$ (i.e. $\Delta_{opt} = 0.4\gamma$, with $\gamma(^{85}\text{Rb}) = 2\pi \times 6\,\text{MHz}$). In this case, the interaction starts slightly off-resonance, but then the atoms are pushed into resonance and finally accelerated out of resonance again. Provided this transient Doppler shift

is symmetric with respect to resonance, the number of emitted photons reaches its maximum. Therefore the optimum detuning depends on the probe intensity and the chosen interaction time. For the parameters given in the caption of fig. 3, $N_{phot} = 580$ photons per atom are expected.

It must be noted that the acceleration could be balanced by a second, counter-propagating probe beam, which provides the same excitation probability as the first one. However, there was no need to investigate this situation, simply because the required time to detect a single atom, $\Delta\tau$, is shorter than the time it takes to accelerate an atom out of resonance.

For longer interaction times, another loss mechanism becomes significant. The small probability to excite a ^{85}Rb atom accidentally to $5P_{3/2}(F' = 3)$ cannot be neglected, simply because the probe laser (resonant with the $5S_{1/2}(F = 3)$ to $5P_{3/2}(F' = 4)$ transition), is only detuned by $2\pi \times 121$ MHz from the from $5S_{1/2}(F = 3)$ to $5P_{3/2}(F' = 3)$ transition. By spontaneous emission from $5P_{3/2}(F' = 3)$, the atoms can then decay to $5S_{1/2}(F = 2)$, where they remain "in the dark", i.e they are no longer excited by the probe laser due to the $2\pi \times 3$ GHz hyperfine splitting between the $5S_{1/2}(F = 2)$ and the $5S_{1/2}(F = 3)$ states. However, even for a 2.7-fold saturated probe transition, the time needed to pump the atom into the other hyperfine state is about $130\,\mu s$ and, hence, significantly longer than $\Delta\tau$. Therefore, these losses can be neglected and no second laser is needed to repump the atoms into the $5P_{3/2}(F = 3)$ level.

Taking into account all these considerations, we expect, on average, $N_{phot} = 660$ photons per atom for $I/I_{sat} = 2.7$, $\Delta\tau = 60\,\mu s$ and an optimal probe detuning $\Delta_{opt} = 0.43\,\gamma$. Due to the 3% detection efficiency of the collection system and the PMT, 20 photons per atom can be actually counted.

4. Signal Analysis

To characterize the performance of the detector, we analyze the stream of events from the PMT. An example of a typical signal is shown in fig. 4, which has been recorded with an average atom number in the observation volume far below one, i.e. the rate of atoms entering the detector, R_A, was lower than the reciprocal interaction time, $\Delta\tau^{-1}$. Several bursts of events, well separated from each other, can be distinguished. We attribute these bursts to single atoms that emit fluorescence photons at a rate R_P while they interact with the probe beam. This gives rise to an intermittend increased photon-detection rate, R_E, which is significantly higher than the average noise-count rate, R_N. From Fig. 4, it is also obvious that these noise counts, which are mainly caused by scattered probe light, cannot be neglected.

The second order autocorrelation, $g^{(2)}(\tau)$, of the measured photon stream is well suited for the further analysis. It should only depend on the rates R_A, R_E, R_N, and $\Delta\tau$, and it is defined as

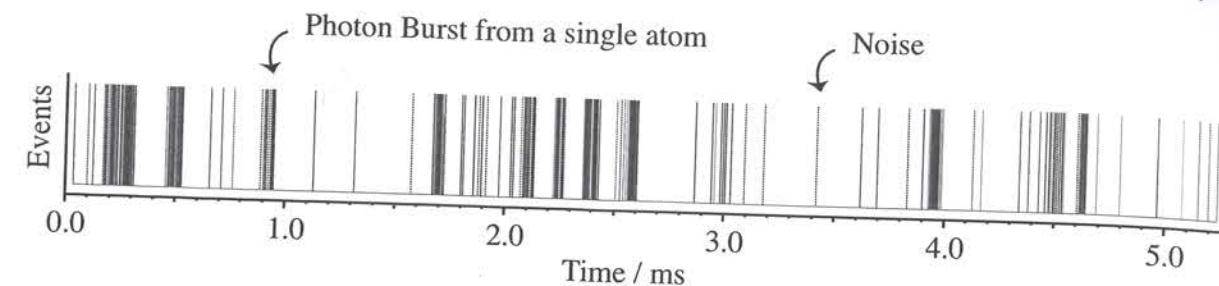$$g^{(2)}(\tau) = \frac{\langle p(t)p(t-\tau)\rangle}{\langle p(t)\rangle^2}, \tag{4}$$

Figure 4. Stream of photons detected by the photomultiplier. A burst of events indicates the presence of an atom, whereas single events between the bursts belong to background noise.
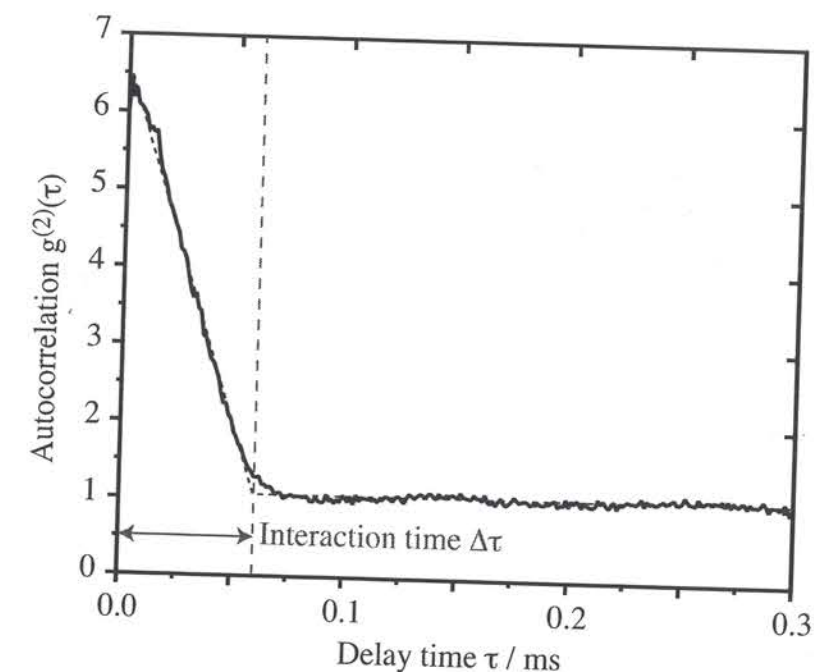

Figure 5. The solid line shows the autocorrelation of a 524 ms long stream of PMT events. Since every falling cloud of atoms is observed for 5.4 ms, a total number of 100 experimental cycles was needed to produce this data. The dashed line is a fit of Eq. (5) to the measured data, and the vertical line indicates the interaction time $\Delta\tau$.

where $p(t)dt$ is the probability to observe a photon in the time interval $[t \ldots t + dt]$. Photons from different atoms are not correlated, and since photons from one-and-the-same atom are emitted only within the interaction time $\Delta\tau$, $g^{(2)}$ must equal *one* for $\tau > \Delta\tau$. If we assume that the event rate R_E is constant while an atom interacts with the probe laser, a linear decrease of $g^{(2)}(\tau)$ is expected in the range $0 \leq \tau \leq \Delta\tau$, and a simple calculation leads to the analytical expression

$$g^{(2)}(\tau) = \begin{cases} 1 + \frac{R_A R_E^2}{(\Delta\tau R_A R_E + R_N)^2}\frac{(\Delta\tau - |\tau|)}{1} & \text{for} \quad |\tau| \leq \Delta\tau \\ 1 & \text{for} \quad |\tau| > \Delta\tau. \end{cases} \tag{5}$$

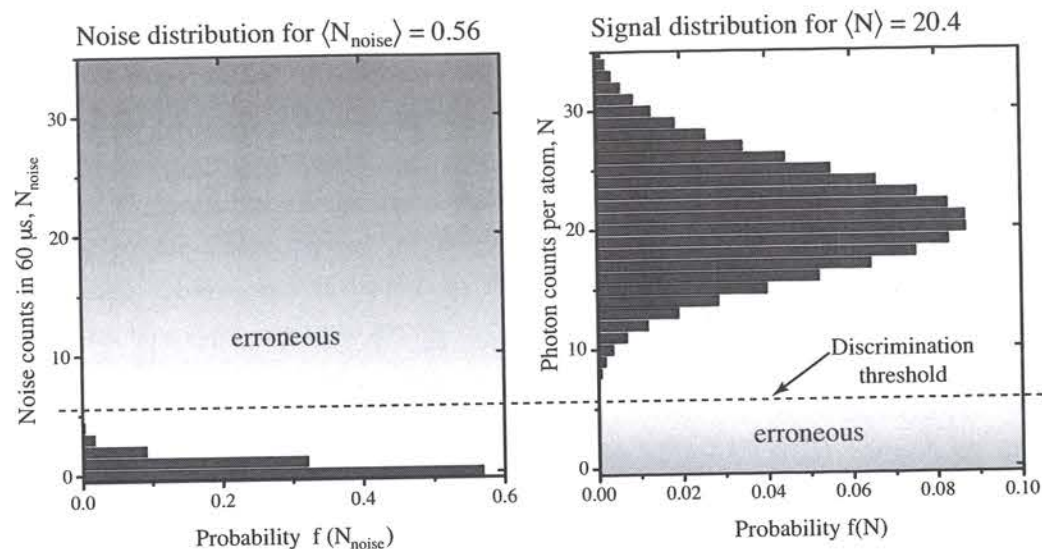Note that this simple model neglects the anti-bunching of the sub-Poissonian light

Figure 6. Assumed Poissonian distribution of the number of noise (left) and signal (right) events for a measurement interval of $\Delta\tau = 60\,\mu s$. The discrimination level is indicated and the corresponding erroneous regions are shown as shaded areas.

emitted from single atoms [17]. This is well justified since this effect is only visible on a sub-μs time scale and therefore is not resolved with a single photo multiplier.

In the experiment, the noise rate, R_N, and the total event rate, $R = R_N + \Delta\tau R_E R_A$, are measured separately. Using these two values as fixed parameters, a fit of $g^{(2)}(\tau)$ from Eq. (5) to the autocorrelation of the experimental data, calculated according to Eq. (4), allows us to determine the average number of events per atom, $\langle N \rangle = \Delta\tau R_E$, and the average duration of an atom's photon burst, $\Delta\tau$. Figure 5 shows the autocorrelation of a typical signal, together with the best fit to this data, yielding $g^{(2)}(0) = 6.60 \pm 0.03$ and $\Delta\tau = 60.7 \pm 0.3\,\mu s$. From these fit parameters, the measured noise rate, $R_N = 9.4 \pm 0.13\,kHz$, and the total number of 22232 photon events in 524 ms (i.e. $R = 42.4 \pm 0.29\,kHz$), we know that a single atom causes an average number of $\langle N \rangle = 20.4 \pm 0.3$ events. This is in good agreement with the theoretical expectation, $N = 20$.

For the time-resolved detection of single atoms, it is essential to discriminate their signal from the background noise. Unfortunately, this noise is mainly caused by light scattered from the probe beam. Hence, it has the same wavelength as the fluorescence photons and cannot be eliminated by interference filters. However, spatial filtering reduces the noise rate to $R_N = 9.4\,kHz$ for a 2.7-fold saturated probe laser with an intensity of $10\,mW/cm^2$, a height of 0.2 mm and a width of 0.7 mm. Under these circumstances, the event rate rises to $R_E \approx 340\,kHz$ when an atom is in the observed volume, and the signal-to-background-noise ratio is ≈ 36. In the interesting time interval of $\Delta\tau = 60\,\mu s$, an average number of noise events, $N_{noise} = 0.56$, is expected, while the average number of events for a single atom is $\langle N \rangle \approx 20.4$. Figure 6 shows a Poissonian probability distribution of the noise and the signal events for a $60\,\mu s$ long discrimination
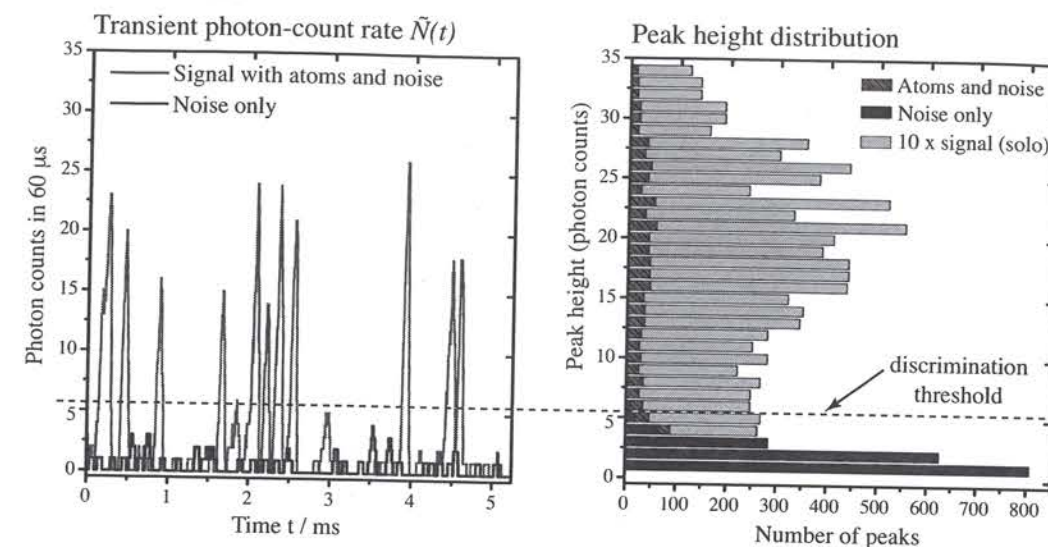
Figure 7. Peak height analysis of the measured signal. **Left:** Photon-detection rate (number of counts in $60\,\mu s$) as a function of time. The evaluation makes use of an integration interval which is sliding smoothly along the stream of measured events, not of a fixed grid with $60\,\mu s$ spacing. Hence, for each peak, the borders of the corresponding interval coincide with the atom's arrival and departure times. For comparison, the same analysis is also shown for the noise level (without atoms). **Right:** Measured distribution of the peak count rates. Since only peaks are considered, there's no signal found with *zero* counts.

interval. For these distributions, the optimum threshold to distinguish atoms from noise is $N \geq 6$. The possible errors can be estimated from Poissonian statistics: On the one hand, the probability to attribute more than five noise events in an arbitrarily chosen $60\,\mu s$ long interval to be due to an atom is as low as 0.0027 %, i.e. with a probability of 21 % the noise gives rise to a single "fake atom" during the total measurement time of 524 ms. On the other hand, the probability to miss an atom because it does not emit enough photons is only 0.0034 %, i.e. 0.03 atoms from the 945 atoms counted in 524 ms are missing, which is negligible.

Based on these considerations, we determine the arrival times of individual atoms from the registered photon stream with the help of the transient photon-count rate, $\tilde{N}(t)$, which is defined as the number of photons counted in the interval $[t \ldots t + \Delta\tau]$. For every time t that coincides with the arrival time of an atom, all its photons fall into this interval, and $\tilde{N}(t)$ reaches a peak value that coincides with the number of photons emitted from the atom. Figure 7(a) shows the transient photon-count rate that belongs to the data from Fig. 4. We easily identify several peaks above threshold which indicate the arrival times of single atoms. For comparison, a trace without atoms is also shown, and obviously, the signal is always below the threshold for atom detection. Figure 7(b) shows the distribution of the peak heights for two photon streams, one with atoms, and the other one without. Some deviations from the ideal situation are evident. The numbers of detected photons per atom, N, scatter over a much larger range than

expected from Poissonian statistics. We attribute this large variation to the different Clebsch-Gordan coefficients of the randomly populated magnetic sublevels, which give rise to a large variation of the saturation intensities of the involved transitions, i.e. $I_{sat} \approx 2.9 \ldots 6.6\,\mathrm{mW/cm^2}$ for π-polarized light, and $I_{sat} \approx 1.6 \ldots 46.4\,\mathrm{mW/cm^2}$ for σ-polarized light. However, it is evident that most atoms can be well distinguished from noise, which itself is never identified as a "fake atom".

5. Summary

We have shown that laser-induced fluorescence from a saturated and (nearly) closed two-level atomic transition allows to monitor single, free moving atoms with a time resolution of $60\,\mu s$. To collect the emitted photons, a mirror setup covering a very large solid angle is used, which focuses the photons onto a photo multiplier. A careful analysis of the measured data based on a second-order autocorrelation shows that, on average, 20.4 photons per atom are detected. In case of a Poissonian distribution of noise and signal events, this signifies that a single atom is detected with 99.9966 % certainty, while noise counts exceed threshold with a negligible probability of 0.0027 %. Such a fluorescence detector represents a useful tool for many experiments in atomic physics, where a state-selective detection of single, freely moving atoms is required. In principle, even the time resolution could be improved significantly by replacing the photomultiplier tube with a silica-based avalanche photodiode, which provides a 5-times higher quantum efficiency.

Acknowledgments

References

[1] C. Th. J. Alkemade, "Single-atom detection," Appl. Spect. **35**, 1-14 (1981)

[2] V. I. Balykin, G. I. Bekov, V. S. Lethokov, and V. I. Mishin, "Laser detection of single atoms," Sov. Phys. Usp. **10**, 651-678 (1981)

[3] Z. Hu and H. J. Kimble, "Observation of a single atom in a magneto-optical trap," Opt. Lett. **19**, 1888-1890 (1994)

[4] F. Ruschewitz, D. Bettermann, J. L. Peng, and W. Ertmer, "Statistical investigations on single trapped neutral atoms," Europhys. Lett. **34**, 651-656 (1996)

[5] D. Haubrich, H. Schadwinkel, F. Strauch, B. Ueberholz, R. Wynands, and D. Meschede, "Observation of individual neutral atoms in magnetic and magneto-optical traps," Europhys. Lett. **34**, 663-668 (1996)
    D. Frese, B. Ueberholz, S. Kuhr, W. Alt, D. Schrader, V. Gomer, and D. Meschede, "Single atoms in an optical dipole trap: Towards a deterministic source of cold atoms," Phys. Rev. Lett. **85**, 3777-3780 (2000)

[6] W. Neuhauser, M. Hohenstatt, P. Toschek, and H. Dehmelt, "Optical-sideband cooling of visible atom cloud confined in parabolic well," Phys. Rev. Lett. **41**, 233-236 (1978)

[7] S. A. Soper, Q. L. Mattingly, and P. Vegunta, "Photon burst detection of single near-infrared fluorescent molecules," Anal. Chem. **65**, 740-747 (1993)

[8] Y.-H. Lee, R. G. Maus, B. W. Smith, and D. Winefordner, "Laser-induced fluorescence detection of a single molecule in a capillary," Anal. Chem. **66**, 4142-4149 (1994)

[9] H. Mabuchi, Q. A. Turchette, M. S. Chapman, and H. J. Kimble, "Real-time detection of individual atoms falling through a high-finesse optical cavity," Opt. Lett. **21**, 1393 (1996)

[10] P. Münstermann, T. Fischer, P. Maunz, P. W. H. Pinkse, and G. Rempe, "Dynamics of single-atom motion observed in a high-finesse cavity," Phys. Rev. Lett. **82**, 3791–3794 (1999)

[11] G. S. Hurst, M. G. Payne, S. D. Kramer, and J. P. Young, "Resonance ionization spectroscopy and one-atom detection," Rev. Mod. Phys. **51**, 767-819 (1979)

[12] V. S. Lethokov, "Laser photoionization spectroscopy of single atoms and molecules," Optica Acta **32**, 1191-1210 (1985)

[13] K. Bergmann, R. Engelhardt, U. Hefter, and J. Witt, "A detector for state-resolved molecular beam experiments using optical fibres," J. Phys. E **12**, 507 (1979)

[14] K. Shimizu and F. Shimizu, "Laser induced fluorescence spectra of the $a^3\Pi_u - X^1\Sigma_g^+$ band of Na_2 by molecular beam," J. Chem. Phys. **78**, 1126 (1983)

[15] U. Hefter and K. Bergmann, "Spectroscopic detection methods" in "Atomic and molecular beam methods," Vol. 1, ed. G. Scoles, Oxford Univ. Press, Oxford, NY (1988)

[16] P. Westphal, S. Koch, A. Horn, J. Schmand, and H. J. Andrä, "Compact and freely movable single atom detector," Rev. of Scientific Instr. **70**, 1326-1332 (1999)

[17] H. J. Kimble, M. Dagenais, and L. Mandel, "Multiatom and transit-time effects on photon-correlation measurements in resonance fluorescence," Phys. Rev. A **18**, 201-207 (1978)

Mein Herzlicher Dank